Université du Québec
en Outaouais (UQO)

Experimental Characterization and Modeling of Short-Range Wireless Propagation Channels in the Unlicensed 60 GHz Band

by

MOHAMAD GHADDAR

Thesis Submitted to the
Department of Computer Science & Engineering
In partial fulfillment of the requirements for the degree of

Philosophiae Doctor (Ph.D.)

en Sciences et technologies de l'information

Members of jury:

Chairman	*L. Logrippo, Ph.D., UQO*
Examiners	*Wojtek Bock, Ph.D., UQO* *Jean-Yves Chouinard, Ph.D., Université Laval* *Mohamed El-Tanany, Ph.D., Carleton University*
Thesis supervisor	*Larbi Talbi, Ph.D., UQO*
Co-supervisor	*Gilles Y. Delisle, Ph.D., UQAT*

Preface

In the recent half decade, an enormous expansion of research activities in telecommunications field occurred to satisfy the emerging growing demands for modern and future 4G short-range wireless communication systems. A great number of indoor HDMI cable replacement applications have appeared in the market, and emphasized the need for robust, very high data rate radio communication systems. Among the HDMI cable replacement applications is the uncompressed high definition (HD) video streaming, downloading from a wireless kiosk, synchronization, Wireless gaming, etc. Such applications require data rates of up to several Gbps. In accordance with Shannon's theorem, such data rates can be achieved by employing wide bandwidths and high allowable transmit power. Power limitation and spectrum congestion is predominantly the main obstacle that restrains RF technology and prevents it from being a potential solution for future generation high-speed communications. Hence, the millimeter (mm)-waves band (30 – 300 GHz) appears relevant to be explored as an alternative for short-range applications as it meets the requirements for sufficient bandwidth, small terminal dimensions and sporadic usage for commercial applications. In the 60 GHz band, the Federal Communications Commission (FCC) and many other countries have allocated 7 GHz of unlicensed spectrum between 57 and 66 GHz. Furthermore, a maximum of 27 dBm of effective isotropic radiated power (EIRP) is approved by the FCC in this band. Today, extensive research and standardization activities are being carried out for indoor communications in the 60 GHz band.

Despite their advances, 60 GHz technologies still present many technical challenges, due to the very short wavelength; the challenges are related to the fact that the characteristics of the propagation channel are more sensitive to the environmental changes than those for traditional WLAN operating at lower-frequency bands. Mm-waves band is still a new area to be explored, and up to date, there is a little known about the propagation characteristics in this band. More propagation measurements and models are needed to support a comprehensive understanding of the propagation characterization for future 60 GHz WLANs. Indoor broadband channel modeling

in extremely high frequencies poses the problem of the accurate description of the propagation at the mm wavelength.

In the literature, typical corridors and office environments have drawn special interests; they are known to be among the most important for indoor high speed applications. This research work involves the measurements and analysis of the propagation characteristics in such environments. Also, analytical deterministic ray-based channel models are derived to validate the frequency dependent experimental data obtained from the considered environments. Such models are very promising tools for engineering applications to analyse theoretically the diverse aspects of the 60 GHz broadband channels and hence, to provide a comprehensive and deep knowledge about their propagation behaviour.

Abstract

This thesis reports broadband propagation measurements and modeling results for indoor wireless local area network (WLAN) applications in the unlicensed 60 GHz band. Based on sweeping-frequency sounding technique (59.6 – 60.6 GHz), the propagation measurements are carried out in two typical indoor environments; a) non-line-of-sight (NLOS) T-shaped intersection of two long corridors at a distance range exceeding 20 meters, with and without the presence of deflecting obstacles (DOs). b) line-of-sight (LOS) rectangular conference room.

On the basis of geometric ray-tracing (RT), deterministic models are derived for the considered environments. Predicted and experimental results are based on the use of directive antennas at both remote terminals in the corridors; however, an omnidirectional conical antenna is used at the remote receiving end for the conference room. The channel transfer functions (CTFs) and the power delay profiles (PDPs) obtained from the RT tool are then compared with the experimental data for each of the considered environments. An interesting agreement is achieved between the predicted and the experimental results in both frequency and time domains. Results demonstrate that mm-waves communications are very susceptible to the propagation environment compared with low frequency bands. In NLOS corridors environment, signal transmission relies mainly on the unavoidable diffraction phenomenon from the intersection corners. However, in the case of LOS conference room and unlike lower frequency bands, rays undergo third order-reflections and higher but these are not important due to the high signal absorption by walls at 60 GHz.

Furthermore, an experimental characterization of the measured propagation data in the considered scenarios is reported in this thesis. The statistical parameters of the multipath propagation characteristics, such as the channel coherence bandwidth, the path loss exponent law (n), the statistics of the RMS delay spread and the shadowing, are evaluated. In the NLOS corridors under consideration, the experimental results show that NLOS mm-wave propagation characteristics are very complex where a severe path loss is recorded; however the presence of transmission route deflecting obstacles (DO) in the intersection has enhanced significantly the propagation characteristics and provided better signal quality and wider coverage to become comparable to LOS channels. The presented measurements and empirical models may aid the development of futuristic mm-wave radio system in short-range wireless applications.

Acknowledgment

First of all, I would like to express my gratitude to my research supervisor, *Dr. Larbi Talbi* who agreed to lead this work by welcoming me in his research team. It was very interesting to work closely with him and thereby gain his expertise. His help and support will always be greatly appreciated.

Also, I would like to thank *Dr. Jules LeBel*, researcher, in the Communication Research Center (CRC) and his team for the achievement of the measurement system. I would like to thank him for the great facilities he provided at the CRC laboratories and for giving me the opportunity to gain an extensive experience in RF measurement system design.

I am grateful to *Dr. Gilles Delisle*, for guiding me during this work and for his efforts and time on reviewing the thesis, his suggestions and revisions related to the submitted papers, and especially for offering his financial support.

Special thanks to *Dr. Luigi logrippo*, professor at UQO for kindly chairing the jury of this thesis. I also wish to thank *Dr. Mohamed El-Tanany,* professor at Carleton University and *Dr. Jean-Yves Chouinard,* professor at Laval University, for accepting to review this thesis and to be members of the jury.

Finally, the research work presented in this dissertation could not have been achieved without the support of my wonderful family, especially, my lovely wife and kids. Being a full time student means being a part time husband and father. They never hesitated to provide me with constant comfort through hardship and life's fluctuations.

Dedication

To my family, especially
my lovely wife, who has always been a great supportive of my success
and educational endeavors,
my sweet daughter Leah,
my wonderful son Hashem,
and special friends

Table of Contents

List of Tables

List of Figures

Glossary

2D	Two Dimensions
3D	Three Dimensions
4G	Fourth Generation
ADC	Analog to Digital Converters
AoA	Angle of Arrival
AoD	Angle of Departure
APS	Antennas and Propagation Society International Symposium
AWGN	Additive White Gaussian Noise
Bc	Coherence Bandwidth
BER	Bit Error Rate
BPSK	Binary Phase Shift Keying
CCECE	Canadian Conference on Electrical and Computer Engineering
CDF	Cumulative Distribution function
CTF	Channel Transfer Function
cm	Centimeter
CMOS	Complementary Metal-oxide-semiconductor
CP	Cyclic Prefix
CRC	Communication Research Center
CW	Continuous wave
DAQ	Data Acquisition System
dB	Decibel (ratio in log scale)
dBi	Decibel isotropic
dBm	Decibel relative to 1 milliwatt
DC	Direct Current (0 Hz)
DDS	Direct Digital Synthesizer
DO	Deflecting Obstacle
E	Electric field
ECMA	European Computer Manufacturers Association
EHF	Extremely high frequency
EIRP	Effective Isotropic Radiated Power
FCC	Federal Communications Commission
FD	Frequency Domain
FEC	Forward Error Correction
FFT	Fast Fourier Transform
FSL	Free Space Loss
Gbps	Giga bits per second
GHz	Gigahertz
GO	Geometrical Optics
G_R	Receiving Antenna Gain
G_T	Transmitting Antenna Gain

GTD	Geometrical Theory of Diffraction
H	Magnetic field
HD	High Definition
HDMI	High definition Multimedia Interface
I	In-phase
ICI	Inter Carrier Interference
IDFT	Inverse Discrete Fourier Transform
IFFT	Inverse Fast Fourier Transform
ISB	Incident Shadow Boundary
ISI	Inter-Symbol Interference
K	Rician factor
k	Wavenumber
kHz	Kilohertz
km	Kilometer
LOS	Line Of Sight
MAC	Media Access Control
Mbps	Megabits per second
MPC	Multipath Component
MS	Microwave Scatterer
Msps	Mega symbols per seconds
NLOS	No Line Of Sight
n	Path loss exponent
ns	nano-seconds
OFDM	Orthogonal Frequency Division Multiplexing
P2P	Point to point
PA	Power Amplifier
PAL	Phase Alternating Line
PCs	Personal Communication Systems
PDF	Probability Density Function
PDP	Power Delay Profile
PHY	Physical layer
PL	Path Loss
P_R	Received Power
P_T	Transmitted Power
Q	Quadrature
QAM	Quadrature Amplitude Modulation
QoS	Quality of Service
QPSK	Quadrature Phase Shift Keying
RC	Raised Cosine (Guard Period)
RF	Radio Frequency
RMS	Root Mean Squared
RSB	Reflection Shadow Boundary
RT	Ray Tracing
RVs	Random Variables
SiGe	Silicon-germanium
SNR	Signal to Noise Ratio
TD	Time Domain

Tx	Transmitter
Rx	Receiver
USB	Universal Serial Bus
UTD	Uniform Theory of Diffraction
UWB	Ultra Wide Band
VNA	Vector Network Analyzer
WCDMA	Wideband Code Division Multiple Access
WDR	Wide Dynamic Range
WiFi	Class of wireless local area network (WLAN) devices based on the IEEE 802.11 standards.
WiGig	Wireless Gigabit Alliance
WiMAX	Worldwide Interoperability for Microwave Access
WLAN	Wireless Local Area Network
WPAN	Wireless Personal Area Network
WSSUS	Wide Sense Stationary Uncorrelated Scattering
WVAN	Wireless Video Area Network
X_σ	Zero-mean Gaussian-distributed random variable
σ_τ	RMS delay spread
τ	mean excess delay
λ	Wavelength
ε_r	Relative Permittivity
σ	Conductivity
Δf	Frequency Separation
$\rho(\Delta f)$	Correlation Coefficient

Chapter 1

Mm-waves Communications Architecture

1.1 Introduction

In the recent half decade, an enormous expansion of research activities in telecommunications field occurred, to satisfy the emerging growing demands for modern and future 4G short range[1] wireless communication systems. As expected, multimedia technologies and indoor HDMI cable replacement applications of the next decade will need to support a reliable data transmission in excess of hundreds of Mbps to few Gbps. Among these applications is the uncompressed high definition (HD) video streaming that enables users to control and display heavy content of information to a remote screen wirelessly, without the use of high speed cables clutters or optics. This type of application requires data rates in the range exceeding 1 Gbps up to several Gbps. Similar data rates are expected for instant content downloading from a wireless kiosk and the regular synchronization which requires gigabytes of file transfer in just few seconds. Also, high-quality wireless gaming that ensures to satisfy users desire to fully control the game without the cables clutters etc. [1]–[4].

When it comes to high data rate connectivity, certainly conventional cabled networks show a very high level of functionality along with the advance of fiber optics connections. Nowadays, various cable types still exist in the market; they are classified depending on their performance and on their applications. For example, the USB cables are quite popular for PCs, the Fire Wire (IEEE 1394) is still used for some multimedia such as home entertainment and digital subscriber line, Ethernet, fiber optics and so on.

1 What is called “short-range” in other contexts means for distances of up to 10 meters. In this thesis the term “short range” may be intended for distances of up to 20 meters.

Despite the fact that cables are certainly very efficient for data transmission rate, however, they exhibit their catastrophic drawbacks as well: Cables are predominantly point to point communications; their lengths are fixed and show no flexibility. Beside the malformed sight, especially when there is a large clutter of cables; wired networks infrastructures are extremely difficult and expensive for carriers to build and maintain in each service access point. Also, cables of portable devices must be always carried around and connectivity matching is mostly daunting. To satisfy modern life facilities, the adoption of computerized information technologies requires a high level of freedom of connectivity "anytime, anywhere" inside and between buildings, automobiles and work places. Of course, this cannot be realized with the use of physical wired networks infrastructures.

Ever since Marconi's first experiments in the late 19th century, there has been a big interest in the possibilities of wireless communications. Since then, wireless links have gone from only being capable of unreliable and low-rate transmissions to the high-capacity networks we see today. Hence, electromagnetism is a paramount to develop the wireless connections that can provide the benefits of the high data rate cables and can be quite appealing to the average consumers. Under these circumstances, high speed wireless communications has become one of the most promising areas for the growth in the 21st century and emerged as one of the largest sectors of the telecommunications industry. The multimedia content to be wirelessly transferred amongst these devices is richer than ever before, requiring higher connection speeds and quality of service (QoS) than afforded by available standard technologies. Clearly, the trend is towards higher throughput and lower latency requirements in the future.

Presently, there are numbers of existing wireless networks namely; Wideband Code Division Multiple Access (WCDMA), as well as Wireless Local Area Networks (WLAN) such as Wi-Fi (IEEE 802.11), Wireless Personal Area Network (WPAN) as Bluetooth and other wireless technologies. So far, the most common and useful option of wireless networking solution is Wi-Fi (IEEE 802.11 a/b/g). This service offers a moderate throughput in the range of few tens of Mbps. For example, IEEE 802.11a/g [5] throughput is currently limited to less than 25 Mbps with a signal bandwidth up to 20 MHz [6], [7], this amount of data transmission is certainly unsuitable for modern multimedia and other WPAN applications. Moreover, IEEE 802.11 is a power

consuming application that is not user friendly in term of power-sensitivity of handheld and portable devices that result in a short battery life. Nevertheless, there is a seemingly constant urge for improving the capabilities of wireless communications in terms of throughput and/or reliability, and there is a variety of new applications and environments for which wireless technology is envisioned. However, while the number of wireless applications continues to grow, bandwidth is still as limited a resource as in the days of Marconi.

In the last decade, ultra wideband (UWB) wireless communications have been the subject of extensive research, due to its unique high-capacity, low power, low cost and potential to run most of the high data rate applications particularly in short-range multiple access wireless communications. Basically, the concept of UWB relies on spreading the transmitted information over extremely large bandwidths. UWB technology has offered a potential solution to avoid spectrum's congestion. However, the power limitation is predominantly the main obstacle that restrains UWB technology and prevents it from being a potential solution for future generation high-speed communications [8]–[10].

As shown in Fig. 1.1, there is an emerging need for high-capacity technologies able to fill the large gap in WPAN and WLAN to meet the huge demand with the advent of more and more high-speed applications and wide-coverage range. The IEEE 802.15.3c (task group c) was the first standard that addresses multi-gigabit short-range WPAN systems in the 60 GHz band. The IEEE 802.11ad is another installment of the successful 802.11 (WiFi) family, hence, the task group ad was established to develop an IEEE standard for 60 GHz WLAN.

New variety of wireless applications have appeared, and emphasized the need for robust, very high data rate radio communication systems. For instance, remotely streaming High Definition (HD) video channels requires data rates in the range from 1 to several Gbps. Similar data rates are expected for instant heavy content files downloading from a wireless kiosk. As a result, a substantial knowledge about the mm-waves channel has been accumulated and a great deal of work has been done toward developing mm-waves communication systems for commercial applications. Today, 60 GHz communications is attracting research interest for multi-gigabits WPAN and WLAN that exceed the 10 m coverage range. The worldwide opening of a massive

amount of unlicensed spectra around 60 GHz has triggered great interest in developing affordable 60-GHz radios. For short range wireless applications, the 60 GHz technology appears as an optimal solution, facilitating a number of key features.

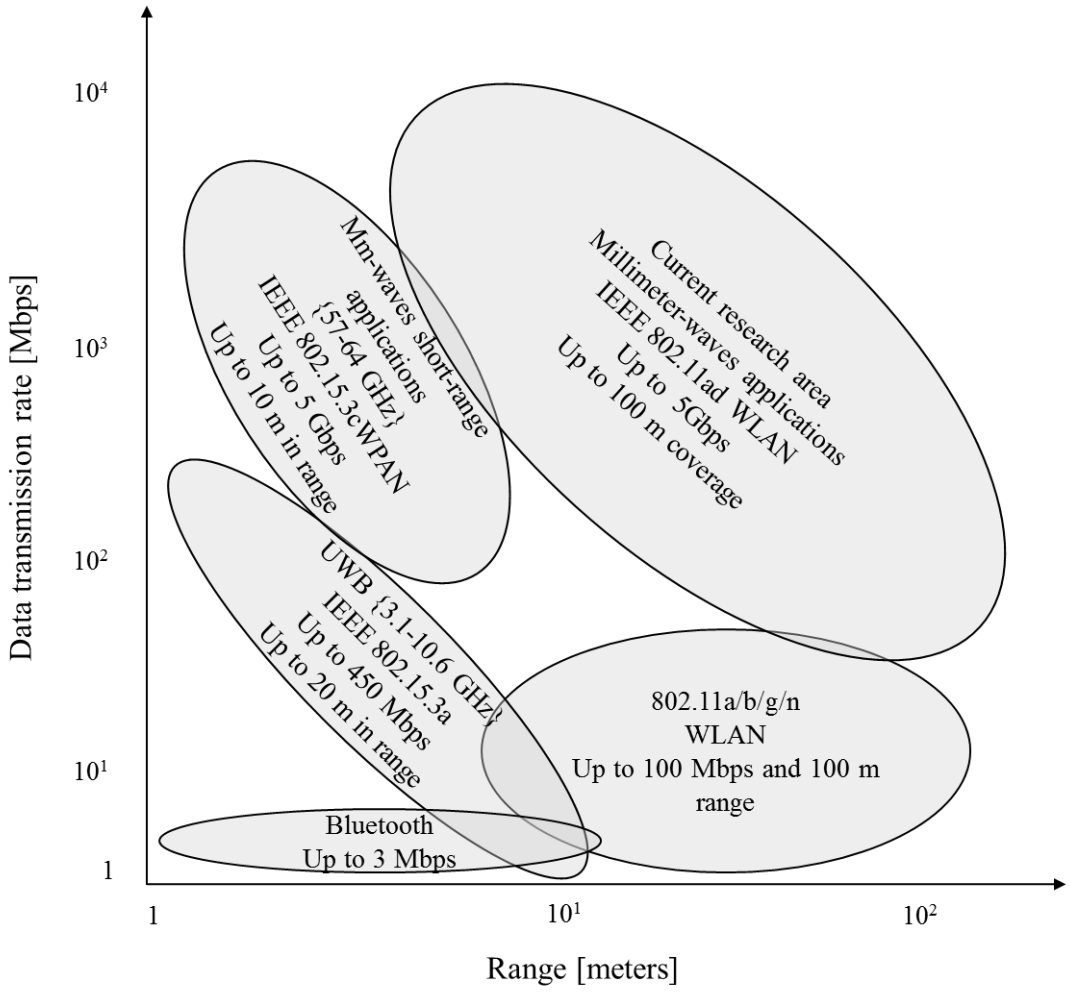

Fig. 1.1 Range and data rates of current and future applications

Following the regulations issued by the Federal Communications Commission (FCC), a maximum of 43 dBm of effective isotropic radiated power (EIRP) is approved in the unlicensed 57-64 GHz band [11]–[13]. Practical fully integrated 60 GHz transceivers became possible using low cost silicon-germanium (SiGe) and complementary metal-oxide-semiconductor (CMOS) [14]–[16]. Hence, the millimeter-wave band appears to be a favorable choice for WPAN and WLAN short-range applications as it meets the requirements for sufficient bandwidth, small terminal dimensions and sporadic usage for commercial applications.

1.2 Industry Standardization of Wireless 60 GHz Technology

As part of the fourth-generation (4G) multi-Gigabits systems, research activities have been made for the standardization and industrialization of wireless 60 GHz band emphasizing the need for robust transmission in compliance with multi-gigabit rates. In September 2009, the IEEE standard 802.15.3c-2009 was the first standard that addresses multi-gigabit short-range wireless systems [17]. In December 2010 ECMA international has released its 2nd edition for high rate 60 GHz PHY, MAC and HDMI PAL for short-range communications, namely, ECMA-387 [18]. Wireless-HD 1.0 specification released in January 2008 and its products are already spread in the market [19], [20]. The IEEE 802.11 ad task group was established in January 2009 to develop an IEEE standard for 60 GHz WLAN. The IEEE 802.11ad is another installment of the successful 802.11 (WiFi) family. The Wireless Gigabit Alliance (WiGig) was formed in May 2009 and released its 60 GHz specifications in 2010. Today, many wireless multi-gigabit commercial applications already existed in the markets, although, relevant international standards for 60 GHz bands are under finalization process.

Multi-Gbps WLAN has focused renewed attention due to the available large amount of unlicensed spectrum (7 GHz) around the 60 GHz frequency band. WLAN connectivity provides access to the internet and local peripherals, there is a need for more ad-hoc connectivity where network users may share files with heavy contents or to redirect the display of video contents to nearby monitor [21]-[24]. Hence, WLANs enabling multi-Gbps for distances of tens of meters have been widely approved by many research groups during recent years making them the most successful technologies. Among these groups is the IEEE 802.11 standard committee which is one of the major organizations in WLAN specifications development, established the IEEE 802.11ad task group to develop an amendment for 60 GHz WLAN systems.

1.3 Mm-waves Technical Challenges

In the mm-waves band, due to the very short wavelength, the challenges are related to the fact that the characteristics of the propagation channel are more susceptible to the environmental changes than those for traditional WLAN operating at lower-frequency band [25]. Mm-waves indoor radio channels are more complex and subject to a severe multipath propagation phenomenon, but are of interest for many researchers [26], [27], because indoor mm-waves for

wireless multi-Gbps communications are playing a dominant role in the present market. Despite the abundance of the bandwidth, 60 GHz still presents many technical challenges that severely limit the propagation of the signal, including the severe attenuation experienced by the signal in free space, combined with the attenuation due to propagation mechanisms from surrounding objects and surfaces. At 60 GHz, an additional attenuation of 15 dB/km is experienced in free space propagation due to the oxygen absorption [28], [29]. Therefore, mm-wave propagation properties may be viewed as potential problems in terms of signal coverage in WLANs.

In NLOS case, mm-waves links suffers greater signal diffusion in the absence of specular reflection, and lack of diffraction around obstacles [30]–[32]. The low diffraction coefficient of scattering objects is inversely proportional to square root of operating frequency, for example a typical 30 dB diffraction loss difference is recorded between 60 GHz and 2GHz [38]. Hence, NLOS communications suffer a severe frequency selectivity, which means consequently a short-range poor coverage in very small geographic area.

The first vital step in the design and optimization of future wireless systems lies in the measurement and modeling of the relevant propagation characteristics. These determine the theoretical performance limits, as well as the practical performance of actual systems operating in the considered environment. The channel modeling in extremely high frequencies poses the problem of the accurate description of the propagation scenarios at the wavelength scale (5mm at 60 GHz). Many channel models have been established for various applications. They range from simple statistical models to more complex geometric and combined statistical/geometric and very complex ray tracing models.

The extremely large transmission bandwidth of 60 GHz systems has several fundamental implications that must be considered when modeling the channel. In such channels, the dielectric properties of different building materials typically show significant variations over the whole bandwidth. Also, the electrical length of the building materials which is expressed by the wavelengths number (k), changes with frequency, hence, the object size varies significantly across the bandwidth. As a result, the propagation mechanisms such as, path-loss, Fresnel

reflection and diffraction coefficients, diffuse scattering, and transmission should be considered as frequency-dependent [33]–[35].

1.4 Framework of Research Activities

Up to date, it has been seen clearly from the various 60 GHz measurement campaigns that completely different results were achieved, even for similar indoor environments [30], [36]–[41]. Moreover, the amount of available measurement data is very limited and more are needed to support a comprehensive study of the 60 GHz propagation characteristics [30]. This thesis is intended as a contribution to the the design and optimization of future WLAN systems that lies in the measurement and modeling of the relevant propagation characteristics in the 60 GHz band.

In the literature, 60 GHz deterministic channel models are narrow-band, they are likely to be performed in space or in time domain, and hence, the frequency-dependent effects are ignored, although 60 GHz systems are likely operating over an extremely wide bandwidth. To the best of our knowledge, in the 60 GHz free licence band, there have not been ray-based deterministic broadband models dedicated to predict deterministically the propagation characteristics across the whole bandwidth of interest that exceeds 500 MHz. Nevertheless, most published deterministic ray-based models use a very limited number of multipath rays for both LOS and NLOS cases [42], [43]. Although, at mm-waves, all multipath components are relevant to allow obtaining accurate models, excluding one or few rays might change the result significantly.

In NLOS channels, most of studies are still evaluating diffraction around corners for relaying the signal while denying the presence of surrounding mm-waves deflecting objects (DOs) and considering them as noise sources. However, at mm-wave frequencies some specific surfaces, shapes and positions of DOs might enhance significantly the NLOS communications. There is no specific information that features and quantifies the constructive characteristics of radio wave propagation. Although providing a route path around obstructions might change the channel propagation characteristics behavior as desired. In this case, a Power Delay Profile (PDP) with a short excess delay might be achieved. Thus, new techniques beyond traditional point-to-point communications must be derived to provide an alternative route for the signal and to extend its coverage to the shadowed areas of the NLOS channels.

1.5 Thesis Contributions

This thesis reflects the output of the research activities in the field of indoor radio communications in the unlicensed 60 GHz band. It was decided to restrict the scope of the research to indoor applications at 60 GHz only. The contributions of the thesis are classified as follows:

I. Mm-waves Propagation Channel Measurements and Characterization

Based on sweeping-frequency sounding technique (59.6 – 60.6 GHz), the most critical statistical parameters of 60 GHz indoor multipath propagation channel are extracted. The channel characterization is based on the evaluation of the channel coherence bandwidth, the statistical fading distributions, the exponent of the path-loss law (n) and the shadowing, the multipath time dispersion characteristics such as the channel mean excess delay (τ_{mean}), exess delay (τ_{max}) and RMS delay spread (σ_{τ}), the statistics for the RMS delay spread. The presented measurements and empirical models may aid the development of futuristic mm-wave radio system for high-speed wireless applications. The obtained results are then compared to the various 60 GHz measurement campaigns published in the literature.

Under various scenarios, the propagation measurements are carried out in two typical indoor environments; non-line-of-sight (NLOS) T-shaped corridors intersection and line-of-sight (LOS) modern rectangular conference room.

In the considered NLOS T-shaped corridors intersection, technique beyond traditional point-to-point communications is derived to provide an alternative route for the data transmission and to extend signal coverage to shadowed areas where LOS is not present. This thesis provides information that features and quantifies the constructive characteristics of radio waves resulting from the presence of DOs in the channel. Hence, three scenarios are considered in a comparative way:

a) no DO present at the corridors intersection,

b) a metallic standing circular cylinder is positioned at the intersection, and

c) a flat metal reflective surface is then positioned at the intersection.

The effect of the antenna directivity on the channel propagation characteristics inside the considered conference room are investigated using two antennas with two different radiation patterns:

a) two omnidirectional antennas are employed at both remote ends of the channel (Omni-Omni).

b) a directional antenna is employed at the transmitting side, while an omnidirectional antenna is used at the receiving side (Direct-Omni).

II. Deterministic Modeling of Mm-waves Propagation Channel

Based on the measured channel transfer functions (59.6 – 60.6 GHz), deterministic models on the basis of geometric ray-tracing (RT) are derived for the considered environments i.e., non-line-of-sight (NLOS) T-shaped corridors intersection and line-of-sight (LOS) modern rectangular conference room.

This thesis has shown that in 60 GHz channels are very sensitive to frequency, all multipath are important and relevant to allow obtaining precise predictions of signal propagation in the channel corresponding to the considered environment. Excluding of one or few rays might change the result significantly.

In the NLOS corridors scenario, the deterministic channel transfer functions are modeled using single, double and up to the fourth-order of multiple reflections from the floor, ceiling and walls, superimposed by single diffractions from corners. The most critical aspect of the mathematical channel modeling is the diffracted field around corridors corners. Based on the uniform geometrical theory of diffraction (UTD), the diffracted field in the shadowed region of the corridors is calculated with a high level of accuracy using the Remely's heuristic diffraction coefficient for a lossy wedge. In the LOS conference room, up to third-order of reflection from the various surfaces of the room are considered, reflections of 4^{th} order or higher are unimportant.

The experimental data are successfully validated in both the NLOS corridors and the LOS conference room. An interesting agreement is achieved between the simulated as well as the

experimental data. Furthermore, the presented NLOS corridors channel models are also validated in the presence of the considered DOs in the intersection.

The achieved RT models are very promising for indoor broadband communications systems in the 60 GHz band where high levels of accuracy and certainty are achieved.

1.6 Dissertation Outline

Chapter 2: 60 GHz Short-range Communications: Applications, Standards and Challenges

This chapter presents an overview of 60 GHz technology and its applications for short-range wireless communication systems. The topics about 60 GHz unlicensed band are addressed and include: motivations, advantages and system design challenges. Then, a further discussion over the 60 GHz standardization and its historical evolution is followed. The chapter also provides a literature survey on the various propagation mechanisms such as, free space and its inherent directivity at mm-waves, specular reflection, diffraction from a wedge and its formulation. Next, the ray-tracing approach and the image theorem are described. The multipath phenomenon and its power delay profile are detailed. The chapter ends by addressing the small-scale fading and its distributions including Rayleigh and Rice.

Chapter 3: Millimeter-Wave Broadband Channel Sounding

This chapter provides the measurement techniques and setup. An introduction to the fundamental tasks of channel soundings is provided with a brief statement about their evolutional history. Then, a technical overview of channel measurement in both time and frequency domains is followed. Next, the antennas choice and arrangements in mm-waves channels are discussed. The basic concept of the advanced channel sounder presented in this thesis is detailed. Also, the various parts of the system setup are described in details including its receiver front end, the controller, the photonic subsystem and the microwave transmitter and the used antennas. Finally, the last section is devoted for the description of the system calibration.

Chapter 4: Deterministic Modeling of the Indoor Channel in the 60 GHz Band

Chapter 4 deals with the ray-based deterministic modeling of indoor short-range propagation channel. This chapter begins by an introduction to discuss many challenging aspects of mm-waves propagation modeling, especially the 60 GHz broadband channels. Then the general ray-based model considerations are presented, including information about building database, the ray tracer algorithm and antenna modeling. In the next phase of this chapter, two environments are considered for modeling. First, the NLOS corridors environment, it consists of three worthy studying and analyzing scenarios when DOs are present in the channel. Second, the LOS conference room deterministic ray-based channel model is followed. The end is devoted for a detailed discussion.

Chapter 5: Characterization and Analysis of 60 GHz Wideband Measurements

Chapter 5 presents the propagation measurements and their statistical analysis in the 60 GHz band. This chapter gives insight into the experimental procedure in the previously discussed measurement environments and the considered scenarios. Then, the experimentally obtained data are processed and analyzed to study most important issues such as small scale fading and their statistical distributions, the channel coherence bandwidth and signal path loss. The reminder of this chapter discusses the OFDM transmission in terms of channel BER, received signal constellation and spectrums to yield a fair comparison among the proposed scenario in term of channel performance, then, a detailed discussion is provided.

Chapter 6: Conclusions and Future Research

Finally, in chapter 6, the main achieved results of this dissertation are summarized; conclusions and future research are drawn.

Chapter 2

60 GHz Short Range Communications: Applications, Standards and Challenges

2.1 Introduction

Millimeter (mm)-wave band appears relevant to be explored, this band is a portion of the electromagnetic spectrum that extends from 30 to 300 GHz corresponding to wavelengths from 10 to 1 mm respectively [44], [45]. Theoretically, Shannon's capacity limit theorem makes it clear that, the increase of signal bandwidth achieves a higher throughput in a communication system.

$$C = B\ log_2(1 + SNR) \tag{2.1}$$

where *C* is the channel capacity in bps, *B* is the signal bandwidth, and SNR is the signal-to-noise ratio. The channel capacity is directly proportional to signal bandwidth, but logarithmically proportional to SNR. Thus, in accordance to equation (2.1), the most effective way of increasing the data rate is by increasing the bandwidth and also, by using a high-order modulation schemes which in turn usually require high SNR.

The FCC allocated 7 GHz of free licensed bandwidth in the 54–66 GHz [11]. In this band, the FCC regulation limits allow a maximum transmit power of 500 milli-watts, that is 27 dBm for an emission bandwidth greater than 100 MHz. Although a large amount of transmit power is approved by the FCC, only a fraction of this power might be transmitted, this is mainly due to the limited capability of the power amplifiers (PAs). Table 2.1 shows the effective isotropic radiated power (EIRP) and frequency band allocated by spectrum regulation authorities of few major regions [12].

Table 2.1 Spectrum allocation, EIRP emission limits and isotropic antenna gains for major countries.

Region	Frequency band [GHz]	Unlicensed bandwidth [GHz]	Maximum EIRP [dBm]	Antenna gain [dBi]
Canada/USA	57- 64	7.0	43	33
Korea	57-64	7.0	27	17
China	59-64	5.0	47	37
Japan	59-66	7.0	57	47
Europe	57-66	9.0	56	35
Australia	59.4-62.9	3.5	52	41

Worldwide spectrum regulations authorities allow much higher transmit power at 60 GHz band compared to other existing WLANs and WPANs technologies. Table 2.2 shows an example of the typical 60 GHz, UWB and IEEE 802.11 systems that operate at powers not exceeding FCC regulation limit as referred to [12]. Table 2.2 shows clearly that the EIRP of the 60 GHz technology exceeds significantly the IEEE 802.11n and the UWB systems.

Table 2.2 Comparison of the typical implementation of 60 GHz, UWB and IEEE 802.11n systems [12].

	Frequency [GHz]	Power [dBm]	Antenna gain [dBi]	EIRP output [dBm]
60 GHz	57 - 64	27	33	43
UWB	3.1 – 10.6	-11.5	1.5	-10
IEEE 802.11n	2.4/5.0	22.0	3.0	25

Spurred by the significantly increasing demand of high data rate applications, the huge unlicensed bandwidth offers a great potential in terms of capacity and flexibility, making 60 GHz technology particularly attractive for indoor short-range Gbps applications shown in Fig. 2.1.

a) Point-to-multipoint communications between computer and its peripherals.

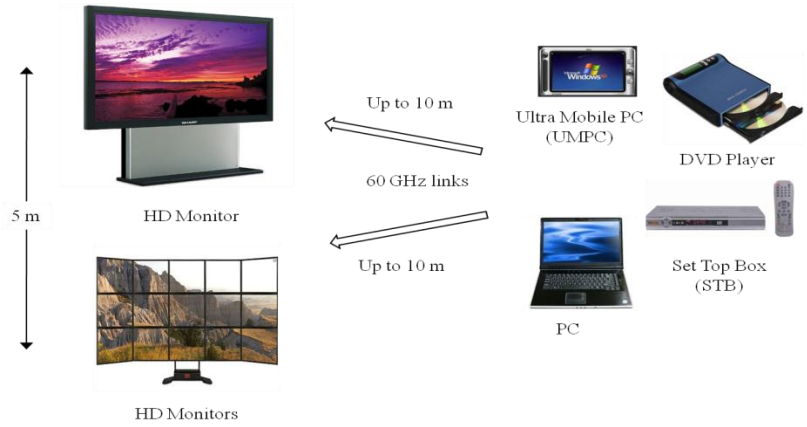

b) Point-to-point video streaming (LOS/NLOS).

c) Point-to-point kiosk file-downloading (LOS).

Fig. 2.1 Various multi-Gigabits applications in the 60 GHz band.

2.2 Features of 60 GHz Communications

Due to the propagation mechanisms, 60 GHz links experience significant attenuations. However, the high attenuation is not considered as a drawback when dealing with security issues, the large attenuation means that 60 GHz systems provide inherent security. Besides, the extremely large signal decaying also limits interference between 60 GHz links located in close vicinities, and prevents 60 GHz channels from interfering with other systems operating in the same band. In addition, the huge path loss at 60 GHz is foreseen as an advantage that enables higher–frequency reuse of resource allocation between adjacent WPAN cells in each indoor environment, thus allowing a very high–throughput network.

The higher frequencies also lead to smaller sizes of RF components including antennas. Compared to 5 GHz systems, the form factor of 60 GHz systems is approximately 140 times smaller and thus can be conveniently integrated into consumer electronic products. Therefore, the small and compact size of antennas at 60 GHz allows the deployment of multiple antennas at the user terminal that are otherwise difficult if impossible at low frequencies.

60 GHz communication channels require a highly directional antenna with very high gain; this brings a new opportunity for spatial reuse amongst adjacent links. Hence, allowing more simultaneous transmissions in a dense WPAN environment when compared with wide radiation patterns. This is because as the gain of antenna increases, the beamwidth of the antenna decreases giving some benefits in terms of reducing unwanted interference provided that the intended power is directed towards the desired users. Fig. 2.2 illustrates a scenario of the increased spatial reuse capability provided by narrower antenna radiation patterns.

It has been shown clearly that directional communications with beam-forming provides approximately five times higher spatial reuse gain over omni-directional communication, when measured in terms of the number of simultaneous active links [46]. Hence, in 60 GHz links directional antennas are preferable and provide more advantages over omni-directional antennas.

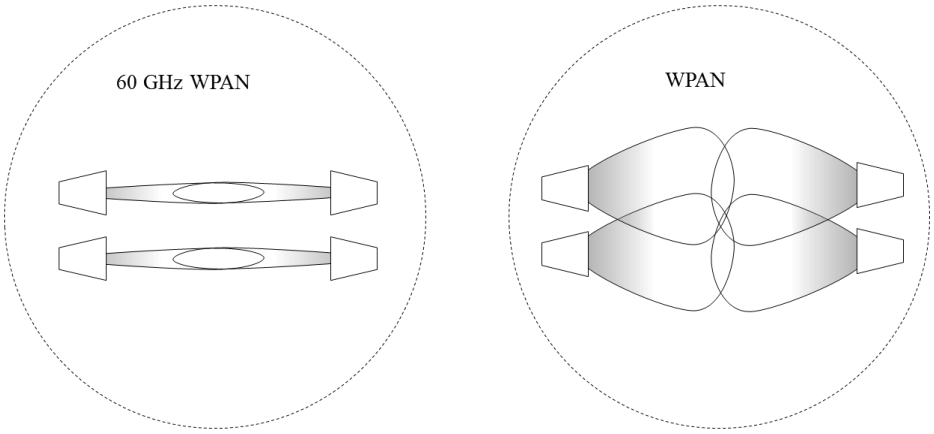

Fig. 2.2 60 GHz simultaneous transmissions in a dense WPAN.

From the above discussion, the conclusion is that the 60 GHz band appears to be a favorable choice for WPAN and WLAN applications as it meets the requirements for sufficient bandwidth and small terminal dimensions.

2.3 Industry Standardization for 60 GHz Communications

As part of the fourth-generation (4G) multi-Gigabits systems, research activities have been made for the standardization and industrialization of wireless 60 GHz band emphasizing the need for robust transmission in compliance with multi-gigabit rates as proposed. Today, many wireless multi-gigabit commercial applications especially Wireless-HD products already exist in the markets, although, relevant international standards for 60 GHz bands are under finalization process.

Several standardization working groups are currently working on specifications in the 60 GHz unlicensed band. The specifications of the ECMA-387 and Wireless-HD 1.0 standards have already been published and commercial consumer products based on these standards are available now [47]. ECMA-387 focuses on a high-rate wireless personal area network (WPAN), whereas Wireless-HD targets the wireless video area network (WVAN). Additionally, two amendments to current IEEE specifications, namely the IEEE 802.15.3c [17] and the IEEE 802.11ad [48], are

targeting the 60 GHz band. The first one seeks a 60 GHz approach to the existing IEEE 802.15.3 WPAN standard, while the second will introduce modifications to the well-known IEEE 802.11 WLAN specification and define a mechanism for fast session transfer between 2.4/5 GHz and 60 GHz operation bands, while coexisting with other systems in the 60 GHz band.

The recently created Wireless Gigabit Alliance (Wi-Gig) is also actively working on a new specification based on 60 GHz technology. The first specification version was finalized at the end of 2009. The current main competitive 60 GHz technology standards are listed in Table 2.3.

Table 2.3 Key industrial 60 GHZ standardization activities.

Forum	**Date of Release**	**Max data rate**	**Applications**
IEEE 802.15.3c	Oct. 2009	5.28Gbps	▪ WPAN ▪ Point-to-point applications ▪ Compatible with WirelessHD specifications
ECMA-38	2nd version Dec 2010	6.35 Gbps	▪ WPAN ▪ Bulk data transfer and multimedia streaming
WirelessHD	Specification 1.0 Jan 2008	~ 4 Gbps	▪ WNAN ▪ Uncompressed A/V streaming and high-speed media transmission
IEEE 802.11 ad	PAR approved, 2012	>1Gbps	▪ WLAN ▪ Fast session transfer between 60 GHz and 2.4/5 GHz
WiGig	2009	>1Gbps	▪ High performance devices (PC,CE,IC, handheld mobile)

2.4 Design Challenges for 60 GHz Systems

Traditionally, in conventional mm-waves wireless communications systems, Gbps data transmission might be achieved under line of sight (LOS) conditions or a strong multipath component that exists between the transmitter and the receiver.

Despite the various advantages offered and the abundance of the bandwidth, 60 GHz based communications suffer a number of critical problems that must be solved. 60 GHz signals suffer a severe attenuation in free space, combined with the attenuation due to propagation mechanisms from surrounding objects surfaces and obstruction losses. Hence, 60 GHz signal coverage is limited to distances range up to few meters.

The impulse response duration of the channel under study is another limiting factor for high-speed transmissions. Despite the increase in the transmitted power and the deployment of highly directional antennas, 60 GHz links exhibit large delay spread values that can easily increase the complexity of the system design especially under NLOS channels where ISI can spread a single symbol over tens or hundreds of symbol periods. Chapters 4 and 5 will provide a more deep discussion about the impact of channel's impulse response on the design of 60 GHz communications. However, the directional antennas can make it more problematic when the LOS path is blocked by human bodies and other objects presented in the channel. Particularly, indoor mm-wave links that are highly susceptible to blockage because of the limited ability to diffract around obstacles whose size is significantly larger than the wavelength (less than 5mm). Therefore, the absence of LOS between terminals makes mm-waves communications even worse.

Under NLOS condition, 60 GHz links suffers greater path losses in the absence of specular reflection, and lack of diffraction around lossy obstacles such as corridors corners [36], [37]. This severe path loss hinders Gbps throughput and limits the coverage up to range not exceeding the 10 m. Hence, laying data transmission in hostile propagation environments have re-emerged as important research topics over the past half-decade to extend the signal coverage, especially over shadowed remote places where line-of-sight (LOS) does not prevail.

2.5 Propagation Mechanisms at 60 GHz

2.5.1 Free-Space Propagation (LOS)

Theoretically, radio links undergo free-space propagation, when a direct unobstructed LOS path exists without reflection, scattering or diffraction between the transmitter and the receiver. The strength of the received signal can be predicted as a function of the T_x-R_x separation distance using the Friis equation, which is given by [49]

$$P_r = P_t G_t G_r \left(\frac{\lambda}{4\pi R}\right)^2 = P_t G_t G_r \left(\frac{c}{4\pi R f}\right)^2 \tag{2.2}$$

where, P_r and P_t are the received and transmitted power, respectively. G_r and G_t are the gains of the terminal antennas, R is the distance between antennas, and λ is the wavelength. From equation (2.2), it can be clearly seen that the received power decreases as the square of the distance between the transmitter and the receiver or the operating frequency. Hence, the free space loss (FSL) is given by

$$FSL = \frac{P_r}{P_t} = G_t G_r \left(\frac{\lambda}{4\pi r}\right)^2 \tag{2.3}$$

2.5.1.1 Mm-waves Inherent Directivity

From equation (2.3), it can be seen clearly that, due to their small wave length, 60 GHz wireless systems experience large free space propagation loss. Regardless of transceiver antennas efficiencies, the free space propagation loss between isotropic antennas is proportional to the squared wavelength (λ^2). At 60 GHz, a wavelength of 5 mm cause additional free space propagation loss (*FSL*) compared with 2.4 GHz for isotropic communication, i.e.,

$$FSL_{Iso} = 10log_{10}(\lambda^2_{2.4\,GHz}) - 10\,log_{10}(\lambda^2_{60\,GHz}) = 27.96\,dB \tag{2.4}$$

On the other hand, for a fixed antenna aperture area, directivity scales as ($1/\lambda^2$), giving a gain of ($1/\lambda^4$), when we account for both transmit and receive antennas. This corresponds to an overall scaling of ($1/\lambda^2$), so that a 60 GHz link with directional transmission and reception can now become 27.96 dB better than a 2.4 GHz link [50].

$$FSL_{Direct.} = 10log_{10}(1/\lambda^2_{2.4\,GHz}) - 10\,log_{10}(1/\lambda^2_{60\,GHz}) = -27.96\,dB \tag{2.5}$$

As a result, the large propagation loss might be mitigated by either increasing the transmitted power or the gain of the transmitting antenna. A practical approach to increase the energy efficiency is the use of highly directional antennas [30] as shown previously in Table 2.2. Therefore, 60 GHz links are inherently directional: directivity is required to overcome the higher path loss at smaller wavelengths and the oxygen absorption of 15 dB/Km experienced at 60 GHz [51]. Recently, the advance of the high gain directional beam-forming technology has made it possible to overcome the large free space propagation loss for the distances of several tens of meters.

2.5.2 Reflection

Reflection occurs when a propagating electromagnetic wave hits upon an object that has very large dimensions compared to the wavelength of the propagating wave. The amplitude of the reflected electric field is dominated by the Fresnel reflection coefficient [52]. The latter is influenced significantly by many different major parameters such as the material properties (permittivity) of the reflecting surface, the polarization of the electromagnetic field, the angle of incidence and the operating frequency of the propagating electromagnetic wave as shown in Fig. 2.3. The complex permittivity that varies with frequency is given by [53]:

$$\varepsilon_r^* = \varepsilon_r - j60\sigma\lambda \tag{2.6}$$

Where, ε_r is the relative permittivity, σ is the conductivity of the reflecting surface in S/m and λ is the wavelength of the operating frequency. The reflection coefficients $R_{||}$ and $R_{\perp}$ for parallel and perpendicular polarizations, respectively, can be expressed as [54]

$$R\ \| = \frac{\varepsilon_r^* \sin\theta_i - \sqrt{\varepsilon_r^* - \cos^2\theta_i}}{\varepsilon_r^* \sin\theta_i + \sqrt{\varepsilon_r^* - \cos^2\theta_i}} \tag{2.7}$$

when the electric field is parallel to the plane of incidence, and

$$R\ \perp = \frac{\sin\theta_i - \sqrt{\varepsilon_r^* - \cos^2\theta_i}}{\sin\theta_i + \sqrt{\varepsilon_r^* - \cos^2\theta_i}} \tag{2.8}$$

when the electric field is perpendicular to the plane of incidence.

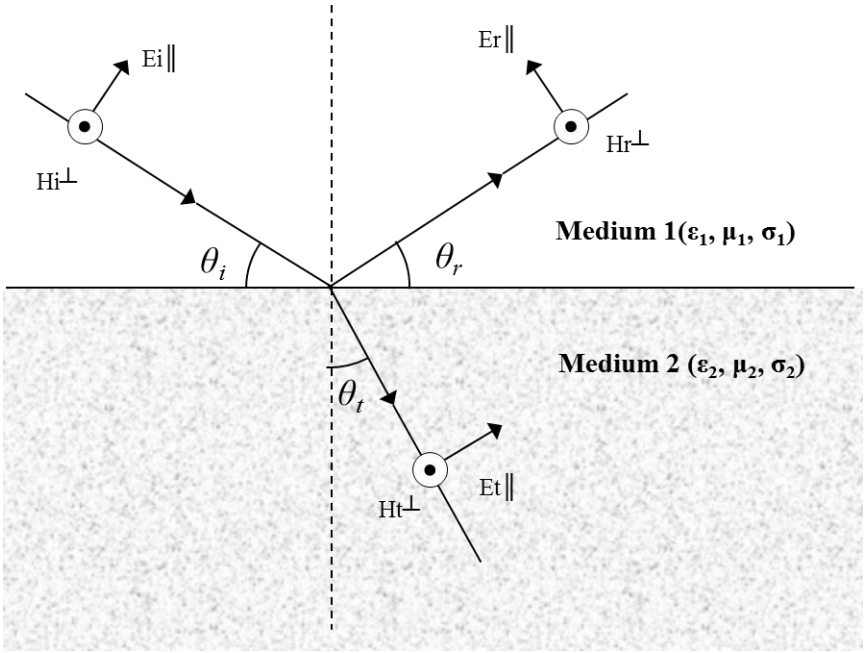

(a) Parallel polarization.

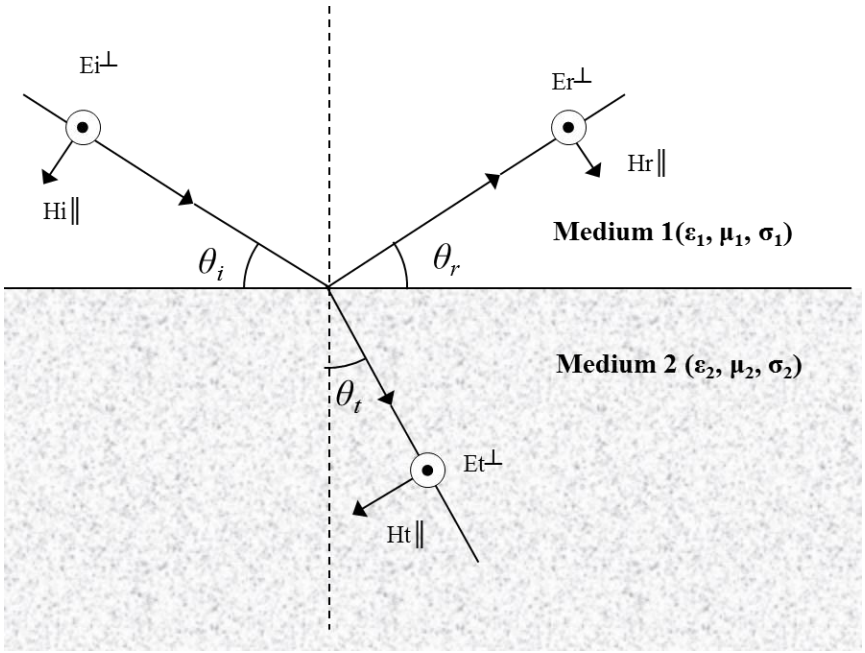

(b) Perpendicular polarization.

Fig. 2.3 Uniform plane wave incident onto a plane boundary.

The magnitude of the Fresnel reflection coefficient for a wave propagating in free space and impinging onto a plasterboard surface is presented in Fig. 2.4. At 60 GHz, the permittivity (ε_r) and conductivity (σ) for plasterboard walls are 2.81 and 0.1536 s/m, respectively, [55], [56]. At 2.4 GHz, ε_r =1.32 and σ =0.0004 [57].

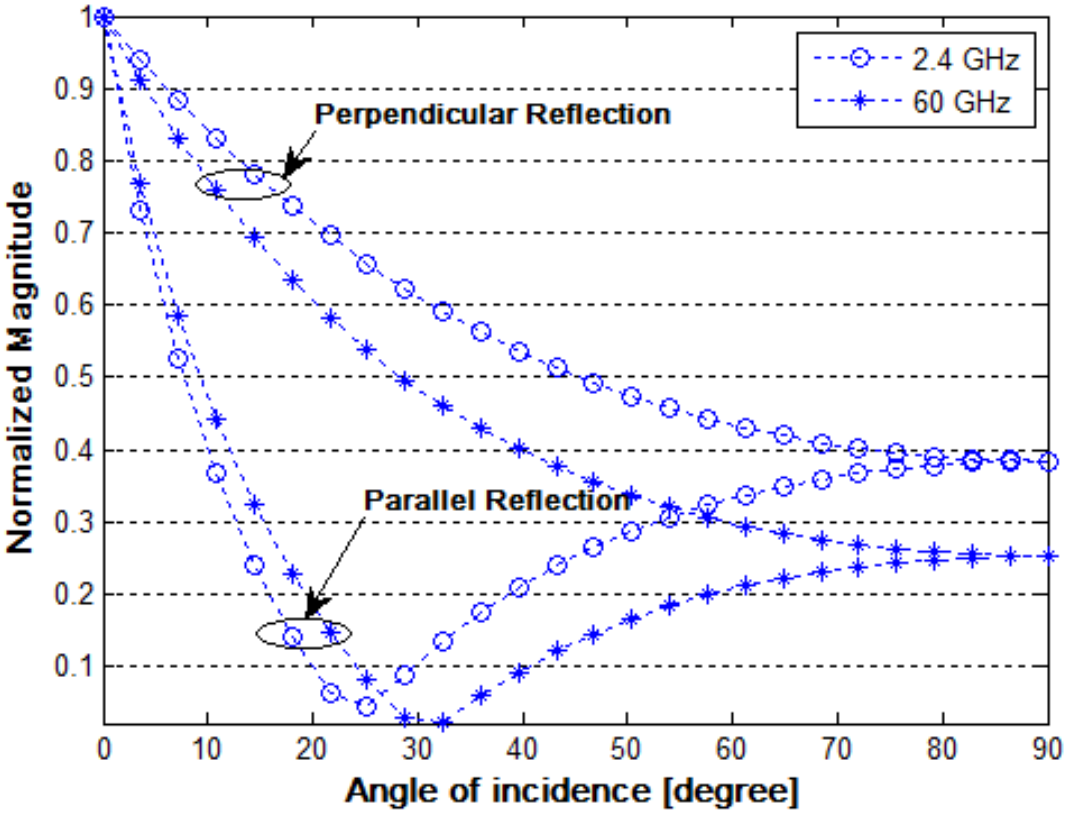

Fig. 2.4 Reflection coefficients for plasterboard at 2.5 GHz and 60 GHz.

2.5.3 Diffraction Phenomenon

The diffraction occurs when the radio path between the transmitter and receiver is obstructed by a surface that has a sharp edge or irregularities. The secondary waves resulting from the obstructing surface are present through the space and even behind the obstacle, giving rise to a bending of waves around the obstacle. This assists in establishing a link even when LOS path does not exist between the transmitter and receiver. Diffraction, like reflection, depends on the geometry and material properties of the object, as well as the amplitude, phase, and polarization of the incident wave at the point of diffraction.

2.5.3.1 Diffraction from a Right Wedge

The energy of the propagating radio wave diffracted from the illuminated edges can be modeled by wedge diffraction coefficients in the context of the uniform theory of diffraction (UTD) [58]. The geometry for the two-dimensional wedge diffraction problem is illustrated in Fig. 2.5. It is customary to label the two faces of a wedge, the 0-face and n-face, respectively, and consider the incidence angle φ' and diffraction angle φ to be measured from the 0-face. The exterior wedge angle is denoted by nπ where, $0 \leq n \leq 2$. The shadow boundaries of Fig. 2.5, controlling as they do the fate of the incident rays, are usually called incident shadow boundaries (ISB). They delineate the regions of space in which direct rays do or do not exist. The Reflection shadow boundary (RSB) delineates the regions of space in which geometrical optic reflected or diffracted rays, do or do not exist. Hence the ISB is located at $\varphi_{ISB} = \pi + \varphi'$ and the RSB is located at $\varphi_{RSB} = \pi - \varphi'$.

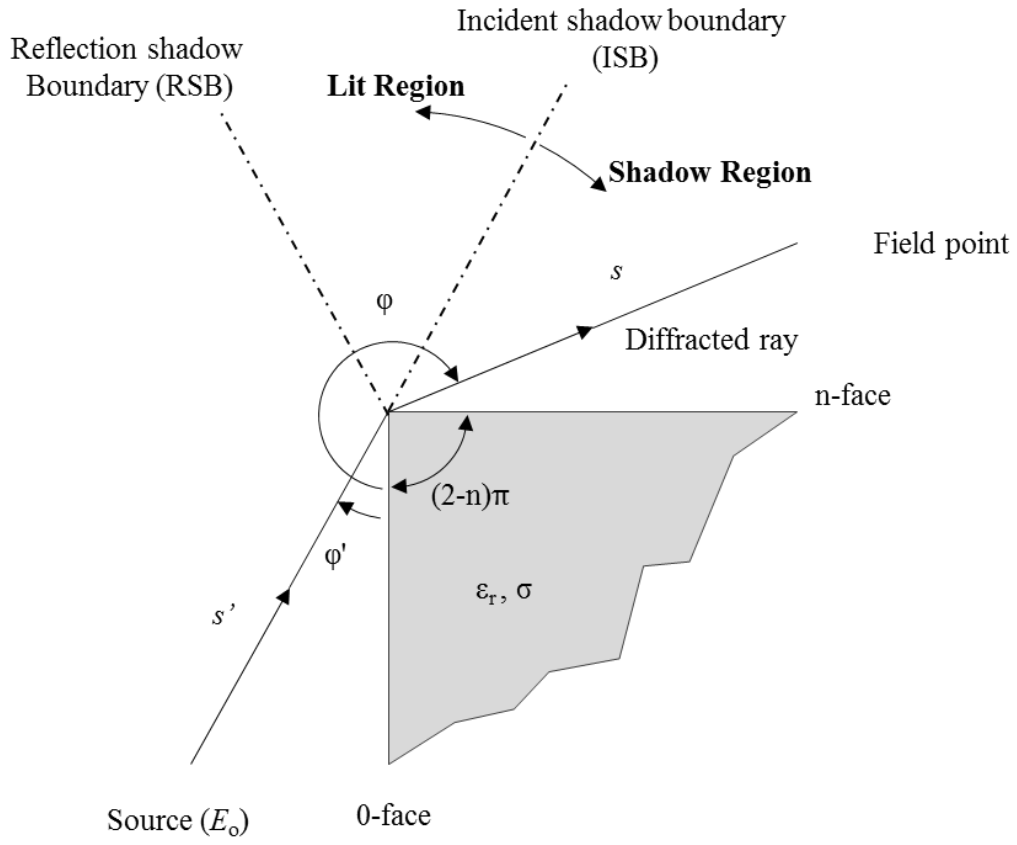

Fig. 2.5 Geometry of diffraction from a right wedge.

2.5.3.2 Heuristic Diffraction Coefficient Formulation

An expression for the dyadic diffraction coefficient of a conducting wedge that is valid in both within and outside the transition regions is given by [58]

$$D = \frac{-e^{-j\pi/4}}{2n\sqrt{2\pi k}\,sin(\gamma)}\,[D_1 + D_2 + R^0_{\parallel,\perp}D_3 + R^n_{\parallel,\perp}D_4] \tag{2.9}$$

where γ is the angle formed by the incident ray and the edge. The components of the dyadic diffraction coefficients in (2.9) are given by

$$D_1 = cot\left(\frac{\pi + (\phi - \phi')}{2n}\right) F[kLa^+(\phi - \phi')] \tag{2.10}$$

$$D_2 = cot\left(\frac{\pi + (\phi - \phi')}{2n}\right) F[kLa^-(\phi + \phi')] \tag{2.11}$$

$$D_3 = cot\left(\frac{\pi - (\phi + \phi')}{2n}\right) F[kLa^+(\phi - \phi')] \tag{2.12}$$

$$D_4 = cot\left(\frac{\pi - (\phi + \phi')}{2n}\right) F[kLa^-(\phi + \phi')] \tag{2.13}$$

$$L = \frac{SS'}{S + S'}\,sin^2(\gamma) \tag{2.14}$$

$$a^{\pm}(\beta) = 2cos^2\left(\frac{2n\pi N^{\mp} - \beta}{2}\right) \tag{2.15}$$

$$\beta = \phi \pm \phi' \tag{2.16}$$

$$2\pi n N^{\pm} - \beta = \pm\pi \tag{2.17}$$

$R^0_{\parallel,\perp}$ and $R^n_{\parallel,\perp}$ are the Fresnel reflection coefficients defined for the 0-face and n-face respectively. The Koujoumjian's heuristic diffraction coefficient deals with the perfectly conducting wedge i.e., $R_{\parallel,\perp=} \pm 1$ for both faces in equation (2.9). In the case of lossy wedge, Lubbers [63] has incorporated the material dielectric to the UTD coefficient by introducing $R^0$and R^n as defined in

equations (2.7) and (2.8) and taking into account the reflection angle which are given as $\theta_0 = \phi'$ for R^0, and $\theta_n = n\pi - \phi$ for R^n. Remley et al. [64] redefined the angular dependence of the diffraction coefficient in the shadowed region as:

$$\begin{aligned} \phi' < \pi \Longrightarrow & \begin{cases} \theta_0 = \phi \\ \theta_n = n\pi - (\phi + \phi') \end{cases} \\ \phi' > \pi \Longrightarrow & \begin{cases} \theta_0 = n\pi - \phi' \\ \theta_n = \phi \end{cases} \end{aligned} \tag{2.18}$$

The transition function F(x) involves the Fresnel integral,

$$F(x) = 2j\sqrt{x}\, e^{jx} \left\{ \sqrt{\frac{\pi}{8}}(1-j) - \int_0^{\sqrt{x}} e^{-jt^2} dt \right\} \tag{2.19}$$

More details about the Fresnel integral are given in [59]–[61]. The diffracted field is thus given by

$$E_d(s) = E_i\, D(L, \phi, \phi')\, A(s', s) e^{-jks} \tag{2.20}$$

The spreading factor *A(s',s)* describes how the amplitude varies along the diffracted ray [58], for spherical wave incidence, the spreading factor is given by

$$A(s', s) = \sqrt{\frac{s'}{s(s' + s)}} \tag{2.21}$$

The received signals strengths predicted by different mathematical constructions are graphed in Fig. 2.6. Keller's expression for a perfectly conducting wedge [62] results in discontinuity at the RSB and ISB boundaries. Koujoumjian and Pathak [58] fixed this problem. But their formulation does not consider the constant dielectric of the wedge. Lubbers' expression gives significant improvements for the cases of grazing diffraction angles. However, it inevitably leads to nonphysical dip when the angle of diffraction is small. With Remley et al. formulation, the diffracted rays always decrease smoothly and monotonically away from the shadow boundaries. Further detailed diffraction formulations are provided in [65]. Using Koujoumjian's heuristic diffraction formulation over a perfect conducting wedge, the effect of the frequency on the diffracted field is shown in Fig. 2.7. When operating in the 60 GHz band, an additional 15 dB of signal loss is recorded compared with the 2.5 GHz band.

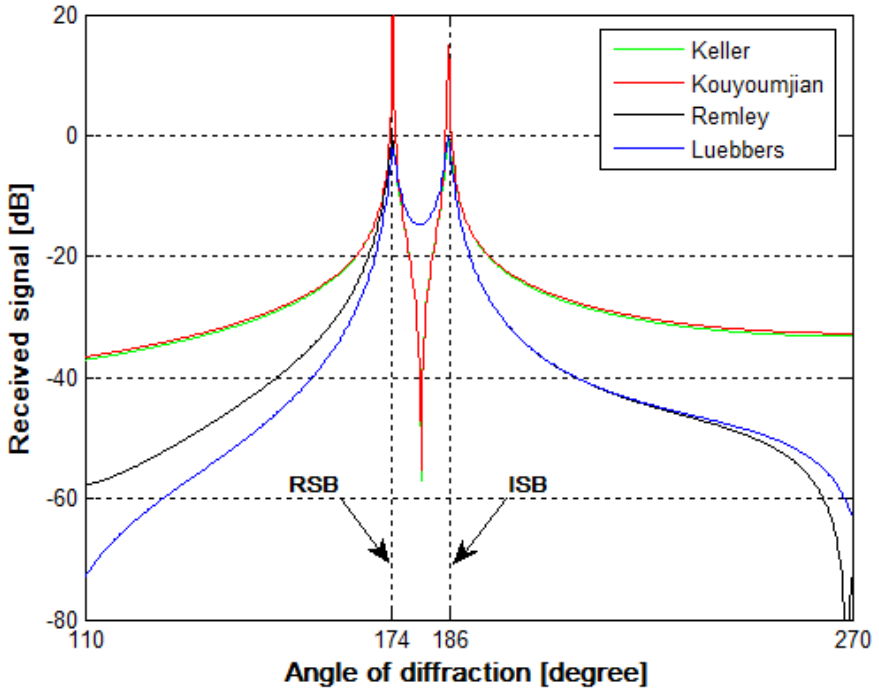

Fig. 2.6 Comparison of different formulations of the diffraction coefficient for a right wedge (s' = 10m, s = 10m, f = 60 GHz, ε_r = 2.81, σ = 0.1536 S/m).

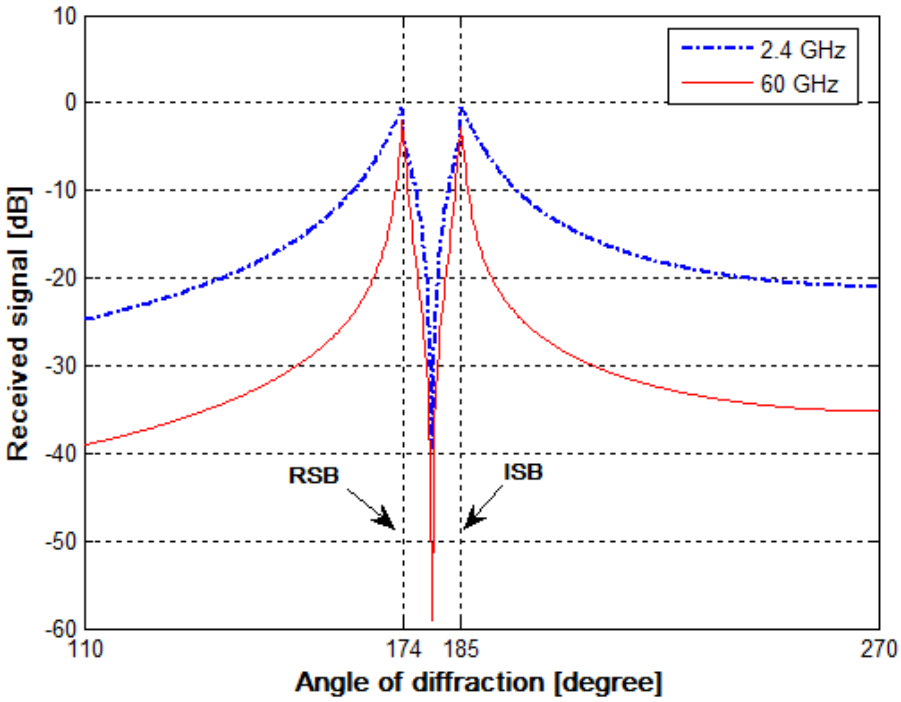

Fig. 2.7 Diffracted signals at 2.4 GHz and 60 GHz.

2.6 Ray-Tracing Approach Based Site-Specific Modeling

Ray tracing utilizes the principles of geometrical optics (GO) [66], [67], where propagation is assumed along discrete ray paths from transmitter to receiver. The GO has been developed for the analysis of light wave propagation which corresponds to high frequencies. In propagation problems, the GO is valid only for frequencies higher than 100 MHz [68]. With the input of environmental data, RT models provide accurate site-specific means to obtain useful simulation results for coverage prediction and multipath fading characterization.

Basically, the ray theory propagation phenomenon depends on the frequency, the nature of the environments and its material properties. Hence, the theoretical or ray-based models are based on exact computations making use of information on the physical processes and reliable building database characterizing the main features of the propagation channel. In ray-tracing algorithms, the main physical propagation mechanisms are the unobstructed LOS (free-space) if it exists, superimposed by reflection from flat surfaces and diffraction from corners and surface irregularities. Hence, the ray tracer performs a geometric and an electromagnetic computation to derive the path length and the field strength of each ray respectively. Also, RT technique inherently provides time delay and angle of arrival information for multipath reception conditions. This is important in Broadband signals that are particularly sensitive to the detrimental effects of multipath distortion and dispersion, which may produce a frequency-selective channel.

Ray-tracing technique is particularly attractive for indoor propagation environments due to its ability to provide a high level of detail in the characterization of multipath channels. In general, this assumption is valid when the wavelength is small compared to the geometrical dimensions of objects in the propagation environment. This is a particularly important issue in indoor propagation environments, where feature dimensions may be on the scale of the wavelength of operation, especially at the lower personal communications system frequencies of 5 GHz (6cm) and 60 GHz (5mm) [64].

2.6.1 Image Theorem Method

The reflective properties of surface materials lead to the adoption of the image theory method to provide an efficient technique to compute the different amplitudes and phases of

reflected rays in environments modeled with flat smooth surfaces. The image method is a simple and accurate method for determining the ray trajectory between the transmitter (Tx) and receiver (Rx). Imaging theory replaces reflecting walls and corners with images of the illuminating source [69, 70]. As shown in Fig. 2.8, a ray reaches the receiver R_x from the transmitter T_x, after reflection from both surfaces 1 and 2 at R_1 and R_2, respectively. The imaging theorem is described as placing a mirror at each point of reflection as illustrated in Fig. 2.8. The line joining the new position of both antennas $T_{x\text{-}image}$ and $R_{x\text{-}image}$ yields the total path length travelled by the propagating wave. However the multiple-reflected rays can be analysed in a similar way and the number of images for the k^{th} order reflection will be $n(n\text{-}1)^{k\text{-}1}$, where n is the number of flat reflecting surfaces. The image method is accurate, but can be cumbersome, suffering from computation complexity and time when large numbers of reflecting surfaces are encountered in the channel.

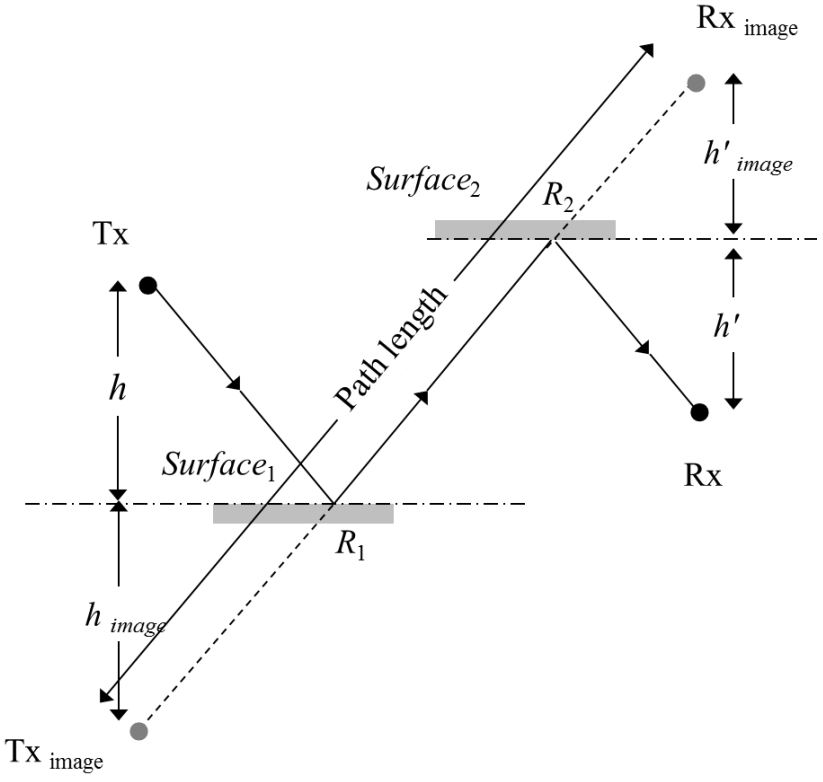

Fig. 2.8 A schematic illustration of the image method.

2.6.2 Formulation

In basic RT models, the prediction of the received power signal envelope is based on the calculations of free-space transmission, reflected and diffracted rays from different objects surrounding the transmitter and receiver. The reflected rays are tested against every object according to the image theory method. Hence, the total geometrical optics field at the receiver is calculated as:

$$E = E_o . A_o e^{-jkr_o} + \sum_{i=0}^{N} E_i A_i R_i e^{-jkr_i} + \sum_{j=1}^{L} E_j A_j D_j e^{-jkr_j} \quad (2.22)$$

where N and L are the numbers of reflected and diffracted rays obtained using ray tracing technique from the transmitter to the receiver, R is the distance travelled by nth ray, K is the wave number, A is the spreading factor, and E is the incident field detected at the point of interaction. The spreading factor is a function of the travelled distance by the nth ray and the source field whether spherical or plane waves are considered.

It is noticeable to mention that, in equation (2.22) the parameters with a subscript "0" account for the direct ray from the transmitter to the receiver, if unobstructed. Equation (2.22) only shows contributions from rays which experience single-reflection or single-diffraction, but it can easily be extended to multiple-interactions along a ray by simply multiplying the appropriate coefficients together [71], [72].

2.7 Multipath Propagation

The multipath mobile radio channel may be modeled as a linear time-varying impulse response filter since the distance d is varying with the time t according to the relation $d = vt$. Hence, the received signal $y(t)$ is the convolution of the transmitted signal $x(t)$and the channel impulse response $h(t, \tau)$, expressed as [73]:

$$y(t) = x(t) * h(t, \tau) \quad (2.23)$$

where $*$ denotes a convolution operator, the variable t represents the time variation due to motion of the receiver, and τ represents the channel multipath delay for a fixed value of t.

Since the received signal in a multipath channel consists of a series of attenuated, time delayed, phase shifted replicas of the transmitted signal. Initiated by Turin [74], the general discrete model of the baseband impulse response of a multipath mobile radio channel can be expressed as

$$h(t,\tau) = \sum_{n=1}^{N(t)} a_n(t,\tau)\, e^{-j\theta_n(t,\tau)} \delta\big(\tau - \tau_n(t)\big) \tag{2.24}$$

in which the impulse response h(t) is the sum of time-varying multipath-impulses $N(t)$, $a_n(t,\tau)$ and $\tau_n(t)$ are the real amplitudes and excess delays, respectively, of n^{th} multipath component at time t, and $\delta(\bullet)$ is the Dirac delta function. The phase $\theta_n(t,\tau) = 2\pi f_c \tau_n(t) + \varphi_n(t,\tau)$ represents the phase shift due to free space propagation of the n^{th} multipath component, plus any additional phase shifts which are encountered in the channel.

The channel impulse response of equation (2.24) serves to describe the radio channel characteristics and their behaviour. In the narrowband channel, multipath fading comes as a result of small path length differences between rays coming from objects surrounding the transmitter and receiver. These differences, on the order of a few wavelengths, lead to significant phase differences. For example, when the reciprocal bandwidth of the transmitted signal *Ts* (symbol duration) is much larger than the delay spread of the channel, therefore $h(t,\tau)$ can be approximated as a single delta function with $\tau = 0$,i.e. the number of multipath components $N(t)=1$ and the channel behaves as a narrowband channel. This delay would be unimportant if all of the energy arrived at the receiver with the same delay spread.

However, on the basis of the previously mentioned, multipath channel behaves as wideband channel, since path length differences between rays coming from different objects surrounding the transmitter and the receiver as well their relative delays are significant. The channel is referred to as frequency selective also known as wideband channel. Therefore, when dealing with a high bit rate data transmission, and in order to avoid significant distortion of the received signal, wideband channel parameters must be investigated. The N constituent multipath components may consist of the line-of-sight (LOS) signal received directly from the transmitter, a variety of signals received from reflecting surfaces, penetrating walls, diffracting edges/corners/curvature shapes, and scattering surfaces. All these fundamental propagation

primitives are incorporated in the ray-tracing algorithms to ultimately yield an assembly of the amplitudes an phases of the rays arriving at the receiver.

2.8 Channel's Power Delay Profile

The power delay profile (PDP) is considered as one of the most important keys in wideband channels in order to quantify the effects of multipath dispersion on the received signal as shown in Fig. 2.9. The mean excess delay ($\bar{\tau}$) and RMS delay spread (σ_τ) are the most important parameters used to evaluate the dispersive properties and performance of the channel [75]. Mean delay is defined as the first moment of power delay profile, corresponding to the centre of gravity of the profile, whereas the rms delay spread is the square root of the profile second central moment.

In time invariant multipath channel and after *PDP* time alignment which is achieved by setting the first perceptible received symbol of the transmitted signal (LOS) to zero "0", $\bar{\tau}$ and σ_τ are calculated as [76].

$$PDP \Rightarrow \begin{cases} P_T = \sum_{i=1}^{n} P_i \\ \bar{\tau} = \frac{1}{P_T} \sum_{i=1}^{n} P_i \tau_i \\ \sigma_\tau = \sqrt{\frac{1}{P_T} \sum_{i=1}^{n} P_i \, \tau_i - \bar{\tau}^2} \end{cases} \tag{2.25}$$

where P_T is the total power of the channel, and P_i is the relative power of each perceptible multipath component. Given the stringent power constraints imposed on system overlay, the type of digital modulation and receivers must be efficient at gathering up this multipath energy with lowest ISI. Channel behaves as narrowband, when the RMS spread is much less than the symbol duration. In this case, ISI encountered in the channel renders to be insignificant.

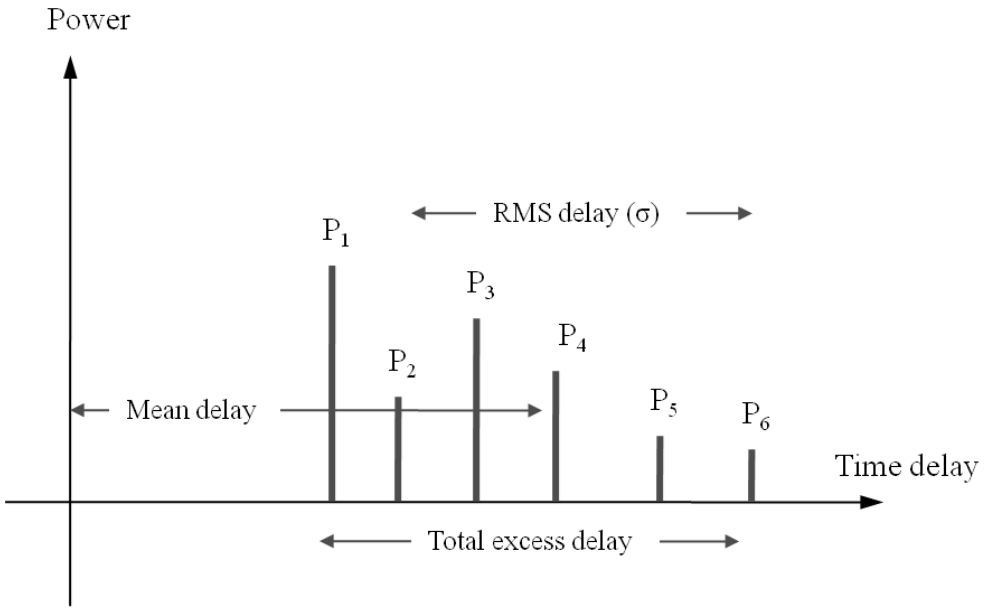

Fig. 2.9 Power Delay Profile (PDP) of a dispersive channel [54].

Different studies show that, if the delay spread of the channel is less than one tenth of the transmitted symbol period, then acceptable performance for voice (i.e. error probability less than 10^{-3}) can be achieved without using an equalizer to compensate for ISI. When the relative amplitude of these different versions of the signal and their relative delays are significant they will start to seriously degrade the modulation process and distort the transmitted signal, the channel is then classified as wideband. Thus, ISI has been recognized as the major obstacle to high speed data transmission over mobile radio channels.

2.9 Small-Scale (fast) Fading

Multipath fading comes as a result of small path length differences between rays coming from scatterers surrounding the transmitter and the receiver. These differences, on the order of a few wavelengths, lead to significant phase differences. Hence, small displacements of one of the antennas can lead to dramatic changes in the received signal envelop. As the mobile receiver moves away from the BS over relatively a fraction of a wavelength, multipath components add destructively or constructively. Their random phases and amplitudes give rise to rapid fluctuation in the received signal strength, thereby inducing small-scale fading [77], [78], signal distortion, or both as shown in Fig.2.10. If the mobile radio channel has a constant gain and linear response

over its bandwidth which is greater that the bandwidth of the transmitted signal, then the received signal will undergo flat fading which might not be a potential problem. By contrast, if strong scatterers exist well off the great circle path between the base and mobile, the time differences may be significant and relative delays are large compared to the basic symbol of the signal transmitted on the channel, the channel then experience significant distortion, which varies across the channel bandwidth. Then, the channel is considered to be a wideband channel. Hence, wideband mobile radio channel has assumed increasing importance in recent years as mobile data rates increase to support multimedia services. The channel is referred to as frequency selective fading when it possess a constant gain and linear phase response over a bandwidth that is smaller than the bandwidth of transmitted signal, consequently the channel impulse response has a multiple delay spread which is greater than the symbol duration of the transmitted signal. This delay would be unimportant if all of the energy arrived at the receiver with the same delay spread. Otherwise, the symbol arrives at the receiver with duration equals to the transmitted duration plus the delay duration of the channel to give rise to ISI which is a common drawback in wideband channels [79].

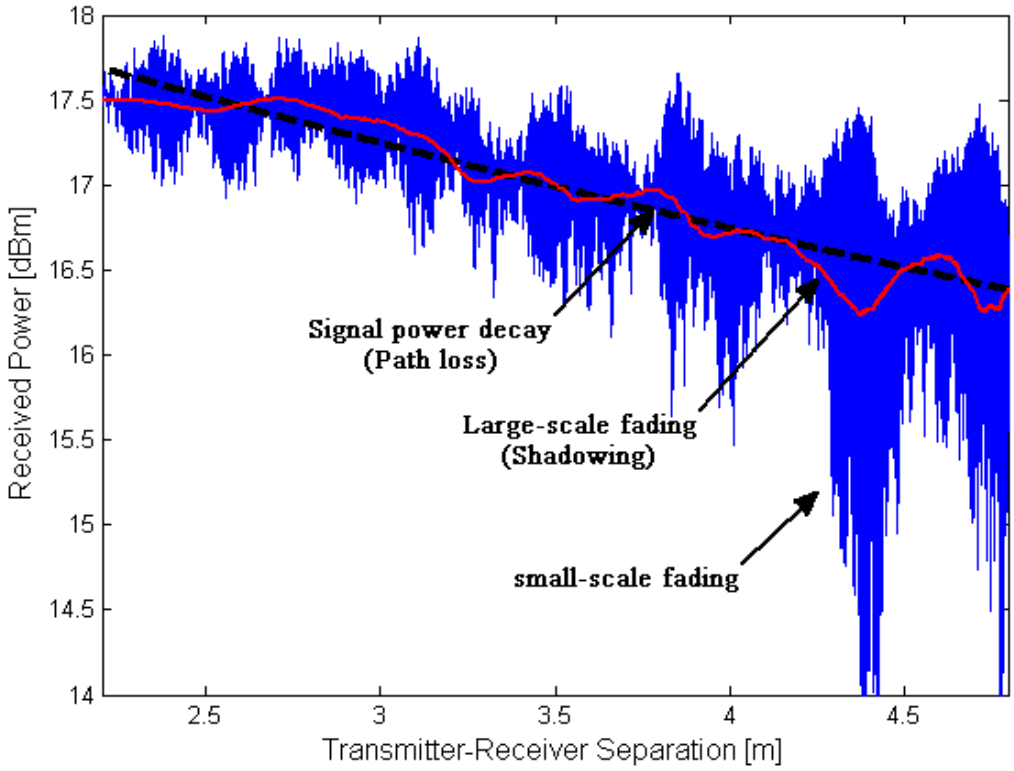

Fig. 2.10 Small-scale and large scale fading.

2.10 Channel Fading Statistics and Distributions

2.10.1 Rayleigh Fading Distribution

In a wireless channel, when a non-line-of-sight exist between the transmitter and the receiver, the received signal is composed of the sum of random multipath waves arriving from the transmitter to the receiver from different routes.

Generally, all path signals are assumed to be independent and random with the same average strength and equally probable angle of incidence. Thus, the resulting signal is the superposition of a large number of complex random signals. In such a case, the central limit theorem can be applied, which leads to the description of the channel as a complex Gaussian, zero-mean random process. This type of processes can be represented by the sum of two independent zero-mean Gaussian processes in the complex plane as shown in Fig 2.11. We can conclude that the magnitude is Rayleigh distributed, whereas the phase is uniformly distributed over the interval [0,2π]. Therefore, the radio channel is often called the Rayleigh fading channel [80]. The central limit theorem shows that, under certain conditions, a sum of enough independent random variables approaches very closely to a normal distribution. In other words, as the number of waves N→ ∞ the distribution approaches a Gaussian distribution, provided that no one of the variables dominates. The sum of real and imaginary components in phase (I) and quadrature (Q) respectively of the complex baseband signal $r(t)$ is:

$$r(t) = \sum_n r_{real}(t) + j\sum_n r_{iamg}(t) = r_{real}(t) + jr_{imag}(t) \tag{2.26}$$

$$(r,\theta) = f\left(r_{real},\, r_{iamg}\right) = \left(\sqrt{r_{real}^2 + r_{imag}^2},\ tan^{-1}\left(\frac{r_{imag}}{r_{real}}\right)\right) \tag{2.27}$$

By central limit theorem, when a large number of multipath components having random amplitudes and independent phases, then $r(t)$ is complex Gaussian. However, in absence of dominant component, then $r(t)$ is zero-mean complex Gaussian $(E|r(t)| = 0)$ centered at the origin of the complex IQ plane, and its envelope $|r(t)|$ is Rayleigh distributed. An IQ sketch of the Rayleigh pdf is shown in Fig. 2.11.

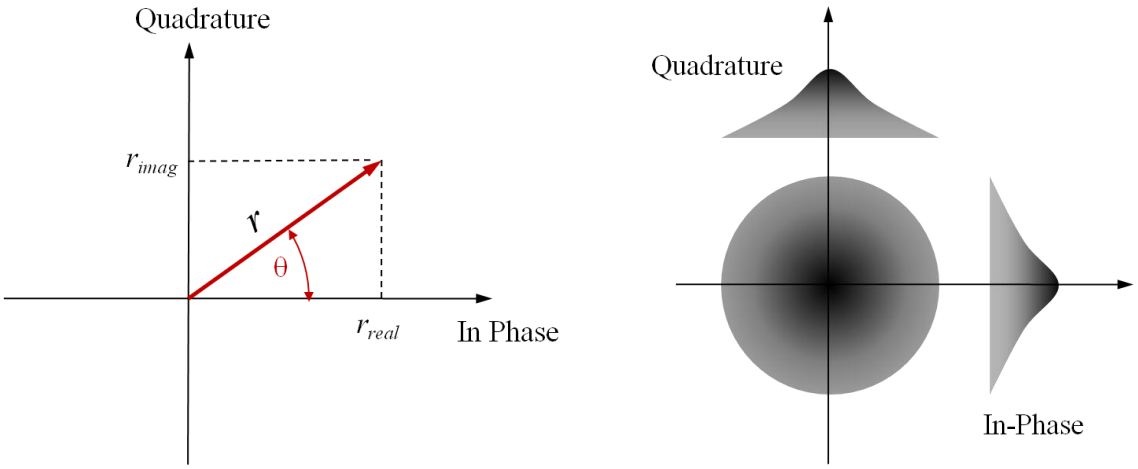

Fig. 2.11 Rayleigh IQ plan.

The Rayleigh distribution has a probability density function (PDF) given by [81]–[83]:

$$p(r) = \begin{cases} \frac{r}{\sigma^2} exp\left(-\frac{r^2}{2\sigma^2}\right) & r \geq 0 \\ 0 & r < 0 \end{cases} \tag{2.28}$$

Where, σ is the standard deviation (RMS) of either the real or imaginary part of the received voltage signal before envelope detection, and σ^2 is the time-average power of the received signal before envelope detection. In presence of dominant component, then $E[r(t)] \neq 0$ and, its envelope follow Rice distribution.

2.10.2 Rician Fading Distribution

The Rician function describes the fading distribution of power in the presence of a dominant multipath component. Adding a specular component to the Rayleigh IQ Plot, yields an IQ Complex Gaussian distribution is centred on the "strong path", its magnitude is Rice distributed, where the probability of deep fade is extremely small. A plot of the Rician IQ plot is shown in Fig. 2.12. The Rician fading distribution has a probability density function (PDF) given by [84]–[86]:

$$p(r) = \begin{cases} \frac{r}{\sigma^2} exp\left(-\frac{(r^2 + A^2)}{2\sigma^2}\right) I_o\left(\frac{A_r}{\sigma^2}\right) & A \geq 0, \ r \geq 0 \\ 0 & r < 0 \end{cases} \tag{2.29}$$

The parameter A denotes the peak amplitude of the dominant wave and I_o is the modified Bessel function of the first kind and zero-order.

$$I_n(z) = \sum_{K=0}^{\infty} \frac{\left({}^{z}/_{2}\right)^{n+2K}}{K!\,(n+K+1)} \qquad z \geq 0 \tag{2.30}$$

And, $I_n(z)$ is the modified Bessel function of first kind and order n. The Rician distribution is often described in terms of a parameter k which is defined as the ratio between the deterministic signal power and the variance of the multipath. It is given by:

$$K = \frac{A^2}{2\sigma^2} \tag{2.31}$$

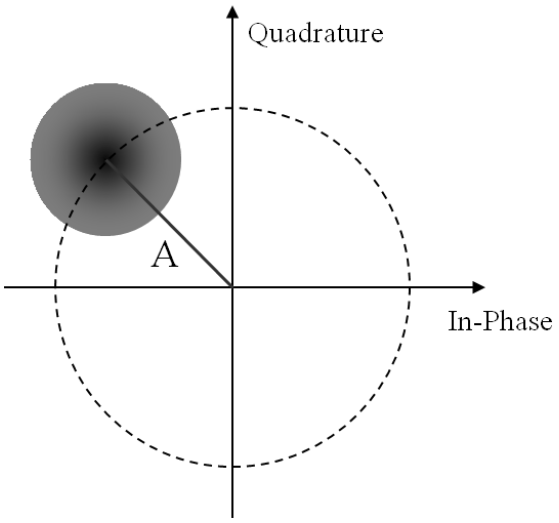

Fig. 2.12 Rician IQ plot.

The parameter k is known as the Rician factor and completely specifies the Rician distribution. As $A \to 0,\ K \to -\infty\, dB$ the dominant path decreases in amplitude, the Rician distribution degenerates to a Rayleigh distribution. Equation (2.29) is plotted in Fig. 2.13 for several values of k, keeping the total signal power constant. For very large values of k, the line-of-sight component dominates completely, very little fading is encountered, and the channel reverts to AWGN behavior. The cumulative Rice distribution is shown in Fig. 2.14. As the k factor increases, the probability of encountering a deep fade reduces, so the mean error rate will decrease. The Rice channel is therefore a more 'friendly' channel than the Rayleigh case, which represents in some senses a 'worst-case' channel.

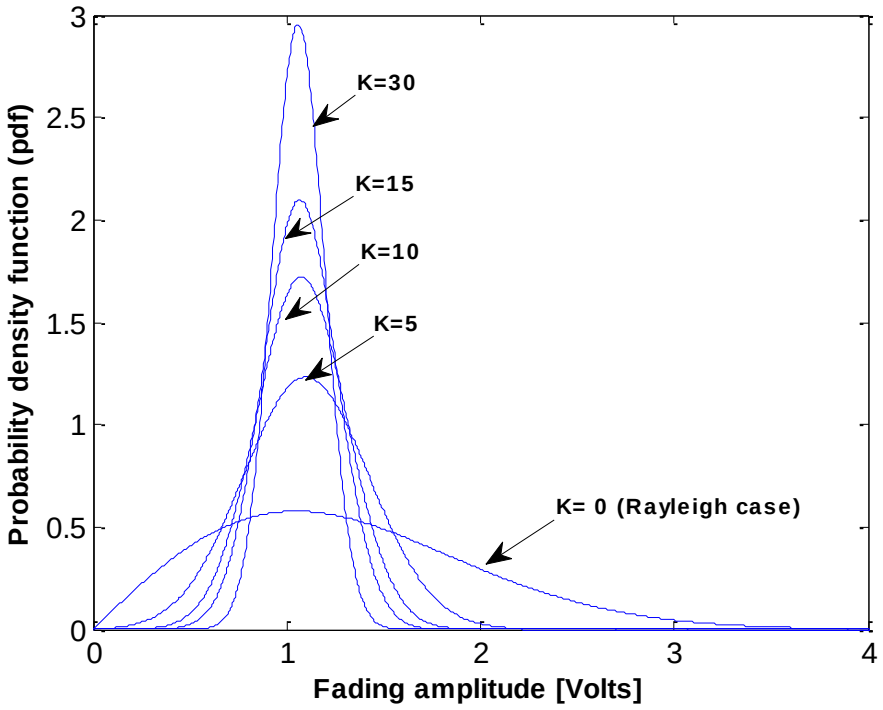

Fig. 2.13 Rice fading PDFs for different values of K with constant dominant component.

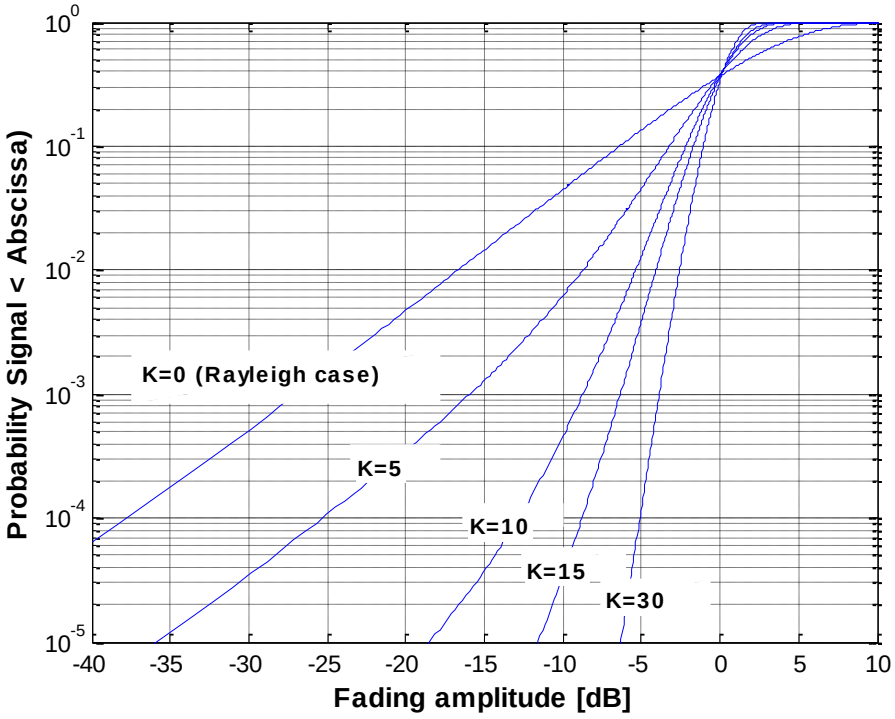

Fig. 2.14 Rice fading CDFs for different values of K.

Chapter 3

Millimeter-Wave Broadband Channel Sounding

3.1 Introduction

In one sense or another, most of studies and research works for modelling wireless communications are based on the measurement data of the channel propagation characteristics. Hence, the channel sounding is a fundamental task for wireless communications engineering. The name "sounding" stems from a transmitter that excites (sounds) the channel, whereas the channel output is recorded at the receiver side. The receiver records the channel output in various forms depending on the choice of the sounding technique. In the early 1960's, the channel sounders had to measure only the received field strength [87]. Since then, their complexity has been increasing drastically as the systems and the required channel models became more complex. During the 1990's, new class of channel sounders have appeared in telecommunications research [88]–[91] and industry to accommodate the transition towards wideband systems that require measuring the channel delays dispersion (or power delay profile). By late 1990s, the demand for higher data rates and hence higher and wider frequency bands has increased substantially. Consequently, special interest focused on the limitations due to the amount of multipath received in the channel. Thus, research generated renewed interests on in directional channel properties [92]–[94].

Earlier, measurement campaigns were mostly performed in macrocells [95], [96]. Since then, the measurement campaigns, however, have been focusing on microcells [97], [98], namely, indoor propagation. In more recent times, the extremely large bandwidth of high throughput systems puts higher demands on the required delay resolution of current channel sounders. Today, the inherently directional mm-waves applications that operate in the 60 GHz band require reliable

and accurate sounding systems, with a great ability to derive precise measurements of amplitudes and phases across the band of interest.

3.2 Time Domain vs. Frequency Domain Measurement Techniques

The characteristics of broadband channels can be measured in either the time domain or the frequency domain, generating the time-varying channel impulse response $h(\tau, t)$ or transfer function $H(f,t)$, respectively. Theoretically, the results are equivalent in both domains and can be transformed from one domain to the other by implementing the Fourier-Transform (FT). However, the practicalities of the measurement approaches are quite different [99], [100]. Time domain measurements obtain the channel impulse response by exciting the channel with short pulses or pseudo-noise sequences then recording the received signal with a sampling oscilloscope [101], [102]. This technique is conceptually simple but in practice the generation of ultra-narrow pulses is a challenging task in terms of analog to digital converters sampling rates and speed. Moreover, the requirements of RF and analog circuits are considered to be complex.

The frequency domain measurements, on the other hand, typically use a chirp-like or other multi-tones signal over a wide range of frequencies to sound the channel [103]. This approach can be most easily implemented by means of a vector network analyzer (VNA). Basically, VNAs sound the channel by slowly sweeping the frequency range of interest and measuring the transfer function between its two ports (S_{21}). The major drawback of the VNA systems is that each measurement sweep takes a significant amount of time, depending on measurement bandwidth [25].

More explicit in this research project, the decision to carry measurements in the frequency domain is due to the fact that frequency-domain sounders are easier to control. As the signal bandwidth becomes extremely large, the sounder excites the channel with signals whose shapes are closer to the ideal waveforms (swept or stepped-frequency sinusoid) that can be more easily controlled as compared to rectangular, Gaussian or raised cosine waveforms [104], [105]. Additional requirements must be considered in the design of the sounding system design,

- The carried measurements are band-limited time-invariant, i.e., $H(f)$ and $h(\tau)$ are considered to be accurate as long as the received signal is sampled according to the Nyquist criterion [106] in the delay domain.

- The measurement sweep time is shorter than the coherence time of the channel. In other words, the sweep time is short enough for the channel not to have changed between the beginning and end of the sounding sequence. Hence, it is essential to avoid movement of people and mobile objects during the measurement campaign, to guarantee that the temporal variations of the channel are sufficiently slow.

- Power spectral density of the sounding signal, $|P_{TX}(jw)|^2$, should be as uniform as possible across the bandwidth of interest. This allows having the same quality of the channel estimate at all frequencies [25].

- The time resolution ($T_{resolution}$) is inversely proportional to the sweep bandwidth (BW_{sweep}), namely,

$$T_{resolution} \approx \frac{1}{BW_{sweep}} \tag{3.1}$$

  The signal bandwidth is large enough in order to reasonably resolve the ambiguity of multipath components that arrive at the receiver within few nano-seconds of interval.

- The phase synchronization for long distances between the transmitter and the receiver is a key problem for wireless channel sounding. Using coaxial cables, it is possible to provide phase synchronization for distances up to about 10 m [25]. Hence, due to the heavy signal losses experienced by the coaxial cables, they become impractical for WLANs measurements. Consequently, long range sounding systems requirements aim to cover hundreds of meters, but in our case we have reached the 20 m range under NLOS which can't be realized using VNAs and omnidirectional antennas.

3.3 Choice of Antennas and Experimental Arrangements

Mm-waves links are inherently directional; directivity is certainly required to gain sufficient link budget for the support of the envisioned high data rate services [107]. The key factor to increase mm-waves link data rate is to reduce the time dispersive characteristics of the channel, i.e., to reduce the multipath propagation effects. In the 60 GHz band and following the FCC regulations, there are no stringent limitations on the transmitted power, where up to 27 dBm of equivalent iotropic radiated power (EIRP) is permitted. Hence, the approach to overcome the high propagation loss for the distances of several tens of meters and to increase energy efficiency is to use high gain antennas. When planning for propagation measurements, the choice of the antenna is influenced by the nature of the measurement environment and the objective for carrying such measurements [108]. In this research work, the main targeted goal of a NLOS corridor measurement campaign was to evaluate the propagation characteristics at a range of 20 m of separation distance between the transmitting and receiving antennas. The other goal is to assess the signal transmission laying and to extend its coverage to longer distances. In this case, high gain directional pyramidal horn antennas are considered. The measurements carried in a conference room highly directional antennas at both ends are undesirable, since the influence of the multipath effects that we want to characterize becomes masked due to the spatial filtering effect of the directional antenna gain function. Two antenna arrangements were considered: a) omni-direct, where an omnidirectional biconical antenna was used at the receiving end, while a highly directive pyramidal horn antenna was used at the transmitting end, b) direct-direct, i.e., directional pyramidal horn antennas are used at both remote ends. The technical specifications and descriptions are discussed later in this chapter.

3.4 The Channel Sounding System Architecture

3.4.1 Basic Concept

As mentioned previously, it is critical that the microwave transmitter and the receiver remain in complete synchronization at all times. The system is designed and implemented at the CRC (communication research center, Ottawa, Canada) laboratories. This versatile sounding system involves an evolutional method of providing RF phase coherence between the transmitter and the receiver where both are connected by means of a single-mode optical fiber cable that

provides the means of RF communications between units. The concept behind using fiber-optic feeding was to allow a flexible and low attenuation link to the transmitter. Therefore, a higher precision of the complex channel transfer function measurement can be achieved. Using laser fiber optics scheme, the microwave transmitter and the receiver may be synchronized for a realistic long-distance up to 1 km.

3.4.2 Experimental Setup and Hardware

The general schematic diagram of the system is illustrated in Fig. 3.1. The versatile channel-sounding frequency-response system introduced in this work was made of complex instrumentation.

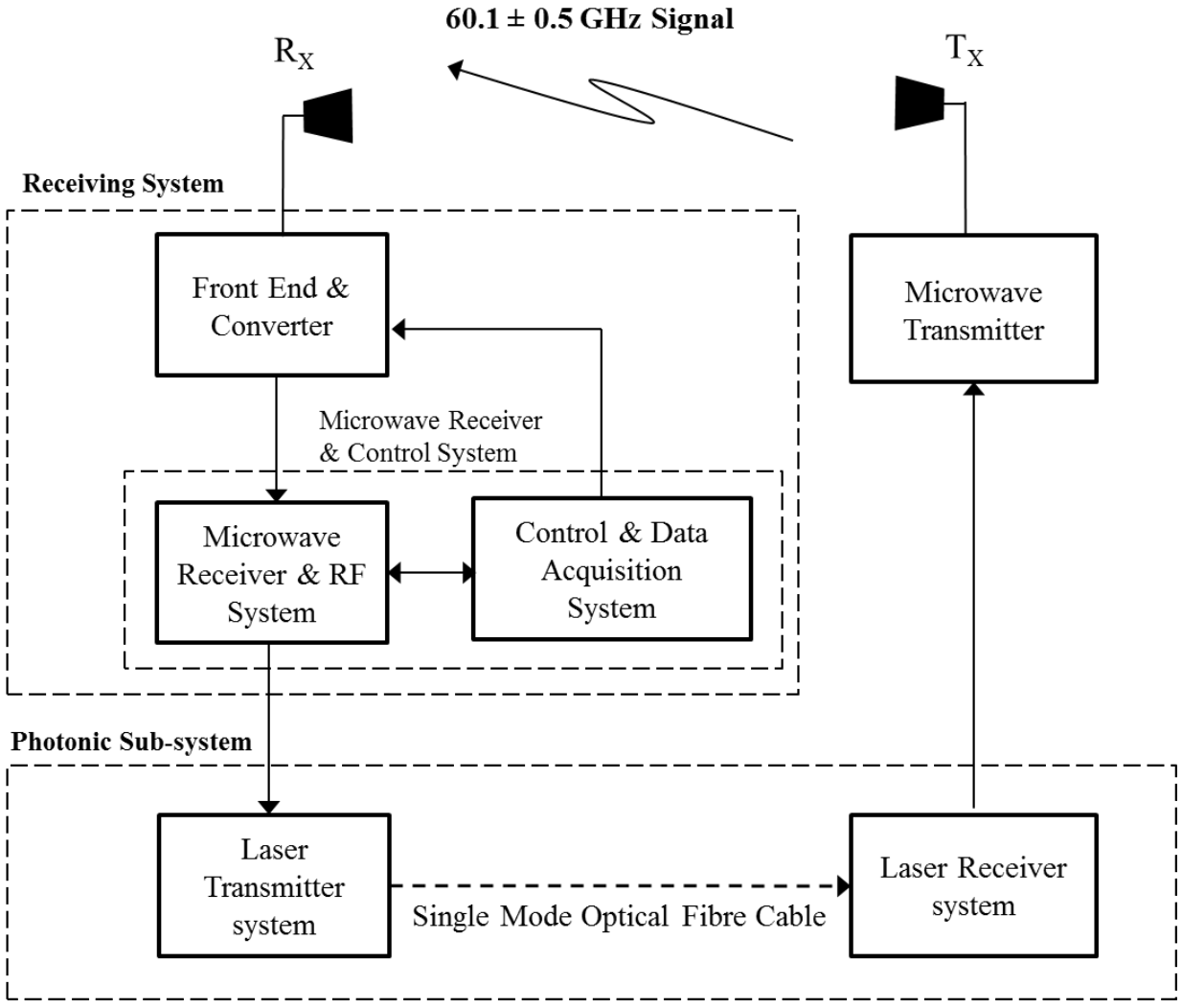

Fig. 3.1 Block diagram of the measurement system.

Using this sounder, adequate and precise frequency response measurement of the propagation channel can be achieved. Precise measurements of amplitude and phase are achieved across the 1 GHz frequency bandwidth (59.6 - 60.6 GHz). Such measurements are programmed at close enough frequency intervals to resolve the phase ambiguity. The measurement samples were usually made at programmed frequency intervals of 100 kHz to yield 10001 data points for each measurement snapshot. However, system is flexible enough so that any frequency interval may be chosen. As a result of the 1 GHz bandwidth, a time resolution of one nanosecond is achieved to enable the analysis and characterization of the propagation in the 59.6 - 60.6 GHz band. The overall measurement sweep time is approximately 3 seconds. This time is short enough to consider channel stationary and to guarantee that no people interfere or disturb the channel during the measurements sweep.

3.4.3 The Receiving System

In the sounding system, the reference signals are generated in the receiver while the transmitter is effectively a slave of the receiver, hence, the various parts of the system will be described following the signal path, i.e., starting from the receiver and ending at the transmitter. The receiver setup is displayed in the photograph of Fig. 3.2. The receiving system consists of two main parts. The first part includes the front end with the antenna which interfaces directly with the wireless propagation channel. The other part of the receiver includes the control and data acquisition system.

3.4.3.1 Front End and Converter System

The block diagram of this part of the receiver is shown in Fig. 3.3(a), it constitutes an interface between the receiver and control system and the wireless propagation channel. Hence, the received signal is first intercepted by the front end antenna and then down converted from 60.1 ± 0.5 GHz to an intermediate frequency of 5.25 ± 0.5 GHz after being mixed with a 54.9 GHz signal. The 54.9 GHz is derived from a 6.1 GHz source multiplied by a factor of 9.

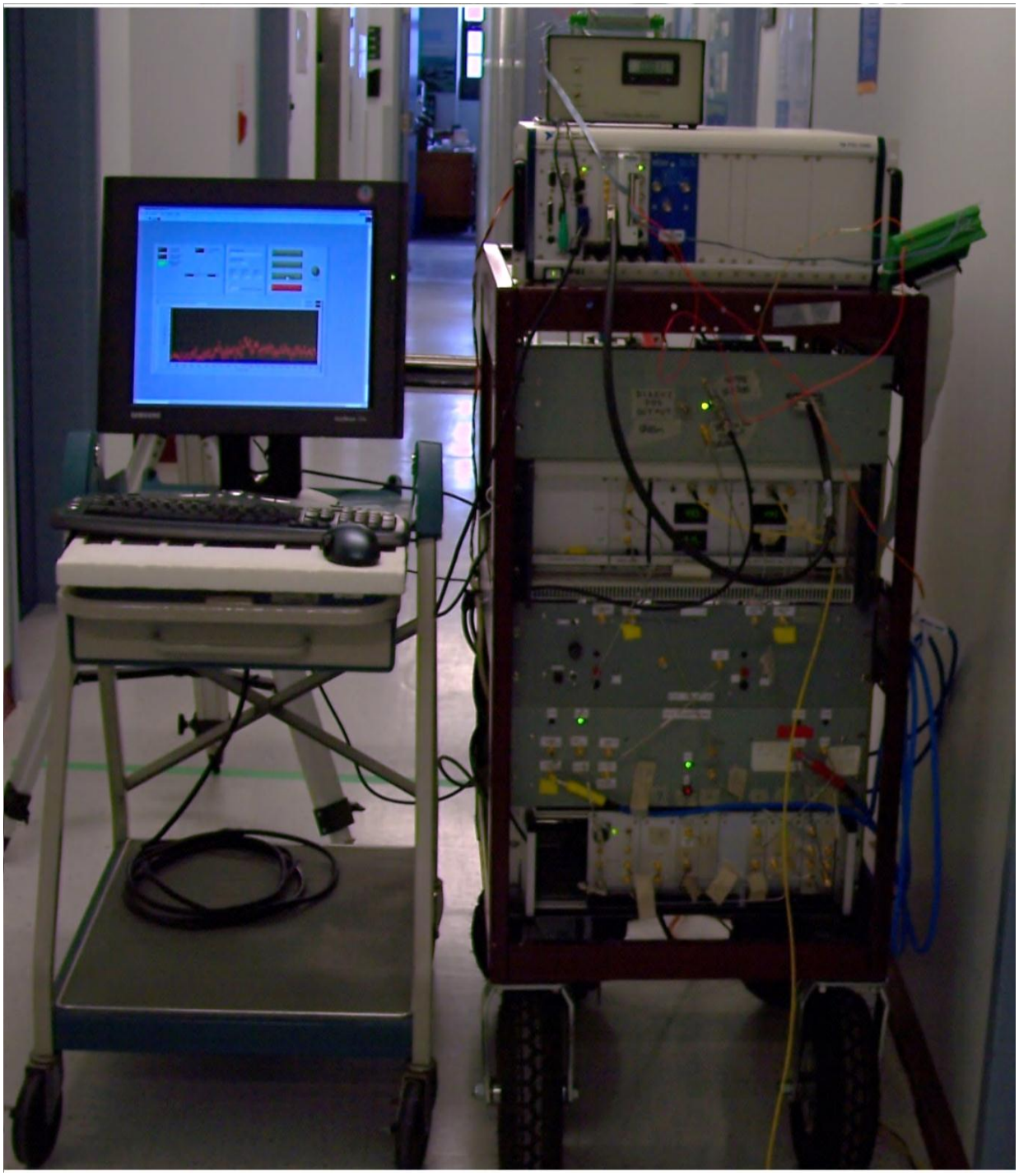

Fig. 3.2 Photograph of the receiver setup.

Stabilization of the frequency measurements is achieved by locking all oscillators and signal generators to a highly stable 10-MHz Rubidium frequency reference. The synthesizer frequency source of 4.25 ± 0.5 GHz is then used to allow conversion from the intermediate frequency to 950

MHz at the output of the receiver's front end. The 6.1 GHz source also provides a reference signal to feed the photonic transmitter of the laser subsystem in order to modulate a 1548 nm light wave.

3.4.3.2 Microwave Receiver and Control System

This part consists of a computer operated component that controls an AD9858 direct digital synthesizer (DDS) that is coupled to a (×16) frequency multiplier to make sounder system operate in the required frequency range. The AD9858 synthesizer is manufactured by Analog Devices' company; it is capable of generating a frequency-agile analog output sine wave at up to 400 MHz. The control and data acquisition units are integrated in the receiver end of the system.

The friendly-user data acquisition system (DAQ) is built using LABVIEW software to interface with graphic and monitoring devices and convert measured samples into digital numeric values. The DAQ is equipped with a high capacity acquisition memory to store multi-gigabits of uncompressed raw data. In very few seconds, this high-speed DAQ system is capable of transferring multi-gigabits of measured samples to the central server through the intranet to allow offline processing. LABVIEW scripts are built to run and drive the high-performance Pentium 4 controller embedded in national instrument NI PXI-8186 card. The program interfaces with the NI PXI-5124E multifunction DAQ card which can be used for high-speed data logging, control applications and high voltage sensing. The NI PXI-5124E card is used to sense the voltage levels from the 70 MHz wide dynamic range (WDR) amplifier outputs.

At the output of the 70 MHz amplifier strip the data signals are detected in the form of in-phase (I) and quadrature (Q). Therefore, full phase information is provided. The LABVIEW platform also provides an interface with the 100 MHz digital waveform generator/analyzer; this NI PXI-6552 card is used to control the DDS. The block diagram of the microwave receiver and control system is illustrated in Fig. 3.3(b). The receiver control system is fed by the 950 MHz output of the front end to modulate an 880 MHz source before being processed by the 70 MHz wide dynamic range receiver system to detect as lowest and as highest as possible multipath signals.

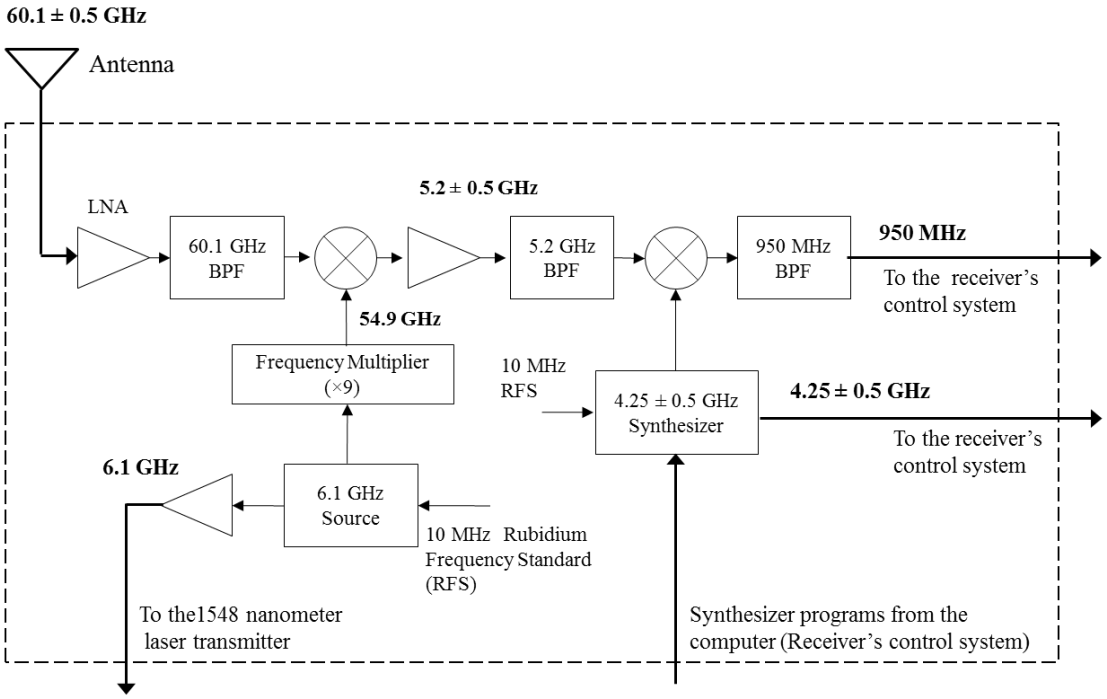

a) Front End and Converter System

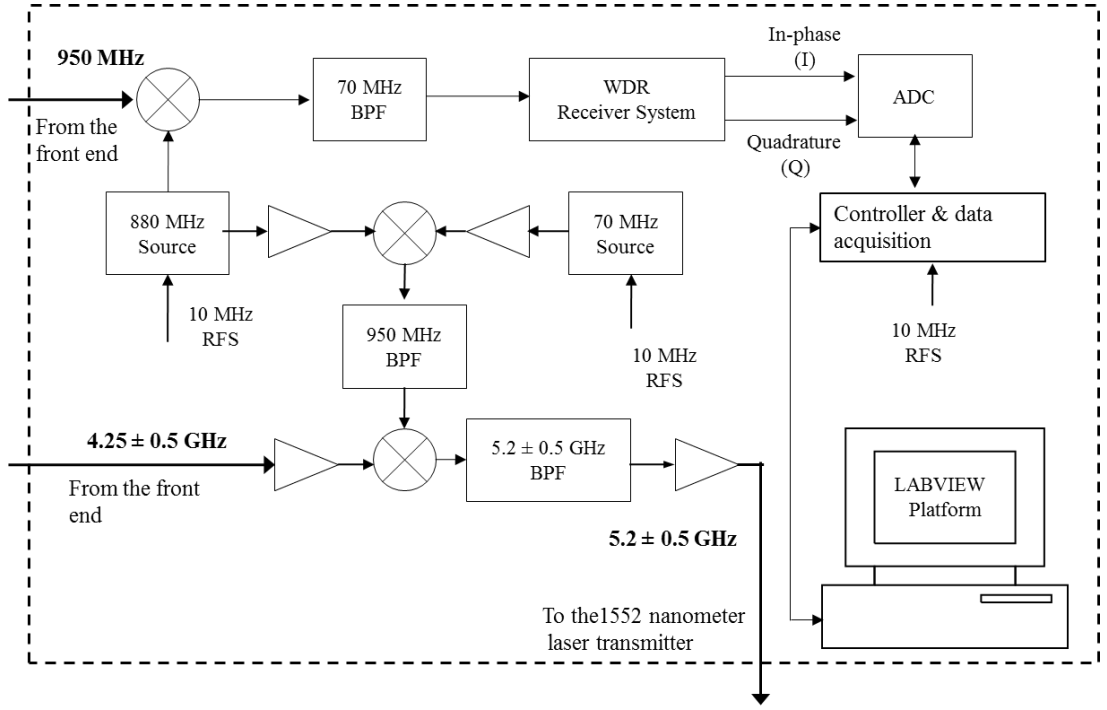

b) Microwave Receiver and Control System

Fig. 3.3 Block diagram of the sounder's receiver system.

Hence, RF signals are not directly converted into baseband but moved to the low-IF band where the analog-to-digital converter (ADC) sampling rate can support the conversion into digital signals. Then, these low-IF signals are sampled with ADC and I/Q quadrature demodulation is done in the digital domain. However, this increases the burden of ADC which requires both higher sampling rate and higher dynamic range. The 950 MHz source of the receiver control side is then mixed with the (4.25 ± 0.5) GHz signal fed by the DDS to generate the (5.2 ± 0.5) GHz used to modulate a 1552 nanometer light wave generated by the laser transmitter.

3.4.4 Laser Transceiver Subsystem

The microwave receiver and the optical transmitter systems are carried in the same chariot shown in Fig. 3.2. As previously discussed, the laser transmitter system is fed from the microwave receiver system by the 6.1 GHz and 5.2 ± 0.5 GHz RF signals to modulate the 1548 nm and 1552 nm light waves, respectively. Both modulated light waves are then combined and supplied to the laser receiver through a 500 m single mode optical fiber cable. A block diagram of the laser transceiver subsystem is provided in Fig. 3.4.

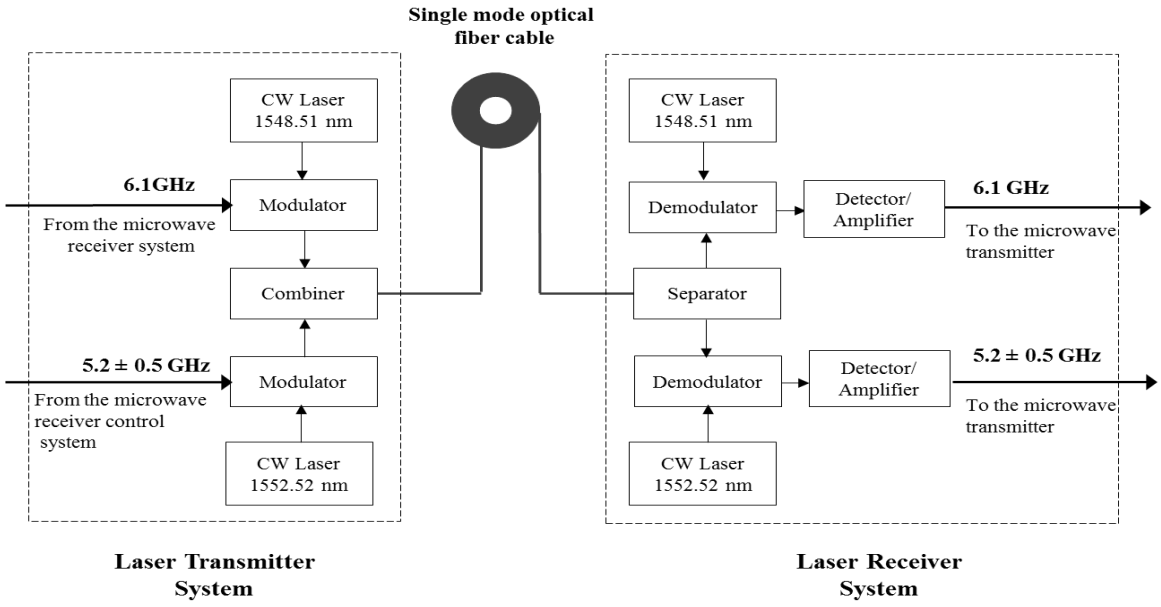

Fig. 3.4 Block diagram of the laser transceiver subsystem.

At the optical receiver an inverse signal processing task begins. Both light waves are separated and then demodulated to recover the two RF signals supplied to the input of the laser transmitter (6.1 GHz and 5.2 ± 0.5 GHz) shown in Fig. 3.4. The input and output signals of the laser subsystem are similar, hence, the main duty of the laser subsystem is to provide a mirror of the microwave receiver's output RF signals. These RF signals are then supplied to the microwave transmitter to derive it in complete phase synchronization with the microwave receiver system.

3.4.5 The Microwave Transmitter System

A photograph of the setup of the microwave transmitter and its block diagram are shown in Fig. 3.5 and Fig. 3.6, respectively. The microwave transmitter is effectively a slave of the microwave receiver and its control system. It receives the two RF signals (6.1 GHz and 5.2 ± 0.5 GHz), processes them in an inverse manner of the method described for the microwave receiver, and then radiates the 60.1 ± 0.5 GHz carrier frequency.

The microwave transmitter is equipped with a power amplifier to magnify the output power level up to a maximum of 4 dBm. The laser receiver system is located on the middle rack of the transmitter console underneath the spectrum analyzer as shown in Fig. 3.5. As a result of this evolutional phase synchronization between the transmitter and receiver via fiber optic, an extremely low phase noise is achieved at the output of the microwave receiver. The transmitter system is phase locked to the receiver and control system.

The signals used in the transmitter are generated in the receiver system, and conveyed to the transmitter by means of the optical cable. The phase noise in the transmitter is identical to the phase noise taking place in the receiver. The difference between the two is insignificant. Since both transmitter and receiver operate from the same frequency multiplier sources, relative phase noise between transmitter and receiver is less than 1 degree, peak-to-peak. This feature enables the system to derive an accurate frequency response of the propagation channel over the entire 1 GHz operational bandwidth of the system.

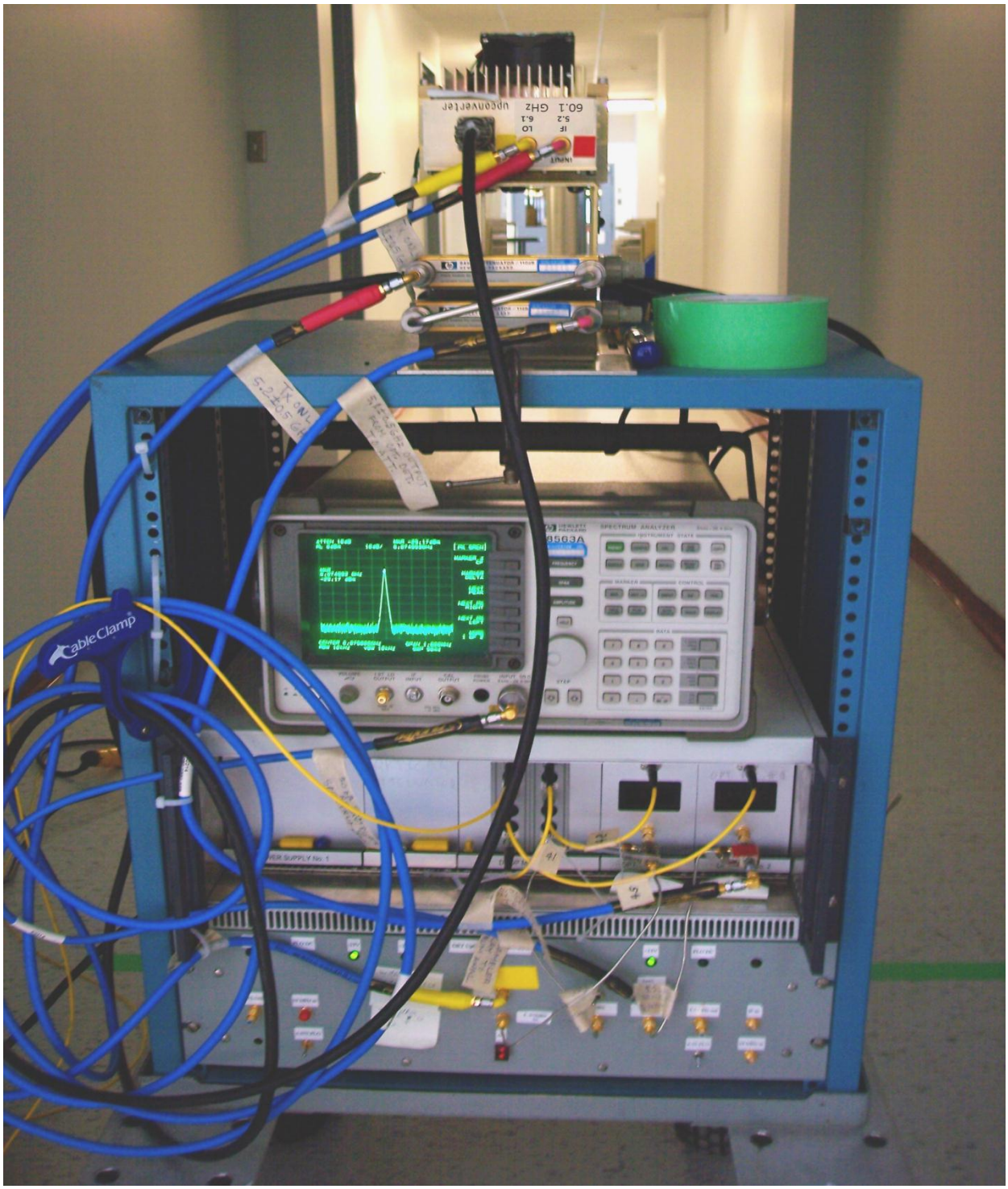

Fig. 3.5 Photograph of the setup of the microwave transmitter designed by the CRC.

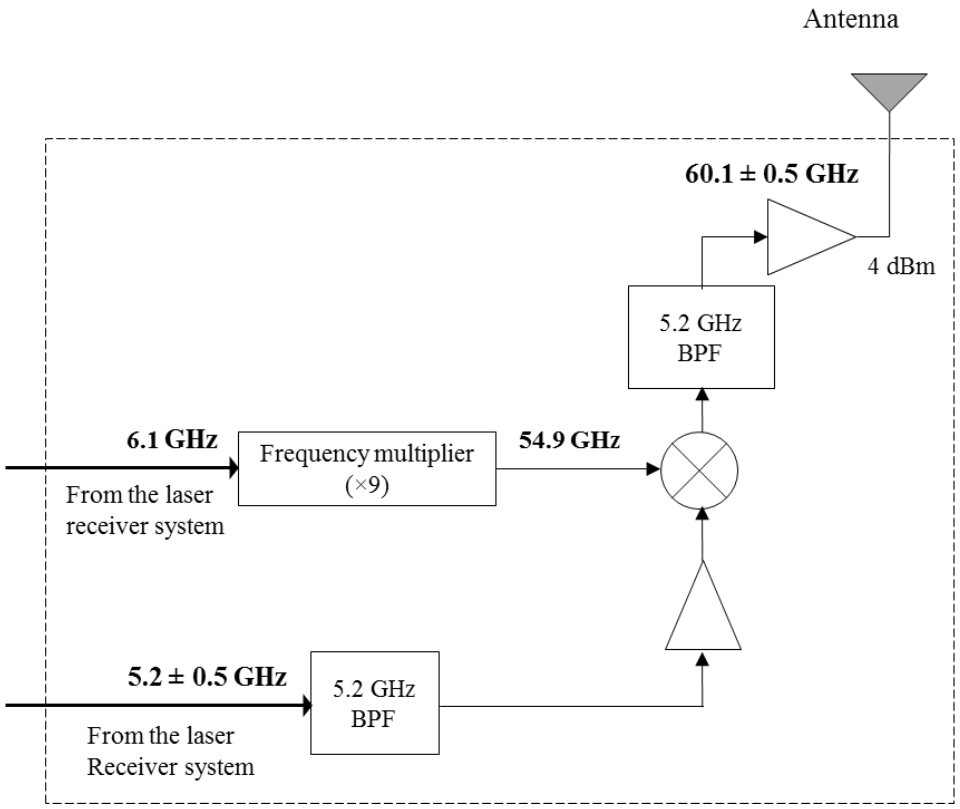

Fig. 3.6 Block diagram of the microwave transmitter system.

3.4.6 Antennas

The pyramidal horn antenna used is displayed in Fig. 3.7(a), it is of model (SGH-15) and manufactured by Millitech Company [109]. The vertically polarized biconical antenna used is shown in Fig. 3.7(b), its nominal gain is 2.3 dBi at the central frequency. In most broadband channel sounders, the antennas are not considered as a part of the calibration procedure. It is necessary to completely remove the frequency dependence effects of the antennas. The frequency dependence patterns of the used pyramidal horn (SGH-15) antenna are provided in [109]. It is important to underline the fact that the gain variation on 59.6 – 60.6 GHz range has insignificant effects on the measured data. This is because the gain of the used antenna is almost constant across the 1 GHz band of interest.

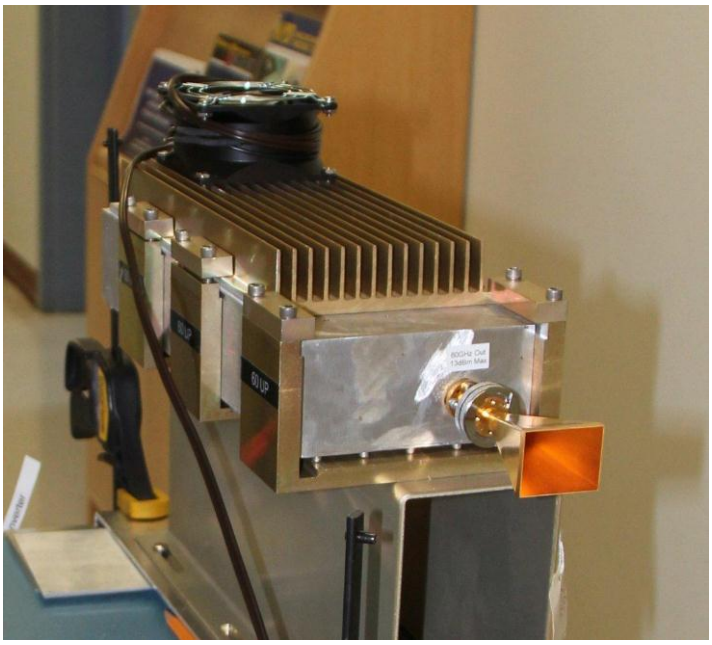

a) Directional horn antenna.

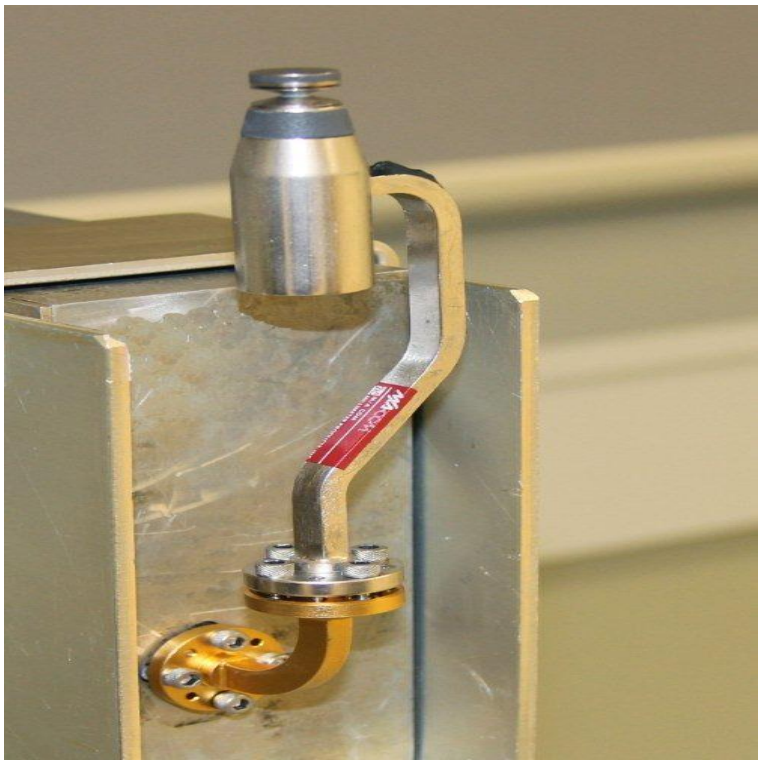

b) Omnidirectional biconical antenna.

Fig. 3.7 Photographs of the used antennas.

The technical specifications of the used antennas are presented in Table 3.1. More details about the SGH-15 horn antenna gain and specifications are found in Millitech Company's website.

Table 3.1 The SGH-15 pyramidal horn antenna technical specifications.

	Pyramidal horn	Biconical
Aperture dimensions	36.4×27.7 mm^2	--
Length	70.485 mm	--
Polarization	Vertical	Vertical
Typical HPBW (Elevation plane)	25^o	12^o
Mid-band gain	23.4 dBi	2.3 dBi
Frequency range (GHz)	V-band (50-75)	V-band
VSWR	1.2	1.4

3.5 System Calibration

Imperfections of the system components used in the measurement process can result in errors. In order to achieve accurate and reliable measurements, the instrumentations of the measurement system must be properly calibrated, since all the measured output frequency responses are relative to the calibration level [110]–[113].

In order to obtain a pure and accurate response ($H(f)_{\text{calibration}}$) from the sounder, it is essential to avoid the impacts of the channel and the antennas. In the versatile sounder presented in this thesis, the calibration is obtained using a reference measurement where the microwave transmitter is directly connected to the microwave receiver (back-to-back) through waveguide

attenuators providing nominal 70 dB of attenuation (without the antennas). The measured calibration signal is shown in Fig. 3.8(a). Taking into account the complex values of the measurements, the phase variation is then computed to reach its total value of 15,489 radians at 60.6 GHz. This corresponds to an equivalent electrical length of approximately 739.7 m using a 500 m (nominal) single-mode optical cable. The phase versus frequency is shown in Fig. 3.8(b).

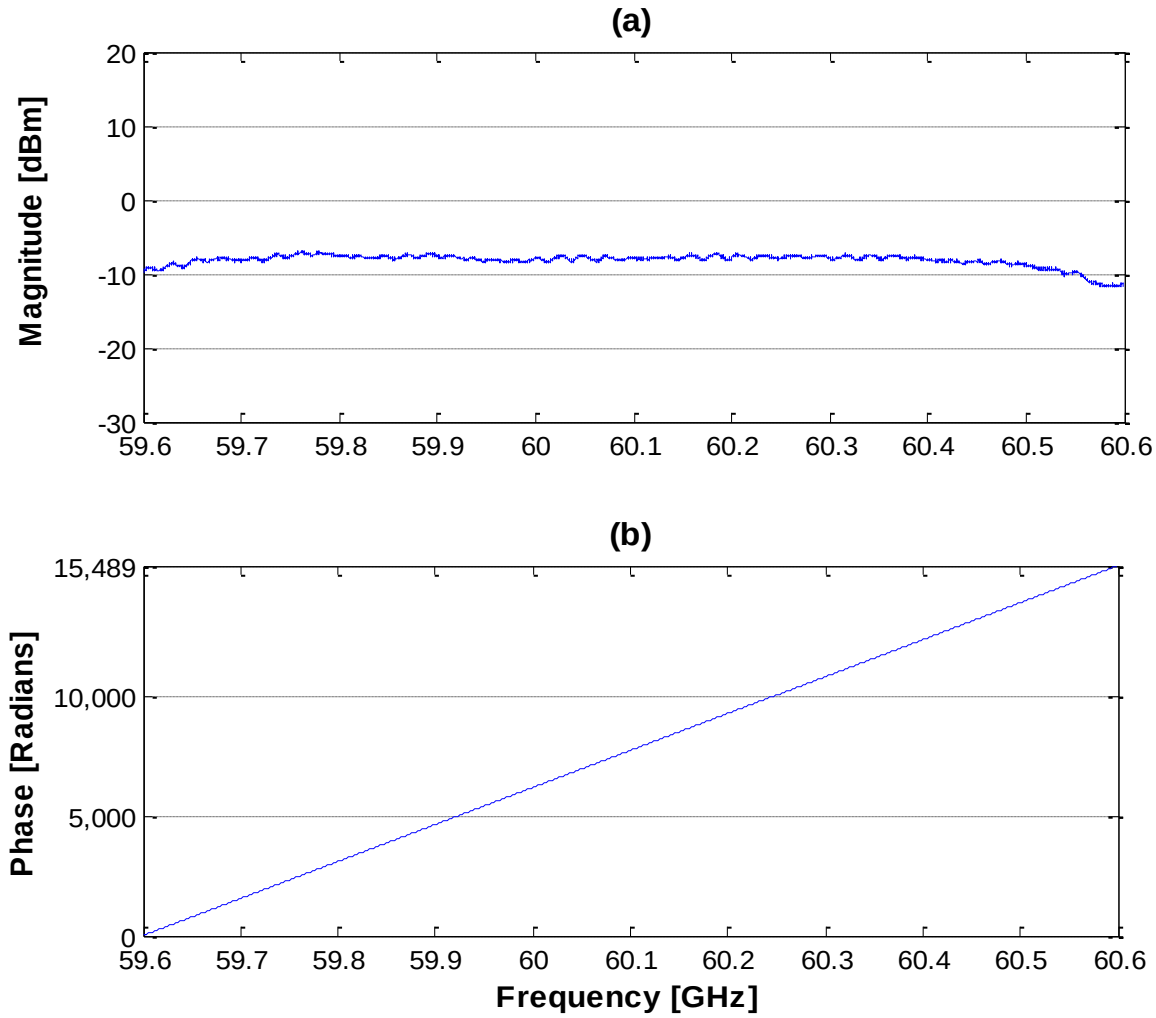

Fig. 3.8 Back-to-back measured frequency response at 60 GHz,

a) Voltage magnitude in dBm,

b) Unwrapped phase in radians.

The calibrated channel transfer function $H(f)_{channel}$ is then obtained from the measured data as follows:

$$H(f)_{channel} = H(f)_{measured} \cdot \frac{H(f)_{corrected}}{H(f)_{calibration}} \tag{3.2}$$

$H(f)_{corrected}$ includes the loss and delay of the cable together with the attenuators used in the calibration measurement and the loss and delay of the antennas with their feed cables, which are removed in the calibration measurement. Also a sample of the calibrated frequency response is shown in Fig. 3.9.

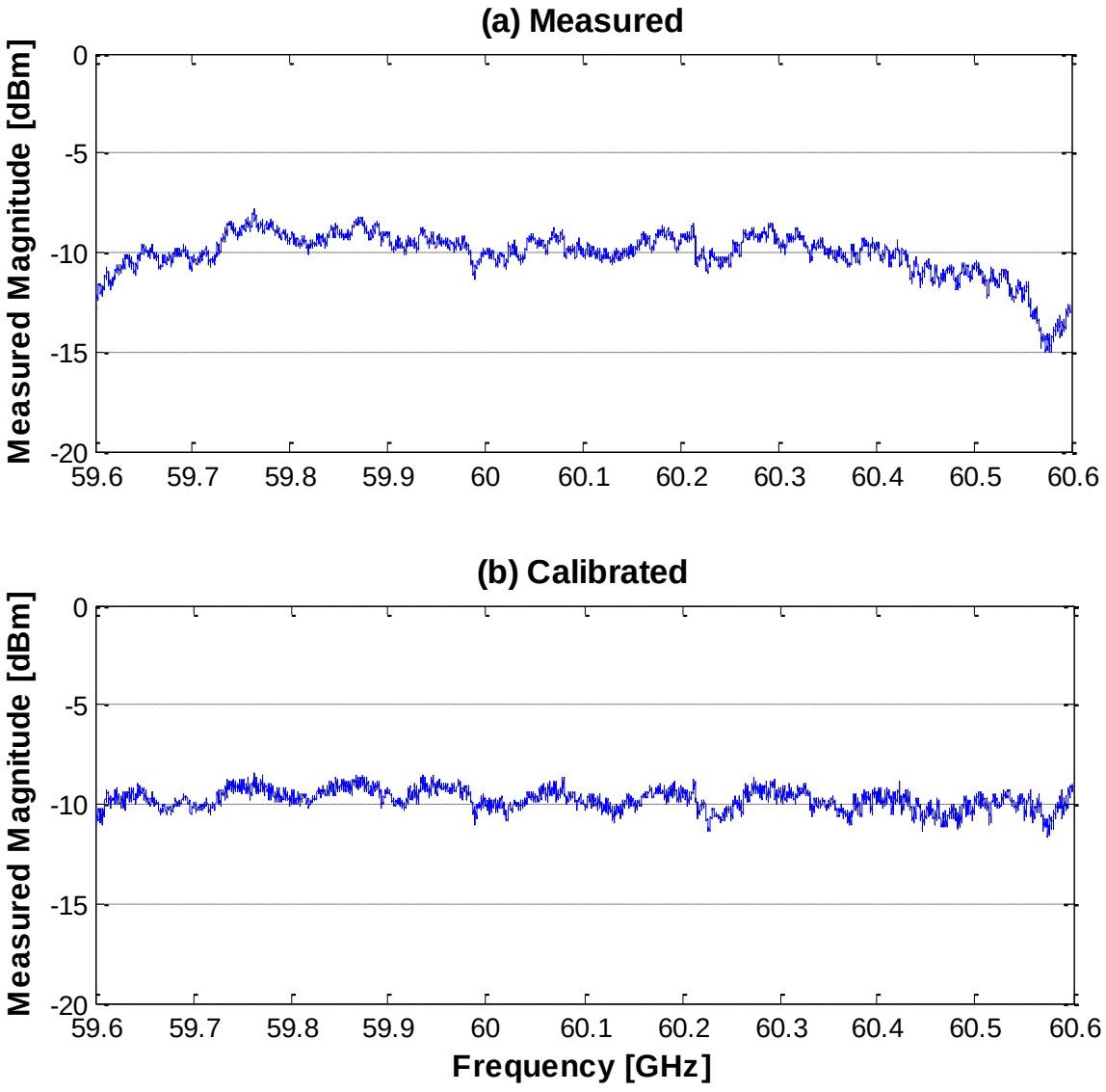

Fig. 3.9 A sample of measured frequency response at 60 GHz,

Chapter 4

Deterministic Modeling of Indoor Channels in the 60 GHz Band

4.1 Introduction

Basically, the channel propagation characteristics can be modeled using two types of models. The empirical models, also called statistical models which are based on statistical methods and their use rely on extensive measurement data; they are characterized by their low computational complexity. Whereas, the deterministic models deal with the fundamental principles of the radio wave propagation phenomena, and they are also called theoretical models. The deterministic propagation models provide a comprehensive understanding of the effects observed on measurement results. Deterministic propagation models are based on electromagnetic wave propagation theory. Their use requires a great knowledge on the propagation environment and allows obtaining precise as well as accurate predictions of signal propagation in the channel corresponding to the considered environment [114].

Nevertheless, most deterministic models consider narrow band measurement and simulation performed in space domain around the central frequency of 60 GHz, in order to approximate the propagation characteristics. Besides, very few ray-based developed models are available in the literature; they consider a very limited number of multipath rays for both LOS and NLOS cases, [115] is among them. Although, at mm-waves, all multipath components are relevant to allow obtaining precise as well as accurate model, excluding one or few rays might change the result significantly. Another deterministic indoor propagation ray-based model is performed in space domain intended to examine the behavior of polarizations at 61.7 GHz [116]. Furthermore, the 60 GHz narrow-band simulation results that are likely obtained in space domain or in time domain do not fit clearly the experimental results.

In a similar way, indoor mm-waves channel modeling has been widely studied in the literature in order to predict propagation characteristics in various locations. Most available research studies suggest that, it is difficult to model mm-waves channel deterministically. They best estimated the propagation characteristics using statistical approaches. Saleh-Valenzuella [117] and its modification (T-SV) models [118] are among the most used models in the literature and standardization area.

However, all of the aforementioned approaches (statistical or deterministic) tend to be inaccurate when it comes to compare them with experimental propagation characteristics. Hence, the main difference between mm-waves and traditional channel-modeling techniques is due to the fact that mm-waves are more susceptible to the propagation environment and hence, frequency-dependent effects cannot be ignored. Parameters related to penetration, reflection, diffraction, and many other propagation effects should be considered frequency-variant and investigated more carefully [119].

Many important aspects of mm-waves-based communication systems have not yet been thoroughly investigated. In particular, modeling the propagation effects of indoor channel requires careful examination before the actual implementation of mm-waves systems. Therefore, a theoretical and/or experimental understanding of the mm-waves channels propagation processes is essential. As a result of the severe propagation characteristics to which they are subject, mm-waves channels pose additional challenges, especially for deterministic modeling.

When studying classic narrowband transmission techniques using deterministic model, the transmitted signal bandwidth is narrow enough to only focus the propagation analysis on the central frequency (or one specific frequency). However this is not the case when dealing with large bandwidth propagation channel. In 60 GHz communications, the frequency components of the transmitted signal cover a vast bandwidth which can reach 7 GHz. Therefore, the performed simulation will necessarily address all the phenomena appearing on the entire bandwidth. Thus, we cannot simply focus on the propagation around the central frequency. This implies that we have to consider in the synthesized link both antennas and material properties of the considered environment on the whole covered frequency band. To the best of our knowledge, in the 60 GHz free licence band, there have not been models dedicated to predict deterministically the

propagation characteristics of the channel across a whole frequency bandwidth that exceeds 500 MHz. In other words, there was no attempt to examine the whole channel transfer function in a deterministic approach, although 60 GHz communications are likely to be operated over an extremely large bandwidth. Hence, it is more convenient and more accurate to fit the frequency response of the channel and then compare their IFFT time domain power delay profile in time domain.

In this chapter, two realistic ray-based channel models for typical indoor environments are considered:

a) Model for NLOS corridors: this model is further analyzed deterministically in the presence of cylindrical and flat surfaced DOs.

b) Model for conference room.

As a result, the presented deterministic ray-based models are intended to be more realistic and accurate where a high level of certainty is achieved. The experimental validations have been performed in frequency domain and their IFFTs in the time domain.

4.2 Model Considerations

This section describes the building database, the antenna model, and the ray tracer.

4.2.1 Building Database

The presented model requires an accurate 3-D indoor database with detailed information describing the scattering objects (walls, doors, windows, corners, etc, …), their dimensions and their dielectric properties including the relative dielectric constant (ε_r) and the conductivity (σ) across the whole frequency band of interest.

4.2.2 The Ray Tracer

The ray tracer performs a geometric and an electromagnetic computation to derive the geometrical paths, the corresponding transfer functions and its IFFT which yield the power delay profiles (PDPs) for predetermined transmitter and receiver positions.

- NLOS corridors channel model: In the NLOS corridors environment, the model counts for multiple reflections of up to 4th order due to the fact that under NLOS all possible contributions are important in the absence of a dominant LOS contributor to the signal. Moreover, the model accounts for the single diffraction using the uniform theory of diffraction (UTD) [92]. After testing the double diffraction interactions in the model, they are found to be unimportant, they might provide an insignificant amount of accuracy to the tracer, however, they decrease the computation time and efficiency, hence, they were not considered.

- LOS conference room channel model: In the conference room, besides free space propagation (LOS), the modeling tool computes the Fresnel equations, considering 3-D multiple reflections from walls, ceiling and floor. Interactions up to the 2nd order reflection have been considered, since at 60 GHz band a great amount of signal absorption is experienced. Many simulations have confirmed that this order provides a compromise between the accuracy of channel parameter and the reasonable computation time required for each additional contribution.

Finally, at 60 GHz, objects which have dimensions compared to 5 mm might influence the signal, taking these objects into account renders the computation process to be complex, time consuming and sometimes impractical. Hence, the presented sophisticated model counts for all possible important scattering objects in the channel.

4.2.3 Antenna Modeling

For vertical antenna polarization, the system considers the angle of departure (AoD) and angle of arrival (AoA) corresponding to each path, when computing the power of multipath components (MPCs). Since typically only 2-D radiation patterns (vertical and horizontal) are available, the developed model is capable to derive the radiation pattern given the measured 2-D patterns in both E and H planes. Varying the simulated radiation patterns in accordance with the measured ones provides better accuracy to the predicted results.

4.3 NLOS Corridors Channel Model

The measurements were carried out within the 2nd floor of the telecommunication laboratory building of the CRC. The first part of the measurement campaign was performed under the NLOS propagation scenarios at the intersection of two corridors. In this environment, the corridors walls are made of plasterboard, the floor is covered with tiles and the ceiling is covered with polystyrene tiles and neon lamps positioned across the corridors. The corridors have metallic elevator door about a meter away from the intersection, a metallic electrical fixture, and a number of wooden office doors with metallic frames. The receiver and transmitter antennas were placed at a height of 1.7 m above the floor level. Both located at 10 m away from the intersection to yield a path length of 20 m as illustrated in Fig. 4.1. Three scenarios are investigated:

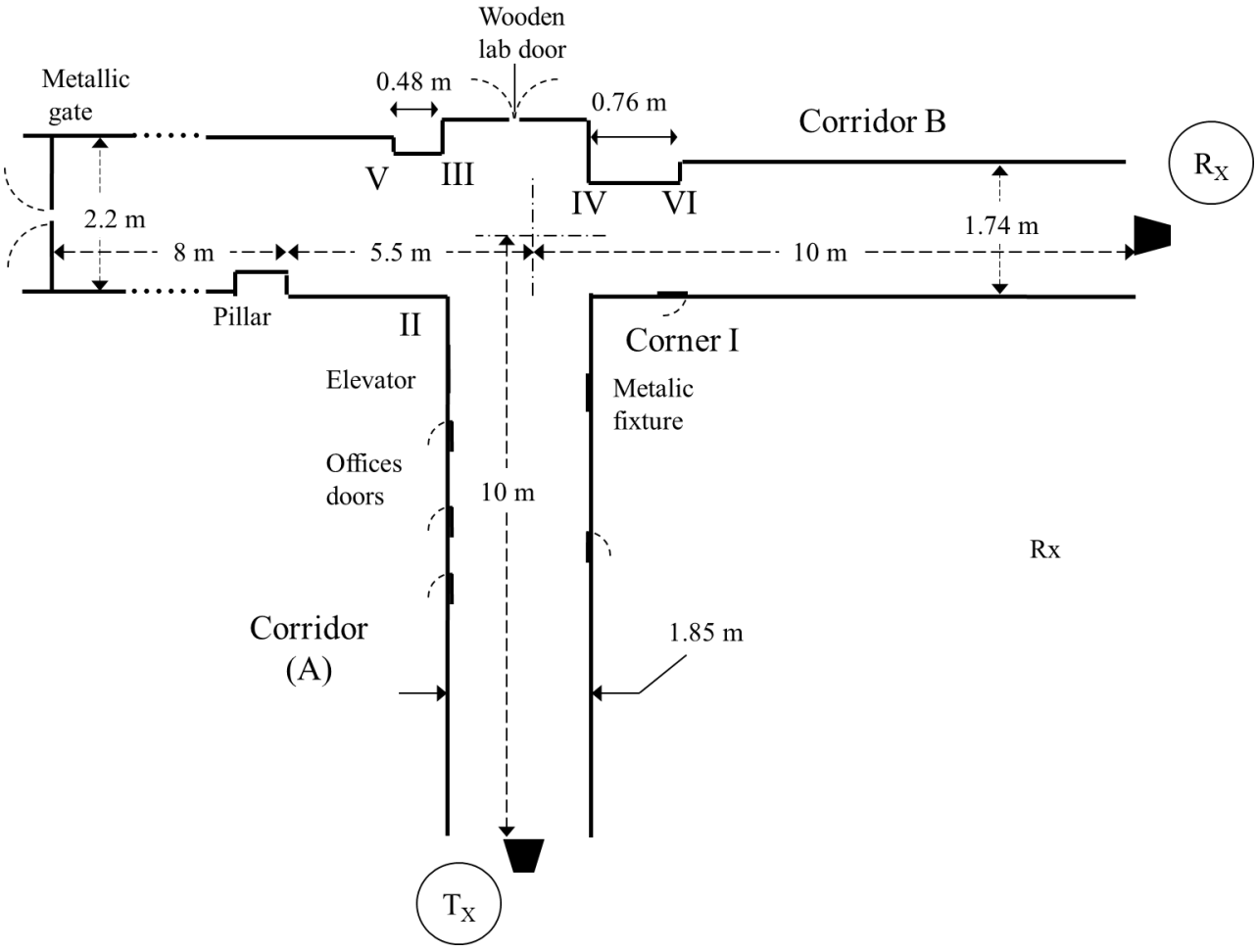

Fig. 4.1 Schematic view of the measurement site for NLOS corridors.

I) No DO is present at the corridors intersection,

II) a metallic standing circular cylinder is positioned at the intersection,

III) a flat metal reflective surface is then positioned at the intersection.

4.3.1 No DO in the Corridors Intersection (Empty corridors).

When the receiver is positioned in a NLOS shadowed corridor, the main propagation mechanisms including reflections, diffractions and their combinations result in quite complicated multipath propagation worthy studying. As shown in Fig 4.2, the multipath propagation is the result of single, double and up to the 4th order of multiple reflections from the floor, ceiling and walls, superimposed by single diffractions from corners, these corners are frequently encountered inside buildings and indoor environments. In Fig 4.2, note that "*h*" and "*w*" are the widths of the corridors *A* and *B*, respectively. Based on the image source method, the 3-D ray-tracing is applied to estimate the received multipath signal strength. The receiving antenna is not far away from the transmitting antenna, thus it is assumed that the received waves are spherical, in which the wave-fronts are spheres centred on the source point and radiating outwards in all directions. The field relative to free space at the receiving terminal is expressed by the following algorithm:

$$E(R) = \sum_{k=1}^{L} \sum_{i=0}^{n} \sum_{j=0}^{n} \left\{ E_o . D_{k,ij} . \frac{\sqrt{\left(s'_{k,i} + s_{k,j}\right)}}{\left(s'_{k,i} + s_{k,j}\right)\sqrt{s'_{k,i} s_{k,j}}} . R_{A,K}^{i} . R_{B,K}^{j} . \left(1 + R_{f,k}^{i}\right) \right\}$$

$$. exp\left[-jk\left(s'_{k,i} + s_{k,j}\right)\right] \qquad (4.1)$$

i =0, 1, 2,… n, and j= 0, 1, 2,… n,

where the subscripts i and j denote the order of i^{th} and j^{th} reflections from corridors A and B, respectively. In (4.1), $i = j = 0$ means that, there are no reflections from the corridors walls (only diffractions from corners present). Hence, the total number of reflected rays reaching the receiver along the corridors is $(i + 1) * (j + 1) - 1$. The subscripts k = 1, 2, 3, …L are for the first, second, third and up to L^{th} wedges, $R_{A,k}^{\ i}$, $R_{B,k}^{\ j}$ and $R_{f,k}^{\ i}$ are the i^{th} and j^{th} Fresnel reflection coefficients (associated with k^{th} corner) from walls and floor in corridors A and B, respectively. $D_{k,ij}$ is the k^{th} corner's diffraction coefficient caused by the i^{th} and j^{th} incident and diffraction angles, respectively.

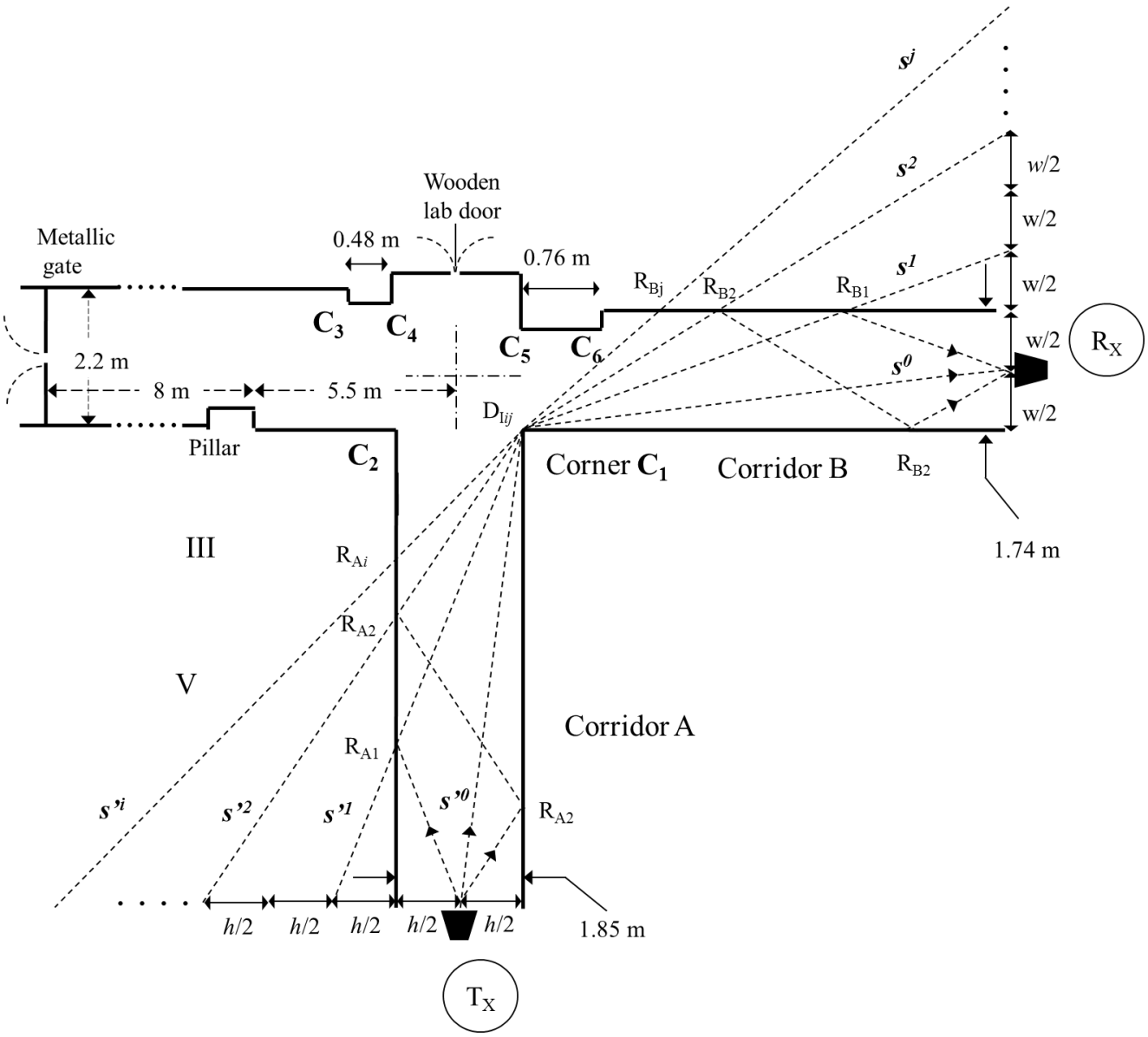

Fig. 4.2 Propagation mechanisms associated with corner C_1 of the NLOS corridor environment.

Due to the nature of NLOS corridor communications, along with the absence of active repeaters (antennas), the signal transmission will be relied on diffractions from corner edges. Of course, there might be signal contributions resulted from double propagation interactions such as n^{th} order reflections from walls and diffraction from corner at the same time. Also, it is noticeable to mention that, when the corridors are narrow and very long, there will be no rays resulting from low order reflections-only (no diffraction from corners) propagation mechanism. If reflections-

only presents, it is the result of high order-reflections from walls, hence, the signal tends to be absorbed by the walls and has no effects on the received signal. Furthermore, the considered corridors have different widths therefore; reflection-only mechanism is not present in the channel.

Much more computational complexity is experienced during the propagation modeling of the NLOS channel. In the ray-tracing algorithms, especially in the No-DO modeling scenario, the choice of the diffraction coefficients is essential in order to achieve the desirable accuracy of the simulated results. In this simulation field, Koujoumjian [85] and Kellers [89, 120] heuristic diffraction coefficients are quite simple to be applied when perfect conducting (PEC) wedges are examined. Based on the modifications of UTD diffraction coefficient for PEC, Lubbers [90] and Remely [91] heuristic diffraction coefficients are available. However, the latter UTD coefficients are convenient in field simulations as they take into account the dielectric properties of the lossy wedges. The Lubbers diffraction coefficient provides quite poor results in the shadow region compared with the results derived by Remely. The conclusion is that, Remely's heuristic diffraction coefficient provides a good approximation when the receiver is in the deep shadow region, and yields the best results in order to fit the experimental data. Note that at the corridors intersections illustrated in the schematic view of Fig. 4.1, at least 6 wedges (corner C_1, C_2, C_3, C_4, C_5, and C_6) were taken into account in the computation algorithm.

For plaster board walls, the relative dielectric constant (ε_r) and the conductivity (σ) are measured in the 60 GHz band [82, 37] as displayed in Table 4.1.

Table 4.1 Materials electrical characteristic in the 60 GHz Band

Material	Relative dielectric (ε_r)	Conductivity (σ) [S/m]
Plasterboard	2.81	0.1536
Concrete	6.14	1.005
Glass	5.29	0.8464

For lossy materials, ε_r is sensitive to the operating frequency [79], however, it might not vary significantly across the bandwidth of interest. The frequency-dependent complex dielectric is then given as:

$$\varepsilon_r^*(f) = \varepsilon_r - j\left(\frac{18\sigma}{f}\right) \tag{4.2}$$

where *f* is the operating frequency in GHz.

Due to the absence of a strong dominant path, it is essential to consider the largest possible number of contributions. Despite the great absorption experienced by the corridors plasterboard walls at 60 GHz, contributions resulted from up to 4th reflection-orders are considered. This is because the diffraction from corner depends strongly on the incidence and diffraction angle and how far from ISB and RSB angles (see Fig. 2.5 and Fig. 2.6). In other words, increasing the order of reflection will increase the incident and diffraction angles which in turn cause the diffracted signal to increase to more than 60 dB as previously shown in Fig. 2.6.

4.3.1.1 Experimental Validation

4.3.1.1.1 Frequency Domain Analysis

At this stage, the experimental frequency response is compared with the result obtained by the deterministic ray-tracing model. Hence, the typical normalized plots of both measured and predicted channel frequency responses are shown in Fig. 4.3. It can be observed that, both results show periodic large and small-scale (fast) frequency selectivity, the fast fades occur at a frequency scale close to 11.3 MHz, also a relative power amplitude variation between 0 dB and -40 dB is observed in both computed and measured frequency responses. To yield a fair comparison between both the measured and simulated results, their cumulative distribution functions are computed and shown in Fig. 4.4.

As a result, it is clearly shown that a good agreement is achieved between both results and hence, the ray-tracing model is validated successfully. Further analysis and discussion of the achieved results is carried out.

.

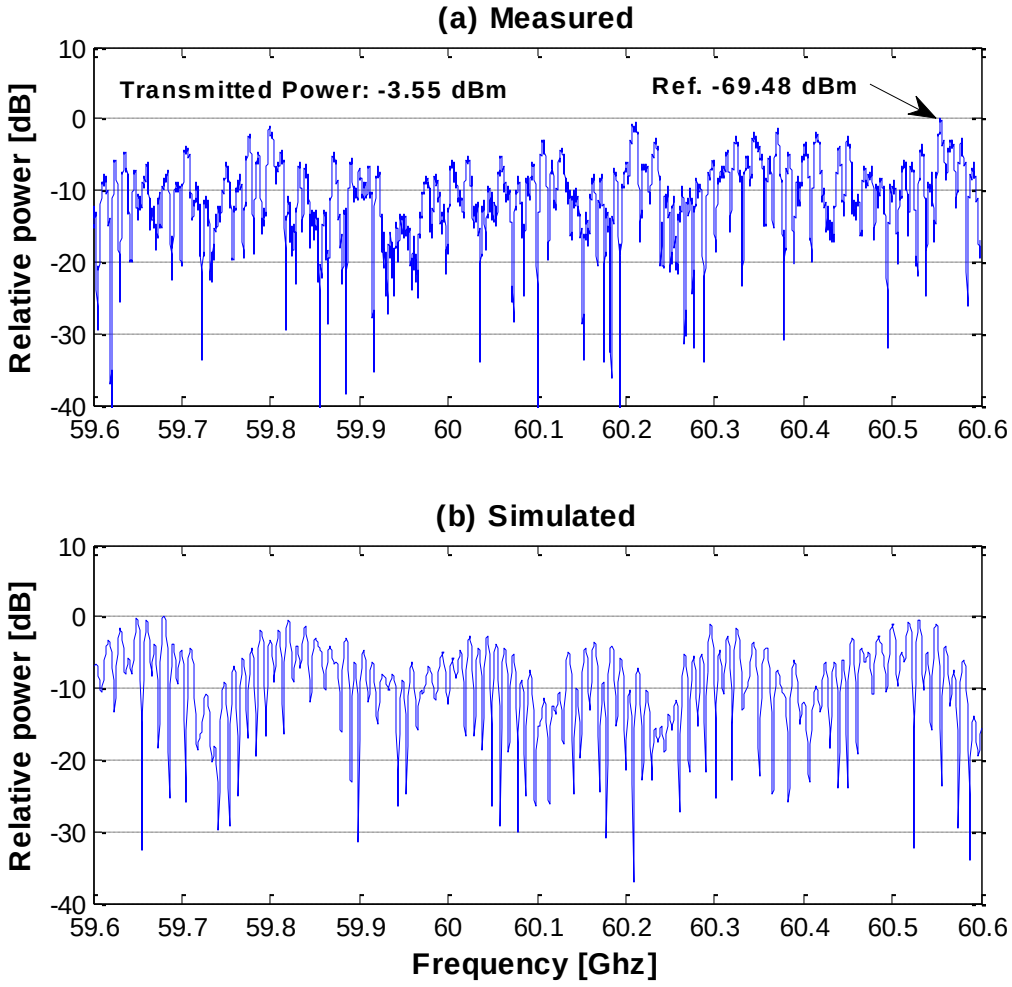

Fig. 4.3 CTF of NLOS corridor environment.

During the results investigations, it is found that the large-scale amplitude variation is caused by the direct rays that reach the receiver after diffracting from corners C_1 to C_6. The interaction of MPCs falling into the same frequency bin gives rise to fading selectivity. In other words, the MPCs sometimes add up in a constructive way, and sometimes in a destructive way, depending on the relative phases of the MPCs [121]. Hence, the only-diffracted MPCs add destructively at a periodic scale of 120 MHz, this is mainly due to the large phase difference they exhibits every 120 MHz as shown in Fig. 4.5-a.

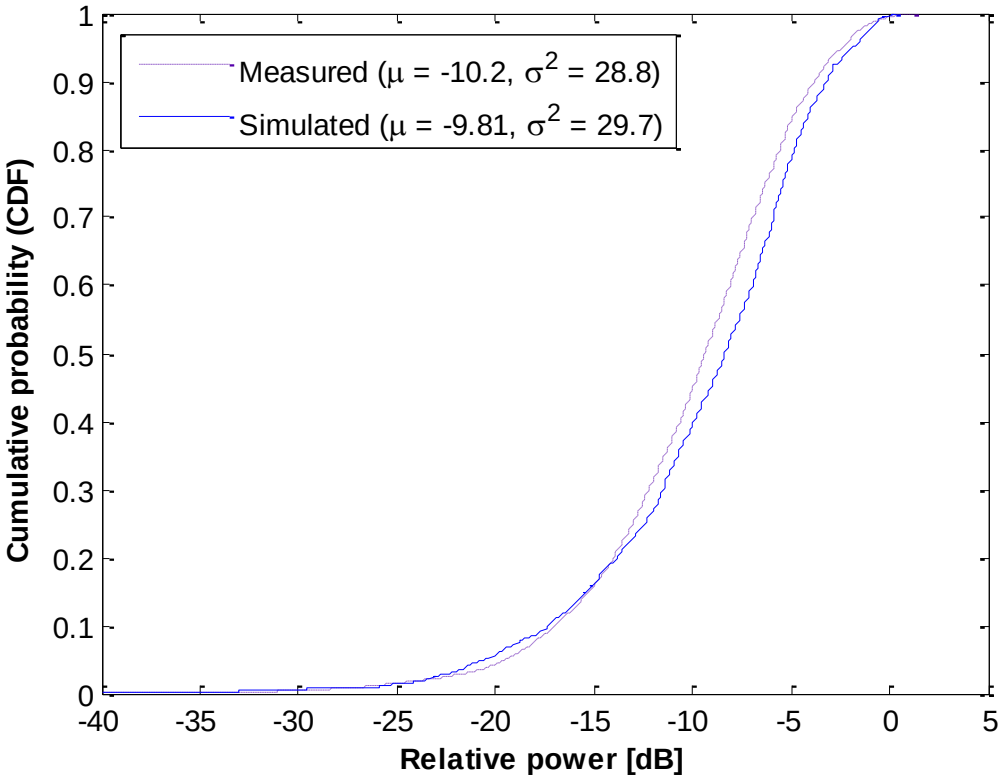

Fig. 4.4 Cumulative probability (CDF) of the experimental and simulated data

However, the small-scale power amplitude variations are mainly induced by the summation of contributions that resulted from diffraction-reflection propagation mechanism. This double interaction mechanism is described as follows; each corner (C_1 to C_6) diffracted ray splits into two components, the first one continues its way to hit and reflect from a pillar surface located at 5.5 m away from the corridor intersection, while the second component reflects from a farther metallic gate located at 13.5 m (reflection) from the intersection. Hence, the fast amplitude variations occur as a result of the paths length differences leading to large phase differences between the reflected-diffracted contributions and the only-diffracted rays from corners. Adding reflected rays from the pillar surface causes a variation that repeats every 27.5 MHz as shown in Fig. 4.5(b), in the case of metallic gate a periodic amplitude variation of 11.3 MHz is observed (Fig. 4.5(c)).

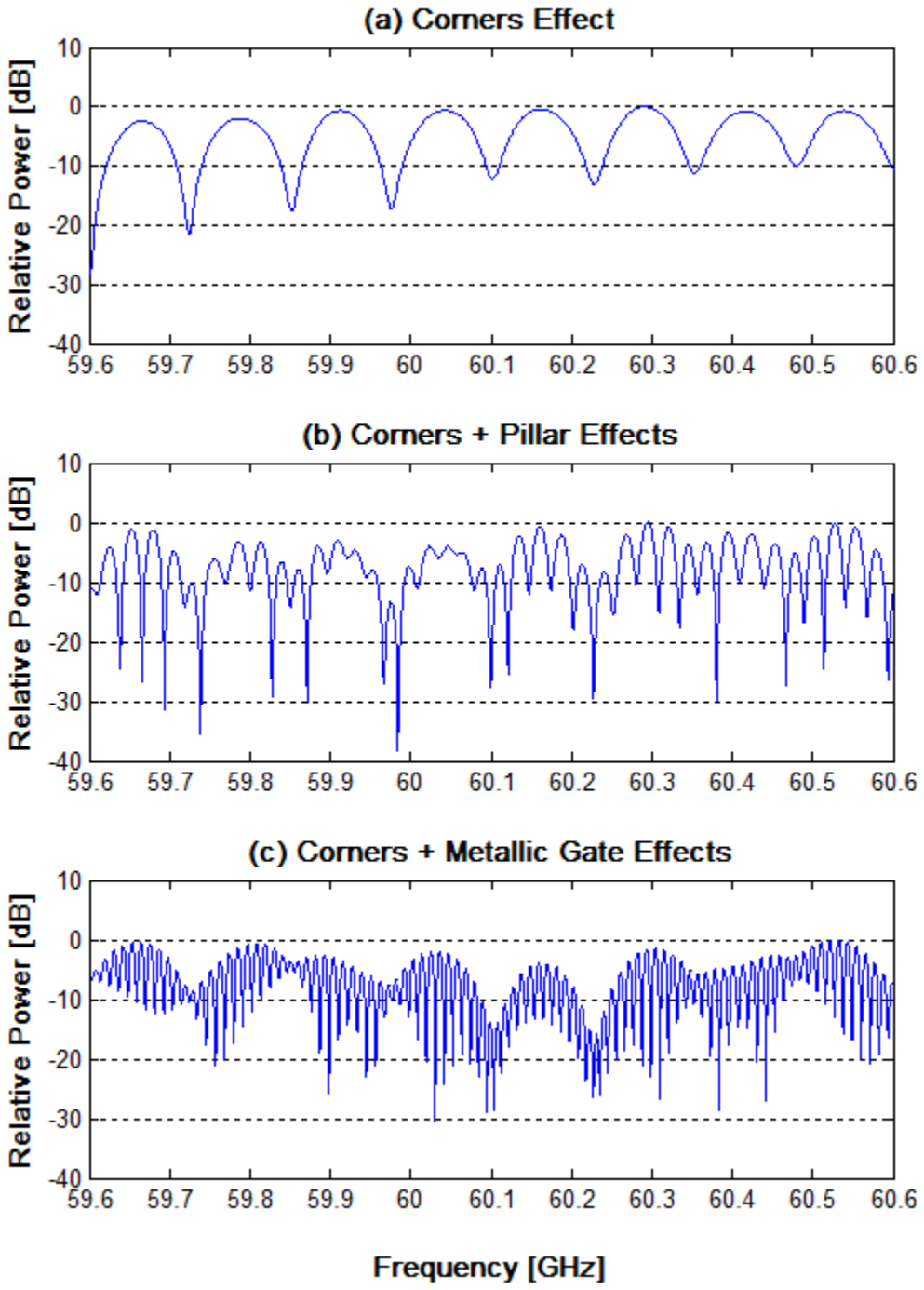

Fig. 4.5 CTF of the NLOS corridors environment.

4.3.1.1.2 Time Domain Analysis

To provide a more accurate channel modeling and to achieve a high level of certainty, the channel PDPs of both measured and predicted results are derived and then compared. The channel PDPs are computed by performing the IDFT (Inverse Discrete Fourier Transform) of the channel transfer function. The time resolution ($T_{resolution}$) is inversely proportional to the sweep bandwidth (BW_{sweep}), namely,

$$T_{resolution} \approx \frac{1}{BW_{sweep}} \tag{4.3}$$

For a sweep of 1 GHz, the introduced measurement system offers a time resolution of 1 ns that corresponds to a spatial resolution of 0.3 m. 1 ns is reasonable to resolve and recombine as much of the energy of several multipath components as possible. At the 20 m of spacing distance separating the transmitting and receiving antennas, the experimental PDP of the No-DO scenario is derived in Fig. 4.6. The strongest power peak of the experimentally measured PDP is recorded at -87.2 dBm but it does not dominate effectively the multipath profile. Then it is followed by gradual smearing and exponential decrease in the power of MPCs with various propagation delays. One can observe six sharp peaks each followed by a MPCs cluster, the power decays exponentially with cluster decay as well as excess delay within a cluster. Clusters 1 to 3 are the most important; they are within 30 dB and their interpretation provides full details about the propagation characteristics of NLOS corridors environment. These clusters are resulted from multiple propagation mechanisms such as combinations of reflection, diffraction and scattering from walls, corners, door frames, and other objects nearby the transmitter and the receiver. Although at 60 GHz, small objects that have dimensions in the size of few millimeters might have strong impact on the received signal.

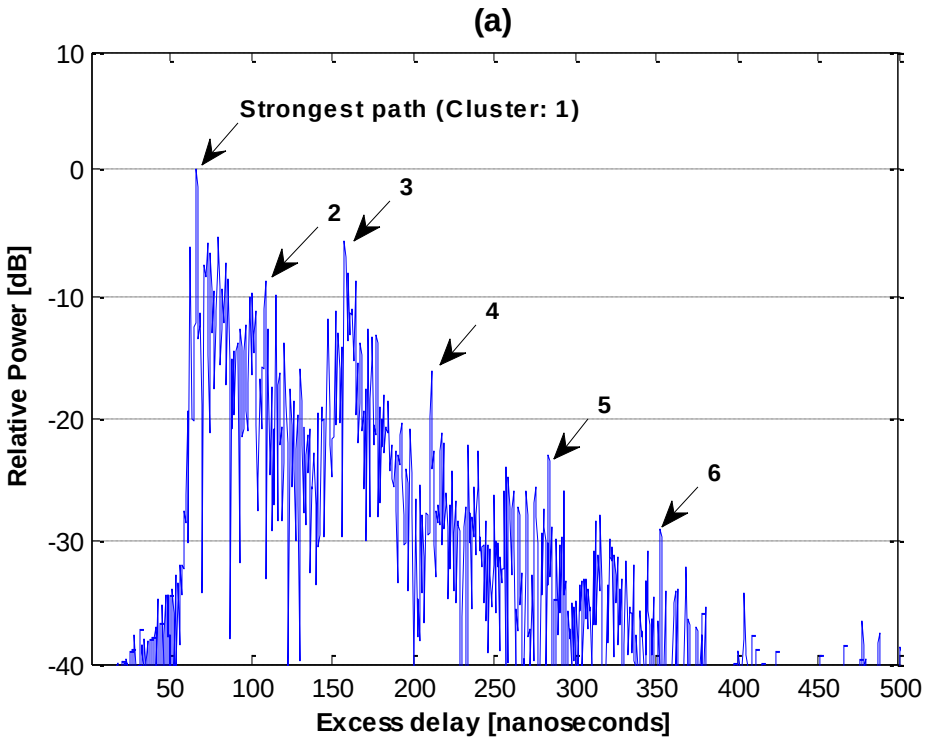

Fig. 4.6 Measured power delay profile for No-DO scenario.

At first glance, it can be concluded from Fig. 4.6 that, the first observable path of the PDP corresponds to the shortest path distance between the receiver and the transmitter. This path that arrives at 62 nanoseconds is the result of the ray that joins both antennas and the corner I, illustrated previously in Fig. 4.1. Simply, it can be concluded that, the main propagation mechanism of this ray is the diffraction. However, the challenging task in the 60 GHz band is to obtain a detailed knowledge about other multipath rays, thus, a deeper time analysis using our model must take place. Using the presented ray-tracer, adequate and precise information about the temporal characteristics of the channel are provided. Hence, the experimental and theoretical normalized PDPs are derived in Fig. 4.7.

A good agreement is achieved between the experimental and simulated data in terms of rays magnitudes and delays. Of course, there are some components that do not appear in the simulated PDP, they might be caused by interaction with other objects such as the doors frames, elevator door frame, cooler, printer, metallic fixture, and metallic hand holder. Furthermore, unlike lower frequency bands, at 60 GHz, the mm-sized objects presented in the channel might have

significant impacts on the received signal, modeling mm-waves objects tends to be very tedious and unrealistic.

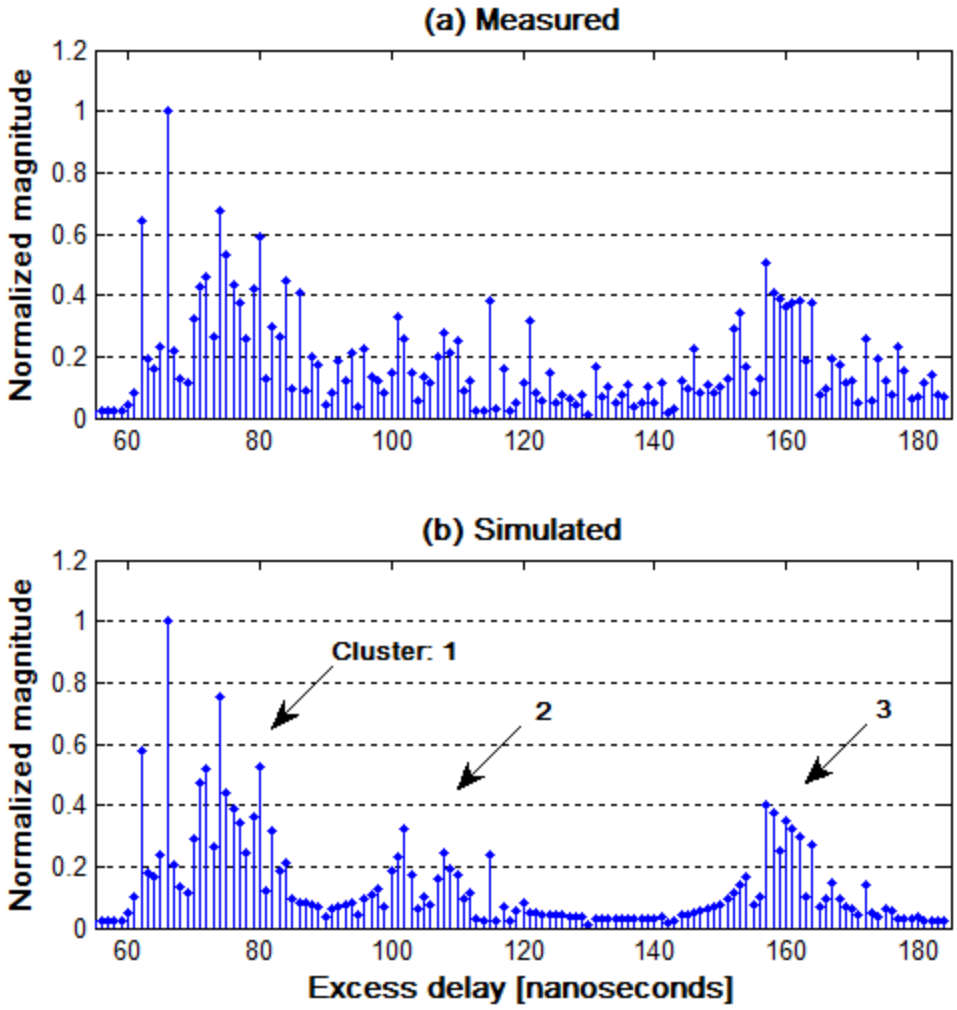

Fig. 4.7 Normalized PDPs of NLOS corridors environment.

Due to their importance, the first three MPCs clusters are considered, since their interpretation provides full details about the propagation characteristics of NLOS corridors environment. In other words, the first, second and third MPCs clusters are caused by the propagation and interaction within the 20 m of antenna separation distance, specifically, in the vicinity of the corridors intersection. The first cluster is within time range of 60 – 85 ns, it is caused by the travelling rays that reach the receiver after corners (1 to 6) single-diffraction, a single reflection from the floor, and multi-reflections from adjacent walls.

The second cluster is the result of MPCs that arrive within 100-120 ns, these rays experience single-diffraction from corners (1, 2, 5 and 6), up to 2nd order-reflections from walls and then reflections from the pillar surface located at 5.5 m from the corridors intersection point. Finally, the third is within 150-170 ns, and caused by the single-diffraction from corners (1 to 6), and then reflection from the metallic gate located at 13.5 m away from the intersection. Cluster-3 is more significant than cluster-2 despite the longer ray traveled distance. This is because the gate surface is a perfect conductor, however, the pillar surface is made of lossy plasterboard materials, (ε_r = 2.81, σ= 0.536 s/m).

Cluster-1 has a specific importance, since it exhibits delay spreads of between 60 and 100 ns which is typical for indoor environments. As mentioned in the previous discussion, cluster-1 is the direct result of only-diffraction (strongest rays), this type of propagation mechanism can be met in most of NLOS corridors which have right corners at their intersections. It is clearly seen that cluster-1 does not decay exponentially from the first detected multipath component as experienced in most multipath clusters. To yield a clear observation and analysis, a zoom-out of the of cluster-1 normalized PDP is shown in Fig. 4.8. The most important MPCs caused by diffraction from corners 1 to 6 are identified. The first perceptible ray is caused by the direct interaction with corner 1. This contribution is not dominant, although its travelled path to the receiver is the shortest compared with other corners. This is mainly attributed to the incidence and diffraction angles properties. In other words, the angles of incidence and diffraction might enhance significantly the diffracted ray as previousely discussed (see Fig. 2.5 and Fig. 2.6). Furthermore, it is noticeable to mention that because of the effect of the incidence and angles, a diffrated ray that undergoes with high order of reflection might be sometimes more important than another ray that subjects to lower order of reflection. For this reason, reflections from walls of up to the fourth order are considered in the channel model despite the high signal absorption. The samples of rays that arrived at 70, 71, 72, 79 and 80 ns are a clear evidence of the importance of incidence and diffraction angles. In most practical cases, the resolution of the receiver is not sufficient to resolve all MPCs. For systems with higher bandwidth, MPCs can be resolved. Despite the high temporal resolution of broadband systems, there is still an appreciable probability that several MPCs fall into one resolvable delay bin, and add up there.

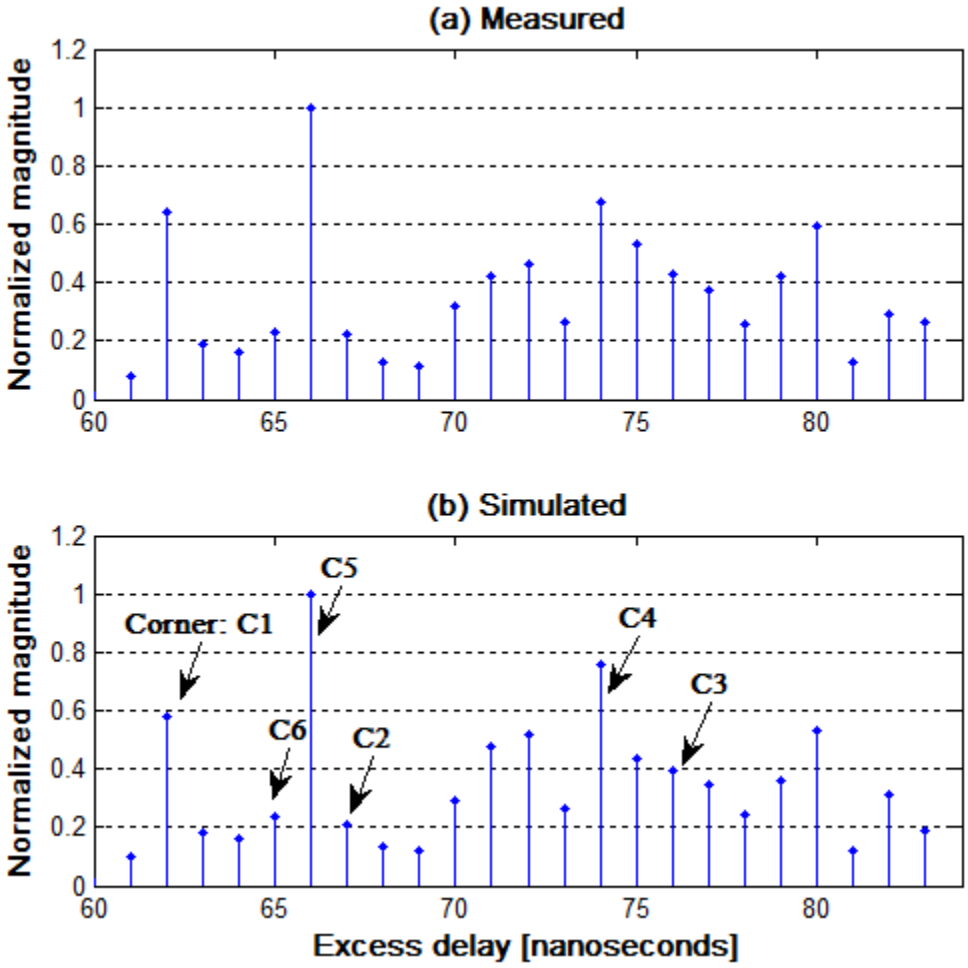

Fig. 4.8 Normalized time impulse response of NLOS corridors (Cluster-1)

In the considered corridors environment, each corner causes a multipath cluster which includes a large number of irresolvable MPCs (about 6 MPCs) that are separated by a fraction of less than one nanosecond. As shown in Fig. 4.9, each multipath cluster spreads over an excess delay of five nanoseconds, these MPCs are caused by diffractions from corners and up to fourth-order reflections from walls and floor. By means of signal processing, rounding to the nearest integer is performed during the IFFT process, this is due to its limited time resolution. As a result, an IFFT time bin is assumed to contain either one or no MPC as previously seen in Fig. 4.8.

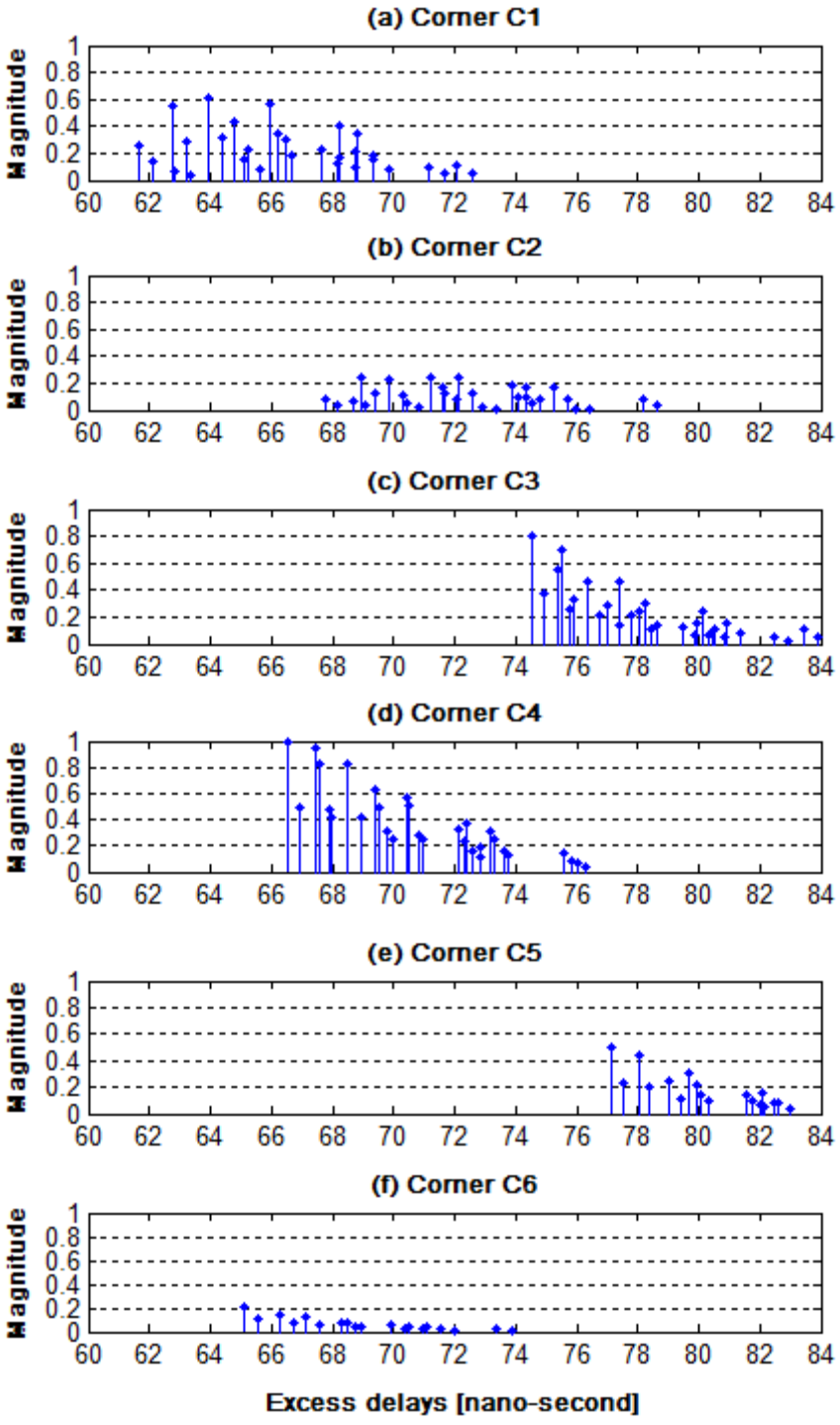

Fig. 4.9 A Theoretical normalized PDPs with respect to the strongest ray of cluster C4.

4.3.2 NLOS Scenario with DO Standing at the Intersection

During the measurements campaign, both antennas were aligned and aimed towards the same point on the DO. The metallic DOs were chosen to relay the maximum possible amount of incident energy. A vertical cylinder of 60 cm of diameter, and a flat surface reflector are used, due to their simple shapes design and their abundance inside buildings such as columns, metallic fixtures and equipment. DOs may be adjusted to smaller sizes; it depends on the antennas radiation patterns and their half-power beamwidth angle. It is possible to reduce the DO size through the use of a narrower radiation beamwidth.

4.3.2.1 A Cylindrical DO

In the case of the presence of a metallic cylinder in the intersection (Fig. 4.10), the diffraction of an arbitrary ray-optical electromagnetic field by a smooth perfectly conducting convex surface is investigated using the uniform theory of diffraction (UTD).

Fig. 4.10 A photograph of the NLOS corridors obtained from the receiver side in the presence of a cylinder.

The geometrical configuration of the diffraction problem being investigated is illustrated in Figure 4.11. Referring to Figure 4.10, it is noticeable to mention that an extension of the incident ray beyond the point of grazing at Q_1 on the convex surface of the cylinder defines the Shadow Boundary (*SB*) which divides the space exterior to the surface into the lit and shadow regions. Region on the either side of the *SB* is the *SB transition region*, in this narrow region, the field descriptions changes rapidly but continuously from the *GO* field to the surface diffracted field.

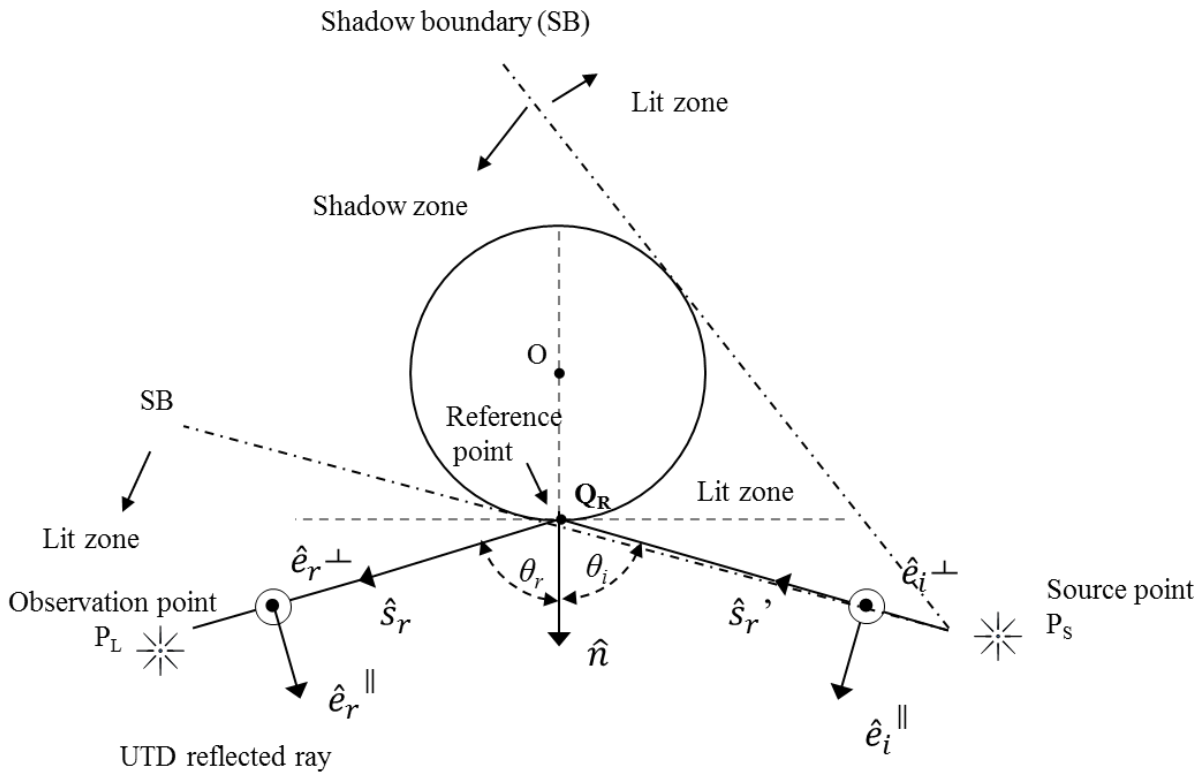

Fig. 4.11 Geometrical configuration of the diffraction over a smooth convex surface.

According to the Geometrical Theory of Diffraction *GTD*, the total exterior field is associated with the usual geometrical optics *GO* incident and reflected rays in the deep lit region, whereas the deep shadow region is associated with the surface diffracted rays. Thus, according to the sketch given in Fig. 4.11, we are able to identify the shadow zone immediately and realize that, in the lit region, there will be both direct and reflected rays in all observation directions. For our

purpose, more attention may be focused on the UTD solution for the electromagnetic field illuminating an infinitely long perfect conducting circular cylinder which is adequately described in [92]. Detailed formulations of the UTD diffraction by a smooth convex surface are provided in [122, 123].

Finally, the UTD solution for the electromagnetic case can be also simply expressed in terms of the corresponding scalar soft and hard cases, respectively. Thus, the form of the UTD solution for the total electric field for P_L in the lit region may be expressed as

$$\overrightarrow{E_{s,h}}(P_L) \approx \vec{E}^i(P_L) + \vec{E}^i(Q_R).\bar{\bar{R}}_{s,h}.A_L(S)e^{-jks^r} \tag{4.4}$$

The notations *s* and *h* stand for "soft" and "hard" cases, respectively; the soft case implies that the electric field is parallel to the plane of incidence, while the hard case means that the electric field is perpendicular to the plane of incidence. The UTD dyadic reflection coefficient $\bar{\bar{R}}$ is described in details in [124]. $A_L(s)$ is the divergence factor (or spreading factor) associated with the reflected field at some distance s^r from the observation reference point Q_r. This governs the amplitude variation of the GO field along the ray path. However, the spreading factor is a function of the principal radii of curvature of the reflected wave front at Q_R and the distance along the reflected ray, this distance is accounted from the point of reflection on the surface of the obstacle to the observation point P_L.

$$A_L(s^r) = \sqrt{\frac{\rho_1^r.\ \rho_2^r}{(\rho_1^r + s^r)(\rho_2^r + s^r)}} \tag{4.5}$$

The UTD reflection coefficients for the lit region are given by [92]

$$\bar{\bar{R}}_{s,h} = -\left\{\sqrt{\frac{-4}{\xi L}}\ e^{-(\xi L)^3/12}\left[\frac{e^{-j(\pi/4)}}{2\xi L\sqrt{\pi}}\ \left(1 - F(X_L)\right) + \hat{P}_{s,h}(\xi L)\right]\right\} \tag{4.6}$$

The term ξ_L is the reflected field Fock parameter, $F(X_L)$ is the Fresnel transition function, and $P_{s,h}(\xi_L)$ are the soft and hard pekeris caret functions, respectively, associated with the reflected field in the lit region.

As shown in the geometrical trace of Fig 4.12, the multipath propagation is the result of single, double and up to the n^{th} order of multiple reflections from floor, ceiling and walls, superimposed by diffractions from the cylinder. Based on the image source method, the 3-D ray-tracing model is applied to estimate the strength of the received multipath signal.

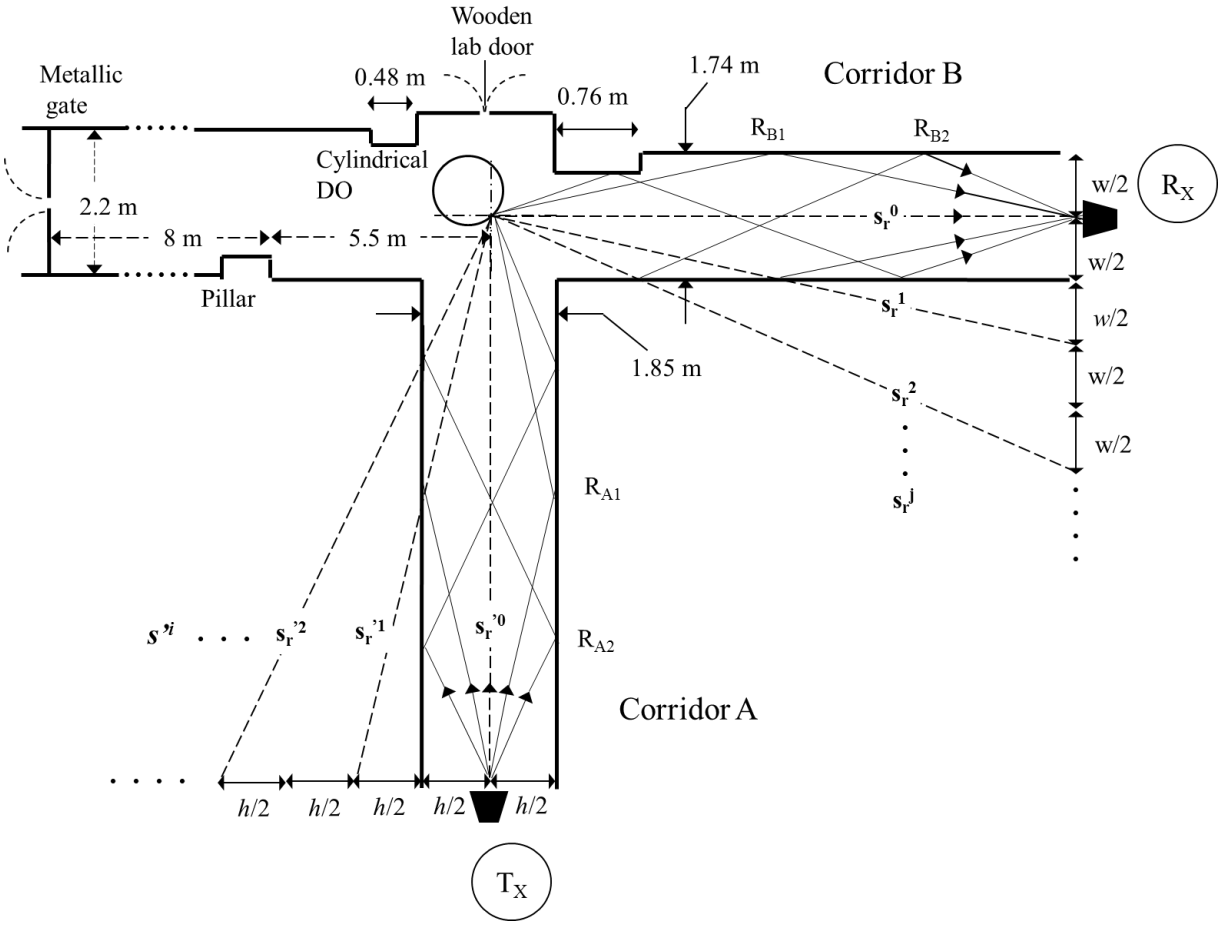

Fig. 4.12 Geometry of multipath propagation mechanisms resulted from the presence of a perfect conducting cylinder in NLOS corridor environment.

The field relative to free space (spherical wave incidence) at the receiving terminal is expressed by the following algorithm

$$E(Q) = \sum_{i=0}^{n}\sum_{j=0}^{n}\left\{\bar{\bar{R}}\left(Q_R,\theta_{ij}\right)_{ij}.\sqrt{\frac{\rho_1^{ij}.\ \rho_2^{ij}}{\left(\rho_1^{ij}+s_r^j\right)\left(\rho_2^{ij}+s_r^j\right)}}\ .R_A^i.R_B^j\left(1+R_f^i\right)\right\}$$

$$.exp\left[-jk\left(s_r'^i+s_r^j\right)\right] \qquad (4.7)$$

Hence the total field can be expressed as the summation of both (4.1) and (4.6) to yield

$$E_{Cyl} = E(R) + E(Q) \tag{4.8}$$

At this stage of the current scenario, the reader might be wondering about the influence of the operating frequency on the received power signal in term of its fading rate and level, or its amplitude, and whether varying the operating frequency could lead to a reduction in the propagation effects induced by the cylinder. Fig. 4.13 provides an image plot of the signal power with respect to the frequency.

Fig. 4.13 reveals an interesting agreement between the experimental measurements and the theoretical results. It is seen clearly that, the theoretical signal variations compare favourably with the measured one, in term of fading, periodicity, and power signal decaying. The only difference might be attributed to the fact that the instrumentation of the sounding system gives rise to a light source of noise and signal instability. The large and small-scale fading of 120 MHz and 27 MHz respectively compare favourably in both results. The amplitude variations are within 30 dB in both frequency responses. Therefore, the proposed modeling is successfully validated by the experimental data.

Observations made from Fig. 4.13 indicate that the installation of a cylindrical DO in the intersection mitigates significantly the level of frequency selectivity. Hence, the deep fades do not exist over the entire 1 GHz bandwidth as experienced in the previous scenario.

A proper understanding of the high rate of signal amplitude variations at frequencies exceeding the 60.37 GHz is greatly attributed to the high rate of change in the differential wave length and hence to the phase differences between the reflected rays. Also, an increase in the operating frequency beyond 60.37 GHz leads to a serious reduction in the received power of about 20 dB. These effects are mainly attributed to the spreading factor which governs the amplitude variation of the GO field along the ray path. In other words, increasing the frequency will increase the electrical size of the cylinder. The cumulative distribution functions of both the measured and simulated results are computed and shown in Fig. 4.14.

The presented model is validated successfully, despite its mathematical and computational complexity due to the presence of the cylindrical DO in the channel.

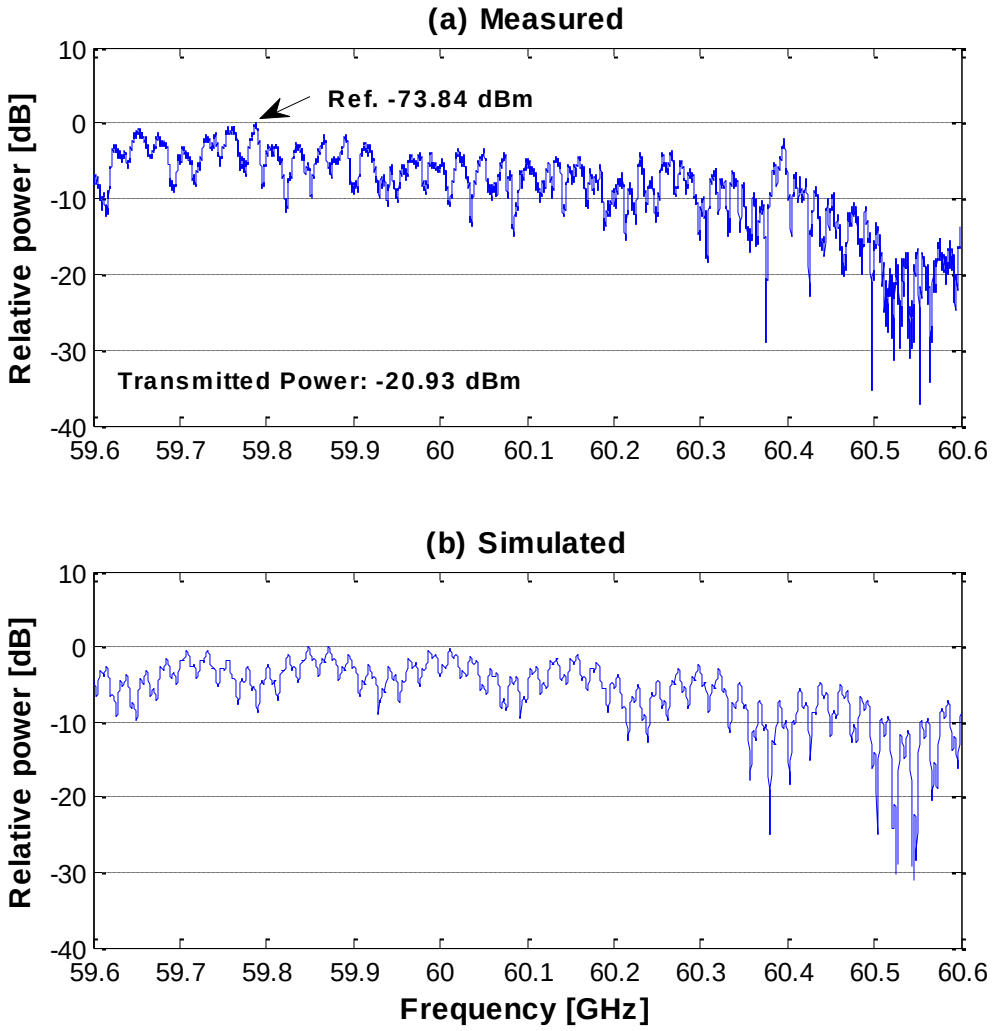

Fig. 4.13 CTF of NLOS corridors in the presence of a perfect conducting cylinder DO.

As part of the carried investigation of the channel propagation in time domain, the normalized PDPs of both measured and predicted data have been derived as shown in Fig. 4.15. A first effect that can be observed is the channel propagation behavior which has been improved remarkably after the deployment of the cylinder. As a result of the specular reflection from the perfect

conducting cylinder, a strong dominating ray has risen up to suppress the other multipath diffracted rays.

As shown in Fig. 4.15 the first perceptible ray of the PDP is detected at 66 ns, the main propagation mechanism that causes this contribution is the diffraction from corner C_5, the travelled distance of this ray is 19.72 m. The cylinder specular ray arrives at 67 ns, and then followed by three contributions detected at 68, 69 and 70 ns. The double interacted ray that is detected at 68 ns is caused by the reflection from the floor and a single-diffraction from the cylinder. The two other rays which arrive at 69 and 70 ns are caused by the first and second order-reflection from the walls respectively, before hitting the cylinder.

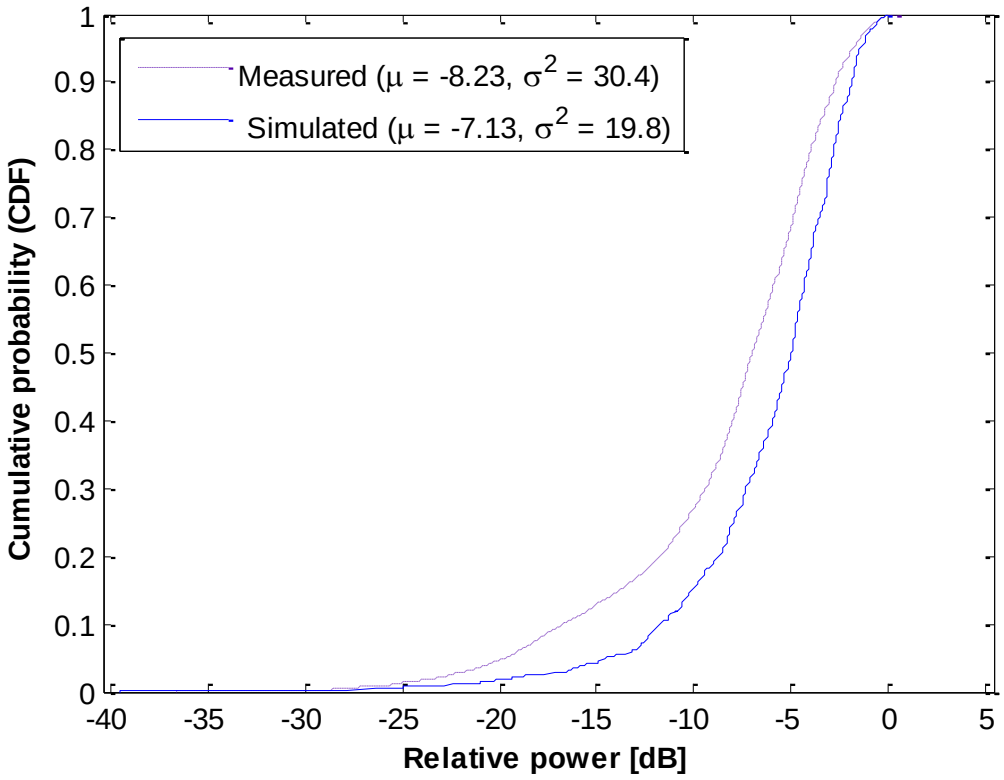

Fig. 4.14 Cumulative probability (CDF) of the experimental and simulated data

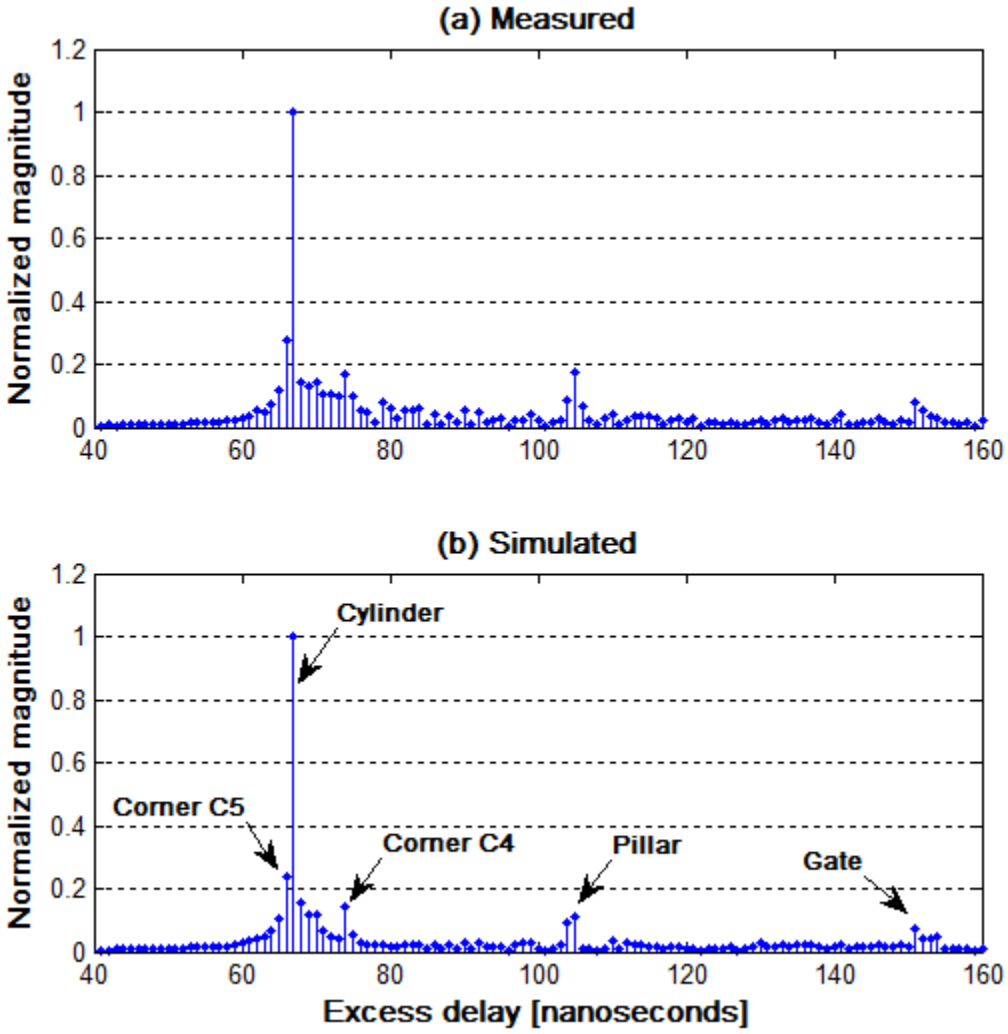

Fig. 4.15 Normalized time impulse response of NLOS corridors environment in the presence of a perfect conducting cylinder.

4.3.2.2 A Flat Reflective DO

The used flat surface DO is shown in Fig. 4.16. It was given the shape of a right corner to help its standing during the measurements. However, from a technical point of view it is considered as flat since measurements were focused on one side of this shape. Hence, during measurements it was oriented 45^{o} from the central line joining both remote terminals. The geometry of the multipath propagation when the DO is a flat surface reflector is shown in Fig.

4.17. Due to the geometry of the measurement site, only one single specular reflection from the flat surface is considered.

Fig. 4.16 A photograph of deflecting objects used in the experiment.

In this scenario, it is important that the strongest reflected ray is achieved when the reflector is oriented 45^{o} from both corridors central lines as depicted in Fig. 4.17. High orders of reflections from walls and the flat surface do not exist since the widths of both corridors A and B are different. Therefore, the received signal is the result of specularly reflected ray from the perfect conducting flat surface reflector, superimposed by a diffracted ray from the right corner of the reflector itself plus other rays caused by the channel (without DO). The diffracted ray from the reflector's corner is modeled using Koujoumjian's heuristic diffraction coefficient for a perfect conducting wedge. The experimental and theoretical channel transfer functions are shown in Fig. 4.18(a) and (b), respectively.

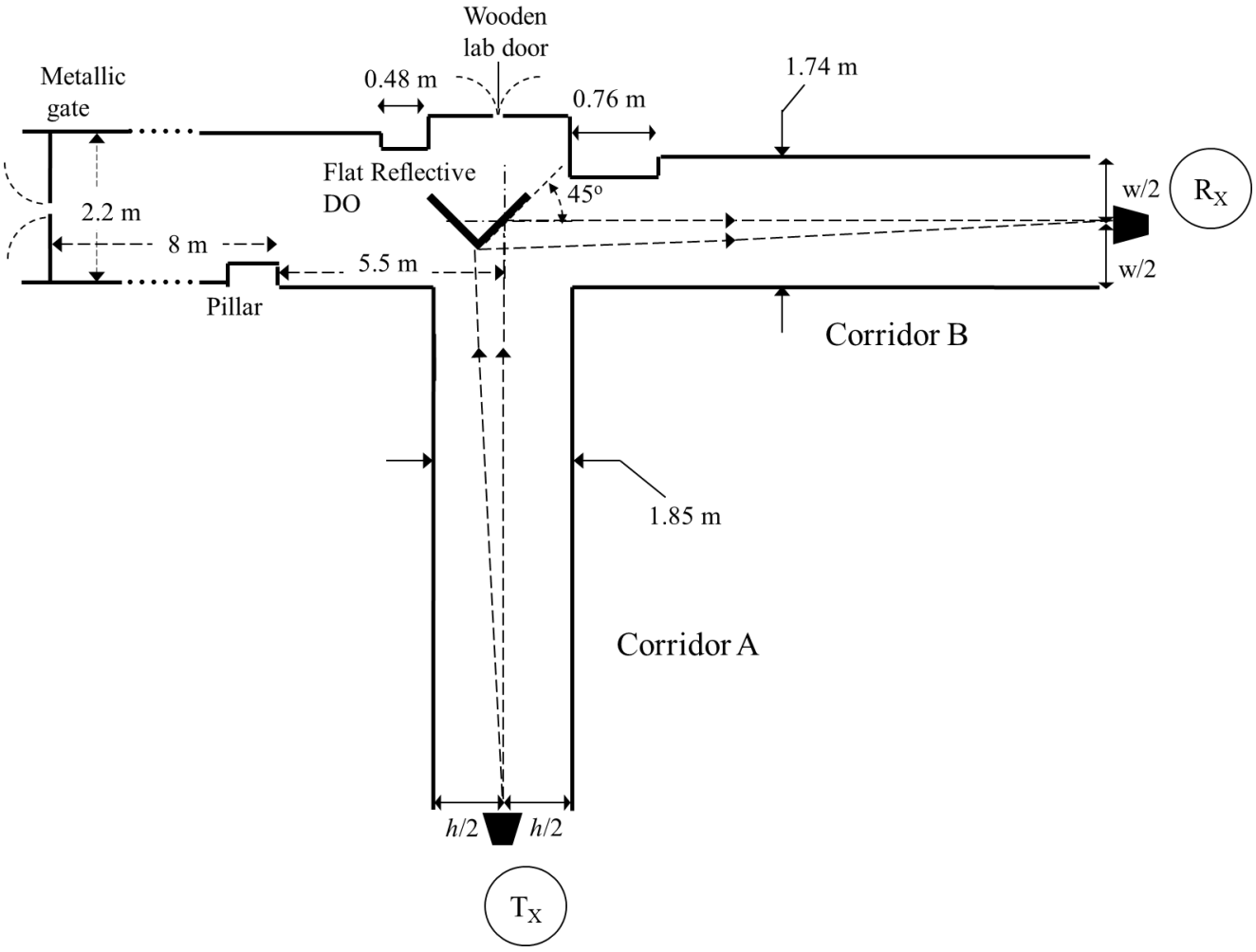

Fig. 4.17 Normalized Geometry of multipath propagation mechanisms resulted from the presence of a perfect conducting cylinder in NLOS corridor environment.

As expected, the flat surface reflector provides a stronger reflection caused by the Fresnel reflection coefficient instead of the UTD diffraction from the convex surface of the cylinder used above. Also, it is interesting to note that the channel is almost flat across the whole bandwidth of interest. Power amplitude variations within 3 to 4 dB are seen in Fig. 4.18, they are caused by the diffracted ray from the right angle of the reflector. The experimental as well as the theoretical results are in a good agreement, the only differences might be attributed to the same reasons

indicated in the previous scenario (cylinder). The cumulative distribution functions of both the measured and simulated results are computed and shown in Fig. 4.19.

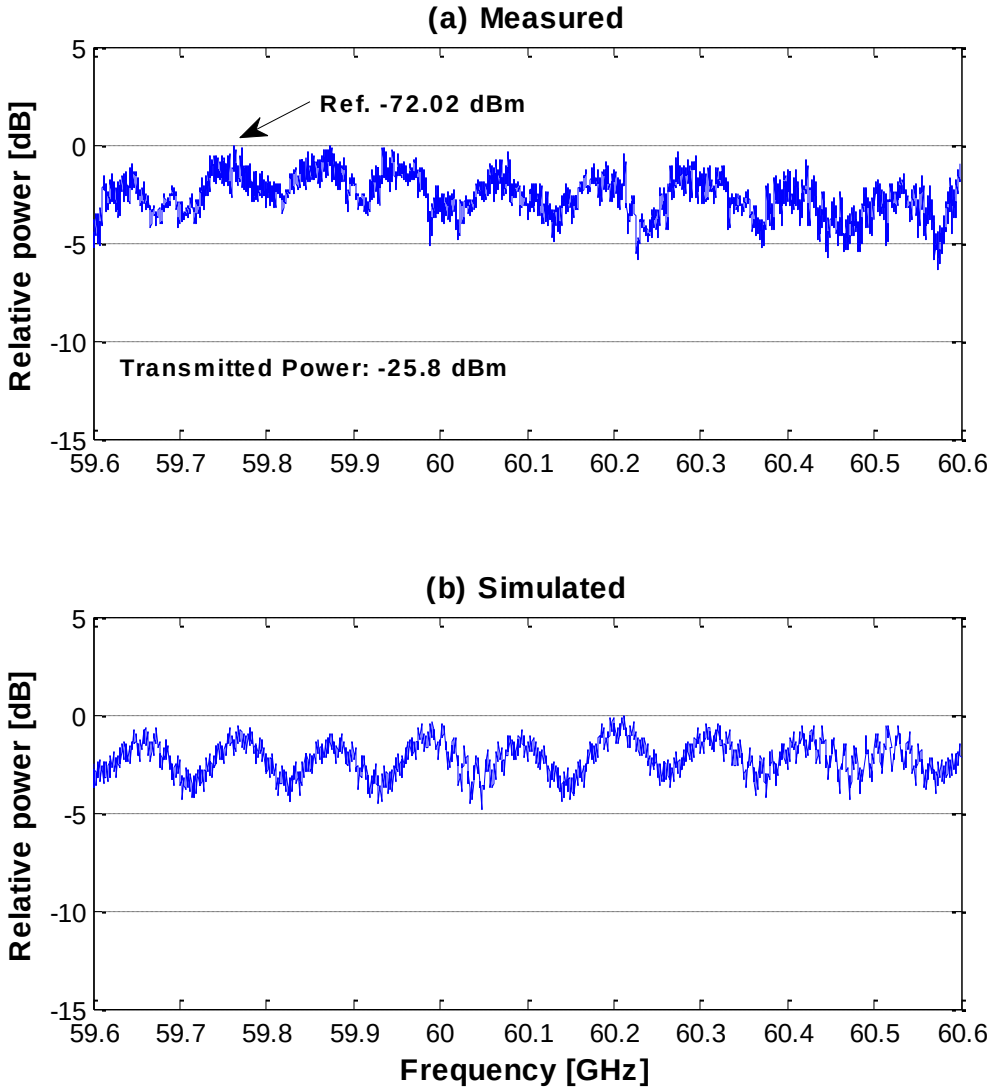

Fig. 4.18 CTF of NLOS corridors in the presence of a flat surface DO.

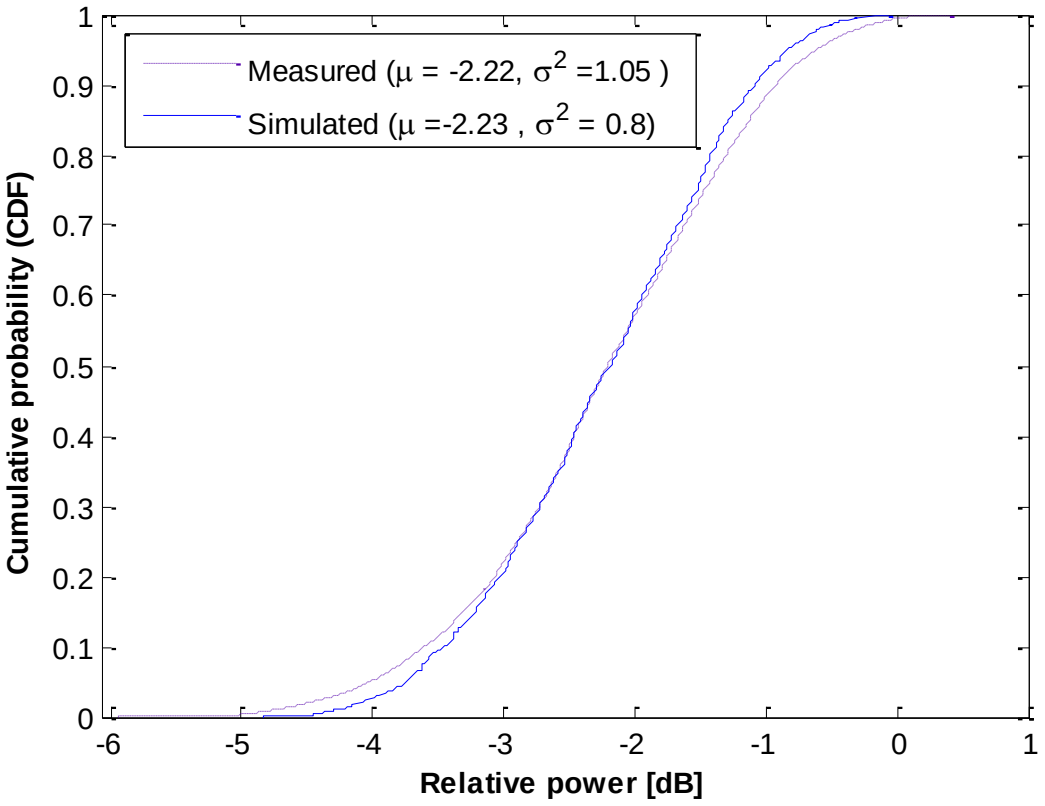

Fig. 4.19 Cumulative probability (CDF) of the experimental and simulated data

To carry further investigation in time domain, the IFFTs of the obtained channel transfer functions are computed to yield the PDPs shown in Fig. 4.20(a) and (b) for experimental and theoretical results, respectively.

The prominent strong ray of Fig. 4.20 exhibits a relative delay of 67 ns, this ray is caused by the specular reflection from the flat surface reflector DO. Its relative path length is 20 m, which is the length of the central line along both perpendicular corridors joining both terminals. The specular reflected ray is then followed by another component detected at 68 ns, caused by diffraction from the reflector corner shown in Fig. 4.16.

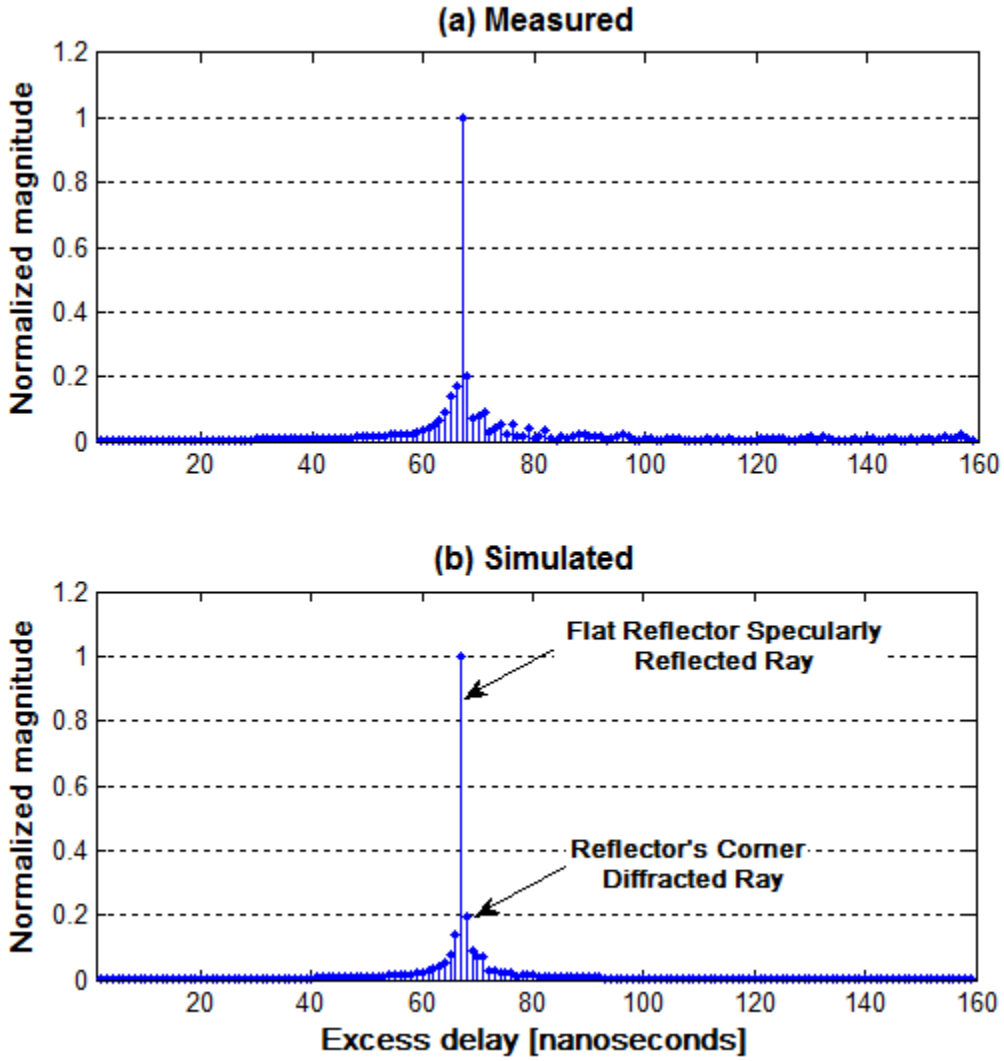

Fig. 4.20 Normalized time impulse response of NLOS corridors environment in the presence of a perfect conducting flat surface reflector.

It is interesting to note that, the strong specular component of the reflector dominates all other multipath components present in the channel.

4.4 LOS Conference Room Channel Model

Conference room environments are known to be among the most important for WLAN office fast downloading applications which operate under direct LOS between the transmitting and receiving antennas. Typical conference room environment are well defined in [125]. There is

still a lack of experimental and modeling results on 60 GHz WLAN system performance for these environments [126]. This section simulates the experimental results in the 60 GHz band targeting to reveal the 60 GHz propagation mechanisms for WLAN and WPAN systems in a conference room environment. Hence, it is of vital importance to accurately identify the frequency and temporal channel properties to ultimately be able to make accurate predictions on the potential performance of 60 GHz systems.

As proceeded in NLOS scenarios, the propagation characteristics will be modelled in terms of the channel transfer function and the time domain impulse response. Such results provide essential information about the spatial structure of the channel propagation needed for broadband systems design in the 60 GHz band. Using the presented model, accurate information about the temporal characteristics of the conference room in the 60 GHz are provided, i.e., the delay, strength and propagation mechanism for each multipath component individually.

4.4.1 Measurement Site Data Base and Description

This environment is described as follow: a typical rectangular shaped conference room with dimensions of 5.83 m (width) × 6.88 m (length) × 2.67 m (height). The walls of this room are typical interior walls made of plasterboard sheets, the floor is concrete and covered with vinyl plastic tiles and the ceiling is also made of concrete and covered with polystyrene tiles and neon lamps positioned all over the ceiling. The room has two large windows made of glass, and a metallic office door. A top view of the considered conference room is shown in Fig. 4.21. The receiver and transmitter antennas were placed on mobile cart and kept at a height of 1.7 m above the floor level. This measurement campaign was performed under LOS propagation scenario, where both antennas are kept at a distance of 5.7 m apart from each other. Also note that the LOS joining both antennas is 2.5 m away from wall A in a parallel manner. During the measurements, the room was emptied except for measurement instruments. In order to guarantee a static environment, it was ensured that no people were present within the room during the measurement campaign.

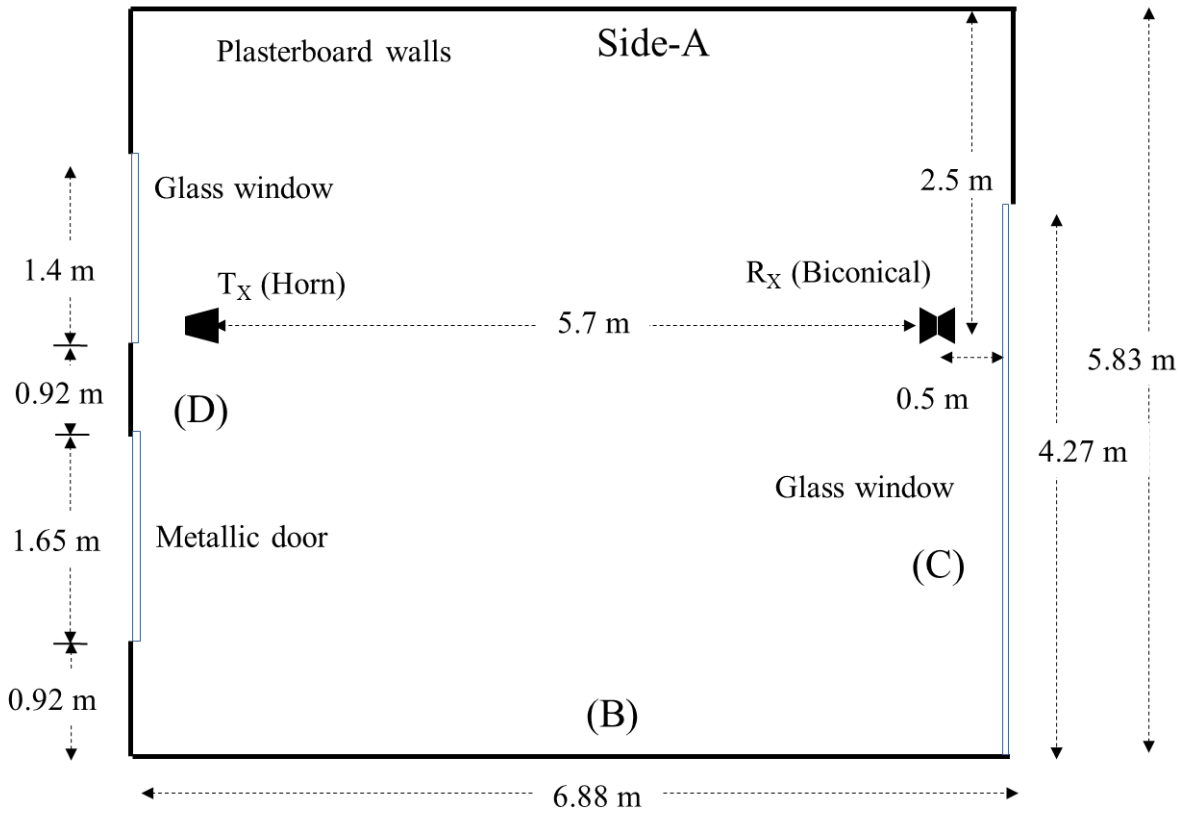

Fig. 4.21 Top view of the conference room plan and identifying the transmitter and the receiver positions in the room.

4.4.2 The Ray-Tracer

In the conference room, LOS scenario is considered, the prediction of the received signal is based on the computation of free-space transmission, superimposed by 3-D multiple reflections from different objects surrounding the transmitter and receiver; hence, it is necessary to test every reflected ray against every surface in the room including walls, windows, doors, floor, ceiling, etc., …. The dielectric properties of the diverse surfaces inside the room including walls, door, and windows are given in Table 4.1. Diffraction from windows and door frames irregularities were tested, they were found to be unimportant compared with free-space and reflection contributions. In LOS channel, diffracted rays might provide an insignificant amount of accuracy to the tracer, hence, for the sake of model simplicity, the computation time and efficiency, they were not considered. The order of reflection is not the same for all reflected rays; it is dominated

by the type of surfaces that faced the ray during its interactions. In the case of interaction with plasterboard surfaces, only up to 2nd order reflections are considered, due to the high absorption experienced at 60 GHz by this type of material. Glass is considered to behave in the same manner as plasterboard. The door is metallic, therefore, 3rd order reflection is considered in the case when the ray interacts with the door surface, and so on. Based on the image source method, the 3-D ray-tracing is applied to estimate the received multipath signal strength. The field relative to free space at the receiving terminal is expressed by the following algorithm:

$$E(r) = \sum_{i=0}^{n} G_R^i \, G_T^i \, R^i \, \frac{e^{-jkr^i}}{r^i} + \sum_{i=n+1}^{m} G_R^i \, G_T^i \, R^{i^2} \, \frac{e^{-jkr^i}}{r^i} + \cdots \tag{4.9}$$

where, G_R and G_T are the gains of the receiving and transmitting antennas respectively, R^i is Fresnel reflection coefficient associated with the i^{th} ray, r^i is the distance length travelled by the i^{th} ray and k is the wave number.

4.4.3 Results Discussion

4.4.3.1 Frequency Domain Analysis

The typical normalized plots of both measured and simulated channel frequency responses are shown in Fig. 4.22. It is seen clearly that, the theoretical signal variations fit favourably the measured one, in term of fading, periodicity, and power signal decaying. The large and small-scale fading compares favourably in both results. The large scale fading in fact resulted from the free-space propagation (LOS-ray). Indeed, the small-scale amplitude variation which results from multi-reflections is periodic, it repeats every 14 MHz, and superimposes the LOS. The cumulative distribution functions of both the measured and simulated results are computed and shown in Fig. 4.23. Using the ray tracing model, a good fit is achieved between the measured and simulated frequency responses. Therefore, the presented conference room channel model is successfully validated.

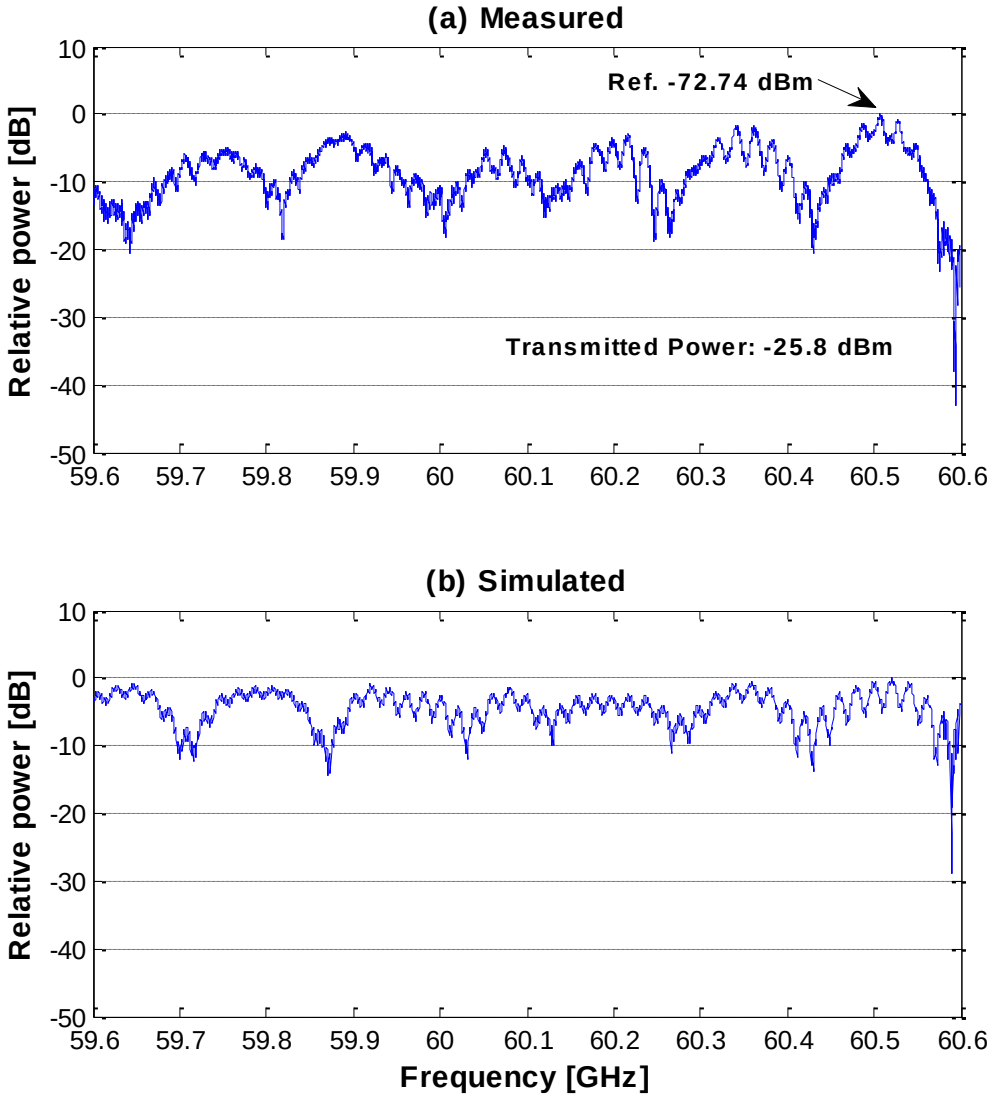

Fig. 4.22 CTF of LOS conference room environment.

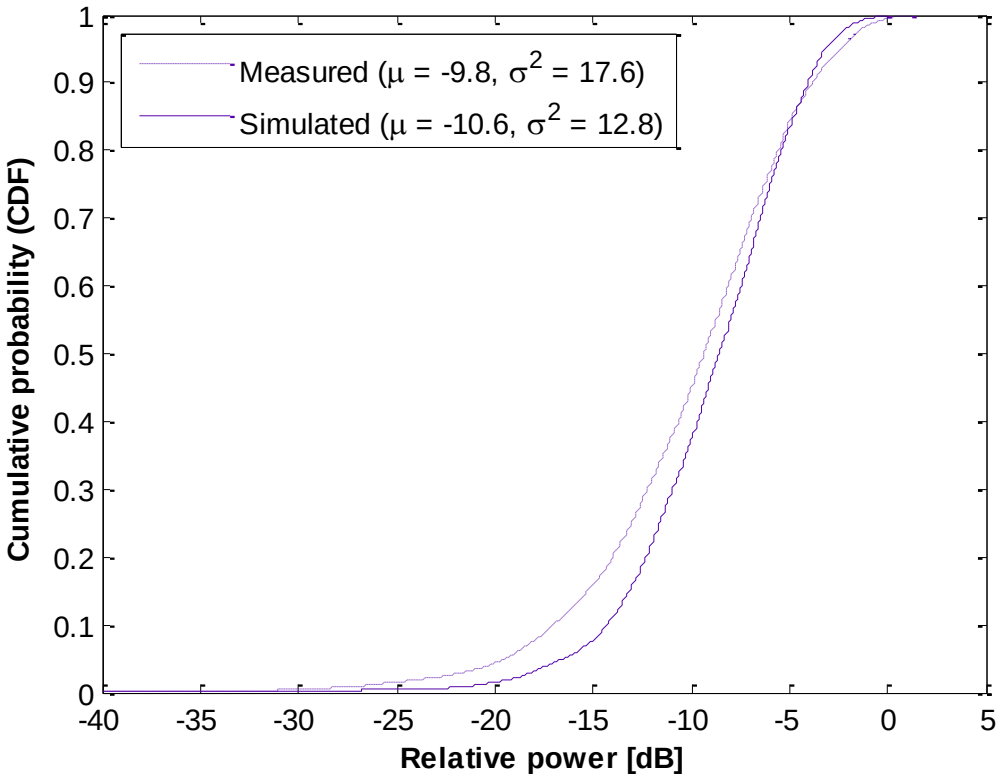

Fig. 4.23 Cumulative probability (CDF) of the experimental and simulated data**.**

4.4.3.2 Time Domain Analysis

To investigate the temporal domain characteristics, the IFFT is performed for both the experimental and the theoretical of the channel transfer function, where both channel PDPs are derived and shown in Fig. 4.24. Both results match well in terms of rays magnitudes and delays.

It can be concluded from Fig. 4.24 that, the first observable path of the PDP corresponds to the shortest path distance between the receiver and the transmitter.

This path arrives at 19 nanoseconds is the result of free-space along the 5.7 m direct LOS ray that joins both antennas, as illustrated in Fig. 4.21. The first MPCs cluster (Cluster-1) is within time range of 19–30 ns; it is caused by 1st and 2nd order of reflections, whereas Cluster-2 is the result of 3rd and 4th order of reflection associated with rays arriving within 65-75 ns time range.

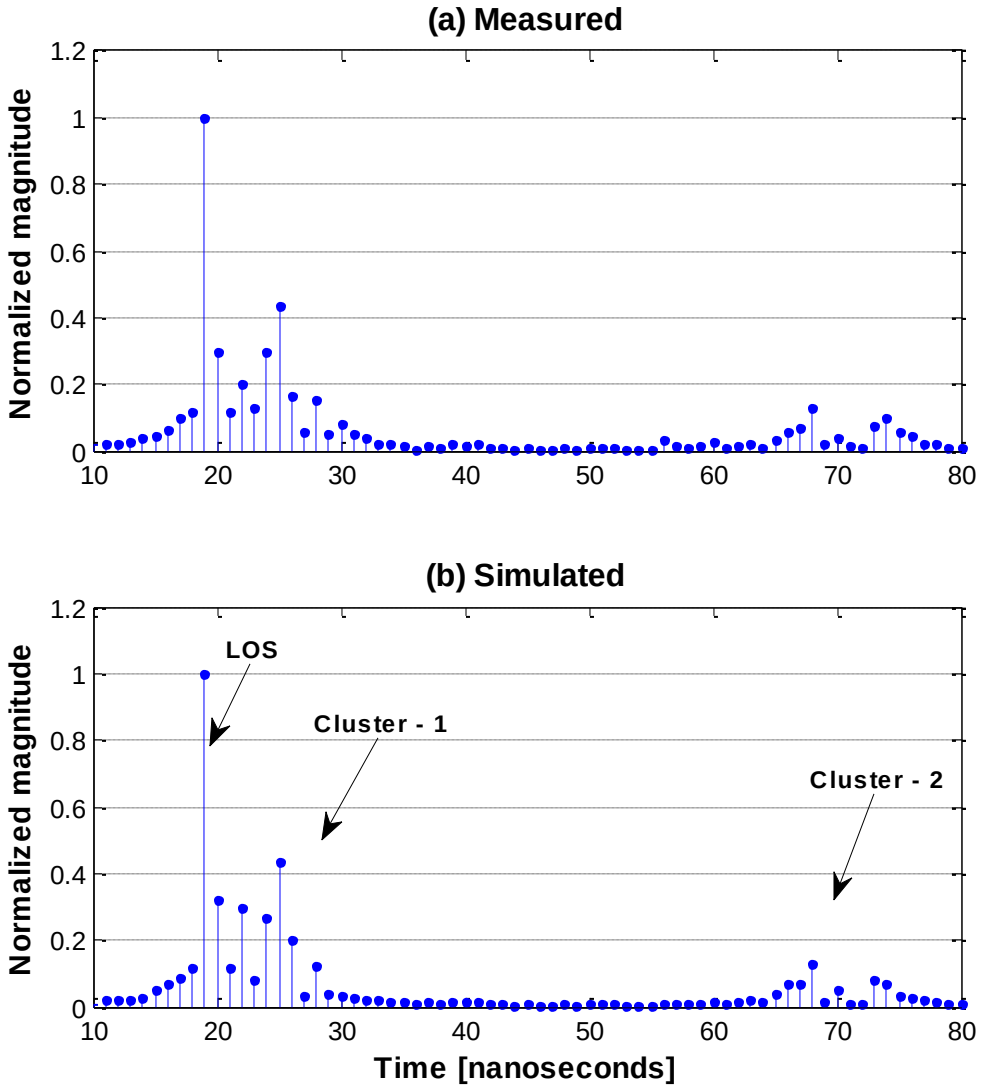

Fig. 4.24 Normalized PDPs of conference room environment.

To have a clear observation and deeper analysis, a zoom-out of the cluster-1 normalized PDP is shown in Fig. 4.25. The first perceptible ray is detected at 19 ns, it is the interpretation of the direct LOS that experiences a free-space propagation mechanism, hence, this contribution dominates the channel. The 1st-order reflected rays from the concrete floor and ceiling are identified and detected at 20 and 22 ns respectively. The walls A and B 1st-order reflected rays are detected at 25 and 29 ns respectively. The contribution AC which is caused by double reflection from wall A and the glass (on side-C of the room) is identified, its delay is 28 ns. More 2nd order contributions are disguised due to the FFT and the sounder limited resolution of 1 ns.

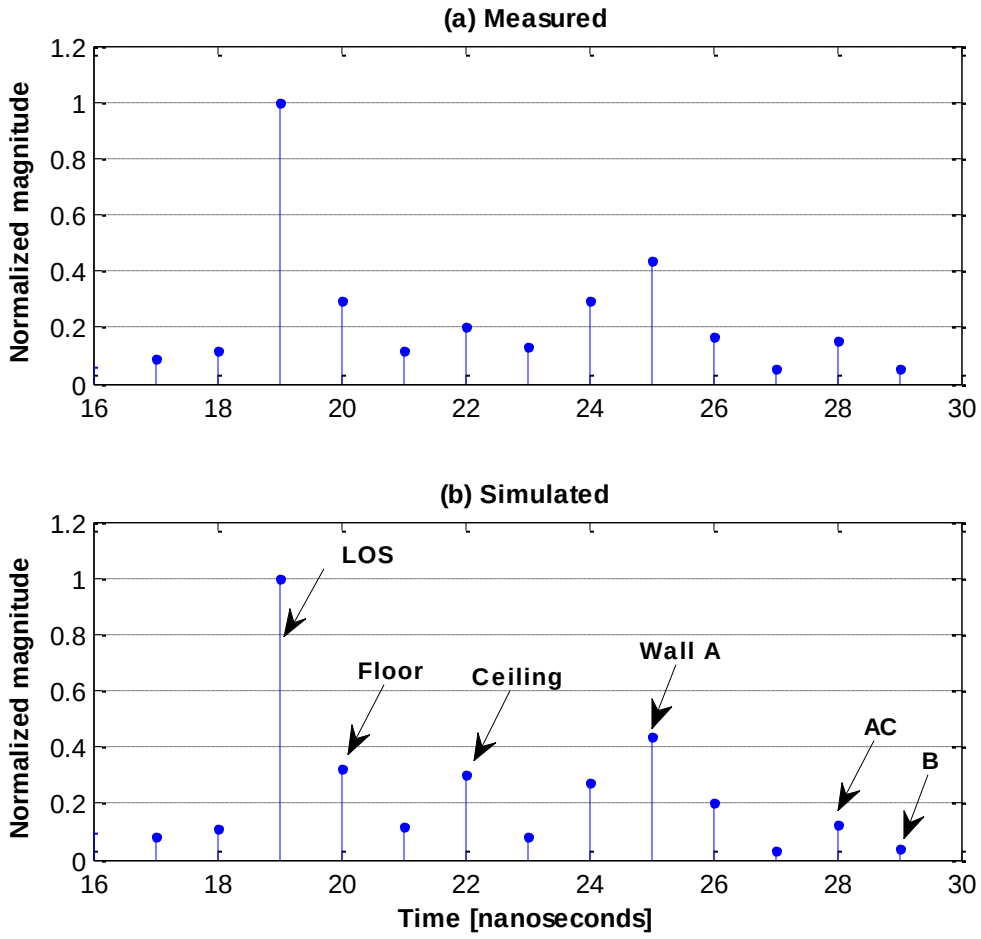

Fig. 4.25 Normalized time impulse response of the conference room (Cluster-1).

4.5 Discussion

This chapter sought to validate the experimental propagation characteristics of 60 GHz communications in two typical indoor environments. Based on sweeping-frequency sounding technique (59.6 – 60.6 GHz), the propagation measurements are carried out in two typical indoor environments; NLOS T-shaped corridors intersection and LOS modern rectangular conference room. As a result of the analysis carried out, it is found that, in the 60 GHz band, ray-based channel modeling requires a great knowledge and very precise and detailed information about the environment material properties and geometry.

In the literature there are few ray-based models in the 60 GHz band, they rely on very limited number of rays. However, our analysis shows that, at 60 GHz all multipath are important and relevant to allow obtaining precise as well as accurate predictions of channel propagation characteristics corresponding to the considered environment. For example, in the NLOS corridors environment (without DO), the far gate and the far pillar contributions appeared to be unimportant at first glance, however, excluding them have caused the result to change dramatically. As a result of our deep analysis, it is concluded that the models that rely on few important rays render to be inaccurate and impractical, especially a strong dominant component is not present in the multipath channel.

60 GHz channels have properties that can be fundamentally different than those of the traditional wideband channels; they are very susceptible to the propagating environment. Due to the extremely large bandwidth of the 60 GHz systems, frequency-dependent effects cannot be ignored; hence, the propagation characteristics and other effects should be considered frequency-variant and investigated more carefully. This implies that we have to consider in the synthesized link both antennas and material properties of the considered environment on the whole covered frequency band.

In the NLOS corridors scenario (without DO), the UTD is a perfect tool to predict the diffracted field around the intersection corners, Remely's heuristic diffraction coefficient for a lossy wedge is accurate to calculate the diffraction field in near and far zones of the shadowing region where LOS does not prevail.

In the case when a metallic cylinder is present in the channel, the presented model became complex somehow in terms of mathematical modeling and computation; however, it is validated successfully. The problem of the diffraction of an arbitrary ray optical electromagnetic field by a smooth conducting convex surface of slowly varying curvature is investigated in this thesis. The obtained results have demonstrated clearly that, an accurate prediction of the diffracted field over a smooth cylinder is achieved using the UTD by smooth convex surface introduced by Pathak et al [122, 123]. This model is a very promising tool for engineering applications in order to analyse theoretically the diverse aspects of the 60 GHz broadband channel in the presence of a

cylindrically shaped object in the NLOS channel. Moreover, the presented model provides a great analysis tool to assess the NLOS propagation mechanisms and parameters required for 60 GHz WLAN systems design based on the presence of a cylinder in the channel. After the validation of the proposed model, is it proven theoretically that the presence of a cylinder in the NLOS 60 GHz channel gives rise to a strong dominant multipath diffracted component comparable to LOS when the latter is not present.

At 60 GHz, the difference of propagation characteristics among the various environments lies mainly in the number of MPCs that fall into one bin. This number is influenced by the nature of the environment; the more objects present in the environments, the more MPCs can occur. For example, within delay bins empty room environments tend to have fewer MPCs than NLOS corridors environments. Furthermore, the delay of the considered bin plays a role: for larger excess delays, there are more feasible paths causing this particular delay. Thus, fading depth increases with increasing delay.

As mentioned previousely, the time bin width of one nanosecond offered by the measurement system appears to be reasonable. Given the 1 GHz channel bandwidth, the time (delay) axis is divided into resolvable delay bins of length 1ns, where all MPCs falling into one such bin cannot be resolved as distinct paths and are thus simply superposed. In the considered corridors environment, each corner causes a multipath cluster which includes a large number of irresolvable MPCs (about 6 MPCs) that are separated by a fraction of less than one nanosecond. As shown in Fig. 4.8, each multipath cluster spreads over an excess delay of five nanoseconds, these MPCs are caused by diffractions from corners and up to fourth-order reflections from walls and floor.

Chapter 5

Characterization and Analysis of 60 GHz Wideband Measurements

5.1 Introduction

Up to this date, it has been seen clearly from the various 60 GHz measurement campaigns (whether LOS or NLOS) that, totally different results are achieved even for similar indoor environments [127]–[132], this is mainly due to the high sensitivity of millimeter waves. Moreover, the amount of available measurement data is very limited compared to the importance of 60 GHz communications, and more are needed to support a comprehensive knowledge of the propagation characteristics in this band. Besides, there is no adequate information on channels models that feature and quantify the constructive characteristics of radio waves resulted from the presence of deflecting objects (DOs) in the channel. Hence, the aim of this chapter is to present results of experimental investigations to reveal the propagation characteristics and the essential channel statistical parameters required for WLANs design in the 60 GHz unlicensed band.

The remainder of this chapter is structured as follows: Section 5.2 gives insight into the NLOS corridors intersection environment. Based on the presence of deflecting objects, the experimental procedure for various measurement scenarios are described. Also, the experimentally obtained data are processed and analyzed in section 5.2 to study most important issues such as small scale fading and their statistical distributions, the channel coherence bandwidth, and the path losses. Moreover, the channel temporal characteristics and delay spreads are provided and discussed. Section 5.3, provides further data analysis to characterize the propagation characteristics in a conference room environment. The frequency and time domain parameters are extracted and data are processed as followed in the NLOS corridors environment. Section 5.4 discusses the OFDM transmission in terms of channel BER, received signal constellation and spectrums to yield a fair

comparison among the proposed scenario in term of channel performance. Then, section 5.5 is devoted for summary and discussion. Finally, a conclusion is provided in section 5.6.

5.2 NLOS T-Shaped Corridors Intersection Environment

5.2.1 Experimental Procedure

The measurements were carried out within the 3rd floor of the telecommunication laboratory building of the CRC. In the corridors intersection, the measurement campaign was performed under the NLOS propagation scenarios described in chapter 5. The transmitter was located in corridor (A) and displaced at different positions ranging from 1m to 10 m away from the corridors intersection while the receiver was located at a fixed position on the corridor (B), i.e., 10 m away from the intersection, as illustrated in Fig. 5.1.

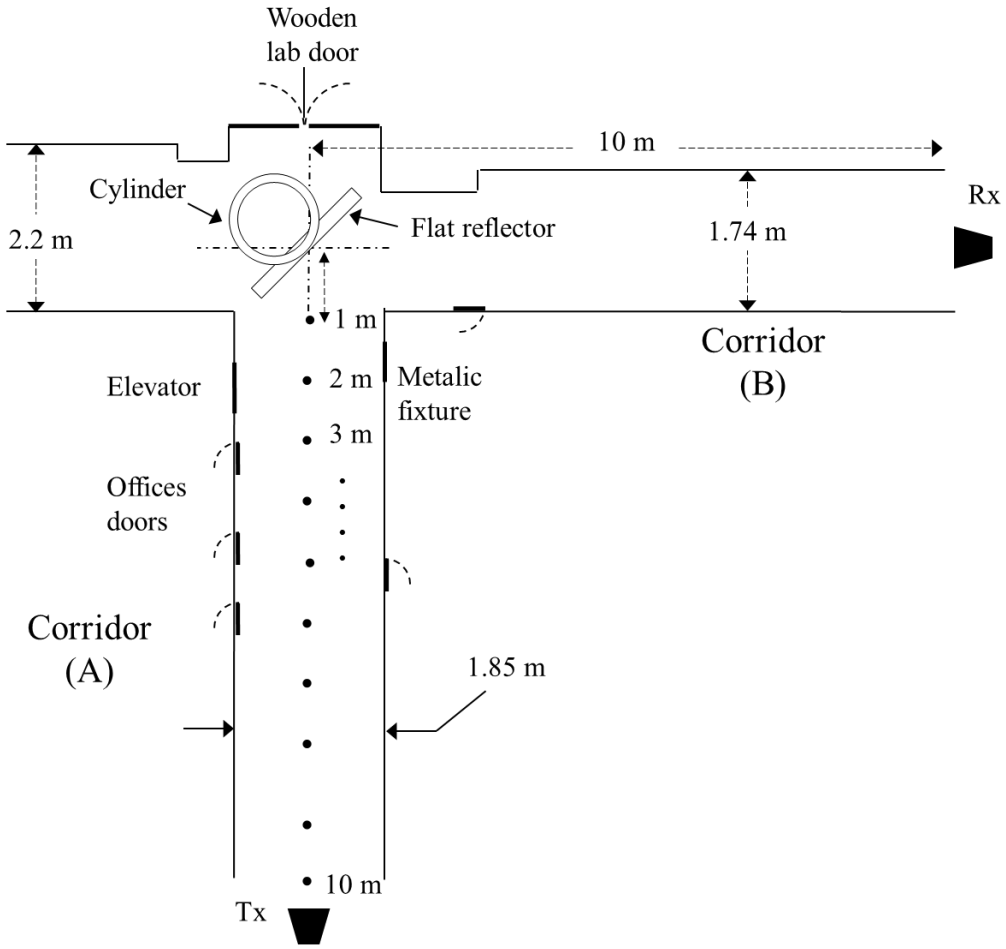

Fig. 5.1 A schematic view of the measurement site

As previously stated, the measurement system is designed to measure the channel propagation characteristics in the frequency domain. One of the first tasks in the experimental procedure is to measure the complex transfer function of the propagation medium. In the measurement system, the basic technique used was to collect the data in the form of in-phase (I) and quadrature (Q) voltages while pointing both antennas towards the DO. Measurements have been performed over a bandwidth of 1 GHz (59.6 – 60.6 GHz) with a center frequency of 60.1 GHz. The measurement frequency resolution is 100 kHz to yield 10,001 data points for each measurement snapshot.

The experimental procedure is described by measuring the frequency response, $H(f)_{measured}$ and repeating the procedure for each DO independently. Fig. 5.2 shows the scanned channel transfer functions for various scenarios when both transmit and receive antennas are 10 m away from the corridors intersection. It is clearly seen that each DO provides a totally distinct frequency response.

From Fig. 5.2, it can be observed that at 60 GHz, the fast fades occur on frequency scale of 11.3 MHz. This is because multipath rays combine constructively or destructively according to their relative phase difference ($\Delta\phi = \pi$). Hence, nulls due to cancellation between rays occur when the difference in path length (Δd) is a multiple of a half-wavelength [79].

Under NLOS, it can be seen clearly that the channel frequency selectivity is more severe when no DOs are present in the channel (Fig. 5.2(a)). In fact, the relative signal strength may reach the -115 dB level at some specific frequencies. However, the presence of a DO in the channel has mitigated significantly the channel selectivity. When a flat surfaced DO is present, the signal fades are shallow and almost constant over the whole considered frequency band (Fig. 5.2(c)), i.e., the frequency components are almost affected in a similar way; this phenomenon is known as flat fading. This is mainly due to the presence of a strong dominant multipath component comparable to LOS, which in turn results a strong correlation among the frequency components of the channel transfer function [81, 133].

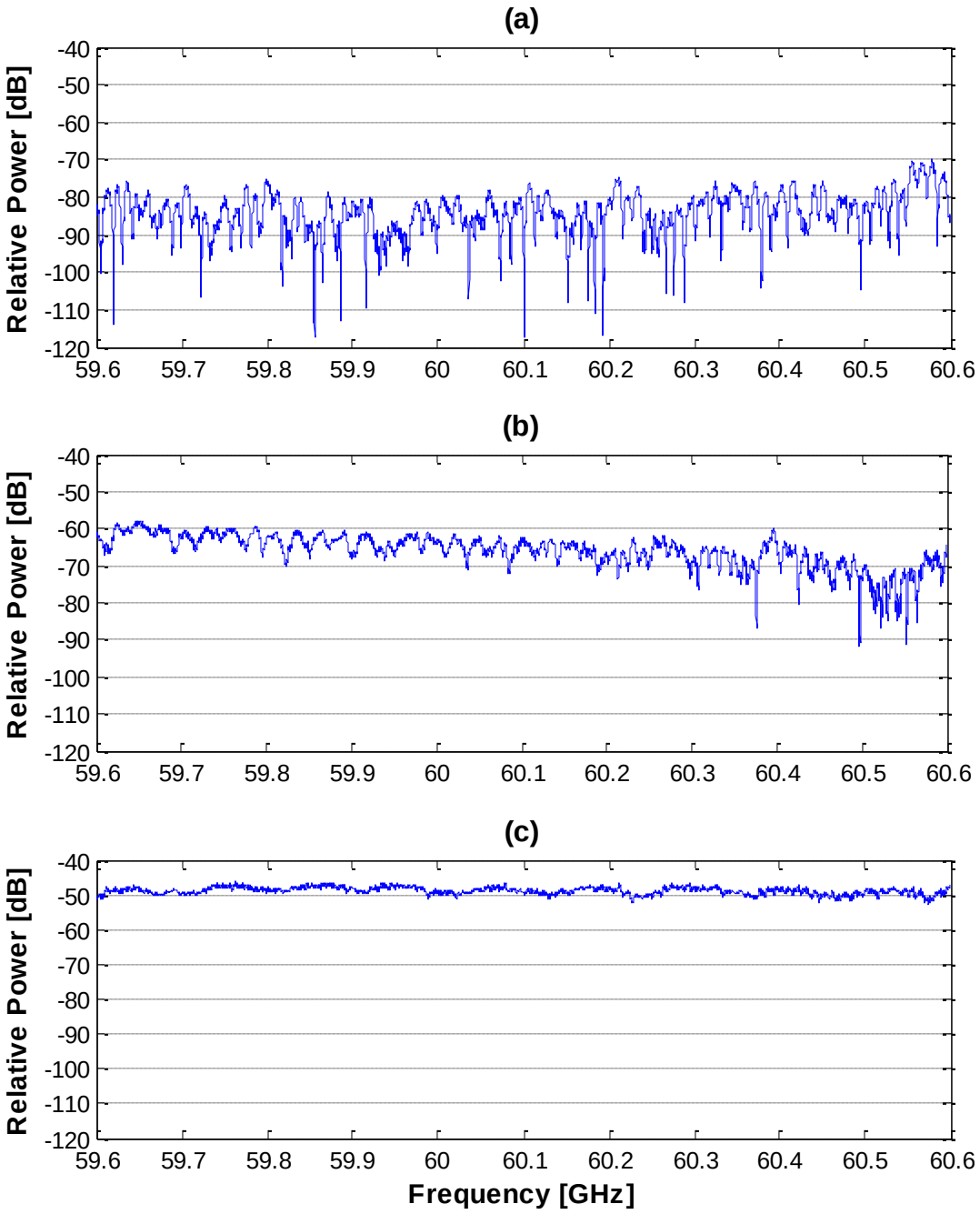

Fig. 5.2 Measured frequency response in a NLOS corridors intersection in the 60 GHz band:

a) No-DO is presented in the hallway,

b) Cylindrical DO,

c) Flat surface DO.

5.2.2 Frequency Domain Analysis

5.2.2.1 The Channel Frequency Correlation

Compared with conventional wireless systems, the 1 GHz under consideration is an extremely wide bandwidth, hence, it is essential to study and verify whether there are frequency dependencies among the spectrum components. For a wide-sense stationary, uncorrelated scattering (WSSUS) channel, the correlation between two components of the channel transfer function with a frequency separation (Δf) is defined by [133].

$$\rho(\Delta f) \cong \int_{-\infty}^{\infty} H(f) H^{*}(f + \Delta f) df \tag{5.2}$$

Due the oscillatory behaviour, the smallest frequency separation value is normally chosen to estimate the coherence bandwidth. This agrees with observations made in [134] that coherence bandwidth characterization using spaced tones [135, 136] is not satisfactory unless measurements are taken over a large number of points [137]. The frequency correlation functions for each of the considered measurement scenarios are estimated as shown in Fig. 5.3.

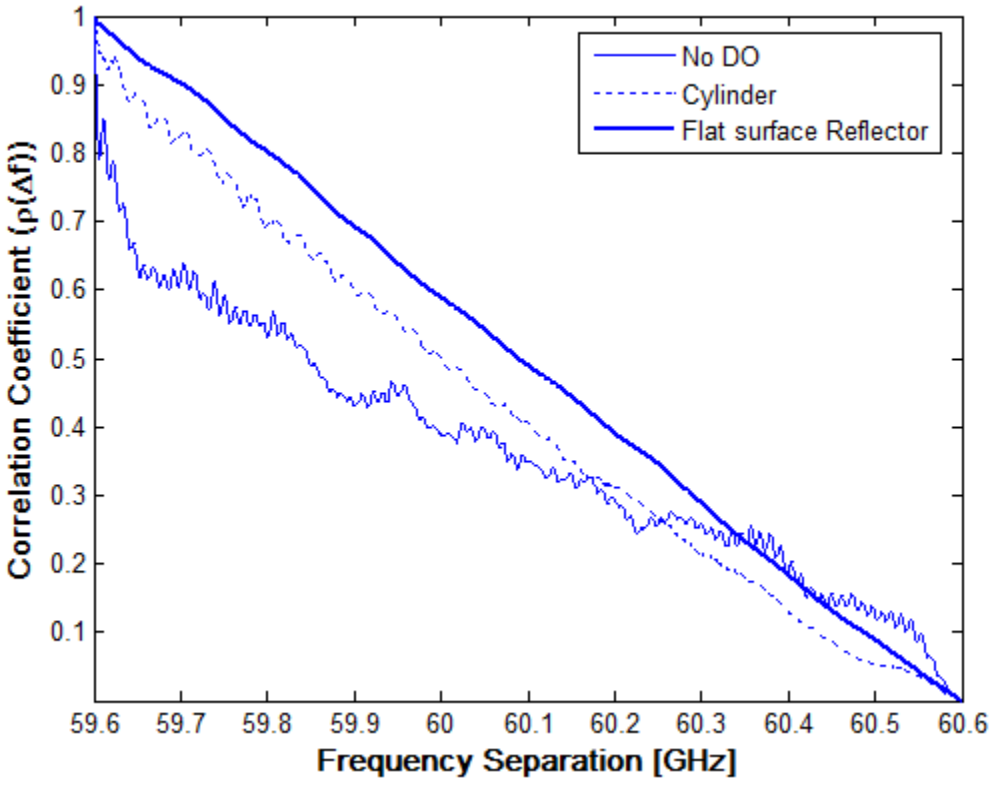

Fig. 5.3 Frequency correlation functions obtained for various scenarios.

Whether a DO is present at the corridors intersection or not, the correlation coefficients are at relatively high level for the lower frequency separations. Hence, the correlation behaviour shows a systematic dependency on frequency. In Fig. 5.3, it is clear that in the No-DO case, the decrease of the normalised correlation function is not monotonous, it drops faster, implying larger delays since all multipath components contribute to the total received signal. Moreover, in the mm-wave radio channel, these multipath echoes produce oscillatory behaviour with declining trend [138, 139]. Also, the presence of DO configuration shows a higher level of correlation implying that a strong dominant multipath component is present.

5.2.2.2 Channel Coherence Bandwidth

The coherence bandwidth is a statistical measure of the range of frequencies over which the channel can be considered "flat" (i.e., a channel which passes all spectral components with approximately equal gain and linear phase). Another definition of the coherence bandwidth is the range of frequencies (maximum frequency difference) over which two frequency components have a strong potential for amplitude correlation [81]. When the correlation is examined for frequency separation (Δf) for which the correlation coefficient equals a certain value, this value is termed the coherence bandwidth of the channel (B_C).

In the literature, the correlation coefficient $\rho(\Delta f)$ has no definitive value, some references use 0.9 to characterize the coherence bandwidth of fading channels ($B_{0.9}$), while others use the values 0.6 and 0.7 referred as $B_{0.6}$ and $B_{0.7}$ respectively. There is a high degree of uncertainty regarding the correlation coefficient$\rho(\Delta f)$, while the accuracy is necessary in order to establish whether the effective transmission bandwidth is within the constraints of the channel's performance or whether counter-measure techniques such as equalisation or diversity would have to be employed to help mitigate the effects of multipath propagation.

For all of the considered scenarios, the coherence bandwidth values estimated at 0.5, 0.7 and 0.9 correlation levels are shown in Table 5.1. It can be seen clearly that the coherence bandwidth varies significantly among the considered correlation levels. When NO-DO is present, the coherence bandwidth varies between 2.7 and 246.2 MHz, similarly, huge bandwidth differences

of 367.3 and 388.8 MHz are recorded in the case of cylindrical and flat surface DOs, respectively.

Table 5.1 Estimated coherence bandwidth values for 0.5, 0.7 and 0.9 correlation level using autocorrelation function of equation (5.2).

Measurement Scenario	Coherence bandwidth (MHz)		
	$\mathbf{B_{0.5}}$	$\mathbf{B_{0.7}}$	$\mathbf{B_{0.9}}$
No-DO	246.2	37.3	2.7
Cylindrical-DO	401	194.2	33.7
Flat Surface-DO	491	292.6	102.2

Hence, this method appears to be uncertain and irrelevant in time invariant channel, where the transmitter and receiver are at fixed position. Although [140] stated that, it is wrong as frequently made in the literature, to characterize the coherence bandwidth from snapshot measurements of the frequency response $H(f,t)$ using the autocorrelation function in (5.2).

Based on time domain analysis, an analytic expression of coherence bandwidth was first introduced by Jakes [139] by assuming that the coherence bandwidth of a wireless channel is inversely proportional to its root-mean-square (RMS) delay spread. The same issue was subsequently studied by various authors [81, 141–143]. Since many practical channel environments can significantly deviate from the homogeneous assumption, various measurements were conducted to determine multipath delay profiles and coherence bandwidths [144–146] aiming to obtain a more general formula for coherence bandwidth.

In the literature the coherence bandwidth has been defined by several expressions based on the considered RMS delay spread of the channel. In [147] the coherence bandwidth is approximated as the bandwidth over which the frequency correlation function is above 0.9 is

$$B_{0.9} = \frac{1}{50\ \sigma_{rms}} \tag{5.3}$$

If the definition is relaxed, so that the frequency correlation function is above 0.5, then the coherence bandwidth is approximated as [81].

$$B_{0.5} = \frac{1}{5\ \sigma_{rms}} \tag{5.4}$$

Hence, it is important to note that an exact relationship between coherence bandwidth and RMS delay spread does not exist and equations (5.3) and (5.4) are 'ball park estimate' [81]. In order to yield a fair comparison, $B_{0.5}$ and $B_{0.9}$ in equations (5.3) and (5.4) are computed as shown in Table 5.2.

Table 5.2 Estimated coherence bandwidth values for 0.5 and 0.9 correlation level in time domain analysis using (5.3) and (5.4)

Measurement Scenario	Coherence bandwidth (MHz)	
	$B_{0.5}$	$B_{0.9}$
No-DO	4.46	0.446
Cylindrical DO	10.62	1.062
Flat Surface DO	22.05	2.205

The amplitudes of all frequency tones that fall within 3 dB below the resonant frequency and have linear phase are identified for all considered measurements. For illustrative purpose, Fig 5.4 and Fig. 5.5 show the cases of NO-DO and flat surface DO, respectively. Hence, the various coherence bandwidths are computed based on equal gain and largest possible bandwidth within the selected frequency ranges where the phase response is linear [148] as shown in Table 5.3.

From Table 5.3, it is seen clearly that each scenario has provided a different channel coherence bandwidth. In all cases, the presence of a DO in the channel enhances significantly the channel performance and its potential capability for high speed transmission.

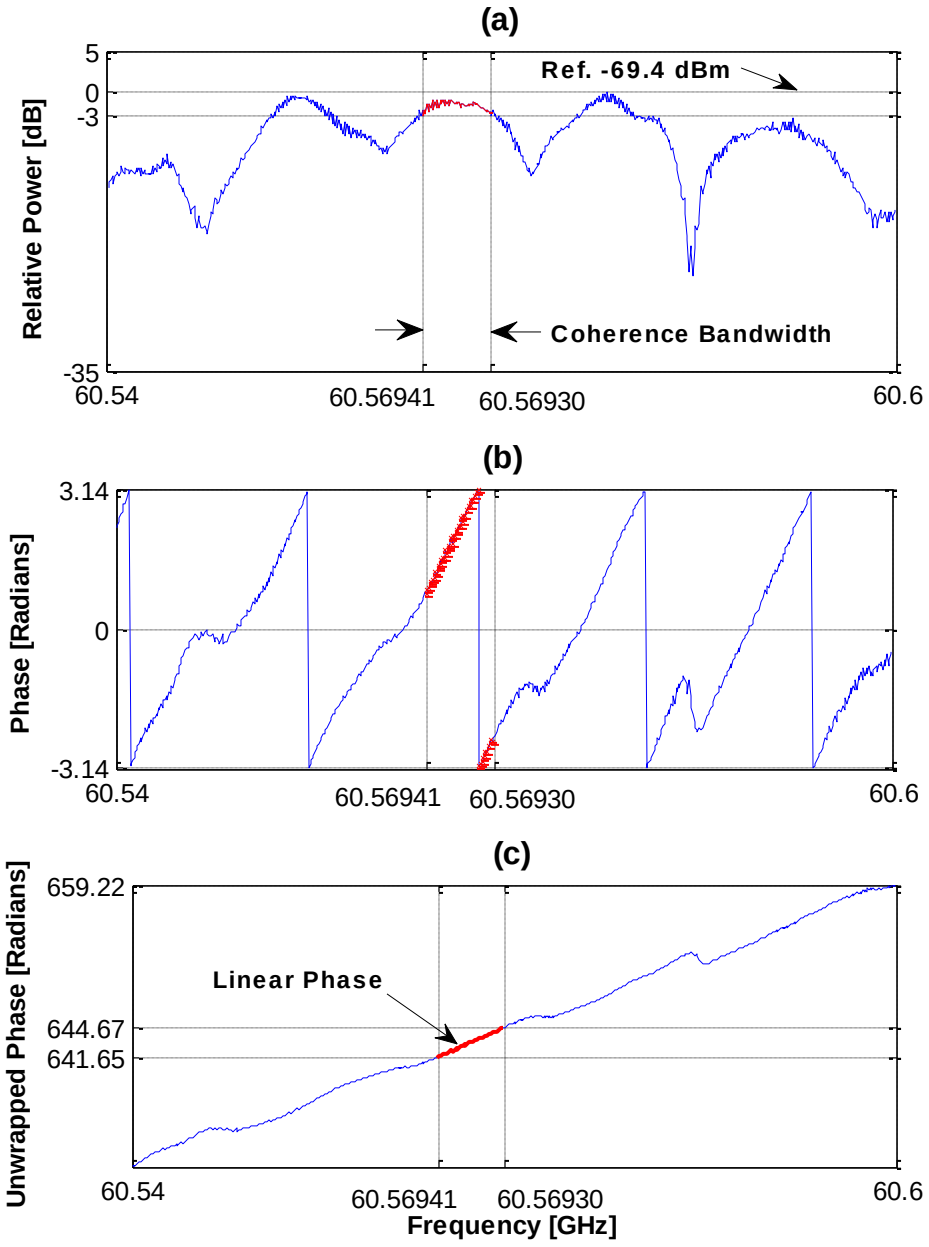

Fig. 5.4 Measured coherence bandwidth when No-DO is present in the channel:

a) Measured frequency response,

b) Phase in radians,

c) Unwrapped phase in radians.

The No-DO scenario appeared to be the worst case. In contrast, a much larger channel coherence bandwidth of 252.2 MHz has been achieved due to the presence of flat surface DO in the channel. In this scenario, it is observed that phase changes uniformly from $-\pi$ to $+\pi$ every frequency interval of 14.5 MHz. In terms of correlation coefficients, the installation of DOs in the channel tends to increase the correlation among the frequency components. The correlation coefficients associated with each scenario are also provided in Table 5.3.

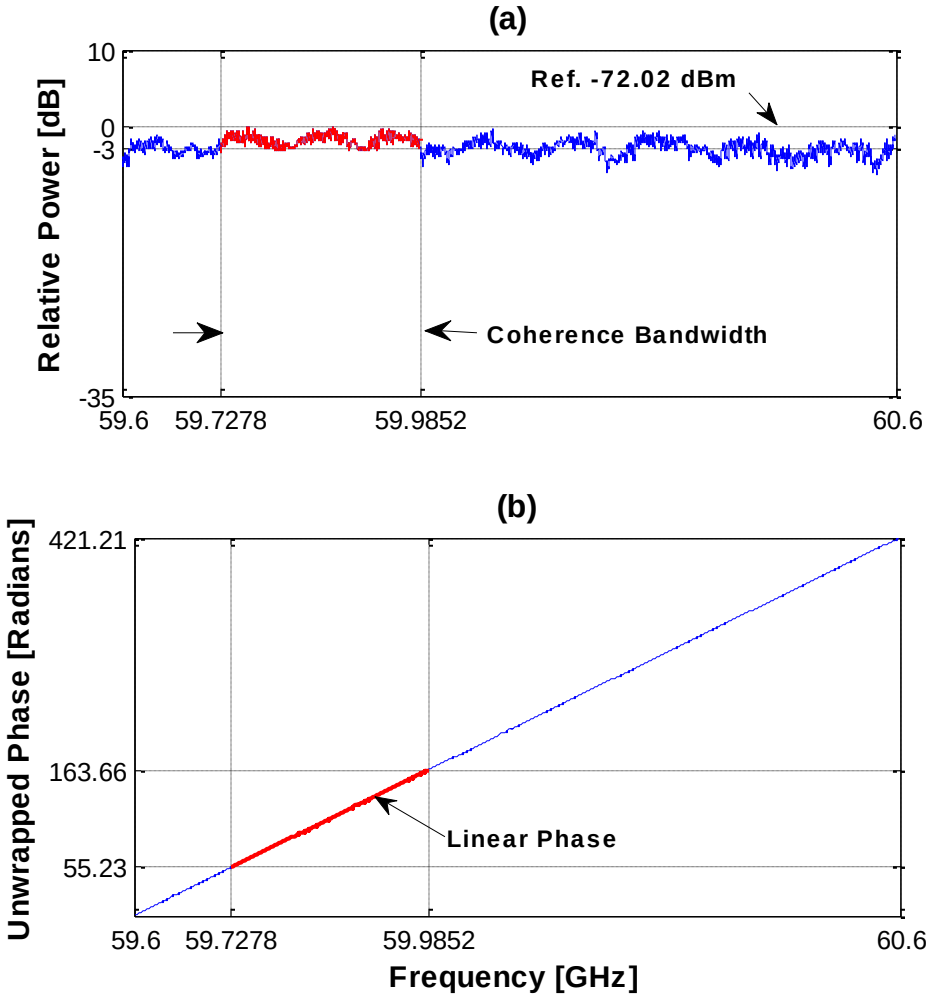

Fig. 5.5 Measured coherence bandwidth when a flat DO is present in the channel:

a) Measured frequency response at 60 GHz,

b) Unwrapped phase in radians.

Table 5.3 Measured coherence bandwidth and associated correlation coefficient

Measurement scenario	No-DO	Cylindrical DO	Flat Surface DO
Coherence bandwidth (MHz)	5.2	20.3	257.4
Correlation coefficient	0.797	0.864	0.92

5.2.2.3 Small-Scale Fading Distributions

As in typical indoor environment, the electric field strength fluctuates rapidly over space, time or frequency if there is a lot of multipath. This is because the field at a particular point is the sum of several components, each with a magnitude and phase. More important, the relative phases of the components change, so that the net magnitude and phase of the sum varies. This variation over space is what we call either small-scale fading or multipath fading.

For this purpose, it is essential to describe with the probability distribution if the signal will exceed a specified reference level. A great number of statistical distributions exist such as Rayleigh, Rice, Nakagami-m and Lognormal [149]–[151]. Due to quasi-random phases of the multipath components, the Channel transfer function $H(f,t)$ can be seen as the sum of a large number of random variables (RVs) with amplitudes $\{a_i(t)\}$ and uniformly distributed phases over $[0,2\pi)$. Assuming that a considerable number of rays have similar magnitudes (except for possibly one dominant ray), the central limit theorem leads to the conclusion that $H(f,t)$ has a complex Gaussian distribution. Without the dominant ray, it is zero mean; otherwise it is non-zero mean. The magnitude $R = |H(f,t)|$of the complex Gaussian process is described by the Rician PDF. Also, in his book [152] Prasad has demonstrated that the amplitudes of the time invariant CTF can be fitted using statistical distribution functions such as Rice distribution.

It will be seen that the Rice factor (K) specifies the depth of the fades within a local area, as the Rician probability density function (PDF) will be used to characterize the amplitude distribution of the channel response. Larger K relate to shallower fades. As expected, the Rice fading distribution fits the experimental data of the channel in presence of DO, since a strong dominant multipath component arises from the specular interaction coming from either the cylinder or the

flat surface. However, when the channel is empty, i.e., no DO is present at the intersection; the measured data behaves as a Rayleigh channel. Obviously, in this latter case no dominant component takes place in the multipath signal. The cumulative distribution functions (CDFs) for all cases are depicted in Fig. 5.6. Statistical distributions of Fig. 5.6 indicate that, the installation of a DO in the channel strengthens the received signal considerably compared with the case when no DO is presented. Also Table 5.4 shows the parameter values of experimental data best fitted curves. Results emphasize that, flat surface DO provides best signal coverage compared with other scenarios.

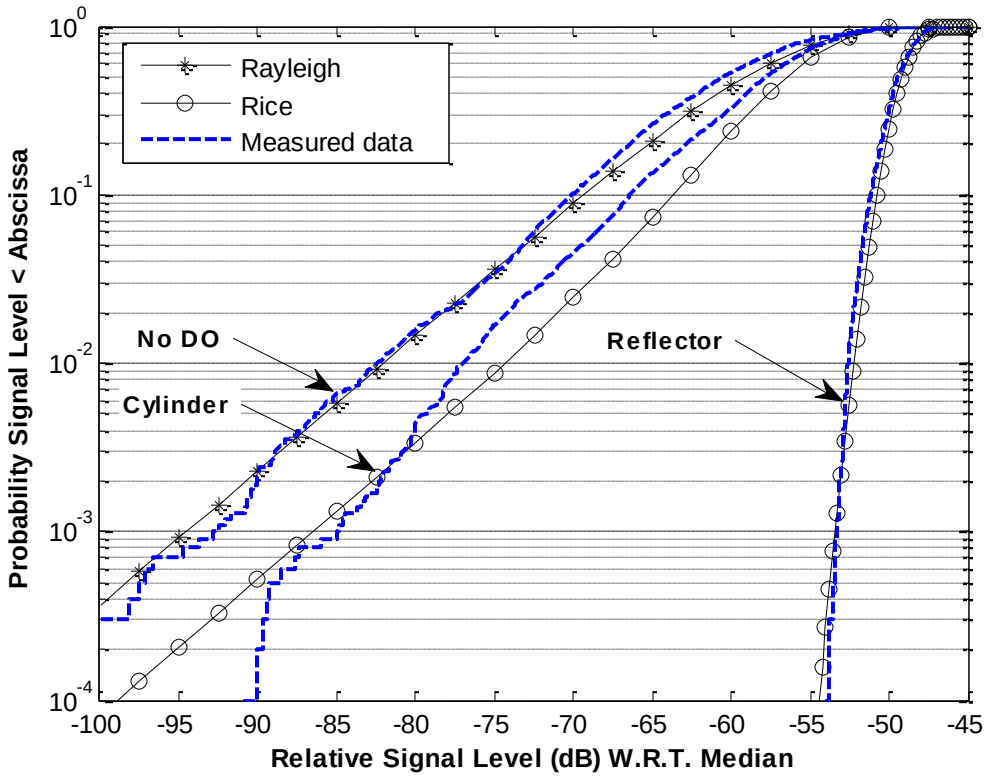

Fig. 5.6 Fitting the CDF of the experimental data with Rice and Rayleigh distributions.

An alternative distribution, for such cases was originally proposed in [153] and is known as the Nakagami-m distribution. This assumes that the received signal is a sum of vectors with random magnitudes and random phases, leading to more flexibility and potentially more accuracy in matching experimental data than the use of Rayleigh or Rician distributions. Because Nakagami fading is a general representation of fading that includes Rayleigh and Rician fading as special

cases [154]. The Nakagami-m distribution has been used extensively in the literature to model signal fading for bandwidths exceeding 500 MHz [155]. The Nakagami-m cumulative distribution functions (CDFs) for all cases are depicted in Fig. 5.7.

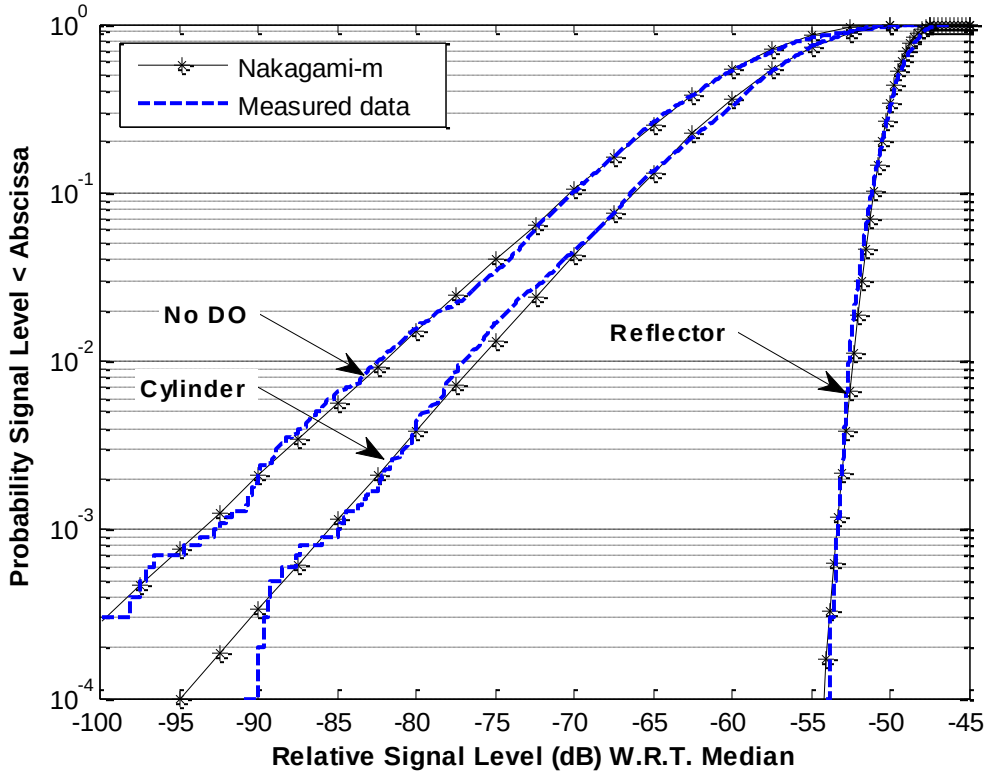

Fig. 5.7 Fitting the CDF of the experimental data with Nakagami-m distribution.

Table 5.4 Experimental data statistical distribution parameters

Measurement scenario:	**No-DO**	**Cylindrical DO**	**Flat DO**
CDF	(Rayleigh)	Rice K = 3.74 dB	Rice K = 16.64 dB
	Nakagami m = 1.017	Nakagami m = 1.6	Nakagami m = 14.3

5.2.2.4 Path Loss (PL)

One of the most important aspects of any characterization of radio propagation is to examine the field strength at the receiver side; hence, the link budget of the overall communication system is studied to relate the transmitted power, the received power, path loss, received noise and additional losses, and to merge them into a single equation.

After taking into account the hardware calibration information and antenna gains, the measured complex frequency responses data $H(f_i, d)$ were used to estimate the average received power at *T-R* separation distance. However, we stress that the averaging of the received power (P_r) over the fading must be done on a linear scale (not in decibels) as

$$P_R(d) = \frac{1}{N}\sum_{i=1}^{N}|H(f_i, d)|^2 \tag{5.6}$$

where, f_i is the i^{th} frequency tone, d is the antenna separation distance and N represents the number of frequency response snap shots measured during a sweep of the 10000 discrete frequencies.

In accordance to Friis equation, the path loss is defined as the ratio of the transmitted power (P_T) to the received power (P_R) averaged over both the small-scale and the large-scale fading. Basically, the path loss, together with the transmit power and the minimum detectable receive power (which in turn depends on the actual system design), determine the system coverage, i.e., the maximal distance between both terminals for acceptable communications. The path loss is then:

$$PL(d)[dB] = P_T[dBm] + G_T[dBi] + G_R[dBi] - P_R(d)[dBm] \tag{5.8}$$

where G_T and G_R are the transmitter and receiver antenna gains in decibels of gain with respect to an ideal isotropic antenna (dBi) [156].

Although the measured path loss values might have the antenna gains subtracted out, providing path loss that would be experienced if isotropic antennas were used on the transmitter and receiver, even though directional antennas were actually employed on the measurement system.

It is important to underline the fact that the gain variation on 59.6 – 60.6 GHz range has insignificant effects on the measured data. This is because the gain of the used pyramidal horn antenna (SGH-15) is almost constant across the 1 GHz band of interest. More details about the SGH-15 horn antenna gain and specifications are found in Millitech Company's website.

In the experiment, we observed that the path loss parameters did indeed change significantly from one DO to another, as shown in Table 5.5. In all cases, the path loss induced by each DO is computed with respect to 20 m of separation distance between the receiver and the transmitter and antennas gain of 23.3 dBi each. From the values of Table 5.5, it is seen clearly that in NLOS channel (corridors), and regardless of the shape of the DO, its presence at the corridors intersection will mitigate significantly the path loss, and hence, strengthen the received signal where a larger amount of received signal power level has been recorded. As expected, it is seen that a flat DO yields a very strong signal compared to the cylinder scenario. In contrast, the weakest signal strength is recorded when no DO is present at the corridors intersection.

Table 5.5 Measured Path Loss (PL) at 20 m of antennas separation distance between the receiver and the transmitter.

Measurement scenario:	**No-DO**	**Cylindrical DO**	**Flat DO**
PL[dB]	83.91	64.42	53.22

The received power decreases with the distance between the transmitter and the receiver. The path loss exponent, *n*, is a measure of decay in signal power with distance, *d*, according to $1/d^n$, *n* depends on the specific propagation environment.

$$PL(d)[dB] = \underbrace{\overline{PL}(d_o)}_{\substack{PL\ at\ reference \\ distance}} + \underbrace{10nlog_{10}\left(\frac{d}{d_o}\right)}_{\substack{PL\ exponent\ at\ relative \\ distance\ d>d_o}} + X_\sigma \qquad (5.9)$$

where $PL(d)$ is the path loss in decibels at a particular distance d in meters from the transmitter, $\overline{PL}(d_o)$ is the average path loss in decibels at a close-in free-space reference distance d_o, and *n* is the path loss exponent. Measurement results reported in the 60 GHz range have shown that the

shadowing fading is log-normally distributed [157, 158], that is $X_\sigma[dB] \sim N(0, \sigma)$, where, X_σ denotes a zero-mean Gaussian-distributed random variable in dB with standard deviation of σ decibels [159, 160]. It is also shown that the value of σ is higher at 60 GHz compared to lower frequencies since the transmission loss at 60 GHz is much higher. The path-loss exponent is then obtained by performing least square linear regression on the logarithmic scatter plot of averaged received power versus distance to equation (5.9).

The exponent n can vary significantly even in the same type of environment, this is due to factors such as type of antenna used, the type of objects present, the layout of the environment, measurement system capabilities, and the height of the T_X and R_X, all which could lead to different propagation characteristics and parameters values. Fig. 5.8 shows the fitted lines of the considered scenarios. The path loss values obtained with respect to a reference distance (d_o) of 1 m from the corridors intersection (11 m from the transmitter). The average path loss fit fairly the plotted lines especially for the flat DO case; this might be caused by the importance of the specular reflection strength.

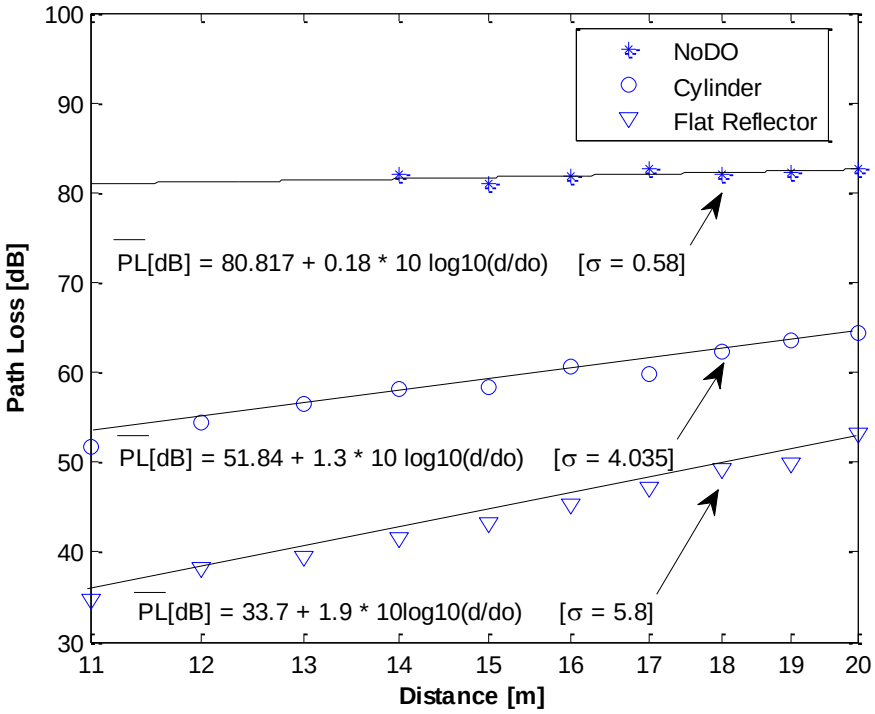

Fig. 5.8 Path loss models in NLOS corridors environments at 60 GHz.

It is observed that the No-DO measurement scenario exhibits a very low path loss exponent (n = 0.18); this is possibly due to the fact that the received signal strength is very weak. In the case of a flat surface DO, the path loss exponent is 1.9, this value is comparable to free space (n=2). It can be noted that in the cylinder DO case the path loss exponent with directive antenna is as small as 1.3. The small values of n observed in such scenario can be justified by the presence of wave guiding (through specular interaction) and the heavy multipath aggregation.

The standard deviations of Gaussian random variables (σ_{dB}) are also shown in Fig. 5.8. The obtained values demonstrate that the shadowing parameters are site-specific, where the highest value is recorded when a flat surface reflector is the DO.

As a result of the above frequency domain channel analysis, it is demonstrated that the presence of DOs in NLOS channel should not be considered as noise sources in the 60 GHz band. Moreover, the installation of DOs in the channel might be a potential solution to increase signal coverage in NLOS environments. Moreover, a well-designed DO with proper shape and surface characteristics would add more strength to the received signal and extend its coverage range to deeper shadowed areas where LOS is not present.

5.2.3 Time Domain Analysis

An estimate of the channel impulse response for each case is derived by performing the IDFT (Inverse Discrete Fourier Transform) to the measured CTFs. The PDPs samples are shown in Fig.5.9. To characterize the dispersive properties of the multipath channel and hence, to evaluate its performance, the mean excess delay (τ_{mean}), maximum excess delay (τ_{max}) and RMS delay spread (σ_{τ}) are computed [34, 35]. For each considered scenario, the channel dispersion parameters are computed following two power thresholds (-30 dB and -40 dB), as given in Table 5.6. Results show clearly that the shortest delays are recorded in the case of flat surface DO, this is mainly due to the fact that the specular reflection from the flat DO give a rise to a strong dominant component which significantly suppresses all other multipath components in the channel.

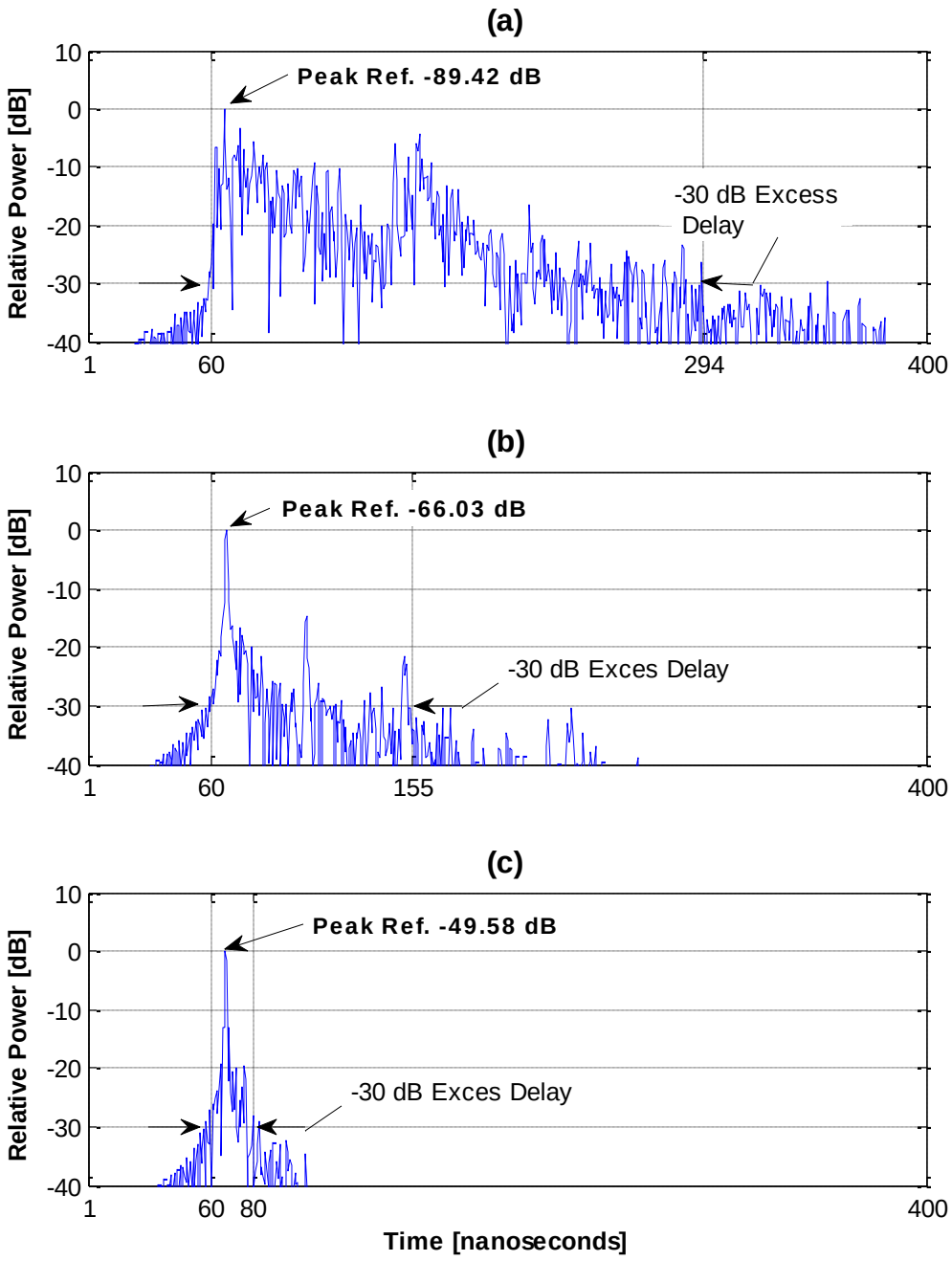

Fig. 5.9 Measured channel PDP obtained in NLOS corridors:

a) No-DO is presented in the corridors intersection,

b) Cylindrical DO,

c) Flat surface DO.

Table 5.6 The mean excess delay (τ_{mean}), exess delay (τ_{max}) and RMS delay spread (σ_τ) obtained at -30dB/-40dB threshold levels.

Measurement scenario:	**No-DO**	**Cylindrical DO**	**Flat DO**
$\boldsymbol{\tau_{mean}}$ **[ns]**	113.8/109.42	77.6/75.56	71.03/69.07
$\boldsymbol{\tau_{max}}$ **[ns]**	234/390	95/196.7	20/63
$\boldsymbol{\sigma_\tau}$ **[ns]**	52.3/46.98	15.6 /19.14	2.17/3.11

Several distribution models have been used to model the statistical RMS delay spread including lognormal, Nakagami, and Weibull. First, the CDF of each distribution is obtained after estimating the maximum likelihood of the distribution parameters. Then the Kolmogorov-Smirnov test was used to identify the distribution which best represented the experimental results. The analysis showed that Nakagami distribution yields the best-fit of RMS as shown in Fig. 5.10.

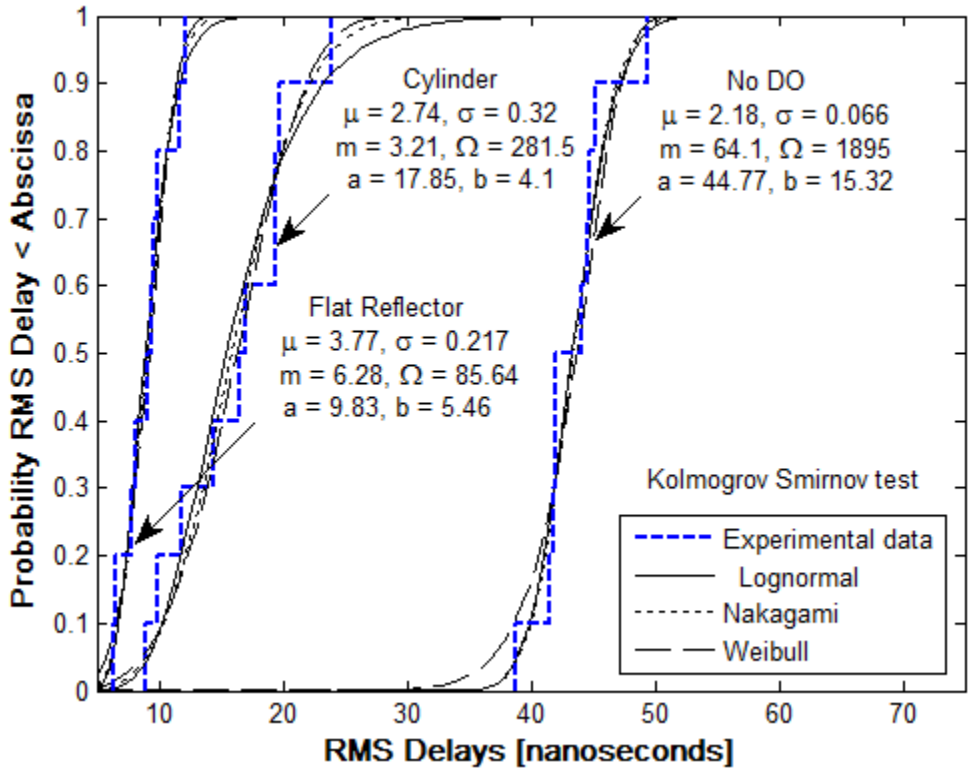

Fig. 5.10 Experimental and simulated CDF of RMS delay spreads in corridors scenarios.

5.3 Conference Room Measurement Campaign

In this section, a conference room environment is investigated. The conference room measurement site data base and description are provided in chapter 5. This measurement campaign was performed under LOS propagation scenario, where both vertically polarized antennas were kept at a height of 1.7 m. The choice of the antenna is influenced by the nature of the conference room environment, and the objective for carrying such measurements. The key factor to increase mm-waves link data rate is to reduce the time dispersive characteristics of the channel, i.e., to reduce the multipath propagation effects. Besides, directivity is certainly required to gain sufficient link budget for the support of the envisioned high data rate. This might be achieved by employing highly directional antennas at both remote ends of the channel. On the other hand, the measurements carried in a conference room using highly directional antennas at both ends might be undesirable, since the influence of the multipath effects that we want to characterize becomes masked due to the spatial filtering effect of the directional antenna gain function. Therefore, in a rectangular room, a fixed base station and a mobile should be considered. The base station uses a directional antenna that can be pointed towards the mobile to improve reception. The mobile terminal should incorporate an omnidirectional antenna to allow the user to move freely around the coverage area.

To investigate the effect of the antenna directivity on the path loss propagation and on the time dispersion parameters inside the considered conference room, two kinds of antennas, directional and omnidirectional, are used. The omnidirectional antenna has been specifically considered to provide a vertically polarized 360^{o} field in the azimuth. Therefore, two measurement scenarios are investigated:

I) omnidirectional antennas are employed at both remote ends of the channel (Omni-Omni).

II) a directional antenna is employed at the transmitting side, while an omnidirectional antenna is used at the receiving side (Direct-Omni).

As proceeded in NLOS corridors, the experimental data obtained from the empty conference room campaign are processed and analyzed in terms of the channel transfer function and the time domain impulse response. Such results provide essential information about the channel propagation characteristics needed for extremely broadband systems operating at 60 GHz.

The receiver was kept stationary while the transmitter was displaced with an increment of 0.5 m along the line joining both the transmitting and receiving antennas as illustrated in Fig. 5.11. Hence, the propagation characteristics were recorded at each position of the transmitter.

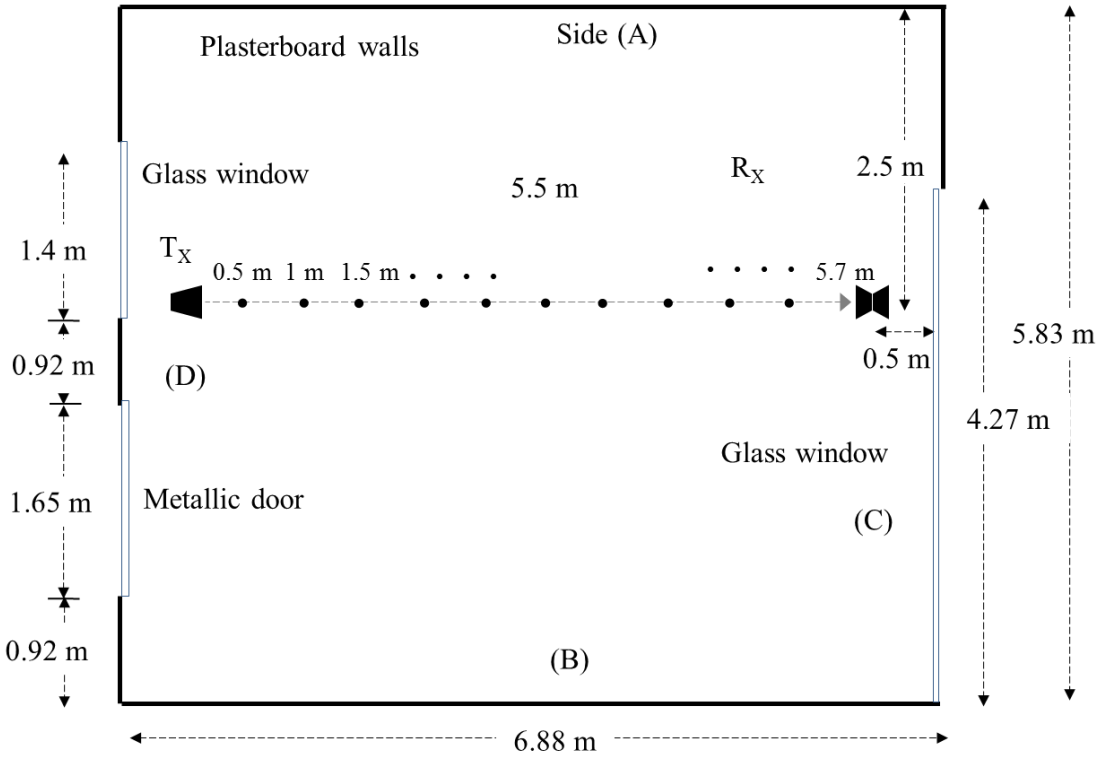

Fig. 5.11 Top view description of the considered conference room environment.

The transmitter output power (as measured at the input to the antenna) was set at -6.44 dBm. The relatively low transmitter power was necessary in order to maintain the linear operation of the transmitter power amplifier, as well as avoid saturating the receiver low noise amplifier at short link distances. The typical plots of measured channel frequency responses obtained at 5.7 m of antennas separation distance are shown in Fig. 5.12(a) and (b) for the considered Omni-Omni and Direct-Omni scenarios, respectively. As expected, employing a directional horn transmitting antenna has provided a better result in terms of multipath fading. In the 60 GHz channel, the use of highly directional antennas ensure the spatial filtering of one or several rays to maximize the received signal power and hence, to provide a desirable flatter frequency response.

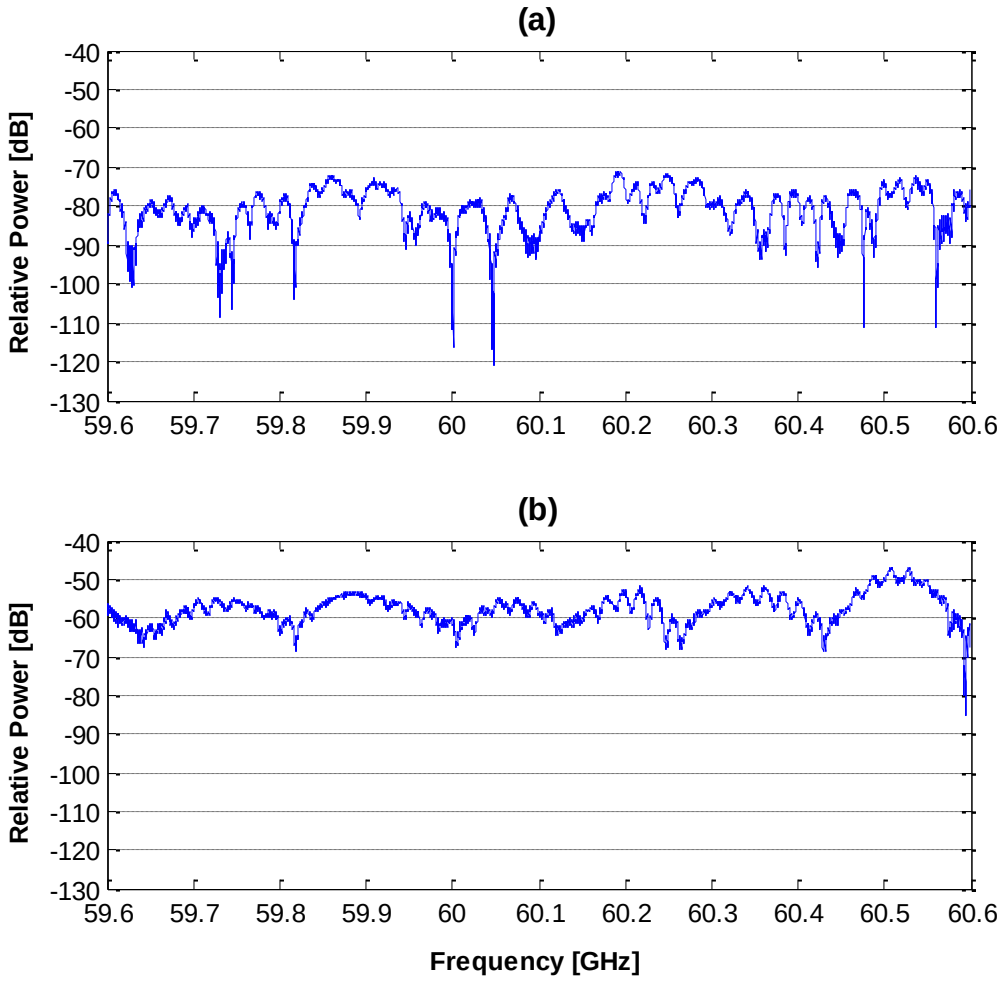

Fig. 5.12 Measured frequency response inside an empty conference room in the 60 GHz band:
a) Tx: omnidirectional, Rx: omnidirectional (Omni-Omni),
b) Tx: directional, Rx: omnidirectional (Direct-Omni).

5.3.1 CDFs of the Experimental Data

The cumulative distribution functions (CDFs) of the fading amplitudes for both configurations are depicted in Fig. 5.13. In the Direct-Omni configuration the experimental channel transfer function fits Rice distribution with K = 6.83 dB. The statistical distribution parameters are displayed in Table 5.7. The deployment of the directional antenna at the

transmitting side strengthens the received signal compared with the Omni-Omni configuration. This is clear evidence that a high directivity is required for 60 GHz communications. In the Omni-Omni configuration, the channel behaves as a Rayleigh (or Nakagami with m=1) where a great amount of fading selectivity is observed.

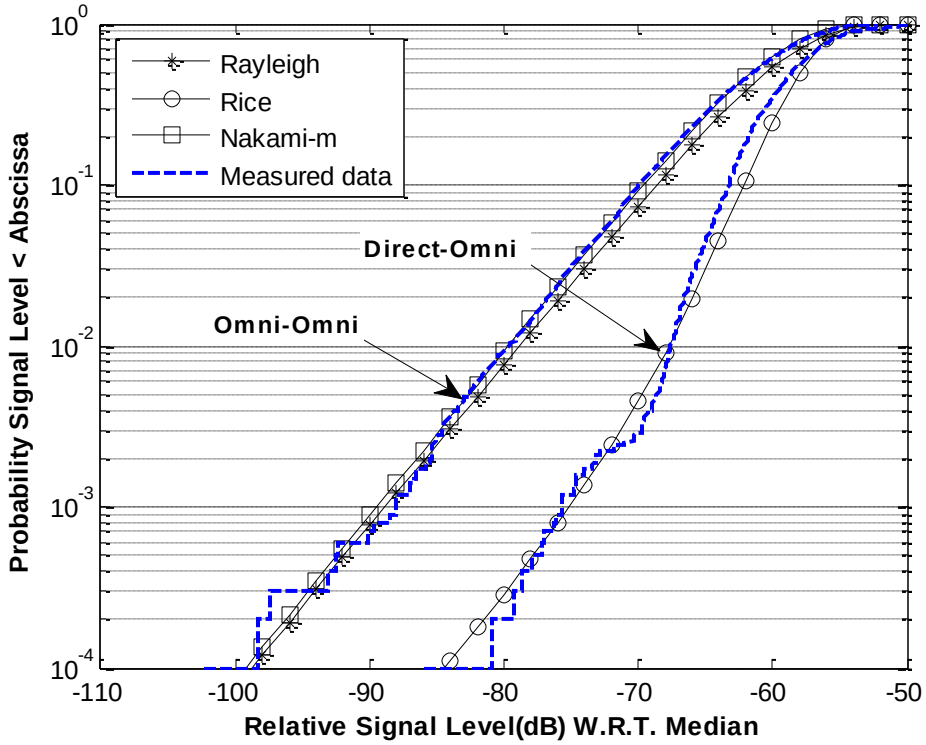

Fig. 5.13 Fitting the CDF of the experimental data obtained in the conference room.

Table 5.7 Experimental data statistical distribution parameters

Measurement scenario:	**Omni-Omni**	**Direct-Omni**
CDF	(Rayleigh)	Rice K = 6.83 dB
	Nakagami m = 1.017	Nakagami m = 1.9

5.3.2 The Path Loss

Fig 5.14 shows the measured path loss values versus distance for the conference room measurements under both configurations Omni-Omni and Direct-Omni. Fig. 5.8 shows the fitted lines of the considered scenarios. The path loss values obtained with respect to a reference distance (d_o) of 0.5 m from the transmitter.

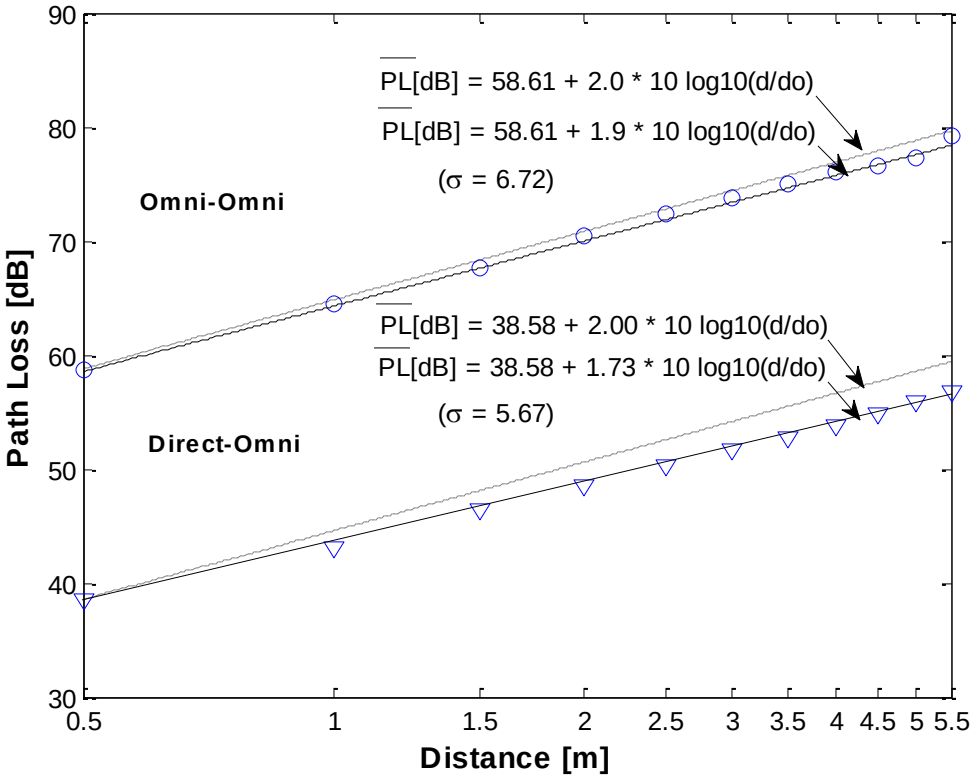

Fig. 5.14 Path loss models in a conference room environment at 60 GHz.

The resulting path loss exponents for the Omni-Omni and Direct-Omni cases are *n*=1.9 and *n*=1.73, respectively. The odd observation in the 60 GHz band is that the Omni-Omni scenario exhibits a larger *n*; this is due to the fact that, the use of omnidirectional antennas at both ends cause the environment to be more reflective. Furthermore, unlike lower frequencies, at 60 GHz the low gains of the used omnidirectional antennas cause the multipath components to get faded and absorbed by the walls before reaching the receiving antenna.

At 5.5 meters of antenna separation distance, frequency domain parameters such as path loss and coherence bandwidths associated with each configuration are displayed in Table 5.8. Direct-Omni configuration provides a better performance in term of path loss (23 dB), compared with the Omni-Omni case. This is mainly due to the 23.3 dBi additional gain provided by the directional horn antenna.

Table 5.8 PL and coherence bandwidth extracted at 5.5 m away from the transmitter

Measurement scenario:	**Omni-Omni**	**Direct-Omni**
PL [dB]	79.64	56.76
Coherence Bandwidth [MHz]	12.6	12.6

5.3.3 Channel Temporal Analysis

An estimate of the channel impulse response for each case is derived by performing the IDFT (Inverse Discrete Fourier Transform) to the measured CTFs. The PDPs obtained for both Omni-Omni and Direct-Omni radiation combinations are shown in Fig 5.15(a) and (b) respectively.

The strongest power peaks (-88.95 and -83.71 dBm) of both PDPs correspond to the first observable path resulted from the direct LOS joining both terminals as previously demonstrated in chapter 5. Both dominant rays are detected at 19 ns, followed by gradual smearing and exponential decrease in power multipath components with various propagation delays. In Fig. 5.15(b) it is clearly seen that some multipath rays become masked, this is mainly due to the spatial filtering effect of the directional antenna gain function. Table 5.9 provides the time dispersive parameters such as the mean excess delay (τ_{mean}), the excess delay (τ_{max}) and RMS delay (σ_τ) obtained at -30dB/-40dB levels. Channel delays are obtained when the receiver is 5.7 m away from the base station antenna.

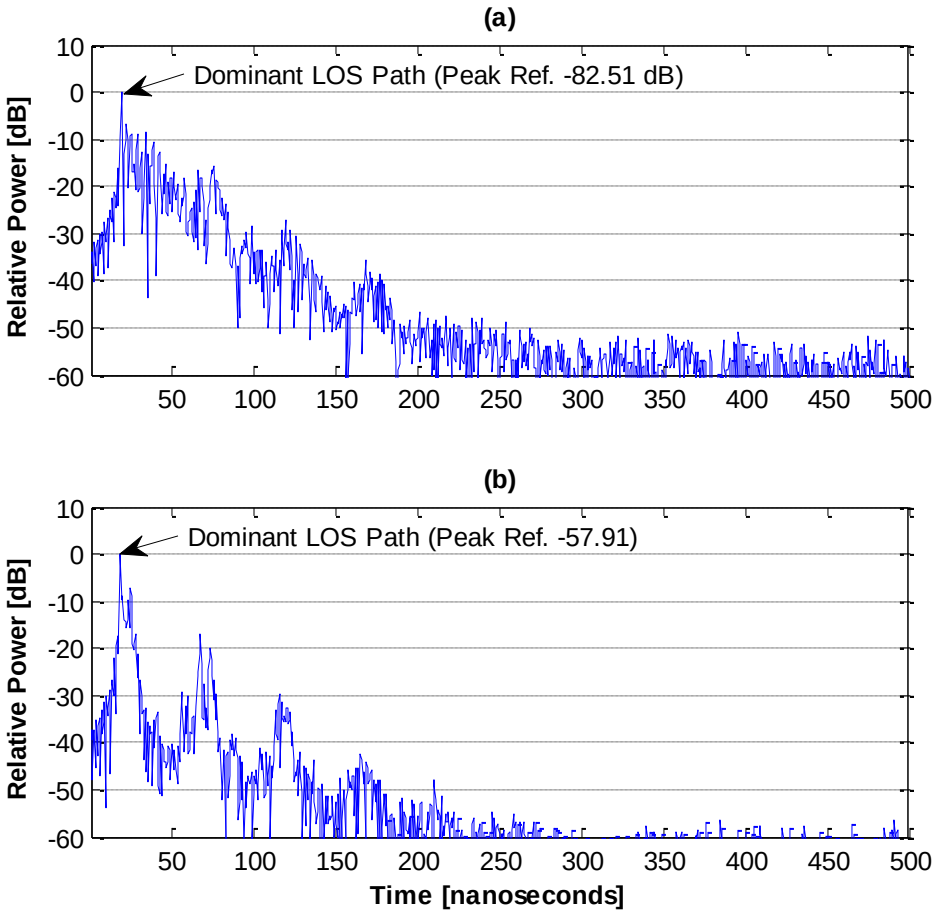

Fig. 5.15 Measured channel PDPs obtained in the conference room:
a) Tx: omnidirectional, Rx: omnidirectional (Omni-Omni),
b) Tx: directional, Rx: omnidirectional (Direct-Omni).

Table 5.9 Mean excess delay (τ_{mean}), exess delay (τ_{max}) and RMS delay spread (σ_τ) in nanoseconds obtained at -30dB/-40 dB threshold levels.

Measurement scenario	**Omni-Omni**		**Direct-Omni**	
Threshold	**-30 dB**	**-40 dB**	**-30 dB**	**-40 dB**
$\boldsymbol{\tau_{mean}}$ [ns]	32.2	33.13	24.1	25.34
$\boldsymbol{\tau_{max}}$ [ns]	122	179	63	123
$\boldsymbol{\sigma_\tau}$ [ns]	16	16.9	8.94	11.72

Based on the Kolmogorov-Smirnov test the analysis showed that the best-fit of RMS delay in Omni-Omni scenario can be the Nakagami distribution however in a Direct-Omni scenario Weibull appears to be the best fitting distribution. This is apparent in Fig. 5.16 and Fig. 5.17, which show the experimental and simulated CDFs in both Omni-Omni and Direct-Omni radiation combinations respectively.

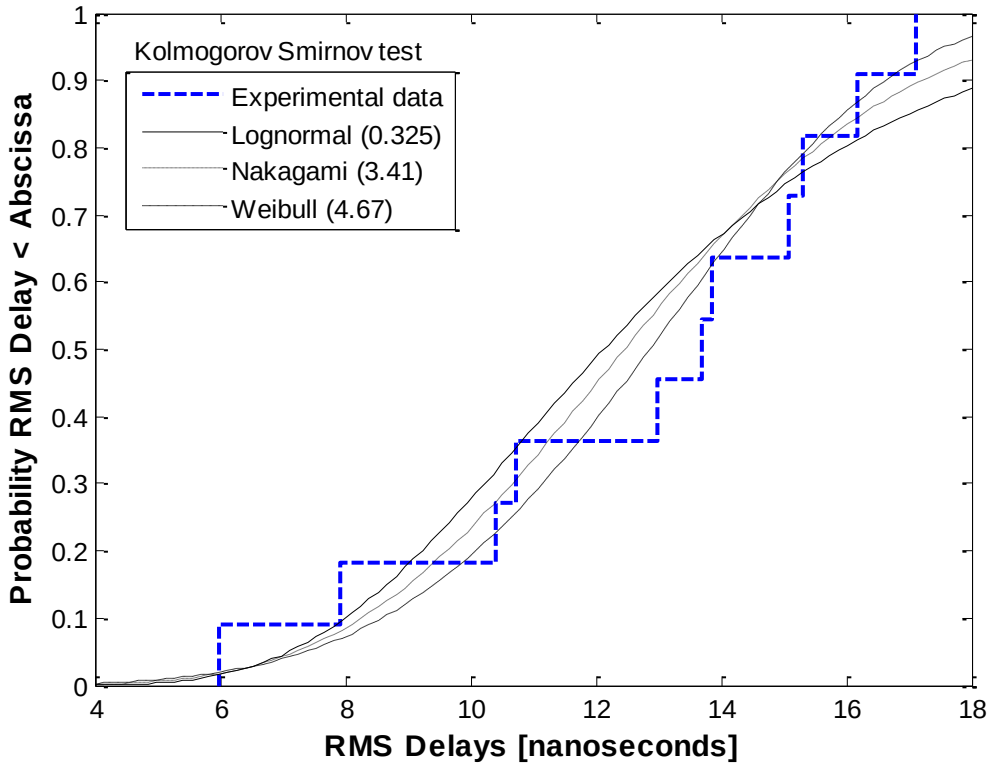

Fig. 5.16 Experimental and simulated CDF of RMS delay spreads in Omni-Omni scenario.

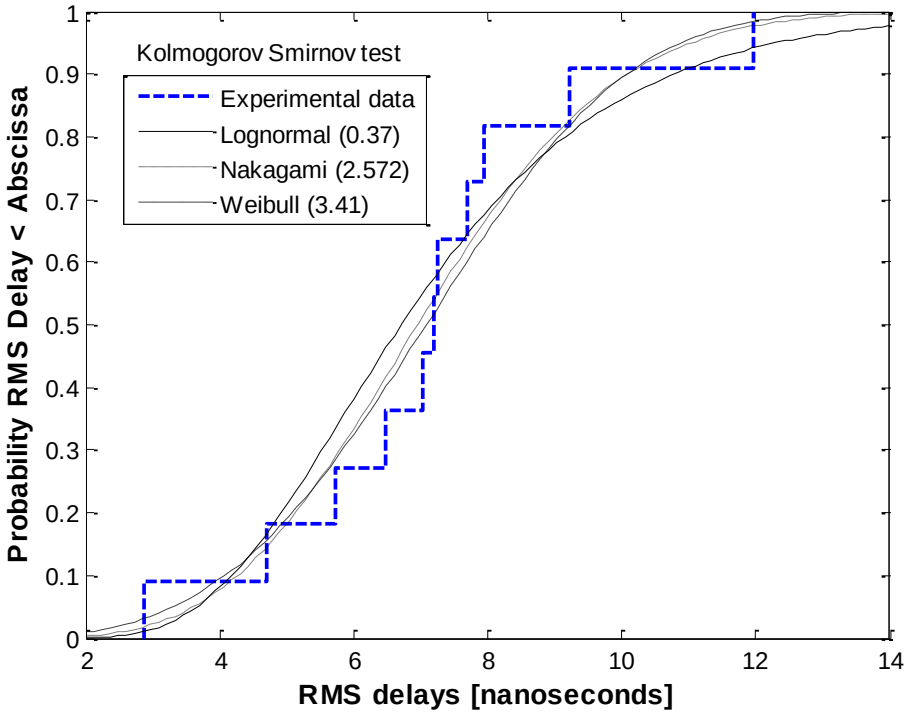

Fig. 5.17 Experimental and simulated CDF of RMS delay spreads in Direct-Omni scenario.

5.4 FDM Transmission in NLOS Corridors

5.4.1 Performance and Analysis

Based on measured channel excess delays presented in Fig. 5.18 and the standards values presented in Table A.1 and Table A.2 (Appendix A), it is clearly seen that:

- In the case of No-DO scenario, a channel excess delay of more than 234 ns has been recorded; hence, a TCP of 234 ns renders to be unacceptable under the 60 GHz OFDM standard specifications. However, the integration of DO in the channel offers shorter CPs durations that are compatible with specifications of the aforementioned standards.
- A cylindrical DO yields an excess delay of 95 ns, hence making systems that use a cyclic prefix of 119 ns and longer to perform properly at a distance of 20m.
- The deployment of a flat surface DO completely changed the propagation characteristics of the channel to become comparable to LOS transmission. The very short cyclic prefix of 22 ns that might be zero-padded and extended as desired makes systems that use CP of about 25 ns duration (IEEE 802.15.3c, IST-MAGNET and Wireless HD) or longer work properly.

This implies that mm-waves radio coverage might be extended to distances that even exceeding the 20 m range.

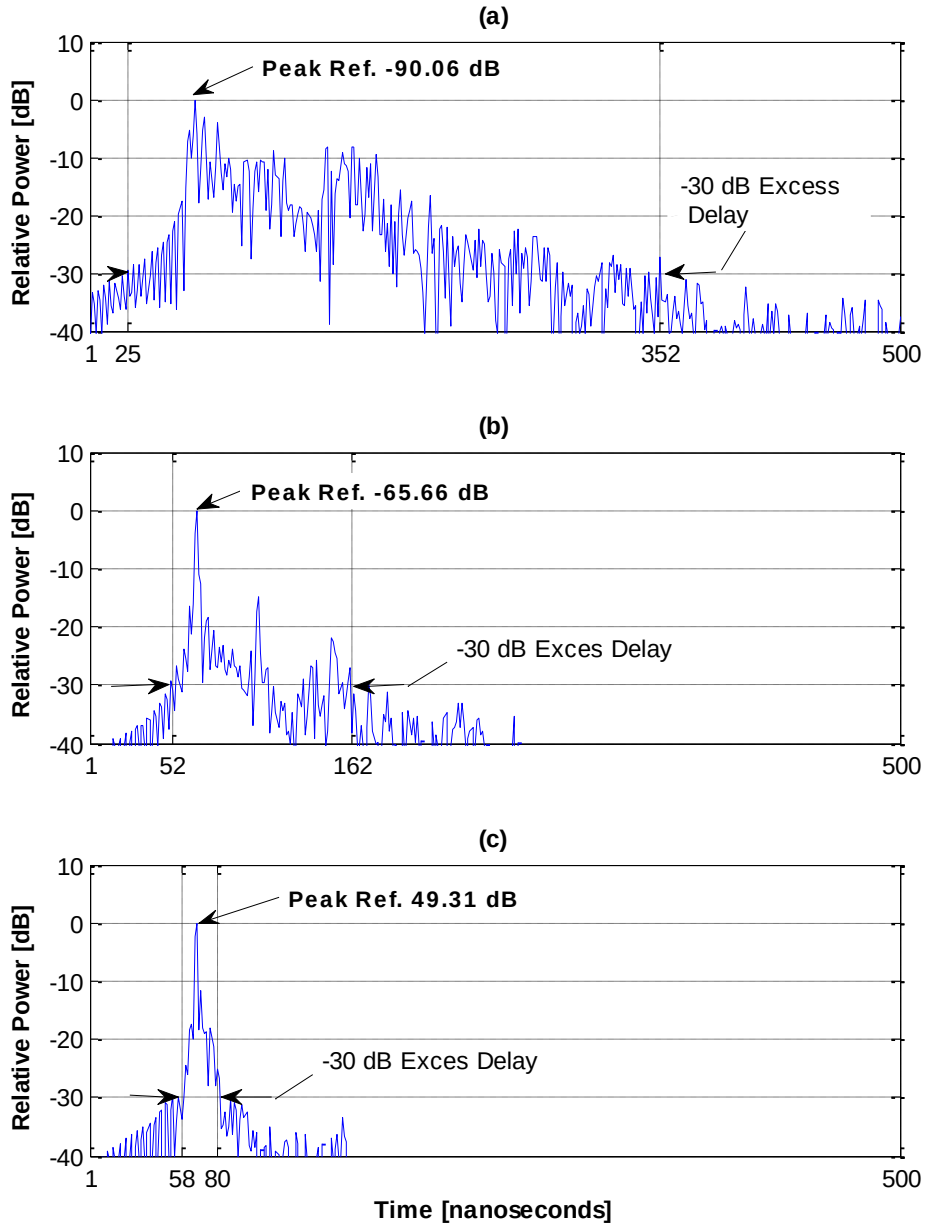

Fig. 5.18 Measured channel PDP obtained in NLOS corridors (540 MHz bandwidth),

a) No-DO is presented in the corridors intersection,

b) Cylindrical DO,

c) Flat surface DO.

5.4.1.1 Bit Error Rate (BER) Performance

The OFDM transmission scheme used to generate the various OFDM results is illustrated in Fig. A.2 (page 135). AT the receiver, the OFDM received signal is expressed as:

$$r(t) = s(t) \otimes h(t) + n(t) \tag{5.10}$$

where $s(t)$ is the time domain transmitted signal, $h(t)$ is the measured channel impulse response of the channel, $n(t)$ is the channel noise assumed to be additive white Gaussian noise (AWGN) and "⊗"denotes the convolution operator.

To get insight into the effectiveness of the proposed models and validate some related analytical results, further extensive signal processing and computer simulation have been conducted. OFDM parameter sets are based on operating modes given in Table A.2, namely IST-MAGNET and EASY-A where 736 and 192 data subcarriers are used respectively. The transmission performance of each scenario is examined in term of bit error rate (BER) using quadrature phase shift keying (QPSK) digital modulation, where one tap least square (LS) channel equalization has been considered. The various BER against bit energy to noise (E_b/N_o) curves are sketched as shown in Fig. 5.19. The BER curve of No-DO scenario is not presented, due to its very long excess delay that exceeds the OFDM timing specifications of all standards presented in Table A.1 and Table A.2. However the presence of a DO in the channel (wheither a cylinder or a flat DO) has allowed the investigation of OFDM transmission performance using CPs of 119 ns and 178 ns in accordance to EASY-A and IST-MAGNET parameters, respectively. It can be concluded from Fig. 5.19 that better results are achieved by using a flat shaped DO scenario where an error floor near 10^{-5} is recorded at E_b/N_o of 12.6 and 14.8 dB in both OFDM transmission modes. Obviously, increasing the number of data subcarrier leads to an increase in the BER; hence, a difference of 2.2 dB between both standards is recorded in the case of a flat DO. As compared with the flat DO case, the cylindrical DO shows penalties of about 5 dB and 8 dB when operating under EASY-Y and IST-MAGNET, respectively. As aforementioned, the main goal of this section is to show that the presence of DO in the channel will improve significantly the OFDM BER transmission performance, although further improvement of more than 7 dB might be achieved using an appropriate coding scheme. Fig. 5.20 shows BER performance of the best scenario (flat Surface DO) using various digital modulation schemes, such as QPSK, 16 QAM (Quadrature Amplitude Modulation) and 64-QAM.

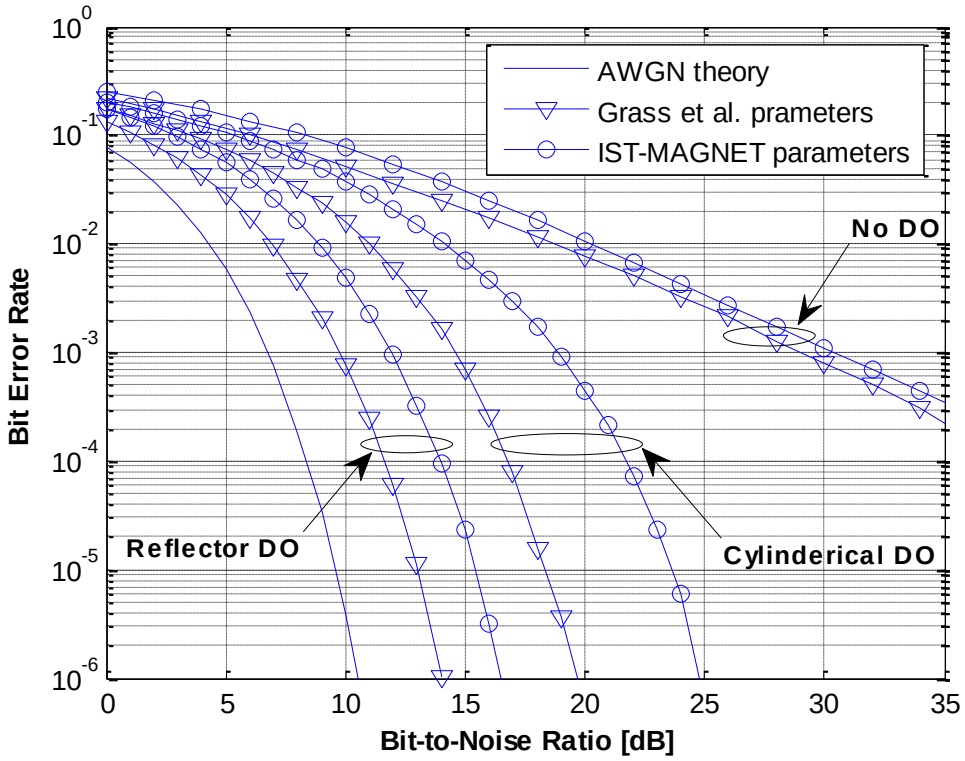

Fig. 5.19 Computed uncoded channel BER performance using QPSK digital modulation.

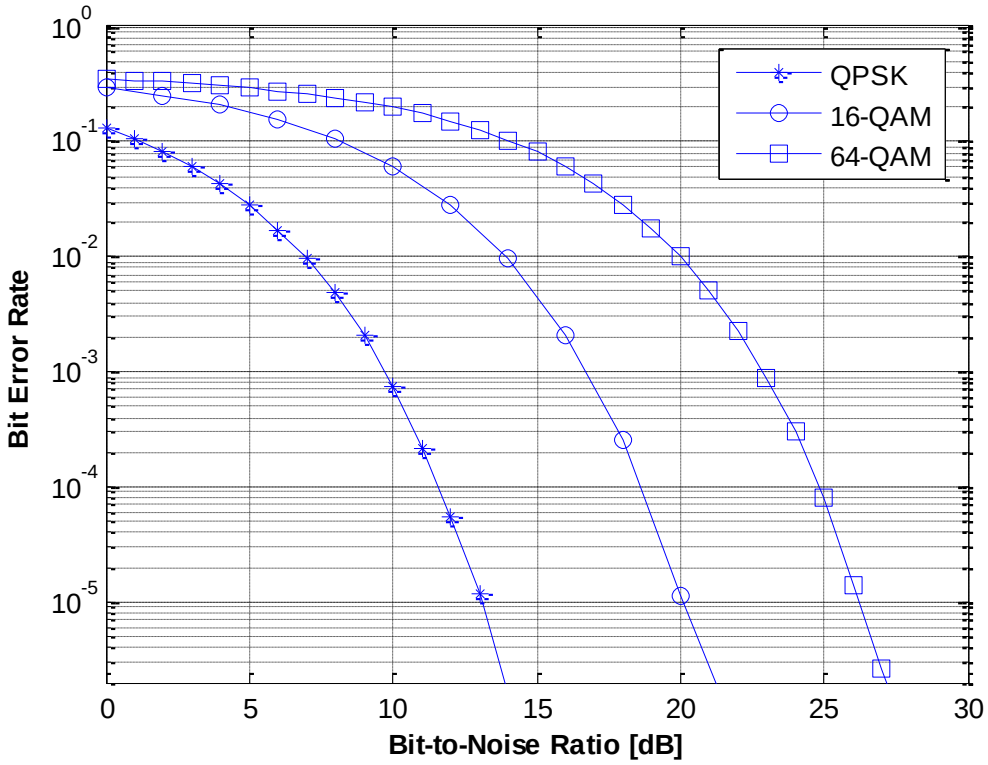

Fig. 5.20 Computed uncoded channel BER performance in the presence of flat surface DO

5.4.1.2 Constellation Diagrams

The performance of the demodulated OFDM signal is evaluated. Fig. 5.21 shows examples of constellation diagrams for the considered scenarios. This scatter spread gives a strong hint about the BER statistics as a function of SNR value where the signal degradation translates into more disperse constellation points. Using 16QAM digital modulation scheme and a SNR of 20 dB as recommended in [161], a scatter plot of the real and imaginary parts of the transmitted and received data constellations is shown in Fig 5.21.

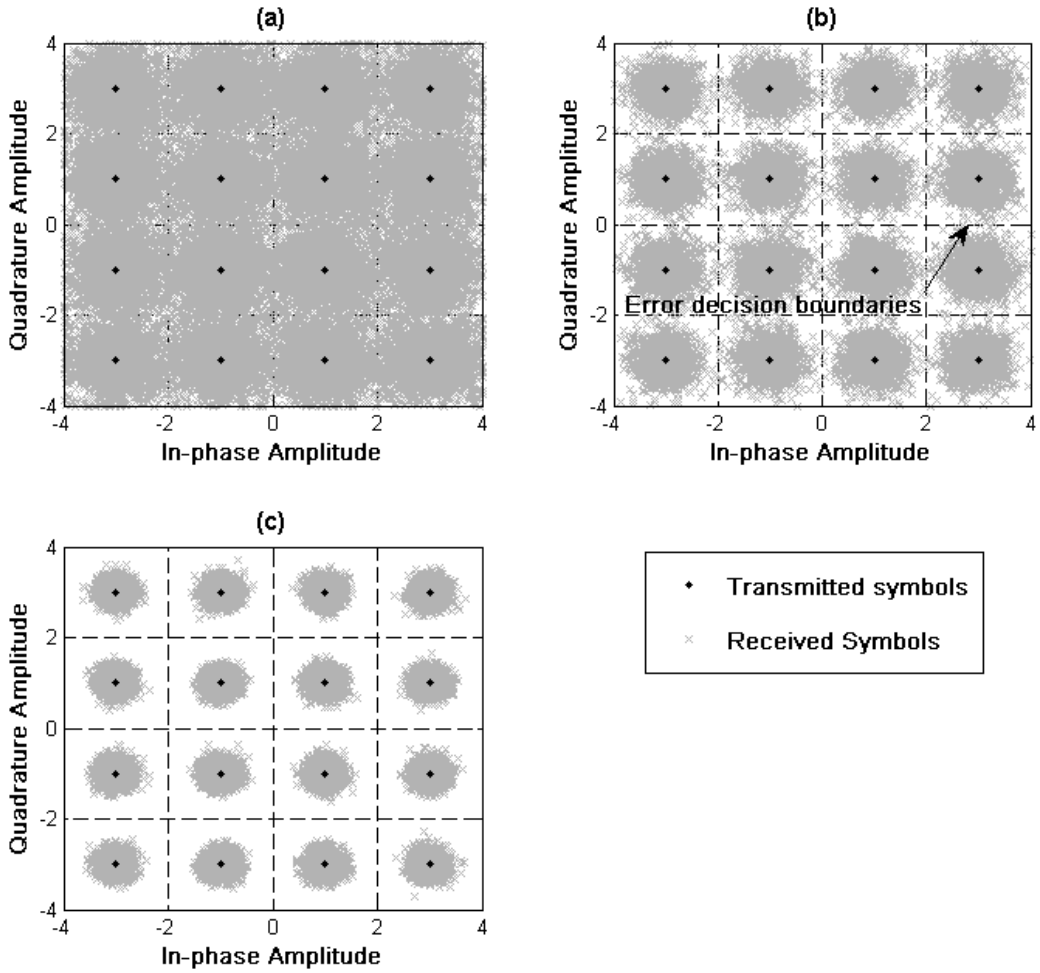

Fig. 5.21 Transmitted and received 16QAM data constellations at an SNR of 20 dB,

a) No-DO is present in the hallway,

b) Vertical circular cylinder,

c) Flat surface DO.

It is clear that, in the case of No-DO, the received data scatter spread far away from transmitted constellation points, and hence the transmitted data interfere among each other, and the data recovery appears to be very complex. In the case of cylindrical shape DO, a robust modulation with a powerful forward error correction (FEC) scheme and interleaving must be used in order to provide a good quality of communications. In contrast, the flat DO provides a clean constellation which indicates a successful demodulation processing. Hence, this model validates the methodology of combining both DO and OFDM techniques for longer communication range in NLOS UWB channels.

5.4.1.3 Power Spectral Density of the Received OFDM Signal

Based on measured data, the 16-QAM signal spectrums are recovered. According to the EASY-A standard, 5 direct current (DC) subcarriers are reserved as null subcarriers to simplify digital-to-analog and analog-to-digital conversions, they appear at the central frequency of the spectrum in Fig 5.22. The DC subcarriers if used for transmission, they might be heavily distorted by the DC offsets of the ADCs (analog to digital converters) and DACs, by carrier feed through, and so forth, they should thus be avoided for data [152]. Fig. 5.22 shows plots of the power spectral density of the OFDM 540 MHz signal bandwidth which is created using 256 bins FFT, 192 subcarriers are activated for data transmission. It is clear that, in the absence of DO the spectrum suffers a large amount of deep fades; these types of channels are frequency selective, carriers at these specific frequencies do not allow data information to pass through, hence, a complex coding and efficient interleaving signal processing must be performed to recover a fraction from the transmitted data information. However, in the presence of the flat DO, the power amplitudes of all frequency tones fall within 3 dB (half-power) below the resonant frequency. Hence, the OFDM spectrum appears uniform across the entire subcarriers transmission band except the DC one and the fading is considered to be flat within transmission band. It is clearly visible in the plot of Fig. 5.22 that its spectrum suffers from out-of-band radiation which decreases rather slowly. These sidelobes are caused by the spectrums of the individual carriers following a sinc function.

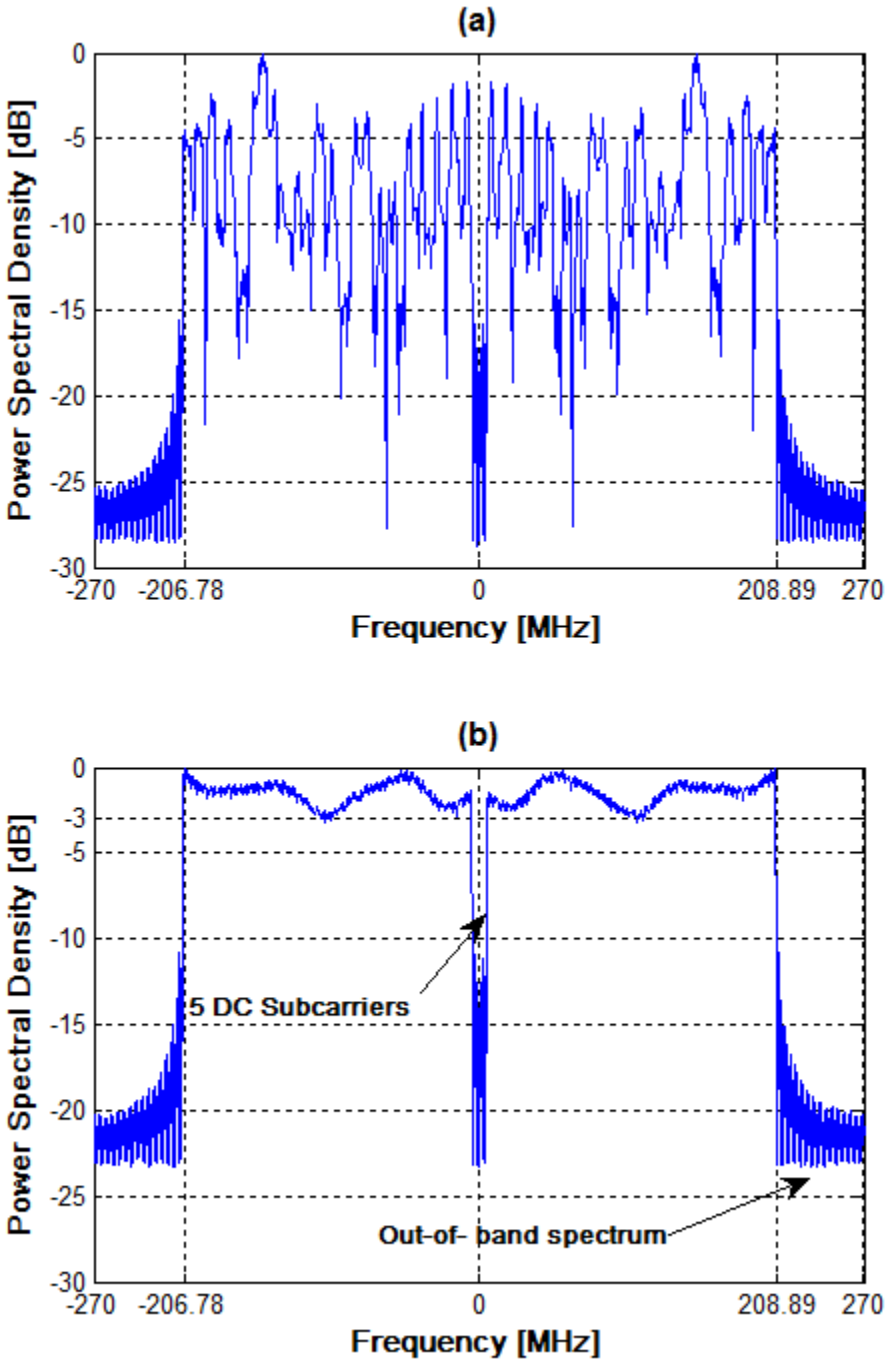

Fig. 5.22 Recovered OFDM power spectrum,

a) No-DO is present in the hallway,

b) Flat surface DO.

One of the simplest solutions offered to counter the effects of out of band interference is the sidelobe suppression by windowing of the OFDM transmit signal in the time domain [162, 163]. Several conventional windows might be used including Hanning window as shown in Fig. 5.23. Also note that, windowing the entire OFDM symbol using raised cosine [162] makes the spectrum decrease faster and results in a significant reduction in the out of band radiation.

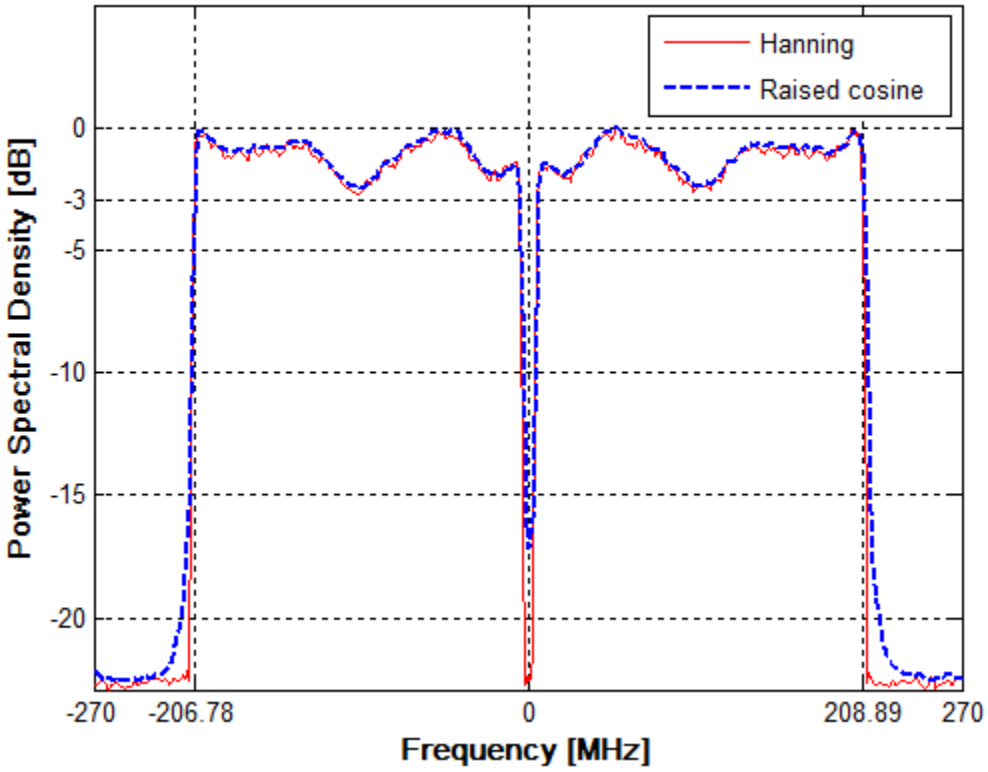

Fig. 5.23 Out-of-band radiations of the recovered OFDM power spectrum are countered using Hanning and Raised-cosine windows.

5.5 Discussion

The severe path loss of 60 GHz link limits its transmission rate and coverage up to a range not exceeding the 10 meters [64], [164], [129], hence, high directivity is required to overcome this great path loss. Recently, the advance of the highly directional beam-forming technology of more than 18 dB of gains has made it possible to overcome the large propagation loss for the distances of several tens of meters [165, 166]. This provides about 30 dB baseband SNR for LOS transmission at both the transmitter and the receiver [30]. Besides, in typical indoor channel

environments without beam steering or directional antennas, ISI can spread a single symbol over tens or hundreds of symbol periods.

In NLOS case, 60 GHz links suffers greater path losses in the absence of specular reflection, and lack of diffraction around lossy obstacles such as corridors corners [36, 37]. Hence, under NLOS, the use of mm-waves over long distances is a very challenging task. Laying data transmission in wireless communications have re-emerged as important research topics over the past half-decade to extend the signal coverage, especially over shadowed remote places where line-of-sight (LOS) does not prevail. Most published channel modeling studies in the 60 GHz are still evaluating the heuristic diffraction coefficients around corners for relaying the signal while denying surrounding DOs and considering them as noise sources. However, some specific surfaces, shapes and positions of DO might enhance significantly the NLOS communications.

Based on results obtained from different indoor 60 GHz measurement campaigns, the PL exponent, n, ranges from 0.4 to 2.1 and from 1.97 to 5.4 for LOS and NLOS scenarios respectively [12]. In the case of a flat surface reflector DO, our measurements shows that path loss exponent is 1.9, this value is comparable to LOS typical corridor environment, where *n* varies from 0.87 to 2.29 [12]. Moreover, the recorded value is in good agreement to the values obtained by 60 GHz measurements performed under LOS conditions in corridor environment [108, 167, 168]. Also, Peter Smulders in his work [108] has grouped results from various 60 GHz indoor measurement campaigns including offices and corridors. Then he has averaged the values for these groups. As a result, the averaged values ($\bar{n}$) obtained are 1.92 and 1.6 in case of LOS corridors and office environments, respectively. The corridors averaged exponent is very comparable to the 1.9 value obtained from our NLOS corridors measurement campaign in the presence of flat surface DO. Also in the case of offices environment, our LOS conference room measurement campaign (will be detailed later) shows a path loss exponent of 1.7 which is comparable to the value (n=1.6) stated above.

Table 5.10 shows the path loss exponents obtained from various corridors measurement campaigns and compared to that obtained in our campaign in the presence of a flat surface DO.

Table 5.10 Path loss exponent, *n*, reported in the literature.

scenario	*n*	References
LOS	2.0	[167]
LOS	1.87	[168]
LOS	1.92	[108]
NLOS in the presence of flat reflector DO	1.9	Our campaign

The average RMS delay spreads obtained from various corridors measurement campaigns are compared to that obtained from our measurement campaign in the presence of a flat surface DO as shown in Table 5.11. Basically, the RMS delay spread decreases as the directivity of the employed antennas increase, note however, that such reduction in RMS delay spread is achievable when the antenna patterns are aligned to the most significant AoA and AoD, respectively. This can be explained by the spatial filtering introduced by the directive antennas which can remove the undesired paths by focusing on the direction of the strongest dominant multipath component.

Table 5.11 Mean RMS delay spread (σ_τ) in different indoor corridors environments

Corridors size	σ_τ	**Antenna**	**Ref.**
NLOS (20×1.82×2.7) m^3 in the presence of Reflector DO	9.61	T_X, R_X, 23.4 dBi horn	Our campaign
LOS (30×3) m^2	10	T_X, R_X, 20 dBi horn	[169]
LOS (44.7×2.4×3.1) m^3	70	T_X, R_X, 9 dBi biconical horn	[170]
LOS (41×1.9×2.7) m^3	31.6	T_X, R_X, 10 dBi horn	[171]

Many research studies have presented experimental measurements deploying a directional antenna at one side of the channel and an omnidirectional antenna at the receiving side or vice versa [167, 172 – 175]. Such measurements provide essential information about spatial (angular) structure of the propagation channel. In office environments, the value of *n* for LOS ranges from

1.16 to 2.17 [12]. In a typical conference room and on the basis of Direct-Omni antenna configuration the path loss exponents obtained from various measurements are displayed in Table 5.12. Table 5.13 shows the average RMS delay spreads obtained from various conference room measurement campaigns in the 60 GHz band and compared to that obtained in this work.

Table 5.12 Path loss exponents for conference room environments reported in different publications.

PL exponent obtained under LOS in this work, n = 1.9 (Omni-Omni), and n = 1.73 (Direct-Omni)		
scenario	n	References
LOS	1.6	[108]
LOS	1.7	[167]
LOS	1.77	[172]
LOS	1.73	Our campaign

Table 5.13 Mean RMS delay spread (σ_τ) in different indoor LOS office environments.

Measurement scenario:	$\boldsymbol{\sigma_\tau}$ [nanoseconds]		Ref.
Conference, empty	17.75 T_X, biconical-Omni R_X, biconical-Omni	11.85 T_X, horn, HPBW 25^o R_X, biconical-Omni	[our campaign]
Conference, empty 90 m^2(area)×2.6 m (height)		11 T_X, horn (60^o) R_X, lens-horn (4.6^o)	[176]
Office, empty (8×10) m^2 LOS (center of the room)	17.5 T_X, Omni, HPBW 120^o R_X, Omni, HPBW 120^o		[177]
Office, empty (12.8×6.9×2.6) m^3		9 T_X, horn, R_X, Omni	[137]
Office, furnished (12.8×6.9×2.6) m^3		9 T_X, horn, R_X, Omni	[137]
Office, empty (20×20) m^2	16 T_X, Directional, HPBW 60^o R_X, Omni-dipole		[178]

Chapter 6

Conclusions and Future Work

As part of next generation communications systems, high-speed multi-gigabits wireless LANs can only be achieved in the mm-wave frequency band (30–300 GHz). Today, the unlicensed 60 GHz band is a unique choice for short-range applications as it meets the requirements for sufficient bandwidth, small terminal dimensions and sporadic usage for commercial applications. However, mm-waves propagation characteristics are very sensitive to the propagating environment. Due to the special importance of 60 GHz short-range communications, more measurement data and modeling studies are required to support a certain and precise description of the propagation characteristics in this band.

6.1 Summary of Findings

This thesis is intended to be as a contribution to the design and optimization of future WLAN systems that lie in the measurement and analysis of the propagation characteristics in the 60 GHz band. This work also provides adequate information on channels models that feature and quantify the constructive characteristics of radio waves resulted from the presence of deflecting objects (DOs) in the channel. The reported results focus on the evaluation of the importance of deflecting obstacles present in the NLOS environment under investigation. The thesis has clearly demonstrated that the presence of obstacles must not be treated as a destructive source for the propagating mm-waves signals. However, their presence strengthens the received signals and extends their coverage to shadowed areas where LOS is not present. NLOS results obtained in the presence of DO and in similar environment are compared with LOS that presented in the literature. The computed path loss exponent (n) and RMS delay spread (τ_{rms}) highlight good agreement with those published in the literature.

Another major objective of this reported work sought to model deterministically the propagation characteristics of indoor broadband communications in the 60 GHz band. Based on a ray-tracing technique, this thesis presents efficient and accurate deterministic models for the environments

under consideration. The presented novel models have the advantage of predicting the mm-waves propagation characteristics across an extremely wide bandwidth that exceeds the 500 MHz.

Two typical indoor environments are considered; a) NLOS T-shaped corridors intersection and b) LOS modern rectangular conference room.

- Based on mathematical channel modeling, the experimental data are successfully validated. An interesting agreement is achieved between both the simulated and the experimental data in both frequency and time domain. Therefore, the achieved RT models are very promising for indoor communications systems in the 60 GHz band where high levels of accuracy and certainty are achieved.

- Furthermore, using the presented RT models the experimental are also validated successfully when a cylinder is present in the intersection of the T-shaped corridors. This model is a very promising tool for engineering applications in order to analyse theoretically the diverse aspects of the 60 GHz broadband channel in the presence of a cylindrically shaped object in the NLOS channel.

- This thesis has clearly demonstrated that 60 GHz communications are very susceptible to the propagation environment. In NLOS corridors environment, signal transmission relies mainly on the unavoidable diffraction phenomenon from the intersection corners. In the case of LOS conference room and unlike lower frequency bands, rays undergo third order-reflections and higher are not important due to the high signal absorption by walls at 60 GHz.

- Note that, major considerations must be taken into account when modeling 60 GHz channels, they are summarized as follows:

    1. Ray-based channel modeling requires a great knowledge and highly accurate information about the environment including its geometry and the material electrical properties of the surrounding surfaces.

2. All multipath are important and relevant to allow obtaining precise as well as accurate predictions of signal propagation in the channel corresponding to the considered environment. Excluding one or few rays might change the result significantly.
3. Due to the extremely large bandwidth of the 60 GHz systems, frequency-dependent effects cannot be ignored; hence, the propagation characteristics and other effects should be considered frequency-variant and investigated more carefully over the whole covered frequency band of interest.
4. Finally, the UTD is a perfect tool to predict the diffracted field around corridors corners. Remely's heuristic diffraction coefficient for a lossy wedge is the most accurate to calculate the diffraction field in shadowed regions where LOS is not present. The obtained results have demonstrated clearly that, an accurate prediction of the diffracted field over a smooth cylinder is achieved using the UTD by smooth curved surface introduced by [122, 123].

- Under NLOS and imperfect mm-waves propagation conditions, targeting smooth surfaced DO in the channel, might be a practical solution to lay electromagnetic waves to the shadowed remote locations in WLANs where LOS is not present. Based on NLOS propagation measurements, results indicate that the presence of an DO in a Rayleigh channel changes its behavior to a Rician one.

- In the NLOS corridors case, the link suffers a great path loss; regardless the shape of the DO, its presence at the corridors intersection will mitigate significantly the path loss, and hence, will strengthen the received signal. Additional signal strength of 30 dB is achieved by targeting a flat surface DO.

- Moreover, a channel excess delay of 238 ns is recorded at a range of 20 m. However, the presence of DO at the intersection gives a rise to a strong specular contribution which in turn suppresses the undesired multipath and offers an extremely short excess delay of about 20 ns. The very short cyclic prefix of 20 ns that might be zero-padded and extended as desired makes systems that use CP of about 25 ns duration (IEEE 802.15.3c, IST-MAGNET and Wireless

HD) or longer work properly. This implies that mm-waves radio coverage might be extended to distances that even exceed the 20 m range.

6.2 Suggested Future Work

The results obtained in this measurement campaign are very promising and encouraging for mm-waves short-range communications. Today, extensive research and development activities in the 94, 120 and 194 GHz bands are being carried out for indoor communications. Due to the limitations of the presented measurement system, the propagation characteristics assessment is based on a frequency swept of 59.6 – 61.6 GHz. However, results might be scalable to higher frequency bands. Therefore, further improvements are required to remove the limitations of the measurement system and enable the measurement of indoor propagation characteristics at higher frequencies. It would be more interesting to extend the measurement campaign to a wider variety indoor environments such as medium and small size offices, laboratory and residential. The propagation characteristics and other effects should be considered in spatial domain and investigated more carefully.

Mm-wave links are inherently directional and rely on LOS transmission, and might be effectively blocked by the unavoidable movement of people and other obstacles leading to a catastrophic interruption of the systems. Thus, it is of interest to assess the impact of the presence of moving people presence on the characteristics of the propagation channel, and consequently, on the transceiver design of indoor 60 GHz systems. This implies realistic system performance predictions requiring accurate modeling of these effects under various conditions. Several empirical and statistical models for the human body shadowing are available in the literature. However, there is no deterministic published model introduced to simulate the effects of the human body on an indoor environment in the unlicensed 60 GHz band.

For a comprehensive approximation of the human body a special interest will be focused on its shape and material, while assuming it can be modeled by a circular cylinder. The UTD by a smooth curved surface introduced in this thesis may be used to predict the diffracted field from a cylindrical shaped body.

Appendix A

A Theoretical Review of Orthogonal Frequency Division Multiplexing (OFDM)

A.1 OFDM Features

- More resistant to frequency selectivity compared with single carrier transmission, where each subcarrier exhibits a flat fading [179 – 182].
- Efficient elimination of ISI and ICI through use of cyclic prefix.
- Sub-channels overlapping allow for an efficient use of the allocated spectrum; IFFT/FFT operation ensures that sub-carriers do not interfere with each other.
- Inherent resistance against other narrowband interference systems. Narrowband interference will affect at most a couple of sub-channels. Information from the affected sub-channels can be erased and recovered by using a forward error correction (FEC) codes.
- OFDM is more resistant to frequency selective fading than single carrier systems; only few sub-carriers are affected as depicted in Fig A.1. Due to frequency selectivity of the channel, the lost symbols might be recovered using adequate channel coding and interleaving. In contrast, in a single carrier signal the data will be lost sporadically.
- Less susceptible to sample timing offsets than single carrier systems [183, 184].
- Provides good protection against co-channel interference and impulsive parasitic noise.
- The computational complexity of OFDM tends to be much lower compared with conventional single-carrier equalizer-based systems [185].
- As the OFDM transmitter simplifies the channel effect, thus a simple receiver structure is enough for recovering transmitted data. If coherent modulation schemes are used, then very simple channel estimation is needed. In turn, no channel estimator is needed if differential modulation schemes are used [186].

- In a relatively slow time-varying channel, it is possible to significantly enhance the capacity by adapting the data rate per subcarrier according to the value of SNR for that particular subcarrier [187].
- The preservation procedures of orthogonal property in OFDM are much simpler compared to CDMA or TDMA techniques even in very severe multipath conditions [188].

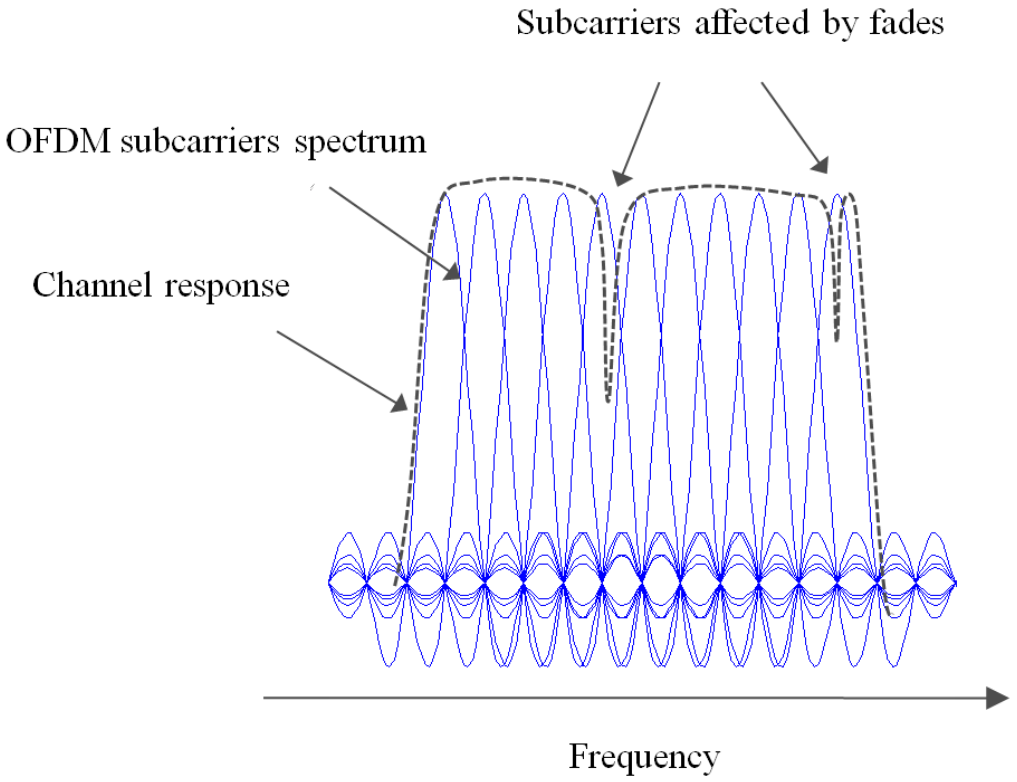

Fig A.1 OFDM spectrum in a frequency selective channel.

A.2 OFDM Block Diagram for Transmission and Reception

Putting together the various operations of the OFDM signal processing [189, 190], the block diagram of a typical OFDM transceiver may be sketched as shown in Fig. A.2.

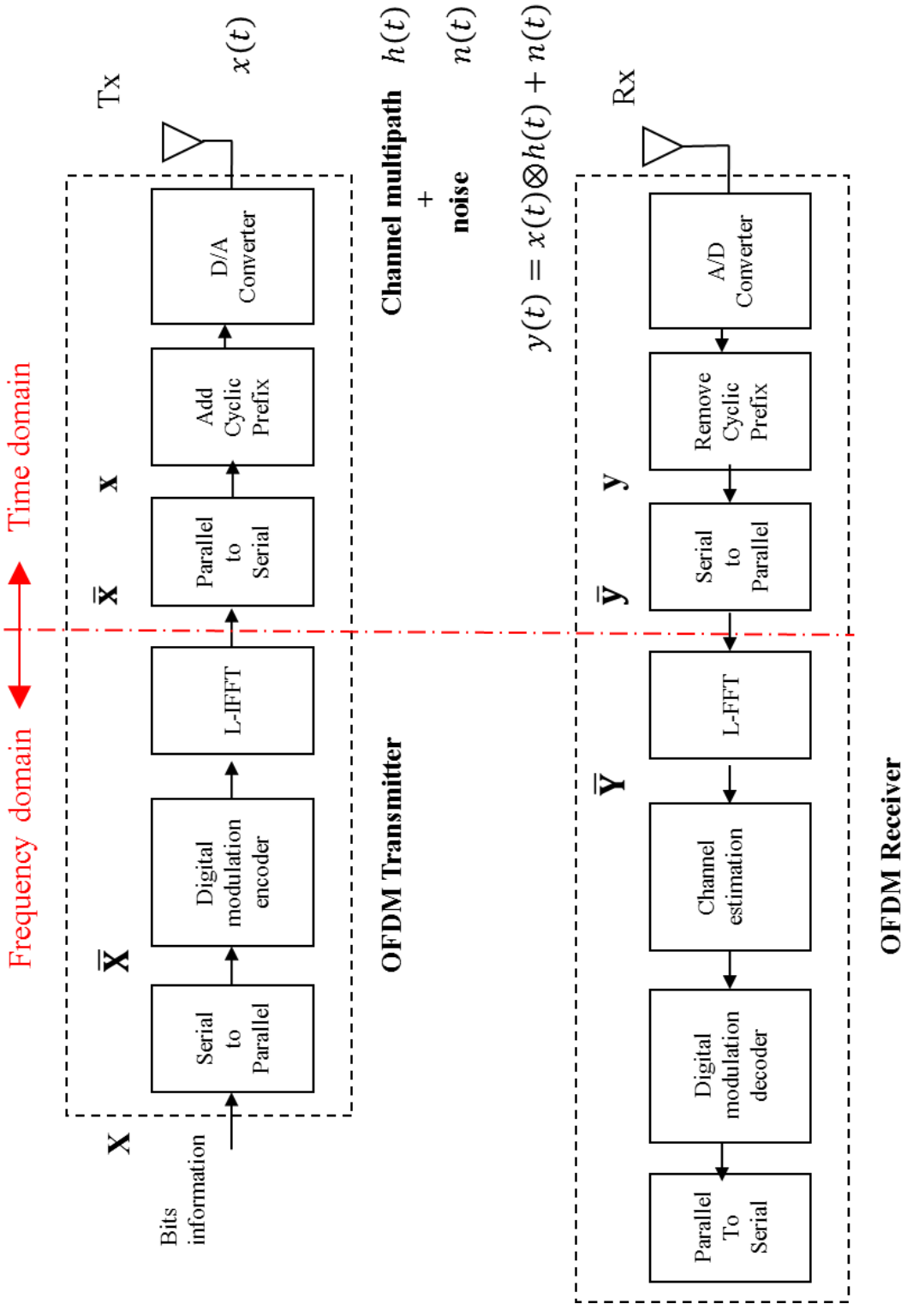

Fig. A.2 OFDM Transceiver Block Diagram.

The transmitter section converts digital data to be transmitted into a mapping of subcarrier amplitude and phase. It then transforms this spectral representation of the data into the time domain using an Inverse Discrete Fourier Transform (IDFT). The Inverse Fast Fourier Transform (IFFT) performs the same operations as an IDFT, except that it has much more computational efficiency, and so is used in all practical systems. Data to be transmitted is typically in the form of a serial data stream. In OFDM, each symbol typically transmits $\log_2(M)$ bits, and so a serial to parallel conversion stages is needed to convert the input serial bit stream to the data to be transmitted in each OFDM symbol. The data allocated to each symbol depends on the modulation scheme used and the number of subcarriers.

As a result the serial to parallel conversion stage involves filling the data payload for each subcarrier. At the receiver the reverse process takes place, with the data from the subcarriers being converted back to the original serial data stream. When an OFDM transmission occurs in a multipath radio environment, frequency selective fading can result in groups of subcarriers being heavily attenuated, which in turn can result in bit errors. These nulls in the frequency response of the channel can cause the information sent in neighbouring carriers to be destroyed, resulting in a clustering of the bit errors in each symbol.

A.3 Adding Cyclic Prefix (CP)

One of the most important problems for wireless communications is the multipath delay spread. OFDM deals with it very efficiently. The parallel transmission implies that the input data stream is divided in L subcarriers and the OFDM symbol duration is made LTs seconds, which also reduces the relative multipath delay spread, relative to the symbol time, by the same factor. Hence, the ISI is almost eliminated by introducing a guard time (also referred to as cyclic prefix CP) for each OFDM symbol as shown in Fig. A.3.

The guard time is chosen larger than the expected delay spread (τ) such that multipath components from one symbol cannot interfere with the next symbol [191, 192].

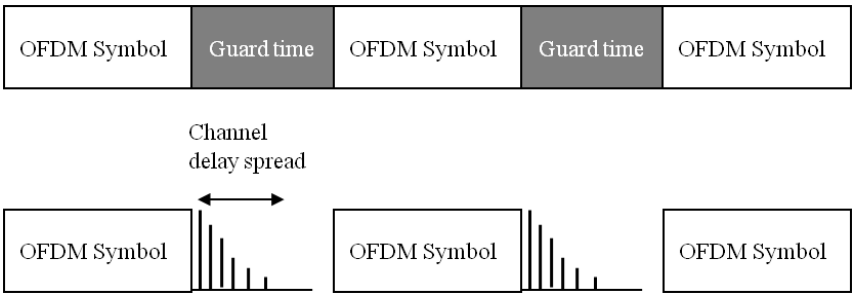

Fig. A.3 OFDM frame with cyclic extension.

A.4 Circular Convolution and DFT

When an input data stream x[n] is sent through a linear time-invariant finite impulse response (FIR) channel h[n], the output is the linear convolution of the input and the channel i.e.,

$$y[n] = x[n] * h[n] \tag{A.1}$$

However, circular convolution is defined as [186]

$$y[n] = x[n] \otimes h[n] = h[n] \otimes x[n] \triangleq \sum_{k=0}^{N-1} h[k]x[n-k]_N \tag{A.2}$$

and the circular function $x[n]_L = x[n \bmod L]$ is a periodic version of $x[n]$ with period L. It is easily verified that y[n] is also periodic with period L. from the definition of the DFT, circular convolution in time domain leads to multiplication in frequency domain. Hence, the circular convolution allows DFT where the DFT of the channel output is given by

$$DFT\{y[n]\} = DFT\{x[n] \otimes h[n]\} \tag{A.3}$$

in the frequency domain

$$Y[k] = H[k]X[k] \tag{A.4}$$

It is noticeable to mention that the duality between circular convolution and in the time domain and simple multiplication in the frequency domain is a property unique to the DFT. The N point DFT is defined as

$$DFT\{x[n]\} = X[k] \triangleq \frac{1}{\sqrt{N}} \sum_{n=0}^{N-1} x[n] \mathrm{e}^{-\mathrm{j}\frac{2\pi kn}{N}} \qquad (\mathrm{A}.5)$$

Where its inverse, the IDFT is defined as

$$IDFT\{X[k]\} = X[\mathrm{n}] \triangleq \frac{1}{\sqrt{N}} \sum_{n=0}^{N-1} \mathrm{X}[k] \mathrm{e}^{\mathrm{j}\frac{2\pi kn}{N}} \qquad (A.6)$$

If the channel and input are circularly convoluted then if h[n] is known at the receiver, the original data sequence x[n] can be recovered by taking the IDFT of $Y(k)/H(k)$. Unfortunately the channel output is not a circular convolution but a linear convolution. However, this circular convolution can be faked by adding a cyclic prefix (CP), onto the transmitted vector; this makes the signal to appear periodic with period N as shown in Fig. A.4. For a channel delay spread that has a duration of v+1 samples, adding a guard band of at least v samples between the OFDM symbols makes each OFDM symbol independent of those coming before and after it, and so only a single OFDM symbol of length L can be considered in time domain $x = [x_1 x_2 \dots \dots . . x_N]$.

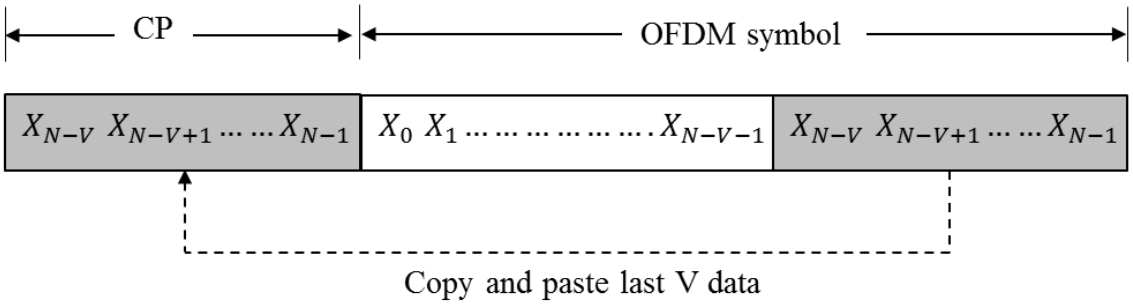

Fig. A.4 OFDM cyclic prefix of length V.

Applying a cyclic prefix of length v, the transmitted signal is

$$\mathrm{x_{cp}} = \underbrace{\mathrm{x_{N-v} x_{N-v+1} \dots \dots x_{N-1}}}_{\mathrm{CP}} \underbrace{\mathrm{x_0 x_1 \dots \dots x_{N-1}}}_{\mathrm{OFDM\ symbol}}$$

The output of the channel is then, $y_{cp} = h * x_{cp}$, where h is a length v+1. The output y_{cp}, contains$(\mathrm{N} + \mathrm{v}) + (\mathrm{v} + 1) - 1 = \mathrm{N} + 2\mathrm{v}$ samples.The first v samples of y_{cp} contain interference from the preceding OFDM symbol and so are discarded. The last v samples disperse into the subsequent OFDM symbol, so they are also discarded. This leaves exactly N samples for desired

output y, which is precisely what is required to recover the N data symbols of x. Here is an illustrative example processed using MATLAB platform, where the sequences x[n], h[n] and the added cyclic prefix with their convolutions are shown in Fig. A.5.

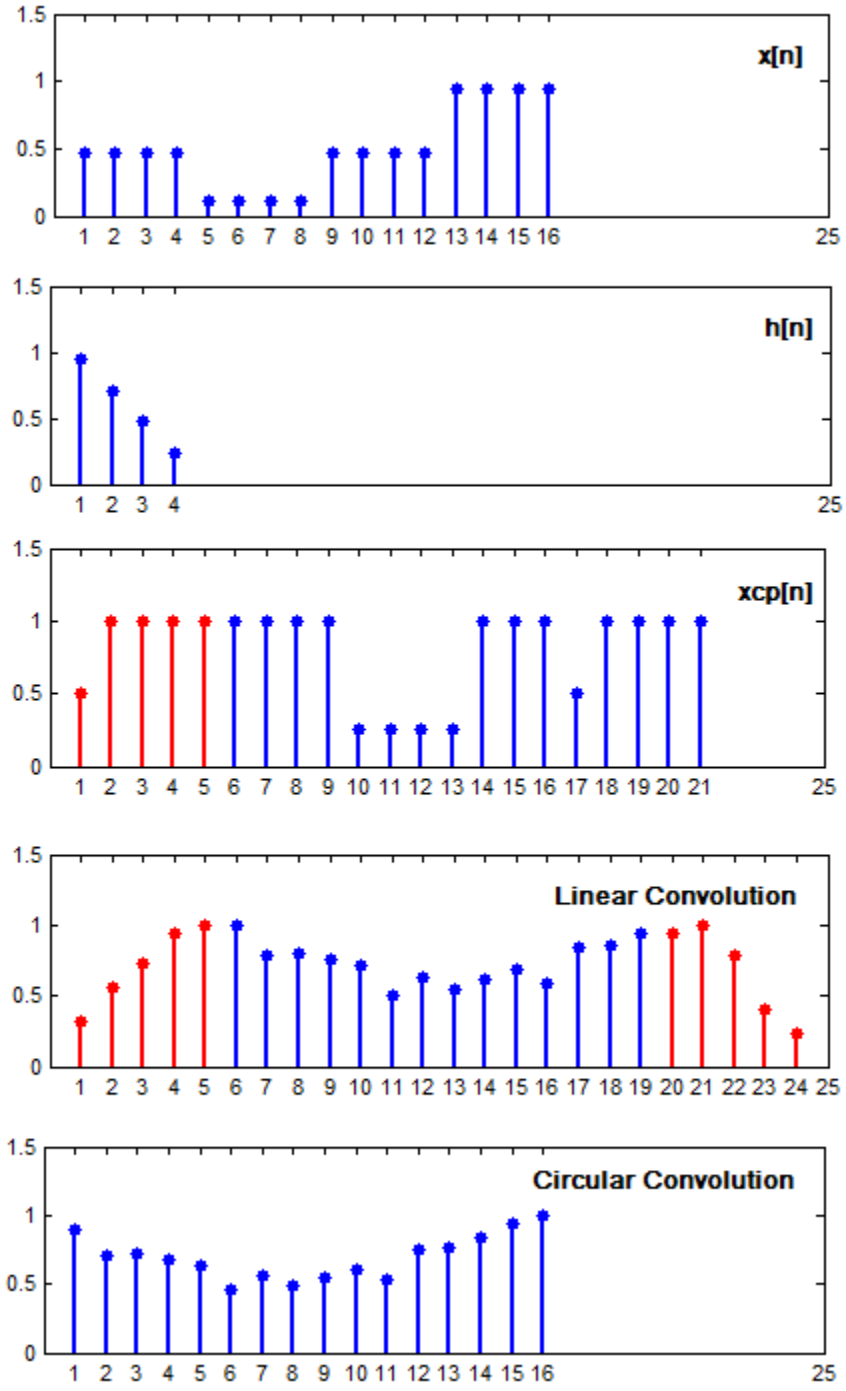

Fig. A.5 Circular *vs*. linear convolution with an added CP.

A.5 OFDM Channel Matrix Representation

From previous section, it can be clearly seen that the ICI term vanishes, and the channel will only induce a multiplicative distortion. AT the receiver, the OFDM received signal is expressed as [193]:

$$y(t) = x(t) * h(t) + n(t) \tag{A.7}$$

where, $x(t)$ is the time domain transmitted signal, $h(t)$ is the finite length channel impulse response of the channel, $n(t)$ is the channel noise assumed to be additive white Gaussian noise (AWGN) and "$*$"denotes the convolution operator.

To gain more insight into the system, it is sometimes desirable to express the system in matrix form [194– 196]. Hence, the received signal y can be expressed in matrix form as such

$$\boldsymbol{y} = \mathbf{H}\mathbf{x} + \mathbf{w} \tag{A.8}$$

where, boldface letters represent vector or matrix quantities. Hence, full channel matrix is equivalent to the following representation

$$\begin{bmatrix} y_{N-1} \\ y_{N-2} \\ \vdots \\ \vdots \\ \vdots \\ y_0 \end{bmatrix} = \begin{bmatrix} h_0 & h_1 & \dots & h_v & 0 & \cdots & 0 \\ 0 & h_0 & \dots & h_{v-1} & h_v & \ddots & 0 \\ \vdots & \vdots & \ddots & \ddots & \ddots & h_{v-1} & h_v \\ 0 & \dots & 0 & h_0 & \dots & \ddots & \vdots \\ \vdots & \vdots & \ddots & \ddots & \ddots & \ddots & \\ h_2 & h_3 & \cdots & h_{v-2} & \dots & h_0 & h_1 \\ h_1 & h_2 & \cdots & h_{v-1} & \dots & 0 & h_0 \end{bmatrix} \begin{bmatrix} x_{N-1} \\ x_{N-2} \\ \vdots \\ \vdots \\ x_0 \end{bmatrix} + \begin{bmatrix} w_{N-1} \\ w_{N-2} \\ \vdots \\ \vdots \\ w_0 \end{bmatrix} \tag{A.9}$$

This matrix form can be written more compactly as

$$\boldsymbol{y} = \widehat{\mathbf{H}}\mathbf{x} + \mathbf{w} \tag{A.10}$$

This equivalent model shows that the inserted cyclic prefix allows the channel to be modeled as a circulated convolution matrix $\widehat{\mathbf{H}}$over the *N* samples of interest. The matrix $\widehat{\mathbf{H}}$is *N* ×*N*, so it has an eigenvalue decomposition

$$\widehat{\mathbf{H}} = \mathbf{M}\boldsymbol{\Lambda}\mathbf{M}^H \tag{A.11}$$

Where, $\mathbf{\Lambda}$ is a diagonal matrix of eigenvalues of $\widehat{\mathbf{H}}$and $\mathbf{M}^H$is a unitary matrix whose rows contain the eigenvectors of $\widehat{\mathbf{H}}$.The notation $(\cdot)^H$is the conjugate transpose (Hermitian) operation. It is straightforward to show that the DFT operation on $x[n]$ can be represented by the matrix multiplication

$$\mathbf{X} = \mathbf{F}\mathbf{x} \tag{A.12}$$

where,$\mathbf{X} = [X(0)X(1), \ldots\ldots, X(N-1)]^T$, $\mathbf{x} = [x(0)x(1), \ldots\ldots, x(N-1)]^T$ and F is an $N\times N$ matrix given by

$$\mathbf{F} = \frac{1}{\sqrt{N}}\begin{bmatrix} 1 & 1 & 1 & \ldots & 1 \\ 1 & W_N & W_N^2 & \ldots & W_N^{N-1} \\ \vdots & \vdots & \ddots & \vdots & \vdots \\ 1 & W_N^{N-1} & W_N^{2(N-1)} & \ldots & W_N^{(N-1)^2} \end{bmatrix} \tag{A.13}$$

where, $W_N^k = e^{-j\frac{2\pi k}{N}}$ and, $\mathbf{F}^{-1} = \mathbf{F}^H$

Each low-rate data stream is associated with a subcarrier of the form $S_k(t) = e^{j2\pi f_k t}$ where, f_k is the frequency of the k^{th} subcarrier. Hence, Applying the DFT to the received OFDM vector in Equation (A.8)

$$\begin{aligned} \mathbf{Y} = \mathbf{F}\boldsymbol{y} &= \mathbf{F}(\mathbf{h}\mathbf{x} + \mathbf{w}) \\ &= \mathbf{F}\mathbf{h}\mathbf{x} + \mathbf{F}\mathbf{w} \end{aligned} \tag{A.14}$$

By letting$\mathbf{x} = \mathbf{F}^{\mathrm{H}}\mathbf{X}$**,** where$\mathbf{F}^{\mathrm{H}}$is the IDFT matrix. The received OFDM vector then becomes

$$\begin{aligned} \mathbf{Y} &= \mathbf{F}\mathbf{h}\mathbf{F}^{\mathrm{H}}\mathbf{x} + \mathbf{F}\mathbf{w} \\ &= \mathbf{H}\mathbf{X} + \mathbf{W} \end{aligned} \tag{A.15}$$

A.6 Channel estimation and equalization for coherent detection

To estimate the transmitted bits at the receiver, knowledge of the channel random phases and amplitude changes is required. The receiver applies either coherent detection or non-coherent detection to estimate the unknown phase and amplitude changes introduced by multipath fading channel [197]. The coherent detection requires an estimate of the channel. In contrast, non-coherent detection does not require estimation of the channel reference values, but uses differential modulation where the information is transmitted in difference of the two successive

symbols. The receiver uses two adjacent symbols in time or two adjacent subcarriers in frequency to compare one with another to acquire the transmitted symbol.

Channel estimation for coherent detection involves sparsely insertion of pilot symbols in a stream of data symbols and measuring the attenuation in these pilot symbols to find the channel impulse response. In general, channel estimation is simpler in the frequency domain than in the time domain.

A.6.1 LS Channel estimation

By employing a least square estimator (LSE) at the receiver, the demodulated OFDM signal in frequency-domain can be expressed in matrix notation as

$$\widehat{\mathbf{H}}_{\mathbf{LS}} = \underline{\mathbf{X}}^{-1}\overline{\mathbf{Y}} = \left[\frac{X_k}{Y_k}\right]^T \qquad k = 0,1,2,\ldots.N-1 \tag{A.16}$$

$$\underline{\mathbf{X}} = \mathrm{diag}\{\mathrm{X}(0), \mathrm{X}(1), \ldots \mathrm{X}(\mathrm{N}-1)\}$$

$$\overline{\mathbf{Y}} = \{\mathrm{Y}(0), \mathrm{Y}(1), \ldots \mathrm{Y}(\mathrm{N}-1)\}^{\mathrm{T}}$$

Hence the LS estimator used to minimize the parameter$\left(\overline{\mathbf{Y}} - \underline{\mathbf{X}}\overline{\mathbf{H}}\right)^{\mathbf{H}}\left(\overline{\mathbf{Y}} - \underline{\mathbf{X}}\overline{\mathbf{H}}\right)$, where $(\cdot)^{\mathbf{H}}$ denotes the conjugate transpose (Hermitian).

A.6.2 MMSE channel estimation

The optimal linear minimum squared error (LMMSE) estimator employs the second-order statistics of the channel to minimize the mean-square error. LMMSE estimator is complex and normally used as a base for designing new estimators. The channel auto-covariance matrix of H is given by [198]

$$\mathbf{R}_{\mathbf{HH}} = \mathrm{E}\{\overline{\mathbf{H}}\overline{\mathbf{H}}^{\mathbf{H}}\} = \mathrm{E}\left\{\left(\underline{\mathbf{F}}\bar{\mathbf{h}}\right)\left(\underline{\mathbf{F}}\,\mathbf{h}\right)^{\mathrm{H}}\right\} = \underline{\mathbf{F}}\mathbf{R}_{\mathbf{hh}}\underline{\mathbf{F}}^{\mathbf{H}} \tag{A.17}$$

Then, the LMMSE estimator is

$$\widehat{\mathbf{H}}_{\mathbf{MMSE}} = \underline{\mathbf{R}}_{\mathbf{HH}}\left(\underline{\mathbf{R}}_{\mathbf{HH}} + \boldsymbol{\sigma}_{\mathbf{N}}^{\mathbf{2}}\left(\underline{\mathbf{X}}\underline{\mathbf{X}}^{\mathbf{H}}\right)^{-1}\right)^{-1}\widehat{\mathbf{H}}_{\mathbf{LS}} \tag{A.18}$$

Where, $\boldsymbol{\sigma}_{\mathbf{N}}^{\mathbf{2}} = \mathbf{E}\{|\overline{\mathbf{N}}|^{\mathbf{2}}\}$, is the noise variance.

The MMSE estimator yields much better performance than LS estimators, especially under the low SNR scenarios. A major drawback of the MMSE estimator is its high computational complexity, especially if matrix inversions are needed each time the data changes.

A.7 Cyclic Prefix vs. Subcarrier Spacing in OFDM Systems

As noticed previously, the insertion of cyclic prefix in OFDM symbols converts the linear convolution channel to a circular one and therefore, keeps the OFDM sub-channels orthogonal in rich multipath channel [199, 200]. Generally, subcarrier spacing and cyclic prefixes (or guard interval) in OFDM systems are dedicated to strengthen the spectrum efficiency (SE) and hence reducing ISI to extend the system radio coverage. The channel cyclic prefix (TCP) is adjusted to the duration that exceeds the excess delay of the channel impulse response (τ_{max}). This allows a higher number of subcarriers (ΔFFT) to ensure efficient interleaving at the binary and subcarrier levels. Also note that, the subcarrier spacing must be less that the coherence bandwidth of the channel to ensure flat fading across the OFDM subcarriers. Depending on the propagation channel characteristics and targeted data rates, different values of T_{CP} may be used. High SE modes are performed with reduced guard interval sizes well adapted to higher data rates that implicitly induce smaller radio coverage. Hence, the various 60 GHz communications standards consider the parameter p which is defined as:

$$p = \frac{T_{FFT}}{T_{CP}} = \frac{1}{T_{CP}\ \Delta_{FFT}} \qquad (A.19)$$

Depending upon the OFDM standards specifications, the p-value is adjusted in a way that the subcarrier spacing is small enough to generate no selective OFDM sub-carriers and ensure high spectrum efficiency [201] as shown in Fig.A.6.

High values of the ratio p involve a high number of sub-carriers for a given cyclic prefix. A short cyclic prefix results in a wider subcarrier spacing which leads to RF phase noise degradation. Also small sub-carrier spacing involves degradations and frequency offsets in the RF stages [12, 13, 202].

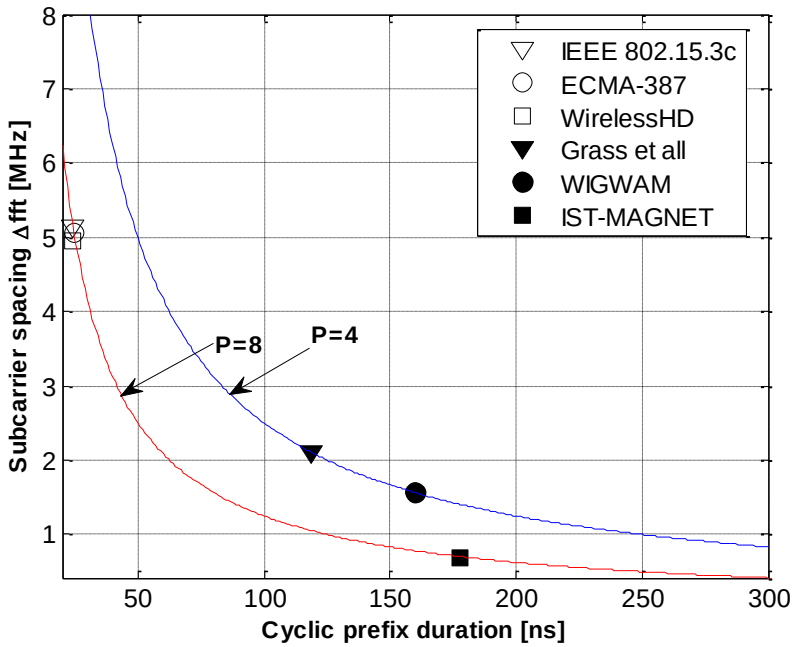

Fig. A.6 Cyclic prefix duration impact on the OFDM sub-carrier spacing.

Hence to increase throughput, a trade-off has to be defined between p and subcarrier-spacing compatible with RF oscillator phase noise and high spectrum efficiency (SE).

$$SE = m.R.\frac{P}{P+1} \qquad (A.20)$$

Where m is the encoded bit number per sub-carrier and R is the code rate of the forward error correction (FEC). As a compromise between tolerated delays spread in 60 GHz channels and immunity to the phase noise generated from the fabricated 60 GHz phase-locked loop (PLL), various OFDM baseband parameters have been introduced depending upon the operation standard as shown in Table A.1 and Table A.2.

A.8 OFDM Standards Specifications in the 60 GHz Band

Several technologies in the 60-GHz band capable of multi-Gbps capacity have been proposed in the last years. Wireless-HD (Jan. 2008), IEEE802.15.3c (Oct. 2009, and ECMA-387 (Dec. 2008) are among several emerging 60 GHz standards that use OFDM modulation in their baseband physical layers. These standards are targeted towards short-range wireless personal area networking (WPAN) such as high definition streamed multimedia and high-speed data transfers.

After the successful IEEE 802.11n 60 GHz free-licence band has attracted considerable attentions from the industries seeking for the next generation WLANs. This became possible with the advance of low-cost 60 GHz circuits that use complementary metal oxide semiconductor (CMOS) or silicon-germanium (SiGe) technology. Standards such as IEEE 802.11.ad and WiGig (July 2010) [203-25], are targeted towards the development and coverage extension of next-generation WLANs that operate at 60 GHz offer a throughput of 1 Gbps. The WiGig is also supported by the WiFi Company. Both standards have recently announced interoperability agreements [206] for 60 GHz technology in WLAN. In the WIGWAM [207] project, the OFDM physical layer implemented so far is capable of providing 1-Gbps with the channel bandwidth of 400 MHz for point to point applications [208, 209].

In order to meet such requirements imposed on 60 GHz WLANs, an OFDM baseband physical layer is newly designed by major technical contributors to the IEEE 802.15.3c [12, 210]. This OFDM PHY layer specifications and hardware have been demonstrated within the framework of EASY-A project and supported by the German Federal Ministry of Education and Science (BMBF) to target multi-gigabit WLANs. Then, was peer reviewed at the direction of the IEEE communications society.

In this channel plan, new OFDM physical layers and RF transceivers are designed to support two channel plans, wideband and narrowband plans. In order to promise good coexistence with legacy 60-GHz devices (e.g. IEEE802.15.3c), the wideband channel plan is kept to be the same as defined in the standard. Between 57 GHz to 66 GHz (9 GHz bandwidth), four independent channels are defined, centered on 58.32, 60.48, 62.64 and 64.80 GHz and each channel allows maximum channel bandwidth of 2160 MHz. The narrowband plan is particularly suited for WLANs where a maximum of 540 MHz channel bandwidth is allowed. As illustrated in Fig. A.7, one wideband channel can be divided into four independent narrowband channels. Over the 7 GHz bandwidth, it is possible to use 12 channels, which is comparable to the IEEE 802.11 a standards supporting 12 channels in the 5 GHz band. The OFDM timing parameters for both wideband (>2160 MHz) and narrowband (~500 MHz) models are summarized in Table A.1 and Table A.2 respectively.

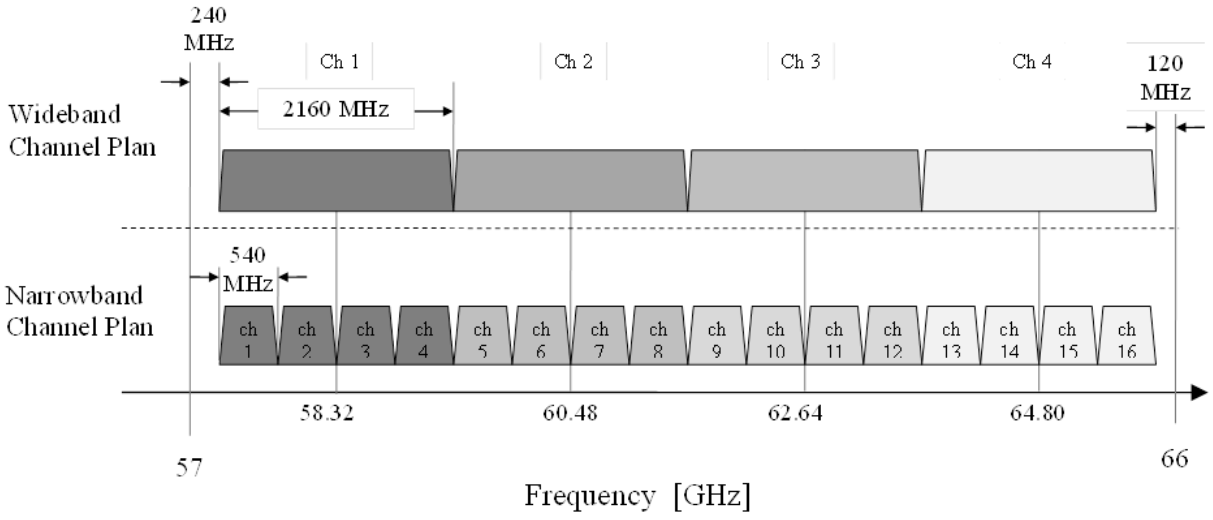

Fig. A.7 Wideband and narrowband channel plan provided in [Choi10 (EASY-A)].

Compared to the OFDM parameters previously developed, the OFDM physical layer presented is less susceptible to phase noise but more sensitive to channel delay spread [12, 210].

Parameter:	**Desciption:**
$\boldsymbol{fs}$	Reference sampling rate/Chip rate/operational bandwidth
$\boldsymbol{T_C}$	Sample/Chip duration
$\boldsymbol{Ncp}$	Cyclic prefix size/Guard interval
$\boldsymbol{Tcp}$	Cyclic prefix duration
$\boldsymbol{N_{FFT}}$	FFT size/Number of subcarriers
$\boldsymbol{T_{FFT}}$	FFT period
$\boldsymbol{\Delta_{FFT} = fs / N_{FFT}}$	Subcarrier frequency spacing
$\boldsymbol{N_{DSC}}$	Number of data subcarriers
$\boldsymbol{N_{PSC}}$	Number of pilot subcarriers
$\boldsymbol{N_{DC}}$	Number of DC subcarriers
$\boldsymbol{N_G}$	Number of guard/null subcarriers
$\boldsymbol{NB}$	Nominal used bandwidth
$\boldsymbol{N_{SYM}}$	OFDM Symbol size
$\boldsymbol{T_{SYM}}$	OFDM Symbol duration
$\mathbf{F_S = 1/ T_{SYM}}$	OFDM Symbol rate

Table A.1 Wideband OFDM physical layer parameters for various standards

	IEEE802.15.3c	**ECMA-387**	**WirelessHD**	**(EASY-A)**
fs	2640 MHz	2592 MHz	2538 MHz	2160 MHz
T_C	0.38 ns	0.3858 ns	0.94 ns	4.63 ns
Ncp	64	64	64	256
Tcp	24.24 ns	24.7 ns	25.22 ns	119 ns
P	8	8	8	4
N_{FFT}	512	512	512	1024
T_{FFT}	193.94 ns	197.53 ns	201.73 ns	474 ns
Δ_{FFT}	5.15625 MHz	5.0625 MHz	4.957 MHz	2.11 MHz
N_{DSC}	336	360	336	768
N_{PSC}	16	16	16	60
N_{DC}	3	3	3	5
N_G	141	133	157	--
NB	1815 MHz	1.9187 MHz	1760 MHz	1757
N_{SYM}	576	576	576	1280
T_{SYM}	218.18	222.23 ns	226.95 ns	593 ns
F_S	4.583 MHz	4.51 MHz	4.406 MHz	1.7 MHz

Table A.2 Narrowband OFDM physical layer parameters for WLANs standards

	IST-MAGNET	**Choi et all**	
		WIGWAM	**EASY-A**
fs	528 MHz	500 MHz	540 MHz
T_C	1.894 ns	2.5 ns	1.852 ns
Ncp	~94	64	64
Tcp	178 ns	160 ns	119 ns
P	8.15	4	4
N_{FFT}	768	256	256
T_{FFT}	1451 ns	640 ns	474 ns
Δ_{FFT}	0.689 MHz	1.5625 MHz	2.11 MHz
N_{DSC}	736	192	192
N_{PSC}	--	16	16
N_{DC}	--	3	5
N_G	--	5	--
NB		333 MHz	449 MHz
N_{SYM}	860	320	320
T_{SYM}	1628 ns	800 ns	593 ns
F_S	0.6143 MHz	4.583 MHz	1.7 MHz

Appendix B

Résumé de la thèse

Cette thèse présente des résultats expérimentaux et de modélisation du canal de propagation intra-immeuble pour les applications réseaux locaux sans fil (WLAN) dans la bande des ondes millimétriques. Basées sur la bande de fréquences autour de 60 GHz, c'est-à-dire, entre 59.6 et 60.6 GHz, les mesures de propagation sont effectuées dans deux milieux internes typiques: a) intersection de deux longs couloirs en forme de T sans-ligne-de-vue (NLOS), avec et sans la présence d'obstacles de déviation du lien de transmission (DO); b)salle de conférence rectangulaire moderne avec ligne-de-vue (LOS).

Sur la base de la technique Tracé de rayons (RT), des modèles déterministes ont été développés pour les milieux considérés. Mise à part la salle de conférence, tous résultats expérimentaux sont obtenus en utilisant des antennes directives aux niveaux de l'émetteur et du récepteur, respectivement. En effet, pour la salle de conférence, une antenne omnidirectionnelle conique est utilisée au niveau du récepteur. Les fonctions de transfert du canal (CTFs) et les profils de retard de puissance (PDP) obtenus à partir de l'outil de simulation RT sont ensuite comparées avec les données expérimentales pour chacun des milieux considérés. Une concordance intéressante est obtenue entre les résultats de simulation et les résultats expérimentaux et ce dans les deux domaines, fréquentielle et temporelle. Ces résultats montrent que la bande des ondes millimétriques (ondes-mm) est très sensible à l'environnement de propagation par rapport aux bandes de basses fréquences. Par ailleurs, la caractérisation expérimentale du canal de propagation sur des scénarios où la ligne de vue est obstruée, fait partie aussi de cette thèse. En effet, les paramètres statistiques de tous les résultats expérimentaux du canal de propagation multitrajet sont analysés. Dans les couloirs NLOS, les résultats expérimentaux montrent que le lien de communication est assez faible, voire, absent. Cependant, la disposition d'un DO dans l'intersection améliore d'une manière significative les caractéristiques de propagation et fournit une meilleure qualité de signal avec une couverture plus large assez comparable aux liens LOS. Les mesures présentées et les modèles empiriques peuvent aider à l'élaboration d'un système de communications sans fil futuriste opérant sur les ondes-mm dans les applications sans fil à débit élevé.

CHAPITRE 1

Les communications sans fil dans la bande des ondes mm

Dans la dernière décennie, une expansion considérable des activités de recherche dans le domaine des télécommunications a eu lieu, pour satisfaire les demandes croissantes pour de nouveaux services, on parle de futurs systèmes 4G de communication sans fil à courte portée. Pour de tels systèmes, les applications multimédias et HDMI, en remplacement de câbles, une transmission de données fiable allant de plusieurs centaines de Mbps à quelques Gbps est à prévoir. Parmi ces applications la vidéo à haute définition (HD), téléchargement des fichiers de contenu riche à haute résolution à partir d'un kiosque sans fil, et les jeux vidéo sans fil offrant aux utilisateurs un contrôle sans encombre, etc… [1] - [4]. Dans la bande de 60 GHz sans licence, de vastes activités de recherche et de normalisation sont en cours pour offrir une couverture plus large et à faible sensibilité aux effets des trajets multiples pour des communications internes WLANs. D'après les règlements de la FCC, la puissance d'émission ne constitue pas un problème puisqu'une puissance d'émission maximale est de 27 dBm et une puissance isotrope rayonnée équivalente (EIRP) de 43 dBm sont approuvés dans la bande sans licence 57-64 GHz [11]- [13]. Toutefois, la bande de 60 GHz fait encore face à des difficultés techniques, en particulier, la couverture du signal. Avec les mêmes gains d'antennes et la puissance transmission permise, une perte en espace libre supplémentaire de 21,8 dB est envisagée sur cette bande en comparaison avec celle autour de 5 GHz [4]. Par conséquent, les liens 60 GHz sont intrinsèquement directionnels: la directivité est nécessaire pour surmonter l'affaiblissement de parcours plus élevé dans les petites longueurs d'onde [30]. Les liens 60 GHz NLOS subissent des affaiblissements de parcours supérieurs en l'absence de réflexions spéculaire, en raison des faibles niveaux de signaux diffractés par des obstacles tels que les coins présents dans les couloirs. Cet affaiblissement entrave les débits de données et limite la couverture à une distance ne dépassant pas les 10 mètres. Par conséquent, l'extension de la couverture du signal mm-ondes vers des endroits ombragés où la ligne de vue (LOS) n'est pas présente s'avère un tâche difficile.

Contexte des activités de recherche

Les différentes campagnes de mesure réalisées à 60 GHz affichent des résultats complètement disparates, même pour des environnements internes similaires [30], [36] - [41]. Les analyses statistiques des résultats disponibles ne trouvent pas de référence fiable reconnue par la communauté scientifique [30]. Pour des environnements de type couloir, très peu de

modèles basés sur la technique RT autour de 60GHz sont disponibles dans la littérature. Ils s'appuient principalement sur des mesures à bande étroite effectuées dans le domaine spatial évaluant la puissance du signal en fonction de la distance dans des endroits obstrués (NLOS) dans des couloirs en utilisant la théorie uniforme de la diffraction (UTD) [12], [13]. En utilisant la technique RT, le canal de propagation à 60 GHz est également modélisé dans un long couloir sous LOS, tel que présenté dans [14]. Pour les modèles RT à bande étroite, les effets dépendant de la fréquence sont ignorés, alors que les systèmes de communication 60 GHz sont susceptibles de fonctionner à des bandes passantes extrêmement larges supérieures à 500 MHz. En outre, ces modèles prennent en considération un nombre très limité de rayons multivoie pour les canaux LOS et NLOS [12]. La plupart des études publiées sur la modélisation de canal de propagation dans les 60 GHz peuvent être améliorées si on évalue les coefficients de diffraction heuristiques à partir de coins pour relayer le signal, tout en négligeant les DOs environnants en les considérant comme des sources de bruit. Toutefois, certains DOs, de forme et position spécifiques, pourraient être utilisées afin d'améliorer considérablement les communications NLOS. À notre connaissance, il n'existe pas de modèles déterministes basés sur RT qui prennent en considération l'effet des DOs présents dans le canal de propagation NLOS dans la bande 60 GHz.

Les contributions de la thèse

Cette thèse présente des modèles statistiques ainsi que des modèles déterministes RT dans la bande de 60 GHz pour révéler les caractéristiques de propagation à large bande dans les deux milieux intra-immeubles typiques et selon divers scénarios:

I. Canal de propagation en NLOS dans une intersection de deux couloirs en forme de T:

a) aucun DO n'est présent à l'intersection,

b) un cylindre métallique est positionné à l'intersection,

c) une surface métallique plate réfléchissante est positionnée à l'intersection.

II. Canal de propagation en LOS dans une salle de conférence moderne rectangulaire :

a) deux antennes omnidirectionnelles sont utilisées à l'émetteur et au récepteur, respectivement (Omni-Omni),

b) une antenne directionnelle est utilisée à l'émetteur et une autre omnidirectionnelle au récepteur (Direct-Omni).

A) Mesures et caractérisation du canal de propagation aux ondes millimétriques

Basés sur des mesures du CTF (59.6 à 60.6 GHz), les paramètres statistiques de propagation multivoies les plus pertinents sont extraits. Ces paramètres nous permettent d'estimer la bande de cohérence du canal, les distributions statistiques d'évanouissement, le gradient des pertes, reliant l'affaiblissement de parcours (n) à l'ombrage, les caractéristiques de dispersion temporelle de trajets multivoies tels que le délai moyen (τ_{mean}), le délai maximal (τ_{max}) et la valeur efficace de l'étalement du retard (σ_τ). Les résultats obtenus sont ensuite comparés aux campagnes de mesures réalisées à 60 GHz et publiées dans la littérature.

B) Modélisation déterministe du canal de propagation aux ondes millimétriques

Des modèles déterministes sont développés et validés expérimentalement en se basant sur les CTF (59.6 à 60.6 GHz) obtenues dans les environnements considérés plus haut. Cette thèse a montré que les canaux à 60 GHz sont très sensibles à la fréquence, tous les trajets multivoies sont importants et pertinents pour permettre l'obtention des prédictions précises des paramètres de propagation du canal correspondant à l'environnement considéré. La négligeance d'un ou de plusieurs rayons pourrait modifier considérablement les résultats. Dans les corridors en T, scénario NLOS, les CTFs déterministes sont modélisées à l'aide de réflexions multivoies du premier ordre, deuxième et jusqu'au quatrième ordre de réflexions multiples sur le sol, le plafond et les murs, qui sont ensuite superposés à une diffraction simple au niveau des coins. Basé sur la théorie géométrique uniforme de la diffraction (UTD), le champ diffracté dans la région ombragée des corridors est calculé avec une grande précision en utilisant le coefficient heuristique de diffraction de Remely pour un coin avec perte (coin diélectrique). Dans la salle de conférence, scenario en LOS, seules les réflexions multiples allant jusqu'au troisième ordre sont considérées, causées par les surfaces de la salle, les réflexions d'ordre 4 et supérieures sont négligeables. Les modèles développés sont validés par des données expérimentales avec un grand succès, que ça soit pour les scenarios NLOS (corridors en T) ou pour ceux en LOS (salle de conférence vide). L'accord obtenu, entre les simulations et les mesures est remarquable, pour tous les modèles développés dans le cas d'un canal NLOS en présence de différents DOs. Les modèles RT obtenus sont très prometteurs pour des systèmes de communication intra-immeubles dans la bande des 60 GHz.

CHAPITRE 2

Communications sans fil à 60 GHz : Caractéristiques et Défis de Conception

La bande des onde-mm apparaît pertinente à explorer, cette bande est une partie du spectre électromagnétique qui s'étend de 30 à 300 GHz correspondant à des longueurs d'onde de 10 à 1 mm, respectivement [44, 45]. Le moyen le plus efficace d'augmenter le débit de données peut être réalisé en utilisant des bandes passantes larges et de haute puissance d'émission autorisée. La FCC a attribué 7 GHz de la bande passante autorisée gratuitement dans la GHz 54-66 [11]-[13]. Dans cette bande, les limites de régulation FCC permettent une puissance d'émission maximale de 500 milliwatts (27 dBm) pour une largeur de bande d'émission supérieure à 100 MHz. La bande passante énorme sans licence offre un grand potentiel en termes de capacité et de flexibilité, ce qui rend la technologie 60 GHz particulièrement attrayante pour les applications Gbps à courte portée. En raison des mécanismes de propagation, les liens 60 GHz présentent des atténuations importantes. Cependant, la forte atténuation n'est pas considérée comme un inconvénient lorsqu'il s'agit de questions de sécurité, l'atténuation signifie que les systèmes 60 GHz assurent la sécurité inhérente. Par ailleurs, le signal de très grande décroissance limite également les interférences entre les liens 60 GHz situés dans les alentours proches, et empêche les chaînes 60 GHz d'interférer avec d'autres systèmes opérant dans la même bande. Les fréquences les plus élevées également permettent à de plus petites tailles de composants RF et des antennes. Par conséquent, la taille petite et compacte d'antennes à 60 GHz permet le déploiement de plusieurs antennes au niveau de l'utilisateur qui sont par ailleurs difficiles, voire impossible dans les basses fréquences. Aussi, les canaux de communication 60 GHz nécessitent une antenne directionnelle avec un gain très élevé, ce qui apporte une nouvelle opportunité pour la réutilisation spatiale entre les maillons adjacents. Traditionnellement, dans les systèmes de communications ondes-mm sans fil conventionnelle, la transmission de données Gbps pourrait être réalisée sous la condition de ligne de vue (LOS) ou d'un composant multivoies fort qui existe entre l'émetteur et le récepteur. Dans l'espace libre les signaux 60 GHz subissent une très forte atténuation, combinée avec l'atténuation due à des mécanismes de propagation des surfaces des objets environnants et les pertes de l'obstruction. Sous les conditions NLOS, les liens 60 GHz subissent des affaiblissements de parcours plus élevés en l'absence de réflexion spéculaire, et le manque de diffraction autour des obstacles à pertes tels que les coins de couloirs [36], [37]. Cette

perte de trajet grave entrave le débit d'ordre de Gbps et empêche la couverture de dépasser les 10 m. Par conséquent, l'utilisation de transmission de données dans des environnements hostiles de propagation a ré-émergé comme thème de recherche important au cours de la dernière demi-décennie en vue d'étendre la couverture du signal, en particulier au cours ombragés où la ligne de vue (LOS) n’est pas présente.

CHAPITRE 3

Système de mesure du sondeur de canal aux ondes mm

Le système de mesure comporte une technique évolutive qui fournit une cohérence de phase RF entre l'émetteur et le récepteur presque parfaite. En effet, ces derniers sont connectés par l'intermédiaire d'une fibre optique à un mode pour garantir la synchronisation en phase. Le concept derrière l'utilisation de fibres optiques est de permettre un lien souple et à faible atténuation. Par conséquent, une plus grande précision des résultats de mesure de la CTF peut être réalisée. L'utilisation de la fibre optique laser permet la synchronisation de l'émetteur et du récepteur à micro-ondes même pour des distances assez grandes allant jusqu'à plusieurs centaines de mètres. Le schéma général du système est illustré sur la Fig.3.1. Les signaux RF sont générés du côté du récepteur et ensuite fournis à l'émetteur distant au moyen d'un laser modulateur/démodulateur. Les deux signaux RF alimentant l'émetteur sont utilisés pour moduler deux signaux porteurs laser (CW). Les deux ondes lumineuses modulées (dans le voisinage de 1550 nanomètres) sont alors combinées et envoyées à l'émetteur micro-ondes à travers un câble de fibre optique mode-unique dont la longueur est 500 mètres. Au récepteur, les deux signaux laser sont séparés et les deux signaux RF sont ensuite récupérés en utilisant des détecteurs optiques. Ces signaux RF entraînent l'émetteur à micro-ondes en synchronisation de phase avec le récepteur. Les antennes utilisées sont montrées sur la Fig. 3.7, elles sont fabriquées par la compagnie Millitech [109], ses caractéristiques techniques sont indiquées dans le Tableau 3.1.

CHAPITRE 4

Modélisation déterministe du canal de propagation intra-immeuble à 60 GHz

Dans ce chapitre, deux modèles réalistes basés sur la technique RT ont été développés pour les scénarios ci-dessous :

a) Modèle pour un canal de propagation en NLOS: le scénario tient en compte la présence d'un cylindre et d'un réflecteur plat (DOs) à l'intersection de deux corridors en T.

b) Modèle pour un canal de propagation en LOS : le scénario étudié est une salle de conférence vide.

La validation expérimentale est effectuée dans le domaine fréquentiel et, par une IFFT, dans le domaine temporel.

Modèle pour un canal de propagation en NLOS

Les mesures ont été effectuées dans le 3ème étage de l'édifice abritant le laboratoire de recherche sur les communications (CRC-Ottawa). Dans ce milieu, les murs des couloirs sont faits de Placoplatre, le sol est couvert de tuiles et le plafond est couvert de tuiles en polystyrène munis de lampes au néon placées le long des couloirs. Les couloirs ont un certain nombre de portes de bureau en bois avec des cadres métalliques. Les antennes réceptrice et émettrice sont placées à une hauteur de 1.7 m au-dessus du niveau du sol. Toutes les deux sont situées à 10 m de l'intersection pour donner une longueur de trajet de 20 m, comme illustré sur Fig. 4.1. Trois scénarios sont étudiés:

A) l'intersection des couloirs vide (absence de DO),

B) un cylindre métallique est installé à l'intersection, et

C) une surface plate métallique réfléchissante est alors installée à l'intersection.

A) Intersection des couloirs vide (absence de DO),

Le choix des coefficients de diffraction est essentiel afin d'atteindre la précision souhaitable des résultats de la simulation. Les coefficients UTD de Remely se trouvent être les plus pratiques car ils prennent en compte les propriétés diélectriques des coins avec perte. En raison de l'absence d'une composante multivoie dominante, il est important de considérer le plus grand nombre possible de contributions. En dépit de la grande absorption causée par les murs des couloirs à 60 GHz, les contributions dues à la réflexion jusqu'au 4^{e} ordre sont prises en compte,

comme indiqué sur la Fig. 4.2. L'augmentation de l'ordre de la réflexion augmente l'angle d'incidence et de diffraction qui, à leur tour, renforce le signal diffracté. La simulation est basée sur la modélisation des CTFs dans le domaine fréquentiel en concordance avec la technique de mesure utilisée pour la collecte de données expérimentales. Des profiles typiques normalisées mesurés et prédites des CTFs sont présentées sur la Fig. 4.3. Les profils des délais de propagation PDPs sont calculés en appliquant l'IDFT sur les résultats CTF. Pour une analyse claire, l'intervalle (60-84 ns) de la PDP normalisée est agrandi est illustré sur la Fig. 4.8. Les contributions multivoies les plus importantes, causées par diffraction des coins de 1 à 6, sont identifiées. Un bon accord est obtenu entre les données expérimentales et simulées autant dans le domaine fréquentiel que le domaine temporel.

B) Cylindre métallique installé à l'intersection.

Dans le cas de la présence d'un cylindre métallique dans l'intersection, la diffraction des rayons du champ électromagnétique-optique par une surface convexe lisse parfaitement conductrice, est appliquée en utilisant la théorie uniforme de la diffraction (UTD). Les CTFs mesurées et simulées sont dérivées. Fig. 4.13 révèle un accord intéressant entre les mesures expérimentales et les résultats théoriques. On voit clairement que les variations théoriques du signal se comparent favorablement avec celle mesurées en termes de l'évanouissement, la périodicité, et la puissance décroissante du signal. Dans du canal de propagation dans le domaine temporel, les PDP normalisées des données mesurées et prédites ont été calculées et illustrées sur la Fig. 4.15. La réflexion spéculaire, causée par le cylindre, conducteur parfait, est un rayon très dominant au point où il rend les autres rayons multivoies diffractés négligeables. Comme indiqué sur la Fig. 4.15, les rayons du canal de propagation sont identifiés avec succès. Le modèle présenté est validé avec succès dans le domaine fréquentiel et dans le domaine temporel.

C) Surface plate métallique installé à l'intersection.

Les CTFs expérimentales et théoriques sont présentés sur les Figs. 4.18 (a) et (b), respectivement. Dans ce scénario, il est intéressant de noter que le canal est presque constant sur toute la bande passante d'intérêt où la puissance des signaux varie entre 3 à 4 dB. Les PDP obtenus sont présentés sur les Figs. 4.20 (a) et (b), respectivement, pour les résultats expérimentaux et théoriques. Il est intéressant de noter que, la forte composante spéculaire réfléchie par le DO domine toutes les autres composantes multivoies présentes dans le canal.

Modèle pour un canal de propagation en LOS

Cet environnement est constitué d'une salle de conférence typique en forme rectangulaire de dimensions 5,83 m (largeur) x 6,88 m (longueur) x 2,67 m (hauteur). Les murs de cette salle sont en Placoplatre, le plancher est en béton et recouvert de tuiles en plastique de vinyle et le plafond est également fait de béton et recouvert de tuiles en polystyrène où on y trouve des lampes au néon. La salle dispose de deux grandes fenêtres en verre et une porte métallique. La Fig. 4.21 illustre la disposition de la salle.

La campagne de mesure effectuée dans cette salle est principalement en LOS, où les deux antennes, d'émission et de réception, sont maintenues à une distance de 5.7 m l'une par rapport à l'autre. Les profils typiques normalisés, à la fois mesurées et simulées, des CTFs sont dérivées et présentés sur la Fig. 4.22. Dans ce cas aussi, on voit clairement que les variations du signal théoriques se comparent favorablement avec celles mesurées en termes de l'évanouissement, la périodicité, et la puissance décroissante du signal. Un aggrandissement du PDP normalisé (16-30 ns) est montré sur la Fig. 4.25. Le premier rayon perceptible est détecté à la 19^{e} ns, il s'agit de la contribution de la composante LOS directe provenant de la simple propagation en espace quasi-libre, par conséquent, elle est la plus dominante dans le canal. Les rayons réfléchis, du 1er ordre, sur le plancher en béton et sur le plafond sont identifiés et détectés aux instants 20 et 22 ns, respectivement. Cependant, les rayons réfléchis, du 1er ordre, sur les murs A et B sont détectés aux instants 25 et 29 ns, respectivement. La contribution AC qui est causée par la réflexion double sur le mur A et sur le mur C, en présence de la fenêtre vitrée, est identifié et manifeste un retard de 28 ns.

CHAPITRE 5

Caractérisation et analyse des résultats expérimentaux large-bandes à 60 GHz

Campagne de mesure dans les deux corridors en T (scénarios NLOS)

Cette campagne de mesure a été effectuée au niveau de deux couloirs en forme de T. Une telle intersection nous offre des scénarios de propagation NLOS. L'émetteur est situé dans le couloir (A) à différentes positions allant de 1 m à 10 m de l'intersection, tandis que le récepteur est maintenu à une position fixe sur le couloir (B), c'est à dire, à 10 m de l'intersection, comme illustré sur la Fig. 5.1. Fig. 5.2 montre les CTFs mesurées pour les différents scénarios discutés plus haut, à savoir, intersection vide, en présence DO cylindrique et en présence DO plat, tout en fixant les stations d'émission et de réception à une distance de 10 m de l'intersection. On voit clairement que chaque DO fournit une réponse en fréquence totalement distincte. Basés sur les mesures du CTF (59.6 à 60.6 GHz), les paramètres statistiques pertinents du canal de propagation multivoies sont extraits.

A) Bande de cohérence

La bande de cohérence est une mesure statistique de la gamme de fréquences sur laquelle toutes les composantes spectrales manifestent un gain presque constant et une phase quasi-linéaire. Par conséquent, les amplitudes de toutes les tonalités de fréquences qui se situent à moins de 3 dB au-dessous de la fréquence de résonance et dont la phase est linéaire sont identifiées pour tous les scénarios mesurés. Des approches différents de l'estimation de la bandes de cohérence sont calculées sur la base de gain égal et une bande passante possible maximale dans les gammes de fréquences choisies où la réponse en phase est linéaire [148] comme le montre le Tableau 5.3.

B) Distributions de l'évanouissement à petite échelle

Les fonctions de distributions cumulatives (CDFs) des différentes les données expérimentales sont représentées sur la Fig. 5.6. Tel que prévu, la CDF des résultats pour le scénario du canal en présence de DO correspond bien à celle de Rice, car une composante multivoie dominante, provenant de l'interaction spéculaire dus signal avec cylindre ou de la surface plane, est bien présente. Cependant, lorsque le canal est vide, la CDF des données mesurées se comportent comme un canal de Rayleigh. Le Tableau 5.4, affichent les valeurs des

paramètres statistiques suite à une optimisation basée sur la meilleure CDF théorique. Les résultats soulignent que la surface plane DO offre une couverture optimale du signal par rapport aux scenarios.

C) L'affaiblissement de parcours (PL)

Dans tous les cas, l'affaiblissement de parcours induit par chaque DO est calculé par rapport à une distance de 20m séparant le récepteur et l'émetteur dont le gain des antennes est de 23.4 dBi chacune. À partir des valeurs du Tableau 5.5, on voit clairement que, dans le canal NLOS (couloirs), et quelle que soit la forme du DO présent à l'intersection des couloirs, l'affaiblissement se voit réduit à cause de cette présence. Le gradient de l'affaiblissement de parcours est alors obtenu en effectuant une régression linéaire des moindres carrés sur l'ensemble des résultats expérimentaux du signal puissance moyenne reçu en fonction de la distance. Les valeurs du gradient sont obtenues par rapport à une distance de référence de 1 m.

D) les paramètres statistiques temporelles du canal

Une estimation de la réponse impulsionnelle du canal de propagation pour chaque cas est dérivée en effectuant l'IDFT aux CTFs mesurées. Les échantillons des PDPs sont présentés sur la Fig. 5.9. Afin de caractériser les propriétés dispersives du canal multivoie et donc, pour évaluer sa performance, les délais moyens (τ_{mean}), délais maximales (τ_{max}) et les valeurs efficaces de l'étalement du retard (σ_τ) sont calculées [34, 35]. Pour chaque scénario, les paramètres de dispersion des canaux sont calculés sur deux seuils de puissance (-30 dB et -40 dB) par rapport à la valeur maximale, telles qu'elles figurent dans le Tableau 5.6.

Campagne de mesure dans la salle de conférence (scénarios en LOS)

Cette campagne de mesure a été effectuée dans une salle de conférence vide où le scénario LOS prévale ne permanence. Les deux antennes, polarisées verticalement, ont été maintenues à une hauteur de 1.7 m du plancher. L'émetteur est maintenu immobile, tandis que le récepteur se déplaçait avec un pas de 0,5 m le long de la ligne reliant l'émetteur au récepteur, tel qu'illustré sur la Fig. 5.11. Les CTFs ont été obtenues pour chaque position du récepteur. Pour étudier l'effet de la directivité de l'antenne sur les paramètres du canal de propagation, deux scénarios de mesure ont été étudiés:

a) Deux antennes omnidirectionnelles sont employées dans le canal (Omni-Omni).
b) Une antenne directionnelle est utilisée au niveau de l'émission, tandis une antenne omnidirectionnelle est utilisée au niveau de la réception (Direct-Omni).

Les profils typiques de CTFs mesurées à une distance 5.7 m séparant les antennes sont présentés sur les Figs 5.12 (a) et (b) pour les scénarios Omni-Omni et Direct-Omni, respectivement. Comme prévu, l'utilisation d'une antenne d'émission directionnelle a fourni un meilleur résultat en termes d'évanouissement multitrajet. Tel qu'observé précédemment dans la campagne de mesures NLOS, les différents paramètres statistiques sont extraits et donnés sur le Tableau 5.7 et le Tableau 5.6. Ces paramètres montrent que le déploiement de l'antenne directionnelle renforce le signal reçu par rapport à la configuration Omni-Omni. C'est une évidence qu'une directivité élevée est nécessaire pour les communications sans fil à 60 GHz. La Fig. 5.14 montre les fonctions linéaires correspondant à la relation entre l'affaiblissement de parcours en fonction de la distance pour les configurations Omni-Omni et Direct-Omni. Les gradients de l'affaiblissement de parcours résultant pour l'Omni-Omni et Direct-Omni sont, respectivement, n = 1.9 et n = 1.73. Dans le Tableau 5.10 et le Tableau 5.11 les gradients de l'affaiblissement de parcours obtenus sont comparés à ceux publiés dans la littérature. On note un bon accord avec nos résultats. Dans le cas NLOS, lorsqu'un DO (réflecteur plat) est placé à l'intersection, nos mesures affichent un gradient de 1.9, valeur très comparable à celle de la littérature pour des couloirs en LOS.

CHAPITRE 6

Conclusion

Cette thèse constitue une contribution vers la conception de nouveaux systèmes, œuvrant sur la bande des ondes mm, à déployer pour les futures WLAN et/ou les nouvelles générations de systèmes HDMI. Ses contributions sont principalement axées sur *l'analyse de résultats expérimentaux obtenus à 60GHz* sur deux scénarios intra-immeubles typiques, d'une part, et la modélisation déterministe du canal de propagation en utilisant *le tracé de rayon exprimé dans le domaine fréquentiel*, d'autre part. Les scénarios traités sont :

a) une intersection de couloirs en forme de T (scénarios en NLOS)

b) une salle de conférence moderne rectangulaire sous ligne-de-vue (scénarios en LOS)

L'analyse des résultats expérimentaux de cette thèse démontre clairement que:

- Dans les couloirs NLOS, la transmission du signal repose principalement sur le phénomène de diffraction au niveau des coins d'intersection.
- La présence de DOs est une solution pratique pour renforcer les signaux reçus et étendre leur couverture aux zones d'ombre où le LOS n'est pas présent.

Les modèles développés dans cette thèse sont validés expérimentalement et démontrent que :

- La modélisation du canal de propagation en utilisant le RT nécessite des informations précises sur l'environnement, y compris sa géométrie et les propriétés des matériaux électriques.
- Tous les trajets multiples sont importants et pertinents pour permettre l'obtention de prévisions précises sur les paramètres du canal de propagation aux ondes mm.

L'UTD est un outil intéressant pour prédire le champ diffracté par des coins de murs. Le coefficient de diffraction heuristique de Remely est plus adapté aux coins ayant des pertes (diélectriques), et il constitue la manière la plus précise pour calculer le champ de diffraction dans les régions obstruées NLOS.

References

[1] Zhou, W. Junyi, M. Rahman, H. Harada, and S. Kato," IEEE 802.15.3c: the first IEEE wireless standard for data rates over 1 Gb/s", IEEE Communications Magazine, Vol. 49, No. 7, pp. 114-121, July 2011.

[2] R. Daniels, and R. Heath, "60 GHz wireless communications: emerging requirements and design recommendations," IEEE Vehicular Technology Magazine, Vol. 2, No.3, pp. 41-50, 2007.

[3] P. Cheolhee, and T. Rappaport, "Short-Range Wireless Communications for Next-Generation Networks: UWB, 60 GHz Millimeter-Wave WPAN, And ZigBee," IEEE Communications Magazine, Vol. 19, No. 4, pp. 70-78, August 2007.

[4] H. Singh, O. Jisung, K. Changyeul, Q. Xiangping, S. Huai-Rong, and N. Chiu, "A 60 GHz wireless network for enabling uncompressed video communication," IEEE Communications Magazine, Vol. 46, No. 12, pp. 71-78, December 2008.

[5] D. Han, J. Kim, and S. Park, "A Dual Band CMOS Receiver With Hybrid Down Conversion Mixer for IEEE 802.11a/b/g/n WLAN Applications," IEEE Lettrs on Microwave and Wireless Components, Vol. 20, No. 4, pp. 235-237, April 2010.

[6] V. Angelakis, S. Papadakis, V. Siris, and A. Traganitis, "Adjacent channel interference in 802.11a is harmful: Testbed validation of a simple quantification model," IEEE Communications Magazine, Vol. 49, No. 3, pp. 160-166, March 2011.

[7] Zhang, X.; Yan, Y.; Du, Z.; Liu, K.; Wideband RC polyphase network for IEEE 802.11a quadrature signal generation," IEEE Electronics Letters, Vol. 46, No. 10, pp. 730-732, May 2010.

[8] Federal Communications Commission (FCC), "Revision of part 15 of the commission's rules regarding ultra-wideband transmission systems, first report and order,"ET Docket 98-153, FCC, Washington DC, February 2002. http://www.fcc.gov/Bureaus/Engineering_Technology/Orders/2002/fcc02048.pdf

[9] W. Pam, and K. Liu, Ultra-Wideband Communications Systems Multiband OFDM Approach, Wiley, 2007.

[10] H. Nikookar, R. Parasad, "Introduction to Ultra Wideband for Wireless Communications" Springer, 2009.

[11] FCC Code of Federal Regulation title 47 Telecommunication, Chapter 1, part 15.255, October, 2004.

[12] S. Yong, P. Xia and A. Garcia, 60 GHz Technology for Gbps WLAN WPAN: From Theory to Practice, Wiley, USA, 2011.

[13] R. Kraemer, and M. D. Katz, Short-Range Wireless Communications: Emerging Technologies and Applications, Wiley, UK, 2009.

[14] S. K. Moore, "Cheap chips for next wireless frontier," IEEE Spectrum, vol. 43, No. 6, pp. 12-13, June 2006.

[15] L. Yang, "60 GHz: Opportunity for Gigabit WPAN and WLAN Convergence", ACM SIGCOMM Computer Communication Review, January 2009.

[16] P. Minyoung, C. Cordeiro, E. Perahia, L. Yang, "QoS Considerations for 60 GHz Wireless Networks," IEEE GLOBECOM Workshop, OR, USA, December 2009.

[17] IEEE 802.15 WPAN Millimeter Wave Alternative PHY Task Group 3c (TG3c), March 2009. http://www.ieee802.org/15/pub/TG3c.html

[18] ECMA-387 High Rate 60GHz PHY, MAC and HDMI PAL, 2009. http://www.ecmainternational.org/activities/Communications/tc48-2009-005.doc
[19] WirelessHD (2009) The first 60 GHz standard now available in consumer electronics products worldwide. http://www.wirelesshd.org/pdfs/WiHD%20CEDIA%20SEPT0901009_FINAL.pdf
[20] EE Times (2009) 60 GHz gains traction at CES. http://www.eetimes.com/electronics-news/4080893/60-GHz-gains-traction-at-CES
[21] R. Stacey," Multi-band, Multi-radio Wireless LANs and PANs Enhancements to 802.11," Asilomar Conference on Signals, Systems and Computers, OR, USA, November 2009.
[22] Y. Nagai, M. Ochiai, N. Shimizu, A. Shibuya, "A Throughput Performance for a Point-to-Multipoint Gigabit WLAN System on 60 GHz millimeter Wave," 7th IEEE Conference Consumer Communications and Networking (CCNC), Kamakura, Japan, January 2010.
[23] P. Smulders, "Exploiting the 60 GHz band for local wireless multimedia access: prospects and future directions," IEEE Communications Magazine., Vol. 40, No. 1, pp. 140-147, Jan. 2002.
[24] M. Park, C. Cordeiro, E. Perahia, and L. Yang, "Millimeter-wave multigigabit WLAN: challenges and feasibility," in Proc. IEEE Int. Sym. On Personal, Indoor and Mobile Radio Commun. (PIMRC), Hilsboro, OR, USA, Sept. 2008.
[25] A. F. Molish, Wireless Communications, 2nd Edition, Wiley, 2011.
[26] H. Vettikalladi, O. Lafond, M. Himdi, "High-Efficient and High-Gain Superstrate Antenna for 60-GHz Indoor Communication," IEEE Letters on Antennas and Propagation, Vol. 8, pp. 1422-1425, January 2010.
[27] C. Liu, E. Skafidas, R. Evans, "Capacity and data rate for millimeter wavelength systems in a short range package radio transceiver," IEEE Transactions on Wireless Communications, Vol. 9, No. 9, pp. 903-906, March 2010.
[28] M. Marcus, and B. Pattan, "Millimeter wave propagation: spectrum management implications," IEEE Microwave Magazine, Vol. 6, No. 2, pp. 54-62, June 2005.
[29] J. Van Vleck, "The absorption of microwaves by oxygen," Phys. Rev., Vol. 71, No. 7, pp. 413-424, April 1947.
[30] A. Maltsev, R. Maslennikov, A. evastyanov, A. Khoryaev and A. Lomayev, "Experimental Investigations of 60 GHz WLAN Systems in Office Environment," IEEE Journal on Selected Areas in Communications, Vol. 27, No. 8, October 2009.
[31] C. P. Lim, R. J. Burkholder, J. L. Volakis, and R. J. Marhefka, "Propagation modeling of indoor wireless communications at 60 GHz," IEEE Antennas and Propagation Society International Symposium, pages 2149 – 2152, 2006.
[32] Y. Lostanlen, Y. Corre, Y. Louet, Y. Le Helloco, S. Collonge, G. El-Zein, "Comparison of measurements and simulations in indoor environments for wireless local networks at 60 GHz", IEEE Vehicular Technology Conference (VTC), Rennes, 2002.
[33] Jinwon Choi; Noh-Gyoung Kang; Yu-Suk Sung; Jun-Sung Kang; Seong-Cheol Kim; "Frequency-Dependent UWB Channel Characteristics in Office Environments," IEEE Transactions on Vehicular Technology, Vol. 58, No. 7, pp. 3102-3111, September 2009.
[34] Yan Zhao; Yang Hao; Parini, C.; FDTD Characterization of UWB Indoor Radio Channel Including Frequency Dependent Antenna Directivities," IEEE Letters on Antennas and Wireless Propagation, Vol. 6, pp. 191-194, April 2007.
[35] N. Deparis, A. Bendjabballah, A. Boe, M. Fryziel, C. Loyez, L. Clavier, N. Rolland, P. Rolland, " Transposition of a baseband UWB signal at 60 GHz for high data rate indoor

WLAN," IEEE Letters on Microwave and Wireless Components, Vol. 15, No. 10, pp. 609-611, October 2005.
[36] N. Moraitis, P. Constantinou, " Indoor channel measurements and characterization at 60 GHz for wireless local area network applications," IEEE Transactions on Antennas and Propagation, Vol. 52 , No. 12, pp. 3180 – 3189, 2004.
[37] P. Smulders, and L. Correia, "Characterisation of propagation in 60 GHz radio channels," IEEE Electronics & Communication Journal," Vol. 9, No. 2, pp. 73-80, 1997.
[38] R. Janaswamy, "An Indoor Pathloss Model at 60 GHz Based on Transport Theory," IEEE Antennas and Propagation Letters, Vol. 5, No. 1, pp. 58-60, 2006.
[39] P. Smulders, "Characterisation of propagation in 60 GHz radio channels," IEEE Transactions on Antennas and Propagation, Vol. 57, No. 10, pp. 2820 – 2829, October 2009.
[40] M. Kyro, K. Haneda, J. Simola, K. Nakai, K. Takizawa, H. Hagiwara, P. Vainikainen, " Measurement Based Path Loss and Delay Spread Modeling in Hospital Environments at 60 GHz," IEEE Transactions on Wireless Communications, Vol. 10, No. 8, pp. 2423 – 2424, August 2011.
[41] A. G. Siamarou and M. Al-Nuaimi, "A Wideband Frequency-Domain Channel-Sounding System and Delay-Spread Measurements at the License-Free 57- to 64-GHz Band", IEEE Transaction on Instrumentation and Measurement, Vol. 59, No. 3, March 2010.
[42] G. Suiyan and P. Vainkainen, 'Millimeter-Wave Propagation in Indoor Corridors", IEEE Letters on Antennas and Wireless Propagation, Vol. 8, No. pp. 1242-1245, 2009.
[43] X. Zhao, G. Suiyan, L. Vuokko, J. Kivinen and P. Vainkainen,"Polarization Behaviours at 2.5 and 60 GHz for Indoor Mobile Communications", Wireless Personal Communications, Kluwer, 2003.
[44] A. Oliver, "Millimeter wave systems – past, present and future". IEE Proceedings, No.136, pp. 35–52, 1989.
[45] J. Wells, Multigigabit Microwave and Millimeter-Wave Wireless Communications, Artech house, 2010.
[46] C. Cordeiro, M. Park, et. Al., "Spatial Reuse and Interference Mitigation in 60 GHz," IEEE 802.11-09/782r0, July 2009.
[47] ECMA international TC48: http://www.ecma-international.org
[48] IEEE 802.11 task group ad, http://www.ieee802.org/11/Reports/tgad_update.htm
[49] S. R. Saunders and A. Zavala, Antennas and Propagation for Wireless Communication Systems, 2nd edition, Wiley, 2007.
[50] H. Singh, J. Hsu, L. Verma, S. Lee and N. Chio, "Green Operation of Multi-Band Wireless LAN in 60 GHz and 2.4 5 GHz," Consumer Communications and Networking. Conference (CCNC), Jan 2011.
[51] Y Yu, P. Baltus and A. Roermund, Integrated 60 GHz RF Beamforming in CMOS, Springer, 2011.
[52] L. Barclay, Propagation of Radiowaves, 2nd Edition, Institution of Engineering and Technology, UK, 2003.
[53] S. Kharkovsky, A. Mehmet, H Ugur and C. Atis, "Measurement and Monitoring of Microwave Reflection and Transmission Properties of Cement-Based Specimens', IEEE Transactions on Instrumentation and Measurement, Vol. 51, No. 6, December 2002.
[54] T. S. Rappaport, "Wireless Communications: Principle and Practice, 2nd edition, Prentice Hall, 2001.

[55] J. Lahteenmaki and T. Karttaavi,"Measurement of dielectric parameters of wall materials at 60 GHz band", IET Electronic Letters, Vol. 32, No. 16, pp. 1442-1444, 1996.
[56] M. C. Luis and F. Paulo, "Estimation of Materials Characteristics from Power Measurements at 60 GHz", IEEE International Symposium on personal, Indoor and Mobile Radio Communications, 1994.
[57] A. Muqaibel, A. Saafi-Jazi, A. Bayram, A. Attiya and S. M. Riad, "Ultrawideband through-the-wall propagation", IEE Proceedings on Microwaves Antennas and Propagation, Vol. 152, No. 6, pp. 581-588, December 2005.
[58] R.G. Kouyoumjian and P.H. Pathak, "A Uniform Geometrical Theory of diffraction for an Edge in a Perfectly Conducting Surface," IEEE Proceedings, vol. 62, No. 11, pp. 1448-1461. Nov. 1974.
[59] P. V. O'Neil, Advanced Engineering Mathematics, 7th Edition, Global Engineering, 2011.
[60] G. Carluccio, F. Puggelli, M. Albani, "Algorithm for the Computation of the Generalized Fresnel Integral," IEEE Transaction on Antennas and Propagation, Vol. 59, No. 10, pp. 3943-3947, October 2011.
[61] G. Carluccio, M. Alban, and P. H. Pathak, "Uniform Asymptotic Evaluation of Surface Integrals With Polygonal Integration Domains in Terms of UTD Transition Functions," IEEE Transaction on Antennas and Propagation, Vol. 58, No. 4, pp. 1155-1163, April 2010.
[62] J. B. Keller, "Geometrical theory of diffraction," Journal of the Optical Society of America, vol. 52, no. 2, pp. 116–130, February 1962.
[63] R. J. Luebbers, "Finite conductivity uniform UTD versus knife diffraction prediction of propagation path loss," IEEE Transactions on Antennas Propagation, vol. 32, pp. 70–76, January 1984.
[64] K. A. Remley, H. R. Anderson, and A. Weisshar, "Improving the accuracy of ray-tracing techniques for indoor propagation modeling," IEEE Transaction on Vehicular Technology, vol. 49, no. 6, pp. 2350–2358, November 2000.
[65] D. A. McNamara, C. W. I. Pistorius, and J. A. G. Malherbe, Introduction to the Uniform Geometrical Theory of Diffraction, Norwood, MA: Artech House, 1990.
[66] W. L. Stutzman and G. A. Thiele, Antenna Theory and Design, 2nd Edition, New York: Wiley, 1998.
[67] M. Born and E. Wolf, Principles of Optics, 2nd ed. Oxford: Pergamon Press, 1964.
[68] P. Pagani, T. Friedman, P. Pajusco and B. Uguen, Ultra-Wideband Radio Propagation Channels: A Practical Approach, John Wiley & Sons Inc. 2008.
[69] M. Dottling, T. C. Becker, and W. Wiesbeck, "Modeling of the DECT outdoor radio channel," Proceedings of the 47th IEEE Vehicular Technology Conference, May 1997.
[70] R. P. Torres, L. Valle, and M. Domingo, "Computer tool to analyze radio channel in arbitrary enclosed spaces using ray tracing," Proceedings of the 48th IEEE Vehicular Technology Conference, May 1998.
[71] C. A. Balanis, Advanced Engineering Electromagnetics, Wiley, New York, 1989.
[72] G. L. James, Geometrical Theory of Diffraction for Electromagnetic Waves. Peter Peregrinus, London, 1980.
[73] J. G. Proakis, "Digital Communications", McGraw-Hill Book Company, 4th Edition, 2007.
[74] G. L. Turin, "A statistical model for urban multipath propagation," IEEE Transactions on Vehicular Technology, Vol. 21, No. 1, pp. 1-9, 1972.

[75] J. Hansen, "An analytical calculation of power delay profile and delay spread with experimental verification", IEEE Communications Letters, Vol. 7, No.6, pp. 257 – 259, June 2003.
[76] S. Ichitsubo, K. Tsunekawa, Y. Ebine, "Multipath propagation model of spatio-temporal dispersion observed at base station in urban areas" IEEE Journal on Selected Areas in Communications, Vol. 20, No.6, pp. 1204 – 1210, August 2002.
[77] C. Chai, T. Thiang,"A Unified Probability Density Function for Small Scale Fading Envelopes.", IEEE 18th International Symposium on Personal Indoor and Mobile Radio Communications, Athens, Greece, 2007.
[78] J. Pardo, M. Lienard, A. Nasr, P. Degauque, "Wideband analysis of large scale and small scale fading in tunnels" 8th International Conference on ITS Telecommunications, pp. 270-273, Montreal, Canada, Oct. 2008.
[79] C. Oestges, N. Czink, B. Bandemer, P. Castiglione, F. Kaltenberger, and A.J. Paulraj, "Experimental Characterization and Modeling of Outdoor-to-Indoor and Indoor-to-Indoor Distributed Channels," IEEE Transactions on Vehicular Technology, Vol. 59, No. 5, pp. 2253-2265, June 2010.
[80] D. Hutchenson, D. Noneaker, "New closed-form bounds on the performance of coding in correlated Rayleigh fading" IEEE Transactions on Communications, Vol. 57, No. 10, pp. 2923 – 2931, October 2009.
[81] F. Catherine, E. Merran, H. Nicholas, and P. Brian, Atatistical Distributions, fourth edition, Wiely, USA, 2011.
[82] L. Bosco, VLSI for Wireless Communications, second edition, Pearson Education, 2011.
[83] X. Liu, "Copula of trivariate Rayleigh distribution with exponential correlation," IEEE Electronic Letters, Vol. 47, No. 10, May 2011.
[84] P. Hallbjomer, "Modified Rice distribution for signals with limited available power," IEEE Letters on Antennas and Wireless Propagation," Vol. 2, No. 1, February 2003.
[85] A. Abdi, C. Tepedelenlioglu, M. Kaveh, G. Giannakis, G, "On the estimation of the K parameter for the Rice fading distribution," IEEE Communications Letters, Vol. 5, No. 3, March 2001.
[86] C. Oliver, Fundamentals of Stochastic Networks, Wiely, New jersy, 2011.
[87] A. Legg, Propagation measurements at 11 Gc/s over a 35 km near optical path involving diffraction at two obstacles," IEEE Electronic Letters, Vol. 1, No. 10, pp. 285-286, December 1965.
[88] J. Howard, K. Pahlavan, "Doppler spread measurements of indoor radio channel," IEEE Electronic Letters, Vol. 26, No. 2, pp. 107-109, January 1990.
[89] P. Smulders, A.Wagemans, "Wideband indoor radio propagation measurements at 58 GHz", IEEE Electronic Letters, Vol. 28, No. 13, pp. 1270-1272, June 1992.
[90] Wales, S.W.; Rickard, D.C.; Wideband propagation measurements of short range millimetric radio channels," IEEE Electronics & Communication Engineering Journal, Vol. 5, No. 4, pp. 249 – 254, August 1993.
[91] Bultitude, R.J.C.; Hahn, R.F.; Davies, R.J.; Propagation considerations for the design of an indoor broad-band communications system at EHF," IEEE Transactions on Vehicular Technology, Vol. 47, No. 1, pp. 235 – 254, February 1998.
[92] B. Maharaj, J. Wallace, L. Linde, M. Jensen, "Linear dependence of double-directional spatial power spectra at 2.4 and 5.2 GHz from indoor MIMO channel measurements," IEEE Electronic Letters, Vol. 41, No. 24, pp. 1338 –1340, November 2005.

[93] M. Steinbauer, A. Molisch, E. Bonek, "The double-directional radio channel," IEEE Antennas and Propagation Magazine, Vol. 43, No. 4, pp. 1045 –9243, August 2001.
[94] K. Haneda, J. Takada; T. Kobayashi, "Cluster Properties Investigated From a Series of Ultrawideband Double Directional Propagation Measurements in Home Environments," IEEE Transactions on Antennas and Propagation, Vol. 54, No. 12, pp. 3778 –3788, December 2006.
[95] U. Martin, "Spatio-temporal radio channel characteristics in urban macrocells," IEE Proceedings on Radar, Sonar and Navigation, Vol. 145, No. 1, pp. 42 –49, February 1998.
[96] J. Wepman, J. Hoffman, L. Loew, W. Tanis, M. Hughes, "Impulse response measurements in the 902-928 and 1850-1990 MHz bands in macrocellular environments," 2nd International Conference on Universal Personal Communications (ICUPC), October 1993.
[97] L. Greenstein, N. Amitay, T. Chu, L. Cimini, G. Foschini, M. Gans, I. Chih-Lin, A. Rustako, R. Valenzuela, G. Vannucci, "Microcells in personal communications systems," IEEE Communications Magazine, Vol. 30, No. 12, pp. 76 – 88, December 1992.
[98] Lempiainen, J.J.A.; Laiho-Steffens, J.K.; The performance of polarization diversity schemes at a base station in small/micro cells at 1800 MHz," IEEE Transactions on Vehicular Technology, Vol. 47, No. 3, pp. 1087 – 1092, August 1998.
[99] S. Orfanidis, Introduction to Signal processing, Pearson Education, 2010.
[100] J. Proakis and D. Manolakis, Digital Signal Processing: Principles, Algorithms, and Applications, Printice Hall, 1996.
[101] D. Cassioli, M. Win, and A. F. Molisch,"The ultra-wide bandwidth indoor channel: From statistical model to simulations",IEEE Journal on Selected Areas in Communications, Vol. 20, No. 6, pp. 1247–1257, 2002.
[102] R. Cramer, R. Scholtz, and M. Win, "Evaluation of an ultra-wide-band propagation channel", IEEE Transaction on Antennas and Propagation, vol. 50, No. 5, pp. 561–570, May 2002.
[103] J. Mar, Y. Lin, and Y. Yeh,"Ultra-wide bandwidth in-vehicle channel measurements using chirp pulse sounding signa" IET Science, Measurement and technology, Vol. 3, No. 4, pp. 271 – 278, 2009.
[104] A. F. Molisch, "Ultra-wideband Propagation Channels", Proceedings of the IEEE, Vol. 97, No. 2, pp.353-371, 2009.
[105] J. Keignart and N. Daniele, "Subnanosecond UWB channel sounding in frequency and temporal domain", in Proc. UWBST 2002, 2002, pp. 25–30.
[106] J. G. Proakis and M. Salehi, Digital communications, 5th edition, McGraw Hill, New York, 2005.
[107] P. Smudlers, Y. Haibing, I. Akkermans,"On the design of Low-Cost 60-GHz Radios for Multigigabit-per-Second Transmission over Short Distances", IEEE Communications Magazine, Vol. 45, No. 12, pp. 44-52, 2007.
[108] P. Smulders, "Statistical Characterization of 60-GHz Indoor Radio Channels", IEEE Transaction on Antennas and Propagation, Vol. 57, No. 10, pp. 2820-2829, 2009.
[109] http://www.millitech.com/pdfs/specsheets/IS000025-SGH.pdf
[110] J. Jaouhar, P. Eggers, G. Pedersen, and K. Thomas," Calibration of a UWB Sub-Band Channel Model Using Simulated Annealing", IEEE Transactions on Antennas and Propagations, Vol. 57, No. 10, October 2009.
[111] M. Zhao, J. Shea, S. Hagness, and D. Weide,"Calibrated Free-Space Microwave Measurements with an Ultrawideband Reflectometer- Antenna System", IEEE Microwave and Wireless Components Letters, Vol. 16, No. 12, December 2006.

[112] C. Liang, S. Liu, and L. Shen, "A Calibrated Pulse generator for Impulse-Radio UWB Applications", IEEE Journal of Solid-State Circuits, Vol. 41, No. 11, November 2006.
[113] G. Matz, A. F. Molisch, F. Hlawatsch, M Steinbauer, and I. Gaspard, " On the Systematic Measurement Errors of Correlative Mobile Radio Channel Sounders", IEEE transactions on Communications, Vol. 50, No. 5, May 2002.
[114] I. Guvenc, G. Sinan, S. Zafer and K. Ulas, Reliable Communications for short-range Wireless Systems, Cambridge University Press, 2011.
[115] G. Suiyan and P. Vainkainen, 'Millimeter-Wave Propagation in Indoor Corridors", IEEE Letters on Antennas and Wireless Propagation, Vol. 8, No. pp. 1242-1245, 2009.
[116] X. Zhao, G. Suiyan, L. Vuokko, J. Kivinen and P. Vainkainen,"Polarization Behaviours at 2.5 and 60 GHz for Indoor Mobile Communications", Wireless Personal Communications, Kluwer, 2003.
[117] A. A. M. Saleh and R. A. Vlenzuela, "A statistical model for indoor multipath propagation", IEEE Journal on selected areas in communications, Vol. e, No. 2, pp. 128-137, 1987.
[118] Y. Shoji, H. Sawada, C. Choi, H. Ogawa, "A Modified SV-Model Suitable for Line-of-Sight Desktop Usage of Millimeter-Wave WPAN Systems", IEEE Transactions on Antennas and Propagation, Vol. 57, No.10, pp. 2940 – 2948, 2009.
[119] M. Ghavami, L. B. Michael and R. Kohno, Ultra Wideband Signals and Systems in Communication Engineering, Wiley, UK, 2004.
[120] J. B. Keller, "The geometrical theory of diffraction," Proceedings of the Symposium on Microwave Optics, June 1953, Eaton Electronics Research Laboratory, McGill University, Montreal, Canada.
[121] S. D. Kumar, Mobile Handset Design, Wiley, 2010.
[122] P.H. Pathak, N. Wang, W.D. Burnside, and R.G. Kouyoumjian, " A Uniform GTD solution for the radiation form sources on a convex surface," IEEE trans. Antennas and propagation, Vol. AP-29, No. 4, pp.609-621, July 1981.
[123] P.H. Pathak and N.Wang, "Ray Analysis of Mutual Coupling between Antennas on a Convex Surface," IEEE Trans. Antenna and Propagation, Vol. 6, pp. 911-922, Nov. 1981.
[124] P.H.Pathak, W.D.Burnside and R.J.Marhefka,"A Uniform GTD Analysis of the Diffraction of Electromagnetic Waves by a Smooth Convex Surface" IEEE Transactions on Antenna and Propagation, vol. AP-28, No.5, September 1980.
[125] A. Sadri,"802.15.3c Usage Model Document (UMD), Draft 06/055r22" IEEE P802.15 Working Group for Wireless Personal Area Networks (WPANs), March 2007.
[126] A. Maltsev, R. Maslennikov, A. Sevastyanov, A. Lomayev, A. Khoryaev, A. Davydov, and V. Ssorin, " Characteristics of inddor millimiter-wave channel at 60 GHz in application to perspective WLAN system", Antennas and Propagation EUCAP Proceedings, 2010.
[127] P. Smudlers, "Statistical Characterization of 60-GHz Indoor Radio Channels", IEEE Transactions on Antennas and Propagation, Vol. 57, No. 10, October 2009.
[128] A. Maltsev, E. Perahia, R. Maslennikov, A. Sevastyanov, A. Lomayev, and A Khoryaev,"Impact of Polarization Characteristics on 60-GHz Indoor Radio Communication System", IEEE Antennas ans Wireless Propagation Letters, Vol. 9, 2010.
[129] S. Geng, J. Kivinen, X. Zhao, and P. Vainikainen, "Millimeter-wave propagation channel characterization for short-range wireless communications," IEEE Trans. Veh. Technol., vol. 58, no. 1, pp. 3–13, Jan.2009.

[130] J. Kivinen, “60-GHz wideband radio channel sounder,” IEEE Trans. Instrum. Meas., vol. 56, no. 5, pp. 1831–1838, Oct. 2007.
[131] C. R. Anderson and T. S. Rappaport, “In-building wideband partition loss measurements at 2.5 and 60 GHz,” IEEE Trans. Wireless Commun., vol. 3, no. 3, pp. 922–928, May 2004.
[132] P. Pagani, N. Malhouroux, I. Siaud, and V. Guillet, Characterization and Modeling of the 60 GHz Indoor Channel in the Office and Residential Environments, Doc. IEEE P802.15-06-0027-01-003c, IEEE P802.15 Working Group for WPANs, Jan. 2006.
[133] A. G. Siamarou,” Wideband Propagation Measurements and Channel Implications for Indoor Broadband Wireless Local Area Networks at the 60 GHz band,” Wireless Personal Communications, Vol. 27, No. 1, pp. 89-98, Hingham, MA, USA: Kluwer Academic Publishers, Oct. 2003.
[134] D.C. Cox, R. Leck, “Correlation bandwidth and delay spread multipath propagation statistics for 910 MHz urban mobile channels,” IEEE Trans. Commun., Vol. 23, No. 11, pp. 1271-1280, 1975.
[135] M. Sanchez, A. Hammoudeh, E. Grindrod, and J. Kermol,”Coherence Bandwidth Characterization in an Urban Microcell at 62.4 GHz”, IEEE Transactions on Vehicular Technology, Vol. 49, No. 2, March 2000.
[136] A. Hammoudeh, J. Kermol, and M. Sanchez, ”Coherence bandwidth measurements in an indoor microcell at 62.4 GHz”, Electronic Letter, Vol. 34, No. 5, 1998.
[137] A. G. Siamarou, “Wireless Local Area Radio Network: Wideband Characterisation and Measurements at 62.4 GHz”’ Phd Thesis, University of Glamorgan, UK, June 2001.
[138] J. D. Parsons, The mobile radio propagation channel, Pentech Press, 1992.
[139] W. C. Jakes, Microwave Mobile Communications, McGraw-Hill, NewYork, 1989.
[140] D. Scammell, A. Hammoudeh, and M. Sanchez, ”Estimating Channel Performance for Time Invariant Channels.”, Electronic Letters, Vol. 40, No. 12, June 2004.
[141] X. Chen, P. Kilfal, C. Orleniuns, and J. Carlsson,“Channel Sounding of Loaded Reverberation Chamber for Over-the-Air Testing of Wireless Devices— Coherence Bandwidth Versus Average Mode Bandwidth and Delay Spread”, IEEE Antennas and Wireless propagation Letters, Vol.8, 2009.
[142] J. D. Parson, The mobile radio propagation channel, Wiley, 2000.
[143] N. Al-Dahir, “Single Carrier Frequency Domain Equalization for Space-Time Blok-Coded Transmission over Frequency Selective Fading Channels”, IEEE Communications Letters, July 2001, Vol. 5, No. 7, pp. 304-306.
[144] O. Delangre, Ph. De Doncker, M. Lienard and P. Degauque, ”Delay spread and coherence bandwidth in reverberation chamber”, IEEE Letters on Antennas and Wireless Propagation, Vol. 8, pp. 678-681, 2009.
[145] N. Namgoong, and J. Lehnert, “ Performance of DS/SSMA Systems in Frequency Selective Fading”, IEEE Transaction on Wireless communication, April 2002, Vol. 1, No. 2, pp. 236-244.
[146] X.Tao, et. al., “Channel Modeling of Layered Space-Time Code under Frequency Selective fading Channel”, Proceedings of ICCT2003, May 2003, Berlin Germany.
[147] W. C. Lee, Mobile Cellular Telecommunications Systems, McGraw Hill Publications, New York, 1989.
[148] D. Scammell, A. Hammoudeh and M. G. Sanchez,” Estimating channel performance for time invariant channels,” Electronic Letters, Vol. 40, No. 12, June 2004.

[149] M. Yacoub, J. Baustia and L. Guedes,"On higher order statistics of the Nakagami-m distribution", IEEE Transactions on vehicular technology, vol. 48, No. 3, May 1999.
[150] R. Mallik, "A New Statistical Model of the Complex Nakagami-m Fading Gain" IEEE Transactions on Communications, Vol. 58, No. 9,pp. 409-412, September 2010.
[151] C. Seol, K. Cheun, and S. Hong"A Statistical Inter-Cell Interference Model for Downlink Cellular OFDMA Networks Under Log-Normal Shadowing with Ricean Fading", IEEE Communications Letters, Vol. 14, No. 11, pp. 1011-1013, November 2010.
[152] R. Prasad, OFDM for Wireless Communications Systems, Artech House, Aug. 2004.
[153] M. Nakagami, The m-distribution – a general formula of intensity distribution of rapid fading, reprint from Statistical Methods of Radiowave Propagation, Pergamon Press, 1960.
[154] M. Rahman, C. Sun, R. Funada, T. Baykas, J. wang, S. Sasaki, H. Harada, and S. Kato," Error Rate Analysis of Band-Limited BPSK with Nakagami/Nakagami ACI Considering Nonlinear Amplifier and Diversity"' IEEE Transactions on Vehicular Technology, Vol. 59, No.3, March 2010.
[155] Q. T. Zhang, A generic correlated Nakagami fading model for wireless communications, IEEE Transactions on Communications, 51 (11), 1745–1748, 2003.
[156] W. L. Stutzman and G. A. Thiele, Antenna Theory and Design, 2nd edition. New York: Wiley, 1998.
[157] H. Thomas, et al., "An experimental study of the propagation of 55 GHz millimeter waves in an urban mobile radio environment," IEEE Transactions on Vehicular Technology, Vol. 43, No.1, pp.140–146, 1994.
[158] H.B. Yang, M.H Herben, and P. Smulders, "Impact of antenna pattern and reflective environment on 60 GHz indoor radio channel characteristics," IEEE Antennas and Wireless Propagation Letters, 2005.
[159] D. C. Cox, R. Murray, and A. Norris, "800 MHz attenuation measured in and around suburban houses," AT&T Bell Lab. Tech. J., vol. 673, no. 6, Jul.–Aug. 1984.
[160] R. C. Bernhardt, "Macroscopic diversity in frequency reuse systems,"IEEE J. Sel. Areas Commun., vol. SAC-5, pp. 862–878, Jun. 1987.
[161] Project: IEEE P802.15 Working Group for Wireless Personal Area Networks (WPANs), IEEE 802.15-05/0634r
[162] T. Weiss, J. Hillenbrand, A. Krohn, and F.K. Jondral, "Mutual interference in OFDM-based spectrum pooling systems," in Proc. IEEE Vehicular Technology Conf., Milan, Italy, 17–19 May 2004, pp. 1873–1877.
[163] S. Kapoor and S. Nedic, "Interference suppression in DMT receivers using windowing," in Proc. IEEE Int. Conf. on Communications, vol. 2, (New Orleans, LA, USA), pp. 778–782, June 2000.
[164] P. Smulders, H. Yang, and I. Akkermans, "On the design of low-cost 60-GHz radios for multigigabit-per-second transmission over short distances," IEEE Commun. Mag., vol. 45, no. 12, pp. 44–51, Dec. 2007.
[165] J.Y. Wang, Z. Lan, et.al., "Robust and highly efficient beamforming procedures for 60GHz WPAN", IEEE 802.15-08-0190-003c, Nov. 2008.
[166] M. Takai et. al, "Directional Virtual Carrier Sensing for Directional Antennas in Mobile Ad Hoc Networks", Proc. ACM MOBIHOC, pp.183-192, 2002.
[167] M. Jacob and T. Kürner, "Radio channel characteristics for broadband WLAN/WPAN applications between 67 and 110 GHz," in Proc. Eur, Conf. Antennas and Propag., pp. 2663–2667, Berlin, Germany, Mar. 2009.

[168] D. M. Matic, H. Harada, and R. Prasad, "Indoor and outdoor frequency measurements for mm-waves in the range of 60 GHz," IEEE proceedings in Vehicular Technology Conference 1998.
[169] R Davies, M. Bensebti, M. Beach, and J. McGeehan,"Wireless propagation measurements in indoor multipath environments at 1.7 GHz and 60 GHz for small cell systems," *IEEE Vehicular Technology Conference*, 1991.
[170] P.Smulders, Broadband wireless LANs: a feasibility study. Ph.D. thesis, Eindhoven University, 1995.
[171] A. Siamarou, and M. Al-Nuaimi, "Multipath delay spread and signal level measurements for indoor wireless radio channel at 62.4 GHz," IEEE Vehicular Technology Conference, 2001.
[172] H. Xu, V. Kukshya, and T. S. Rappaport, "Spatial and temporal characteristics of 60 GHz indoor channels," IEEE J. Select. Areas Commun., vol. 20, no. 3, pp. 620-630, Apr. 2002.
[173] M. Peter et al, "Measurement and analysis of the 60 GHz in-vehicular broadband radio channel", in Proc. of IEEE Veh. Technol. Conf. (VTC- 2007), 2007, pp. 834-838.
[174] B. Neekzad, K. Sayrafian-Pour, J. Perez, and J. S. Baras, "Comparison of ray tracing simulations and millimeter wave channel sounding measurements", in Proc.of 18th Annual IEEE Int. Symp. on Personal, Indoor and Mobile Radio Commun., (PIMRC'07).
[175] M. Fiacco, M. Parks, H. Radi, and S. Saunders, Final report: Indoor propagation factors at 17 and 60 GHz. Technical report, Radio-communications Agency, University of Surrey, August 1998.
[176] T. Manabe, K. Sato, H. Masuzawa, K. Taira, T. Ihara, Y. Kasashima, and K. Yamaki, "Polarization dependence of multipath propagation and high-speed transmission characteristics of indoor millimeter-wave channel at 60 GHz,". IEEE Transactions on Vehicular Technology, Vol. 44, No. 2, pp. 268–274, 1995.
[177] Park, J.H, Kim, Y., Hur, Y.S, Lim, K. and Kim, K.H (1998) Analysis of 60 GHz band indoor wireless channels with channel configurations. IEEE International Symposium on Personal, Indoor and Mobile Radio Communications, pp. 617–620.
[178] M.R. Williamson, G.E. Athanasiadou, and A.R. Nix, "Investigating the effects of antenna directivity on wireless indoor communication at 60 GHz," Proceedings of the IEEE Symposium on Personal, Indoor and Mobile Radio Communications, vol. 2, pp. 635–639, September 1997.
[179] L. Yang, Multicarrier Communications, Wiley, UK, 2009.
[180] M. Alasti, B. Neekzad, J. Hui, R. Vannithamby, " Quality of service in WiMAX and LTE networks: Topics in Wireless Communications," IEEE Communications Magazine, Vol. 48, No. 5, pp. 104-111, May 2010.
[181] N. Cvijetic, D. Qian, J.Hu, " 100 Gb/s optical access based on optical orthogonal frequency-division multiplexing," *IEEE Communications Magazine*, Vol. 48, No. 7, July 2010.
[182] B. Joseph, *Signal Processing for Wireless Communications*, McGraw Hill, 2008.
[183] B. Shreng, J. Zheng, X. You, and L. Chen, "A Novel Timing Synchronization Method for OFDM Systems", IEEE Communications Letters, Vol. 14, No. 12, December 2010.
[184] B. Awoseyila, C. Kasparis, and G. Barry, 'Robust Time-domain Timing and Frequency Synchronization for OFDM Systems', *IEEE Transaction on Consumer Electronics*, Vol. 55, No. 2, pp. 391-399, May 2009.
[185] H. Rohling, OFDM: Concepts for Future Communication Systems, Springer, 2011.

[186] J. G. Andrews, Arunabha Ghosh and Rias Muhamed," Fundamentals of WiMAX-understanding Braodband Wireless Networking", Prentice Hall, Feb, 2007.
[187] R. Parasad, F. J. Velez, WiMAX Networks: Techno-Economic and Challenges, Springer, London, 2010.
[188] R.V. Nee, R. Prasad, OFDM for Wireless Multimedia Communications, Artech House, Boston, MA, 2000.
[189] I. Kim, Y. Han, H. Chung, "An Efficient Synchronization Signal Structure for OFDM-Based Cellular Systems", IEEE Transactions on Wireless Communications, Vol. 9, No. 1, January 2010.
[190] R. Daniels, J. Murdock, T. Rappaport, and R. Heath,"60 Ghz Wireless: Up Close and Personal", *IEEE Microwave Magazine*, Vol. 11, No. 7, pp. 44-50, 2010.
[191] A. Vallvaraj, B. Stewart, D. Harrison, F. McIntosh, "Reducing the PAPR of OFDM Using a Simplified Scrambling SLM Technique with No Explicit Side Information" 14th IEEE International Conference on Parallel and Distributed Systems, 2008.
[192] Q. Daiming, W. Zhiqiang , and T. Jiang, "Extended Active Interference Cancellation for Side-lobe Suppression in Cognitive Radio OFDM Systems With Cyclic Prefix", IEEE Transactions on Vehicular Technology, Vol. 59, No. 4, May 2010.
[193] T. Al-Naffouri and A. Ahmed, "Cyclic Prefix Based Enhanced Data Recovery in OFDM", IEEE Transactions on Signal Processing, Vol. 58, No. 6, June 2010.
[194] M. Ergen, Mobile Broadband Including WiMAX and LTE, Springer, 2009.
[195] R. Prasad, OFDM for Wireless Communications Systems, Artech House, Aug. 2004.
[196] A. Sulyman, M. Hefnawi, " Capacity-aware linear MMSE detector for OFDM-SDMA systems", IET Communications, Vol. 4, No. 9, pp. 1059-1064, 2010.
[197] S. Ahson, M. Ilyas, WiMAX : technologies, performance analysis, and QoS, CRC Press, 2009.
[198] X. Gao, W. Wang, X. Xia, E. Au, and X. You,"Cyclic Prefixed OQAM-OFDM and its Application to Single-Carrier FDMA", IEEE Transaction on Communications, Vol. 59, No. 5, pp. 1467-1480, May 2011.
[199] T. Waterschoot, V. Nir, J. Duplicy, and M. Moonen, "Analytical Expressions for the Power Spectral Density of CP-OFDM and ZP-OFDM Signals", IEEE Signal Processing Letters, Vol. 17, No. 4, pp. 371-374, January 2010.
[200] IST MAGNET, Update D3.2.2a "Candidate Air Interfaces and Enhancements" IST-507102, My personal Adaptive Global Net project, Deliverable D3.2.2b, December 2005.
[201] I. Siaud, A Ulmer-Moll," Advanced Dynamic Binary Interleaving Codes for UWB-OFDM WPAN Systems", IEEE GLOBCOM Workshops, 2009.
[202] I. Siaud, A. Ulmer-Moll,"Harmonized multi-RF band UWB-OFDM air interfaces for WPAN applications", IEEE 20th International Symposium on Personal Indoor and Mobile Radio Communications, 2009.
[203] L. Eastwood, S. Migaldi, Q. Xie, and V. Gupta, "Mobility using IEEE 802.21 in a heterogeneous IEEE 802.16/802.11-based, IMT advanced (4G) network," IEEE Wireless Commun., Vol. 15, No. 2, pp.26–34, Apr. 2008.
[204] R. Merritt, "60 GHz groups face off in Beijing over Wi-Fi's future," EE Times, May 18, 2010. [Online] Available: http://www.eetimes.com/electronics-news/4199522/60-GHzgroups-face-offin-Beijing-over-Wi-Fi-s-future.
[205] E. Perahia, C. Cordeiro, M. Park, and L. L. Yang,; , "IEEE 802.11ad: Defining the Next Generation Multi-Gbps Wi-Fi," IEEE Consumer Communications and Networking Conf. (CCNC), 2010 7th IEEE, Vol., No., pp. 1–5, 9–12, January 2010.

[206] "WiGig White Paper: Defining the Future of Multi-Gigabit Wireless Communications," July 2010, http://www.wirelessgigabitalliance.org/specifications/
[207] http://www.wigwam-project.de
[208] C. Choi, E. Grass, F. Herzel, M. Piz, K. Schmalz, S. Yaoming, S. Glisic, M. Krstic, K. Tittelbach, M. Ehrig, W. Winkler, R. Kraemer, and C. Scheytt,"60 GHz OFDM Hardware Demonstration in SiGe BiCMOS: State-of-the art and Future Development", IEEE 19th International Symposium on Personal, Indoor and Mobile radio Communications, Cannes, September 2008.
[209] C.-S. Choi, M. Piz, and E. Grass,"Prformance Evaluation of Gbps OFDM PHY layers for 60-GHz Wireless LAN Applications" IEEE 20th International Symposium on Personal, Indoor and Mobile radio Communications, Cannes, September 2009.
[210] C. Choi, E. Grass, M. Piz, M. Marinkovic, R. Kraemer, and C. Scheytt, " 60-GHz OFDM Systems for Multi-Gigabit Wireless LAN Applications," IEEE 7th Consumer Communications and Networking Conference (CCNC), 2010.

List of Publications

Ghaddar M., Talbi L., Delisle G. and Lebel J. "Indoor NLOS Propagation Measurements for mm-waves WLAN systems," PIERS Letters, submitted on February 2012.

Ghaddar M., and Talbi L.,"Broadband Propagation Measurement and Characterization in the Unlicensed 60 GHz Band," IET Letters, submitted on February 2012.

Ghaddar M., Talbi L. and Delisle G., "Modeling Indoor Broadband Propagation Channel in the 60 GHz Band" EURASIP Journal on wireless communications and networking, submitted on January 2012.

Ghaddar M., Talbi L., and Delisle G. "Deflecting Obstacles Effects on Signal propagation in the 60 GHz Band," IEEE Transactions on antennas and propagation, submitted on January 2012.

Ghaddar M. and Talbi L., "NLOS UWB Undermining Experimental Characterization and Performance Evaluation Using MB-OFDM," Progress in Electromagnetics Research Symposium (PIERS), Morocco, March 2011.

Rissafi Y., Talbi L. and **Ghaddar M**., "Experimental Characterization of an UWB Propagation Channel in Underground Mines," *IEEE Transactions on Antennas and Propagation*, Vol. 60, No. 1, pp. 240-246, January 2012.

Ghaddar M. Talbi L. and Lebel J.,"Alternate data transmission relaying scheme for outdoor NLOS broadband communication" *IEEE, Antennas and Propagation Society International Symposium* (APS), pp. 1- 4, Charleston, SC, USA, June 1-5, 2009.

Ghaddar M. Talbi L. and Lebel J., "Microwave scatters evaluation for indoor/outdoor broadband coverage and data transmission", *IEEE, 22nd Canadian Conference on Electrical and Computer Engineering* (CCECE), pp. 1071 – 1075, St. Johnn's Newfoundland and Labrador, Canada May3-6, 2009.

Ghaddar M. Talbi L. and Lebel J., "Performance Evaluation of Wireless Indoor Broadband Datacasting Based on Microwave Scatter", International Conference on Wireless Comunications in underground and Confined Area (ICWCUCA), August 2008.

Ghaddar, M., Talbi L., Denidni T.A., Sebbak A., " A Conducting Cylinder for Modeling Human Body Presence in Indoor propagation Channel", *IEEE transaction on Antennas and propagation*, vol. 55, No. 11, pp. 3099-3103, November 2007.